

## Abstract

# Optical Production of Ultracold Polar Molecules

Jeremy Sage

2006

We demonstrate the production of a sample of ultracold RbCs molecules in their absolute vibrational ground state with a translational temperature of  $\sim 100 \mu\text{K}$  and a narrow distribution of rotational states. The molecules are initially formed from laser-cooled  $^{85}\text{Rb}$  and  $^{133}\text{Cs}$  atoms via photoassociation and are produced in excited electronic vibrational levels. A fraction of these excited molecules subsequently spontaneously decay to ground electronic states, populating many excited vibrational levels. We transfer the population of one such level to the  $X^1\Sigma^+(v=0)$  ground state by a stimulated emission pumping (SEP) technique. In order to efficiently produce these ground state molecules it is necessary to have detailed spectroscopic information about the levels to which we photoassociate the molecules, the levels to which they spontaneously decay, and the levels involved in the SEP transfer. To this end, we carry out and analyze photoassociation spectroscopy and resonance enhanced multi-photon ionization spectroscopy of relevant vibrational levels of excited and ground state electronic potentials.

# Optical Production of Ultracold Polar Molecules

A Dissertation  
Presented to the Faculty of the Graduate School  
of  
Yale University  
in Candidacy for the Degree of  
Doctor of Philosophy

by  
Jeremy Sage

Dissertation Director: David DeMille

May 2006

Copyright © 2006 by Jeremy Sage

All rights reserved.

# Acknowledgements

Truly none of this would have been possible without my advisor David DeMille. Conceiving of the idea for this thesis work is only a small part of his influence on my education. In my experience, his willingness and ability to explain the most trivial and complex concepts with equal clarity and enthusiasm is unparalleled. His creativity and knowledge are staggeringly immense and through his patience, humility, and kindness he offered me the opportunity to learn from him as much as I chose.

I had the great fortune to work with Jamie Kerman while he was a postdoc here. His passion and drive propelled our experiment forward at a rate I did not think possible; he showed me how incredibly effective the combination of hard work and a superior intellect can be. Nearly every useful experimental technique I know I learned from Jamie. He is a great friend and I cannot think of anyone I'd rather have with me to beat into submission a complex experiment intent on thwarting our every move.

I must thank Tom Bergeman who is essentially responsible for all of the theoretical analysis of the spectroscopic data we obtained. I am extremely grateful not only for this contribution, but also for his experimental insight. His willingness to discuss his work and explain it to me at a level I could comprehend made our collaboration, for me, both a learning experience and a pleasure.

Thanks to the many graduate students, postdocs, and researchers in the DeMille group, past and present, who have always made time to talk, whether it be about physics or anything but.



Thanks to Matthew Fenselau and Irfon Rees for helping me to survive the first few years of graduate school.

Thank you to my parents for their limitless supply of love and support. Thanks to my sister Holly for stopping by New Haven for a while and saying hello.

And thank you Charlotte for everything else.

# Contents

<b>Acknowledgements</b>	<b>iii</b>
<b>1 Introduction</b>	<b>1</b>
1.1 Applications of Ultracold Polar Molecules . . . . .	4
1.1.1 Quantum Computation . . . . .	4
1.1.2 Chemistry at Ultracold Temperatures . . . . .	7
1.1.3 Many-body Systems . . . . .	7
1.1.4 Electric Dipole Moment of the Electron . . . . .	8
1.2 Techniques of Cold Polar Molecule Production . . . . .	9
1.2.1 Buffer-gas Cooling . . . . .	10
1.2.2 Stark Slowing . . . . .	11
1.2.3 Cooling via Billiard-like Collisions . . . . .	13
1.3 Summary . . . . .	14
<b>2 Cooling and Trapping of Rb and Cs Atoms</b>	<b>15</b>
2.1 Theory of Atomic Laser Cooling . . . . .	15
2.1.1 Temperature in Laser Cooling . . . . .	16
2.1.2 Doppler Cooling: Optical Molasses . . . . .	17
2.2 The Magneto Optical Trap (MOT) . . . . .	21
2.2.1 Simple Model of the MOT . . . . .	21
2.2.2 Trapping $^{85}\text{Rb}$ and $^{133}\text{Cs}$ . . . . .	23

2.2.3	Forced Dark SPOT . . . . .	25
2.2.4	MOT Loading and Loss . . . . .	28
2.3	Dual Species MOT Experimental Apparatus . . . . .	29
2.3.1	Vacuum System . . . . .	29
2.3.2	Magnetic and Electric Fields . . . . .	35
2.3.3	Diode Laser System . . . . .	37
2.3.4	Diode Laser Frequency Stabilization . . . . .	40
2.3.5	MOT Optics Setup . . . . .	46
2.4	MOT Diagnostics . . . . .	52
2.4.1	Atom Number Measurement . . . . .	53
2.4.2	Density Measurement and MOT Spatial Overlap . . . . .	53
2.4.3	Temperature Measurement . . . . .	56
2.5	Summary . . . . .	56
<b>3</b>	<b>Production of Ultracold RbCs* Molecules via Photoassociation</b>	<b>57</b>
3.1	Review of Molecular Theory . . . . .	57
3.1.1	Born-Oppenheimer Approximation . . . . .	57
3.1.2	Molecular Transitions: The Franck-Condon Principle . . . . .	60
3.1.3	Molecular State Labelling and Transition Selection Rules . . . . .	63
3.2	Photoassociation . . . . .	67
3.2.1	Ultracold Collisions . . . . .	67
3.2.2	Photoassociation as Three Channel Inelastic Scattering . . . . .	73
3.2.3	Photoassociation Transitions . . . . .	75
3.2.4	Heteronuclear vs. Homonuclear Photoassociation . . . . .	78
3.3	Experimental Photoassociation and Detection of RbCs* . . . . .	79
3.3.1	Photoassociation Experiment Overview . . . . .	81
3.3.2	Experimental Apparatus and Measurement . . . . .	83
3.4	Results of Photoassociation Experiments . . . . .	89

3.4.1	Photoassociation Spectroscopy . . . . .	89
3.4.2	Photoassociation and Molecular Production Rates . . . . .	98
3.4.3	Measurement of RbCs* Electric Dipole Moment . . . . .	99
3.5	Summary . . . . .	101
<b>4</b>	<b>State-Selective Detection of Ground State RbCs</b>	<b>102</b>
4.1	Detection Method . . . . .	102
4.1.1	Spontaneous Decay . . . . .	102
4.1.2	Resonance-enhanced Multi-photon Ionization Detection . . . . .	103
4.2	Experimental Apparatus . . . . .	108
4.2.1	Ion Detector and Vacuum System . . . . .	108
4.2.2	Photoassociation Laser Frequency Stabilization . . . . .	111
4.2.3	Pulsed Laser System . . . . .	113
4.2.4	Data Acquisition and Processing . . . . .	119
4.3	Results of Ground State RbCs Detection . . . . .	123
4.3.1	Searching for $X^1\Sigma^+$ State Molecules . . . . .	124
4.3.2	Detection of $a^3\Sigma^+$ State Molecules . . . . .	126
4.3.3	Temperature Measurement of $a^3\Sigma^+$ State Molecules . . . . .	136
4.3.4	Ground $a^3\Sigma^+$ State Molecule Production Rate . . . . .	138
4.4	Summary . . . . .	139
<b>5</b>	<b>Production of Ultracold RbCs in the <math>X^1\Sigma^+(v=0)</math> State</b>	<b>140</b>
5.1	Stimulated Emission Pumping and Detection . . . . .	140
5.2	Experimental Apparatus . . . . .	143
5.2.1	Photoassociation and Pulsed Lasers . . . . .	143
5.2.2	Pulsed Laser Timing . . . . .	145
5.2.3	Data Acquisition . . . . .	148
5.3	Ion Dip Detection Diagnostic . . . . .	150
5.4	Results of SEP Transfer . . . . .	155

5.4.1	Observation of Ground State Transfer . . . . .	155
5.4.2	Properties of the Ground State Molecular Sample . . . . .	159
5.4.3	UPM Production Rate . . . . .	162
5.5	Summary . . . . .	163
<b>6</b>	<b>Conclusion</b>	<b>164</b>

# List of Figures

1.1	Overview of the optical production of ultracold RbCs . . . . .	3
1.2	Ultracold polar molecule quantum computer . . . . .	5
1.3	Qubit levels of a UPM quantum computer . . . . .	6
2.1	Simple MOT trapping scheme . . . . .	22
2.2	Hyperfine structure and MOT transitions in RbCs . . . . .	24
2.3	Light-assisted collisions . . . . .	26
2.4	Schematic of vacuum system . . . . .	30
2.5	Schematic of home-made window seal . . . . .	32
2.6	Rb and Cs sources (cold fingers) . . . . .	33
2.7	Schematic of ring electrodes . . . . .	36
2.8	Schematic of tuneable diode laser . . . . .	38
2.9	Slave laser injection . . . . .	39
2.10	Schematic of saturated absorption spectroscopy . . . . .	42
2.11	Laser frequency stabilization setup . . . . .	44
2.12	Schematic of lasers and optics for trap and repump beams . . . . .	47
2.13	Schematic of dark SPOT beams . . . . .	50
3.1	The Franck-Condon principle . . . . .	61
3.2	Hund's coupling cases . . . . .	65
3.3	The photoassociation process. . . . .	68
3.4	Plot of $ S_{0a}^{0,red} ^2$ versus $\Gamma$ . . . . .	74

3.5	The Franck-Condon principle for free-bound transitions . . . . .	77
3.6	Comparison between homonuclear and heteronuclear photoassociation . . .	80
3.7	RbCs levels involved in photoassociation . . . . .	82
3.8	Schematic of optics and electronics for build-up cavity lock . . . . .	85
3.9	Observation of photoassociation to $\Omega = 0^\pm$ levels . . . . .	90
3.10	Comparison between observed and model $\Omega = 0^\pm$ levels . . . . .	93
3.11	Comparison between deeply and weakly bound rotational series . . . . .	94
3.12	Population of the $X$ state via spontaneous emission . . . . .	96
3.13	Photoassociation to an $\Omega \neq 0$ level . . . . .	97
3.14	Measurement of Stark shift in polar RbCs* . . . . .	100
4.1	Detection of ground state RbCs . . . . .	105
4.2	Ion detection . . . . .	107
4.3	Channeltron gain vs. bias voltage . . . . .	109
4.4	Schematic of photoassociation laser lock . . . . .	112
4.5	Schematic of Sirah dye laser . . . . .	114
4.6	Stimulated Raman scattering . . . . .	118
4.7	Time of flight ion signal . . . . .	120
4.8	Search for weakly bound $X^1\Sigma^+$ state molecules . . . . .	125
4.9	Search for $X^1\Sigma^+$ state molecules by comparison of ion data for $0^+$ and $0^-$ photoassociation . . . . .	127
4.10	Detection of ground state $a^3\Sigma^+$ molecules and excited state spectroscopy .	129
4.11	Spectroscopy and population distribution of the $a^3\Sigma^+$ state . . . . .	130
4.12	Dependence of $a$ state population on photoassociation to different RbCs* levels . . . . .	135
4.13	Temperature measurement of $a^3\Sigma^+(v = 37)$ state molecules . . . . .	137
5.1	Formation and detection of $X^1\Sigma^+(v = 0)$ state RbCs . . . . .	141
5.2	Schematic of the TDL60 (“red”) dye laser . . . . .	144

5.3	Schematic of optical setup for SEP and detection beams . . . . .	146
5.4	Time of flight signal for direct ion detection . . . . .	149
5.5	Rb level scheme for ion dip detection diagnostic . . . . .	151
5.6	Ion dip detection in Rb atoms . . . . .	152
5.7	Spectral distribution of a pulsed laser with multiple longitudinal modes . .	154
5.8	Detection of $X^1\Sigma^+(v = 0, 1)$ molecules . . . . .	156
5.9	Scan between $v = 0$ and 1 resonances using ion dip detection . . . . .	158
5.10	Scan between $v = 0$ and 1 resonances using direct detection . . . . .	159
6.1	Scheme for purifying the $X^1\Sigma^+(v = 0)$ molecular sample in a QUEST . . .	167



# List of Tables

2.1	Summary of frequency locking and AOM shifts . . . . .	49
3.1	Summary of observed photoassociation resonances . . . . .	92
4.1	Summary of laser dyes and Stokes orders used to generate the resonant detection pulse . . . . .	116
4.2	Summary of theoretical model of $c/B/b$ mixing . . . . .	134
5.1	Summary of observed ion dip resonances . . . . .	157

# Chapter 1

## Introduction

In 1975 it was suggested that a monochromatic light source could be used to cool a room temperature atomic gas by exerting velocity dependent forces on the atoms [1, 2]. By shining this light with a well chosen frequency on the gas from all directions, it was proposed that a viscous medium within which the atoms move would be created. In 1985 the experimental realization of this idea, termed “optical molasses,” was demonstrated [3]. The sodium atoms used were cooled to a temperature only a few ten-thousandths of a degree above absolute zero. Two years later, an experiment demonstrated that ten million of these atoms could be contained in spherical volume of only 0.5 mm diameter using a novel trapping scheme consisting of well chosen laser polarizations and applied magnetic field; this trap was termed the Magneto Optical Trap (MOT) [4]. It was quickly realized that such samples of ultracold, trapped atoms could have many applications. Indeed, they ultimately have been used, among other things, to do high precision atomic spectroscopy [5, 6], to build an atomic fountain clock [7] which currently defines the second to roughly one part in  $10^{15}$ , to measure gravitational acceleration using matter wave interferometry [8], and to demonstrate Bose-Einstein condensation [9, 10].

Despite the many successes of atomic laser cooling and trapping, it became clear that the techniques involved could be applied only to a small number of atomic species and would not work at all for even the simplest diatomic molecules. Ultracold molecules are

particularly interesting because their rich internal (vibrational and rotational) structure permits applications not accessible with atoms. For instance, it has recently been proposed that a sensitive test of the time variation of the electron to proton mass ratio could be done by exploiting closely spaced vibrational levels in ultracold, trapped  $^{133}\text{Cs}_2$  [11]. Arguably more interesting and fruitful, though, is the production of a sample of ultracold *polar* molecules (UPMs). Due to their extremely strong, anisotropic, and tuneable interactions, UPMs could potentially be used in applications as varied as scalable quantum computation [12], the study of chemistry in the ultracold regime [13], the creation of novel types of many-body systems [14, 15, 16], and the probing of phenomena beyond the standard model of particle physics [17]. It therefore seems worthwhile to investigate techniques capable of cooling polar molecules; however the same complex internal structure that makes these molecules ideal for the above applications is precisely what renders the methods of atomic laser cooling so ineffectual.

It is with this motivation that we began the experiments described in this thesis, ultimately producing a sample of UPMs in their absolute vibronic ground state with a narrow spread of rotational levels and a translational temperature of  $\sim 100\ \mu\text{K}$ . The population of the absolute ground state is essential to most of the applications mentioned above because it allows the molecules to be trapped due to the absence of inelastic collisions [18] and because molecules in this state can have a substantial dipole moment [19, 20]. Our method of UPM production is shown schematically in Figure 1.1. Beginning with a dual species MOT containing  $^{85}\text{Rb}$  and  $^{133}\text{Cs}$  atoms, we form electronically and vibrationally excited RbCs molecules via a process known as photoassociation. After allowing the excited molecules to spontaneously decay to an electronic ground (but vibrationally excited) state, we transfer them to their absolute vibronic ground state by a laser-driven stimulated emission pumping (SEP) technique. While the production of cold polar molecules has been previously demonstrated using different techniques, our optical production yields the coldest sample ever observed. Furthermore, our method can be applied to produce even colder samples, with temperatures limited only by atomic cooling methods.

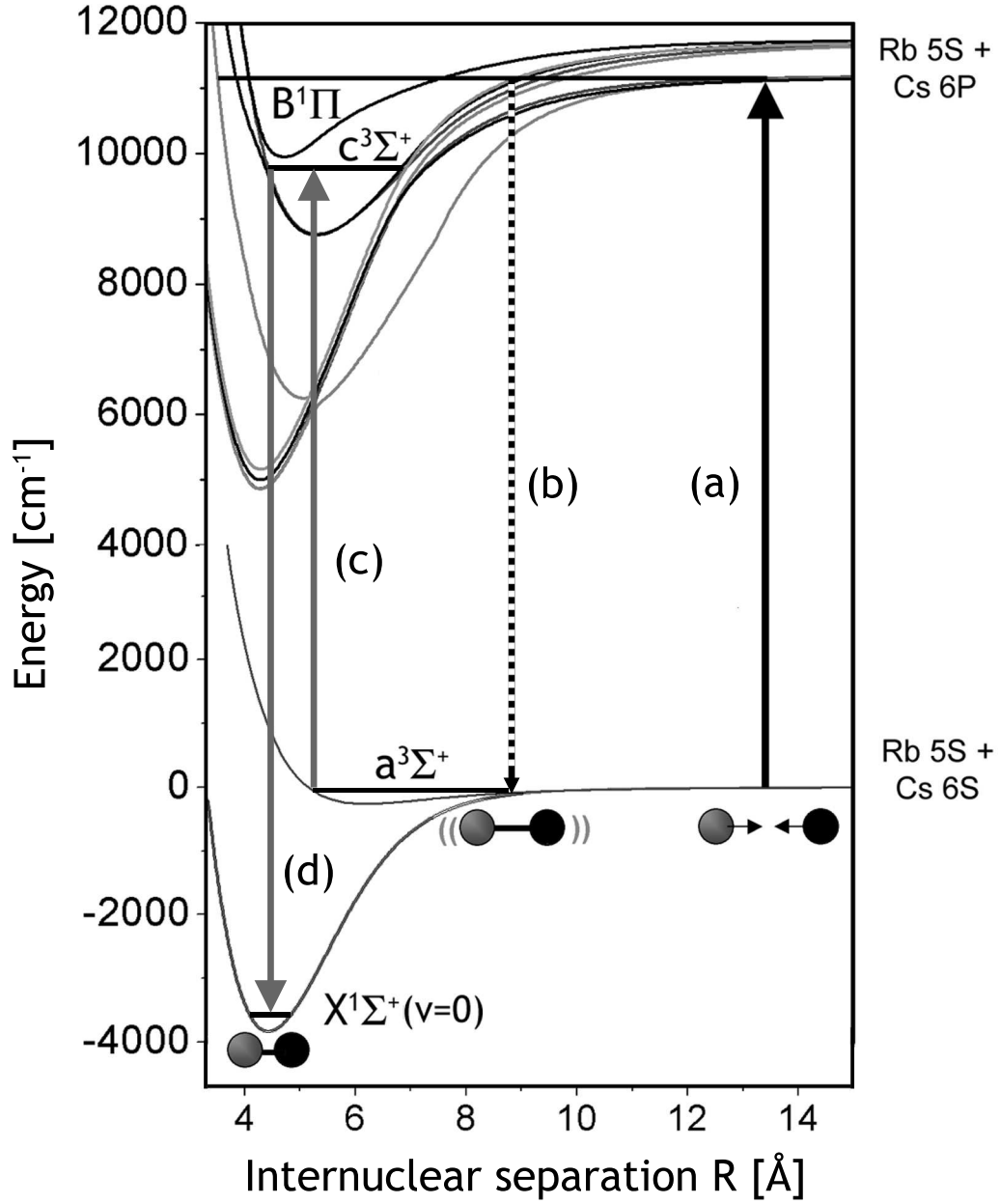


Figure 1.1: Overview of the optical production of ultracold RbCs. The method by which we produce ultracold, polar RbCs is shown. (a) Colliding ultracold Rb and Cs atoms are promoted to an electronically excited molecular bound state via photoassociation. (b) The molecules spontaneously decay to a metastable excited vibrational level in the  $a^3\Sigma^+$  ground state. The molecules in this level are then (c) driven to an intermediate excited state from which they are (d) transferred to the  $X^1\Sigma^+(v=0)$  absolute ground state. Transitions (c) and (d) are together referred to as stimulated emission pumping (SEP) and are both driven by pulsed lasers.

## 1.1 Applications of Ultracold Polar Molecules

The production of a sample of UPMs seems most attractive when considering the many applications for which it might be used. The following sections discuss in more detail some of these potential applications.

### 1.1.1 Quantum Computation

The experiments carried out and described in this thesis work were originally designed with the ultimate goal of creating a scalable quantum computer. A quantum computer could potentially solve currently intractable computational problems, such as the factorization of very large numbers [21]. In the particular implementation of quantum computation our group has chosen to pursue, the qubits are single molecules held in an array by an optical lattice potential [12], shown schematically in Figure 1.2.

The “two-level” system required for information storage is provided by the two lowest rotational levels of the absolute vibronic ground state of the molecule. Gates are performed with resonant microwave pulses that drive transitions between these two levels. Individual qubits are addressed spectroscopically, by applying a linear electric field gradient along the array which Stark shifts the transition frequency of each qubit differently. There are several critical factors that determine the feasibility of all proposals of scalable quantum computation. It is of course important that a viable scheme contain methods to perform both one and two qubit gate operations, as well as individual qubit state readout. We project that our scheme will be effective in addressing these requirements [12]. Equally important, though, is the speed at which gates can be performed in relation to the decoherence time of the qubits; this determines the number of operations (and thus the size of the calculation) that can be done. It is with regard to this point that using molecules that are both *ultracold* and *polar* becomes advantageous.

The dominant source of decoherence in our scheme is predicted to be scattering of the far-detuned laser light used to produce the optical lattice by the molecules. Simply, the

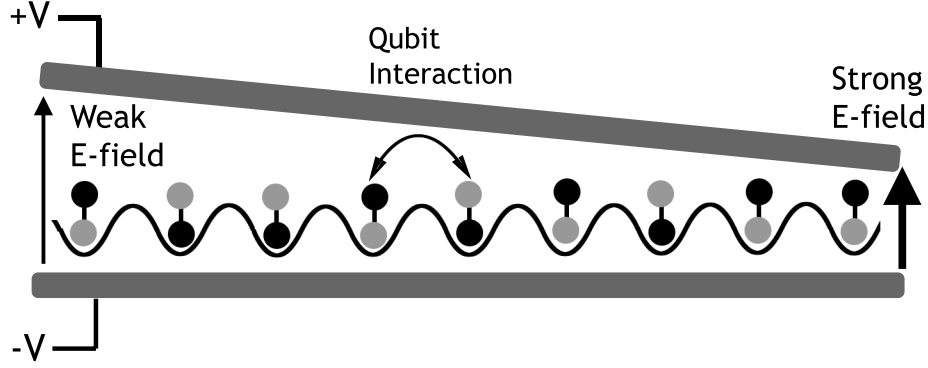


Figure 1.2: Ultracold polar molecule quantum computer. The qubit states are superpositions of the two lowest rotational levels of a ground state UPM. The qubits are held in an array by an optical lattice potential. All gates are performed by driving microwave transitions between qubit states. An electric field gradient along the array allows for individual spectroscopic addressing of the qubits due to the varying induced Stark shifts of the molecular states. The ability to perform fast controlled-NOT gates relies on the strong qubit-qubit interaction of the polar molecules.

lattice is the “environment” with which our quantum system interacts and decoheres. With an ultracold sample of molecules, a relatively small laser intensity is required to hold it, minimizing the interaction strength of the environment with the qubits and the resulting decoherence rate.

The speed at which single qubit (i.e., NOT) gates are performed can be made fast simply by increasing the strength of the microwave field used to implement them.<sup>1</sup> The limit to the quantum computer processor speed is the rate at which two-qubit (i.e., controlled-NOT) gates can be performed.<sup>2</sup> Controlled-NOT gates require an interaction between two qubits; in our scheme, this arises from the dipole-dipole interaction between the molecules. This interaction shifts the molecular levels by an amount which depends on the relative states of the two qubits, as shown in Figure 1.3. Because the state of the qubit is changed only when the microwave pulse energies are resonant with the molecular level splittings, this provides the ability to induce a transition in one qubit only when a neighboring (and

<sup>1</sup>Recent calculations have shown that undesirable motional heating arising from the interaction between molecules will occur if the states are not changed adiabatically. This, in theory, limits the speed of the one-qubit gates; however, they are still much faster than the two-qubit gates so that in practice they will not ultimately limit the speed of the quantum computer [22].

<sup>2</sup>Controlled-NOT gates are gates that flip one qubit depending on the state of the another.

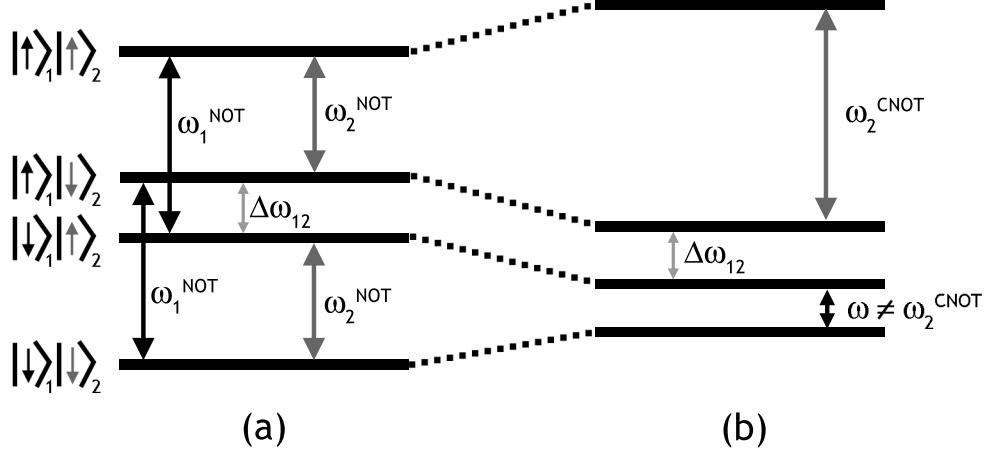


Figure 1.3: Qubit levels of a UPM quantum computer. (a) The levels of two adjacent qubits are shown assuming *no* interaction between qubits. The “up” and “down” arrows used to label the levels refer to the two possible qubit states for each UPM.  $\omega_1^{NOT}$  and  $\omega_2^{NOT}$  are the microwave frequencies to which one must tune to perform a NOT gate on the first and second qubits, respectively;  $\Delta\omega_{12}$  is the difference between these two frequencies resulting from the applied electric field gradient along the qubit array. (b) The qubit levels are shown assuming interactions between the UPMs. The levels are shifted due to these dipole-dipole interactions and the transition frequency associated with performing a NOT gate on the second qubit now depends on the state of the first (unlike the situation in (a)); the frequency  $\omega_2^{CNOT}$  will flip the second qubit only if the first is in the “up” state, allowing one to perform a CNOT gate. Note that the level splittings here are grossly exaggerated; typically  $\omega_2^{CNOT} - \omega_2^{NOT} \ll \omega_2^{NOT}$ .

interacting) qubit is in a particular state [23]. However, the microwave transition must be done sufficiently slowly (in a time greater than the inverse of the level’s frequency shift due to the interaction) so that the difference between the shifted and unshifted levels can be resolved. Otherwise, a qubit’s state will be changed regardless of the state of any of its neighbors. This implies that the speed at which controlled-NOT gates can be performed is proportional to the size of the level shifts. Thus, we aim to use a sample of polar molecules as qubits. Polar molecules have extremely large dipole-dipole interactions (compared with neutral atoms and non-polar molecules) and the level shifts mutually induced between neighboring molecules are therefore large as well.

### 1.1.2 Chemistry at Ultracold Temperatures

There is much experimental interest in studying the dynamics of chemical reactions at ultracold temperatures. Normally, one makes the assumption that reaction rates decrease exponentially as the temperature is reduced due to the reduction in the number of reactants with sufficient kinetic energy to go over a potential energy activation barrier. However, this does not necessarily hold in the ultracold regime because of tunneling. Due to the longer interaction times associated with slow moving reactants, there is a greater probability of tunneling, and reaction rates may be non-negligible [13]. By studying these ultracold reactions using polar molecules interacting with one another, as well as with atoms or non-polar molecules, the reaction potential energy surfaces can be altered with applied electric fields. This opens the possibility to dramatically control reaction rates and scattering cross-sections by varying an external field; resonances may even be observed like those seen in experiments with atoms in which magnetic fields are varied [24, 25, 26].

It also has been proposed that UPMs could be placed into “field-linked” states in which two molecules are bound together only in the presence of an applied electric field [15]. These bound states, which can have large intermolecular separations of hundreds of angstroms and  $\sim$  mK binding energies, are formed from avoided crossings between pairs of molecular potential energy curves; one curve originating from a repulsive dipole-dipole interaction, the other from one that is attractive. Since these bound states exist only when the molecules are polarized by an external electric field, one could imagine holding two UPMs hundreds of angstroms apart in a controlled manner.

### 1.1.3 Many-body Systems

A sample of ultracold polar molecules could be used to create novel many-body systems. For instance, it has been suggested that superfluid Cooper-pairing could be observed in a *single-component* Fermi gas consisting of polar molecules [14].<sup>3</sup> Usually, the inelastic

---

<sup>3</sup>Note that RbCs is a boson and that a fermionic polar molecule (such as  $^{40}\text{K}^{85}\text{Rb}$ ) is required; however, the technique of UPM production discussed in this thesis could potentially be used to make a sample of



collisions necessary for Cooper-pairing are suppressed due to the lack of  $s$ -wave scattering for fermions in the same internal state and because  $p$ -wave (and all higher odd angular momentum) scattering requires an angular momentum potential energy barrier to be crossed. However, the large long-range interactions of polar molecules can overcome this barrier and make the  $p$ -wave scattering cross-sections quite big. In addition, the formed Cooper pairs would not be in a definite state of angular momentum, but in a superposition of all odd angular momenta; this is due to the anisotropic (and therefore angular momentum non-conserving) interactions of polar molecules.

Another idea is to use bosonic ultracold polar molecules trapped in an optical lattice to observe quantum phase transitions [16]. The strong, long-range interactions between the molecules can lead not only to the superfluid and Mott-insulator [27, 28] states but to new phases, as well. These include a supersolid phase which behaves in most ways like a superfluid but possesses some degree of spatial order, and a “checkerboard” state for which the molecules occupy every other lattice site. Furthermore, because interactions between the polar molecules are tuneable with applied electric fields, quantum phase transitions between these different states of matter can be experimentally engineered. This high degree of experimental control could help to answer many unresolved questions in condensed matter theory.

#### 1.1.4 Electric Dipole Moment of the Electron

An electron electric dipole moment (EDM) arises if the electron’s charge is not actually confined to an infinitesimal point and is instead inhomogeneously spread out over some volume of space. The Standard Model of particle physics predicts an electron EDM that is roughly thirteen orders of magnitude smaller than the currently placed experimental limit [29]; however, theoretical extensions to the Standard Model, such as supersymmetry, predict EDMs which are within two to three orders of magnitude of this limit. Thus a search for an electron EDM could either provide evidence for new physics, or serve to

---

such molecules.

eliminate currently viable theories.

An EDM is measured by applying an electric field along the spin of the electron and looking for an energy shift proportional to the field strength. This cannot be done on a free electron because the field will accelerate it into an electrode. Viable techniques instead use unpaired electrons in atoms and molecules [17, 30, 31, 29, 32, 33]. Here an electric field polarizes the atom or molecule and the electron inside feels an effective field due to the polarized charge distribution and spin-orbit effects. The presence of an electron EDM will result in shifts of atomic or molecular levels, proportional to the effective field, which are measured using laser spectroscopy. For atoms (which were used to set the current electron EDM upper bound [29]) and non-polar molecules, this field can be roughly  $10^2$  times larger than the laboratory applied field; for polar molecules it can be an additional  $10^3$  times larger. Thus polar molecules are ideal for measuring level shifts associated with the electron EDM, a fact which current experiments are attempting to exploit. With a sample of UPMs, even more sensitive measurements can be made; the ultracold temperatures allow trapping of the molecules so that they can be interrogated for longer times resulting in narrower spectral lines.

## 1.2 Techniques of Cold Polar Molecule Production

In addition to the optical production of UPMs that is the subject of this thesis, there are other techniques which have produced samples of polar molecules at temperatures which could (and in some cases did) allow them to be trapped; however none have so far been capable of achieving the ultracold temperatures reached by our method and which are crucial to most of the applications mentioned in §1.1. The following sections discuss these techniques in detail.

### 1.2.1 Buffer-gas Cooling

One technique of cooling polar molecules is to place them in an already cold environment and allow them to thermalize with their surroundings. This is the essential idea of buffer-gas cooling, which has been achieved using CaH in a cell filled with  $^3\text{He}$  gas cooled by dilution refrigeration to a temperature of  $\sim 300$  mK [34]. The CaH molecules are created in the cell by laser ablating a solid sample of  $\text{CaH}_2$ . The molecules undergo roughly 100 collisions with the  $^3\text{He}$  buffer-gas before completely thermalizing to a translational temperature of  $\sim 400$  mK. This was all done in the presence of a trap consisting of a quadrupole magnetic field which has a minimum inside the cell and which couples to the spin magnetic moment of the molecule. Such a trap is capable of accumulating so-called “weak field-seeking” molecules; these molecules have their spins anti-aligned with the magnetic field and are thus attracted to the field minimum where their energy is lowest. In this experiment,  $10^8$  of the  $\sim 400$  mK polar molecules were trapped at a density of  $8 \times 10^7 \text{ cm}^{-3}$  and with a trap population decay time constant of 500 ms. The molecules are in their ground electronic and vibrational state as would be expected given their temperature and the energy of the first excited vibrational level.

The advantage of this technique is that the cooling is completely general; it works with any molecule or atom. Furthermore the trapping requires only modest spin magnetic moments ( $\sim 1 \mu_B$ , typical of atoms or molecules with at least one unpaired electron) and is thus also quite general. A disadvantage is that the temperatures are still high. It has been proposed that a stage of evaporative cooling could be implemented whereby the trap depth is gradually reduced allowing the molecules with the largest kinetic energy to escape; however, this method may run afoul of predicted intermolecular Feshbach resonances [35] leading to unwanted chemical reactions, or spin-flip transitions. Also, large amounts of buffer gas remain in the region where the molecules are being held. This gas, which limits the trap lifetimes and the molecular state coherence times, is difficult to remove. Another disadvantage is that the magnetic trap accumulates only weak field-seeking molecules,

which are subject to inelastic collisions: the molecules are trapped in an excited state which can be induced to decay by collisions at the expense of adding kinetic energy and heating them out of the trap. A recent proposal for trapping buffer-gas cooled molecules using an AC microwave trap circumvents this problem with its ability to trap ground state (high field-seeking) molecules [36]. It is suggested that the trap be located in a region separate from where the cooling occurs so that there is no buffer gas present. The trap can be loaded by permitting the molecules to escape through a hole in the surrounding chamber and by subsequently guiding them with electric fields into the trap; the buffer gas, which is non polar and does not feel the strong electric guiding forces, would diffuse away from the trapping region. Furthermore, the physical geometry of such a trap would permit additional sympathetic cooling of the molecules by allowing them to thermalize with a sample of ultracold atoms loaded into the trap from a MOT if evaporation proves impossible.

Additionally, an AC electric trap analogous in operation to a Paul trap [37] has recently been demonstrated that is capable of trapping a sample of high-field seeking polar molecules at  $\sim$  mK temperatures [38]. Though demonstrated using molecules obtained by a technique discussed in § 1.2.2, this trap could work for molecules cooled via the buffer gas technique. A disadvantage of this trap is that its geometry, with electrodes surrounding the molecules from nearly all sides, makes accessing the molecules difficult and precludes the type of sympathetic cooling stage mentioned above; as a result, ultracold temperatures may not be attainable and its application may be limited.

### 1.2.2 Stark Slowing

Another way to obtain a sample of cold polar molecules is to use a well-established technique of supersonic expansion, whereby room temperature molecules are mixed with an inert high pressure gas which is then allowed to quickly expand into a region of low pressure. Subsequent spatial filtering of the expanded gas results in a beam of molecules in their vibrational ground state, with velocity and rotational distributions consistent with a

temperature near 1 K; however, the entire sample is moving at a very high average velocity (nearly 300 m/s) making them impossible to trap and manipulate. A method to slow the cold beam to a low mean velocity was thus proposed and has been implemented; it is known as Stark slowing [39].

The method works by allowing the molecular beam to travel down a linear guide created using a two-dimensional electrostatic trap which transversely confines weak field-seeking polar molecules. Along the longitudinal direction many additional high voltage electrodes, spaced equidistantly, are switched on and off as the molecules travel. When the molecules enter a region of high electric field, they slow down due to the potential energy hill they must climb. The timing of the switching is chosen so that the electrodes are turned off before the molecules leave the region; as a result, there is no longer a potential hill for them to go down and regain their kinetic energy. This process is repeated until the molecules are slowed considerably, reaching final velocities of typically  $\sim 10$  m/s. The technique relies on the molecules having a narrow velocity distribution to begin with because only molecules with a certain initial speed can be slowed with a particular switching rate. This is really not a cooling process because the velocity distribution is not narrowed. The final temperature is essentially the same as it was in the initial cold beam;<sup>4</sup> however, the molecules are now moving slowly in the laboratory reference frame and can potentially be trapped. The experimental group which first demonstrated this slowing technique later used the AC electric trap mentioned in §1.2.1 to do just that. The molecules were driven from a weak to high field-seeking state by applying a resonant microwave pulse after the final slowing stage. They trapped roughly  $10^4$  ND<sub>3</sub> (deuterated ammonia) high field-seeking molecules at a density of  $10^7$  cm<sup>-3</sup> and temperature of 1 mK. The temperature is still a few orders of magnitude greater than the  $\mu$ K temperatures routinely observed in atomic laser cooling experiments.

---

<sup>4</sup>This is not strictly true; there is actually velocity *filtering* taking place because molecules that do not have the correct velocity for the slowing to work leave the guiding region well before the molecules that do. This effectively reduces the temperature of the slow molecules at the expense of reducing their number.

### 1.2.3 Cooling via Billiard-like Collisions

Perhaps one of the simplest ways of producing cold polar molecules that can be trapped is to begin with a cold but fast moving molecular beam (as in § 1.2.2) and collide it with a similar beam consisting of atoms [40]. If the beams are orthogonal and the molecular kinetic energy is judiciously chosen, a sample of molecules with a narrow velocity spread centered around zero can be produced in a single rovibrational level near the beams' intersection point. Faster moving molecules quickly exit this region leaving a pure sample of stationary cold molecules. The technique relies on the fact that the molecules have internal quantized rotational energy levels that can be excited in the collision; the molecules, which begin in a single rotational level, are left in a single but more energetic level following such an inelastic collision by tuning the initial molecular kinetic energy to be just enough to excite the molecules and leave them with zero recoil velocity. Naturally, the initial beams will have a spread in kinetic energy centered around the tuned value (this spread is given by the temperature of the beam) and one would therefore expect the stopped molecules to have a velocity spread around zero. Surprisingly, the kinematics of the collision process predict that this velocity spread is *smaller* than the initial molecular spread and that it does not depend, to first order, on the spread of the atomic beam. Due to the narrowing of velocity spread, this is considered a cooling process. The removed energy and entropy goes into the unstopped molecules that have not been driven to the excited rotational level; these molecules experience an *increased* spread in velocity.

Experiments demonstrating this technique use nitric oxide (NO) polar molecules initially in the  $j = \frac{1}{2}$  rotational level <sup>5</sup> colliding with argon atoms. The initial beam kinetic energies are adjusted by heating or cooling the pulsed valve involved in the supersonic expansion. The density of stopped molecules, which end up in the  $j = \frac{7}{2}$  rotational level, is measured to be  $10^9 \text{ cm}^{-3}$ ; with the beam diameters used, this amounts to a total of  $10^6$  cold molecules. Given the initial molecular beam temperature of 4°K and the masses involved

---

<sup>5</sup>Given the initial beam temperature, the molecules actually begin in a spread of rotational levels; however, only those in the  $j = \frac{1}{2}$  level are cooled.

in the collision, a sample of molecules at 35 mK is predicted; however, the experiments are incapable of measuring temperatures lower than 400 mK. The ultimate achievable temperature is limited by the initial beam temperature (which could be made colder) and by the difference in mass of the colliding atom and molecule (which could be made smaller by choosing a different atom or molecule or both). The cold molecules produced in this technique could be trapped in a deep electrostatic trap like those discussed in §1.2.1. The advantage of this cooling technique is that it is relatively simple and extremely general; it does not require that the molecules have any special internal structure or large magnetic or electric dipole moments.

### 1.3 Summary

It is now hopefully clear why ultracold polar molecules are interesting and what the various efforts are to produce them. The remainder of this thesis is devoted to discussing the many details, both theoretical and experimental, involved in implementing our optical method of UPM production; chapter 2 deals with atomic laser cooling and trapping; chapter 3 discusses the photoassociation of atoms into excited molecules; chapter 4 deals with the spectroscopy done to develop a technique to transfer these excited molecules into the ground state; chapter 5 discusses the demonstration of this technique; and chapter 6 discusses the future directions of our experiments.

## Chapter 2

# Cooling and Trapping of Rb and Cs Atoms

This chapter is devoted to discussing the theoretical principles and the experimental techniques involved in laser cooling and trapping  $^{85}\text{Rb}$  and  $^{133}\text{Cs}$  atoms.

### 2.1 Theory of Atomic Laser Cooling

Atomic laser cooling is achieved by applying forces on atoms through their absorption and spontaneous emission of photons. In the simplest model, an atom can be regarded as a two level system with one ground state and one excited state. Such atoms at rest in the ground state absorb photons which have a frequency (or, equivalently, energy) that is nearly equal to the splitting between these two levels. The atoms subsequently spontaneously decay back to the ground state in a time which is referred to as the excited state lifetime. In doing so, they emit a photon in a random direction (because the decay is spontaneous). Photons carry momentum which must be imparted to the atom during absorption. As a result, the atom gets a "kick" in the direction the photon had been travelling. In a single laser beam that has a frequency close to the atomic energy splitting (near resonance), an atom will receive many absorption kicks in the direction of laser propagation. The



spontaneous emission process also kicks the atom; however, since it is random, over the course of many photon scattering events the net kick due to emission averages to zero. Thus, the atom feels a resultant force only along the direction of laser propagation. This force is given by

$$\mathbf{F}_{scatter} = \hbar \mathbf{k} \Gamma_{scatter}, \quad (2.1)$$

where  $\mathbf{k}$  is the wavevector of the photon and  $\Gamma_{scatter}$  is the scattering rate. In order for there to be cooling of an atomic sample, the force must be dissipative; i.e., energy and entropy must be removed. The simple model discussed above does not, at first, seem to have a mechanism for such dissipation; however, we will see in §2.1.2 that when the motion of the atoms is taken into account, the magnitude of the force in equation 2.1 is actually velocity dependent and therefore dissipative.

### 2.1.1 Temperature in Laser Cooling

Before beginning a discussion of the mechanism of laser cooling, it is worthwhile to address what exactly is meant by “temperature.” The most general definition of temperature can be found by noting that the probability,  $P_r$ , for the sample to be in a particular state,  $r$ , is given by the canonical distribution of statistical mechanics as

$$P_r = \frac{e^{-E_r/k_B T}}{\sum_r e^{-E_r/k_B T}}. \quad (2.2)$$

Here,  $E_r$  is the energy of the sample in state  $r$ ,  $k_B$  is the Boltzmann constant, and  $T$  is the temperature. The canonical distribution is valid for any system in equilibrium with a fixed number of particles and a fixed total energy.<sup>1</sup> One can then define the temperature of the sample in terms of a particular quantity that can be measured, and that has a well-defined temperature-dependent value in the canonical distribution. For example, in laser cooling experiments, it is possible to measure the *spread* of the velocity distribution of the

---

<sup>1</sup>Note, this implies that the system of interest need not be in contact with some thermal reservoir at temperature,  $T$ , as one often assumes when using the canonical distribution.

sample (as will be discussed in §2.4.3). One can relate this spread to temperature via the one-dimensional velocity distribution given by

$$f_{1D}(v) = \sqrt{\frac{1}{2\pi\Delta v^2}} \exp\left[-\frac{(v - v_0)^2}{2\Delta v^2}\right], \quad (2.3)$$

where  $v_0$  is the sample's average velocity and  $\Delta v$  is the  $e^{-2}$  half-width of the distribution. This distribution is obtained from the canonical distribution and must therefore accurately describe the sample. It is also sometimes useful to discuss the sample's distribution in terms of a three-dimensional *speed*. Such a distribution, known as the Maxwell-Boltzmann distribution, is expressed as

$$f_{speed}(v) = 4\pi v^2 \left(\frac{1}{2\pi\Delta v^2}\right)^{3/2} \exp\left[-\frac{v^2}{2\Delta v^2}\right]. \quad (2.4)$$

In the distributions of equations 2.3 and 2.4, the velocity spread is defined as

$$\Delta v = \sqrt{\frac{k_B T}{m}}, \quad (2.5)$$

where  $m$  is the mass of a particle in the sample. We thus arrive at a definition of temperature in terms of the measurable velocity spread of the sample. By defining the temperature by the *spread* of the velocity distribution, one is able to generate a working definition of “cooling.” We say that a sample is cooled only if this spread is decreased. This notion of cooling, and the corresponding definition of temperature, are what will be used throughout this thesis.

### 2.1.2 Doppler Cooling: Optical Molasses

As noted in §2.1 laser cooling must involve velocity dependent forces; it is therefore evident that to explain the phenomenon, we need take into account the motion of the atoms. First, let us imagine that a single atom is moving in one dimension with laser light incident upon it from both directions. Due to the Doppler effect, the atom will see the light propagating

counter to its direction of motion shifted to a higher frequency (blue-shifted) and the light propagating along its direction of motion shifted to a lower frequency (red-shifted). If the laser frequency (as measured in the lab frame) is tuned to the red of the atomic resonance frequency, the atom will see the light travelling opposite to its velocity shifted closer to resonance and the light travelling along its velocity shifted further away. It will then preferentially absorb light opposing its motion and be slowed due to the greater number of momentum kicks it receives in that direction. If we now extend this idea to three dimensions and imagine red-detuned laser light incident from all directions on a room temperature sample of atoms, we can see that the atoms will feel forces only opposing their motion; they will be moving in a viscous medium, dissipating energy, and the sample will cool.

While this gives a heuristic explanation of Doppler cooling, a more quantitative description of the process will allow us to determine the lowest achievable temperature. If we hold to the assumption that our atoms have two levels and that the excited state,  $|e\rangle$ , spontaneously decays to the ground state,  $|g\rangle$ , at a rate  $\gamma$ , then the steady state excited state population,  $\rho_{ee}$ , is given by

$$\rho_{ee} = \frac{I/I_{sat}}{2[1 + I/I_{sat} + (\frac{2\Delta}{\gamma})^2]}, \quad (2.6)$$

where  $I$  is the intensity of the laser incident on the atoms,  $I_{sat}$  is the saturation intensity of the transition<sup>2</sup>, and  $\Delta = \omega_{atom} - \omega_{laser}$  is the laser detuning from resonance;  $\omega_{laser}$  and  $\omega_{atom}$  are the laser frequency (seen by an atom at rest) and the atomic resonance frequency, respectively [41]. The scattering rate is then simply

$$\Gamma_{scatter} = \rho_{ee}\gamma. \quad (2.7)$$

The detuning in equation 2.6 will depend on the velocity,  $\mathbf{v}$ , of the atom due to the Doppler

---

<sup>2</sup> $I_{sat}$  is related to the Rabi frequency,  $\Omega_r = \frac{e}{\hbar} \langle e | \mathbf{E} \cdot \mathbf{r} | g \rangle$ , by  $I/I_{sat} = (\frac{2\Omega_r}{\gamma})^2$ , where  $\mathbf{E}$  is the electric field associated with the laser light; note that for  $I \gg I_{sat}$ , the excited state population in equation 2.6 saturates ( $\rho_{ee} \rightarrow \frac{1}{2}$ ).

effect. If  $\Delta_0$  is the detuning seen by an atom at rest, then the detuning seen by a moving atom is given by the first order Doppler shift as

$$\Delta = \Delta_0 + \mathbf{k} \cdot \mathbf{v}. \quad (2.8)$$

In one dimension, with lasers both counter-propagating and co-propagating along the direction of atomic motion, the total force on the atom can be obtained by plugging equations 2.6, 2.7, and 2.8 into equation 2.1 for  $\mathbf{k} = +k$  and  $-k$ . Assuming that  $\mathbf{k} \cdot \mathbf{v} \ll \Delta_0$ , one finds that [41]

$$\mathbf{F}_{scatter} = \frac{8\hbar k^2 \Delta_0 I / I_{sat}}{\gamma [1 + I / I_{sat} + (\frac{2\Delta_0}{\gamma})^2]^2} \mathbf{v}. \quad (2.9)$$

It can now easily be seen that the direction of force is opposite to the velocity of the atom as long as  $\Delta_0 < 0$ , which is the case for red-detuning. This velocity dependent force is, again, the origin of the cooling. The cooling occurs at a rate given by

$$R_{cool} = \mathbf{F}_{scatter} \cdot \mathbf{v} \quad (2.10)$$

The atoms are heated as well as cooled in the above process. This is because even atoms at rest scatter photons. In doing so, they receive a momentum kick of  $\hbar k$  every time they absorb or emit a photon, which results in an increase in their kinetic energy by an amount  $\frac{\hbar^2 k^2}{m}$  per scattering event. The rate of absorption and emission is, in one dimension,  $2\Gamma_{scatter}$  (there are two laser beams). The rate of heating is then

$$R_{heat} = \frac{2\hbar^2 k^2}{m} \Gamma_{scatter}. \quad (2.11)$$

Equating these two rates results in a steady state velocity spread and final temperature given by

$$T = \frac{\hbar\gamma}{4k_B} \left( \frac{2|\Delta_0|}{\gamma} + \frac{\gamma}{2|\Delta_0|} \right) \quad (2.12)$$

It can be seen from equation 2.12 that for  $|\Delta_0| \gg \gamma$  (the detuning much greater than

the natural linewidth of the excited state) the final temperature is proportional to  $\Delta_0$ . Choosing  $\Delta_0 = -\frac{\gamma}{2}$  maximizes the cooling rate given by equations 2.9 and 2.10 and thus gives the minimum temperature which may be achieved in Doppler cooling. This limit, known as the Doppler temperature [41], is

$$T_D = \frac{\hbar\gamma}{2k_B}. \quad (2.13)$$

When the first experiments in laser cooling were performed and measurements were made on the resulting cold samples of atoms, it was found that the temperature was an order of magnitude lower than that predicted by the above analysis; a value below the Doppler limit was observed [42]. Though initially puzzling, it was later realized that the two level atom model is too simplistic and that more complicated dynamics are involved through the interactions of magnetic sublevels of “real” atoms with laser polarization gradients [43]. These dynamics are termed “sub-Doppler cooling” or “polarization gradient cooling.”

In the experiment discussed in reference [42], the lasers used to create the optical molasses had linear polarization and counter-propagating beams had their polarizations perpendicular to one another. This configuration, known as “lin  $\perp$  lin,” produces a spatial polarization gradient in which the ellipticity oscillates from linear to circular polarization over a period of one half the wavelength of the light. As atoms move in this gradient, they experience an effect known as Sisyphus cooling which allows temperatures below the Doppler limit to be reached. Discussions of this effect are often used to explain polarization gradient cooling in general; however, in the case of the MOT (see §2.2), which is the most commonly used method of laser cooling (and the one used for this thesis work), the lasers are circularly polarized. In this configuration, a different kind of polarization gradient is created; the polarization is everywhere linear and its direction is perpendicular to and rotates around the axis of beam propagation with a spatial period equal to the wavelength of the laser. As a result the mechanism which produces sub-Doppler temperatures in a MOT is fundamentally different from Sisyphus cooling. A thorough discussion of how the

cooling works in this case is beyond the scope of this thesis but is given in reference [43].

## 2.2 The Magneto Optical Trap (MOT)

So far we have seen how a sample of atoms is cooled. In this section we will discuss the MOT, a technique to trap the atoms in a small region that takes advantage of this cooling. We will begin with a model of an atom that is complicated only enough to explain the key ideas; we will then discuss how it works with real atoms, specifically  $^{85}\text{Rb}$  and  $^{133}\text{Cs}$ , and how it can be modified to create a forced dark spontaneous-force optical trap (SPOT) which has certain advantages over the standard MOT.

### 2.2.1 Simple Model of the MOT

We will begin by assuming that we want to cool and trap atoms which have a ground state with total electron spin  $J = 0$  ( $m_J = 0$ ) and three degenerate excited states with  $J = 1$  ( $m_J = -1, 0, 1$ ). We will also assume that the atoms can move only in one dimension (the  $z$ -axis, say) and that two laser beams are incident upon them, the first with  $\sigma^+$  polarization travelling in the  $+z$  direction and the other with  $\sigma^-$  polarization travelling in the  $-z$  direction.<sup>3</sup> This is shown schematically in Figure 2.1. If the laser frequency is tuned to the red of the atomic transition, the atoms are cooled as described in §2.1.2. Now, if a magnetic field,  $\mathbf{B}$ , is applied such that  $\mathbf{B} = B_0 z \hat{\mathbf{z}}$ , then the atomic levels will be Zeeman shifted by an amount depending on their position. Atoms located at  $z < 0$  see a negative magnetic field and so the  $|J = 1, m_J = -1\rangle$  level is shifted up in energy while the  $|J = 1, m_J = +1\rangle$  level is shifted down. As a result, the  $|J = 1, m_J = +1\rangle$  level will be closer to resonance with the laser beams (since they are red-detuned). This implies that these atoms will absorb more  $\sigma^+$  photons than  $\sigma^-$  photons and as a result feel a net force that pushes them towards  $z = 0$ . The reverse holds for atoms located at  $z > 0$  where the magnetic field is positive; they will absorb more  $\sigma^-$  photons and consequently be pushed

---

<sup>3</sup> $\sigma^+$  and  $\sigma^-$  polarization is referenced to the quantization axis of the atom and does *not* refer to the helicity of the light. The  $\sigma^\pm$  field connects a ground state of  $m_J$  to an excited state of  $m_J \pm 1$ .

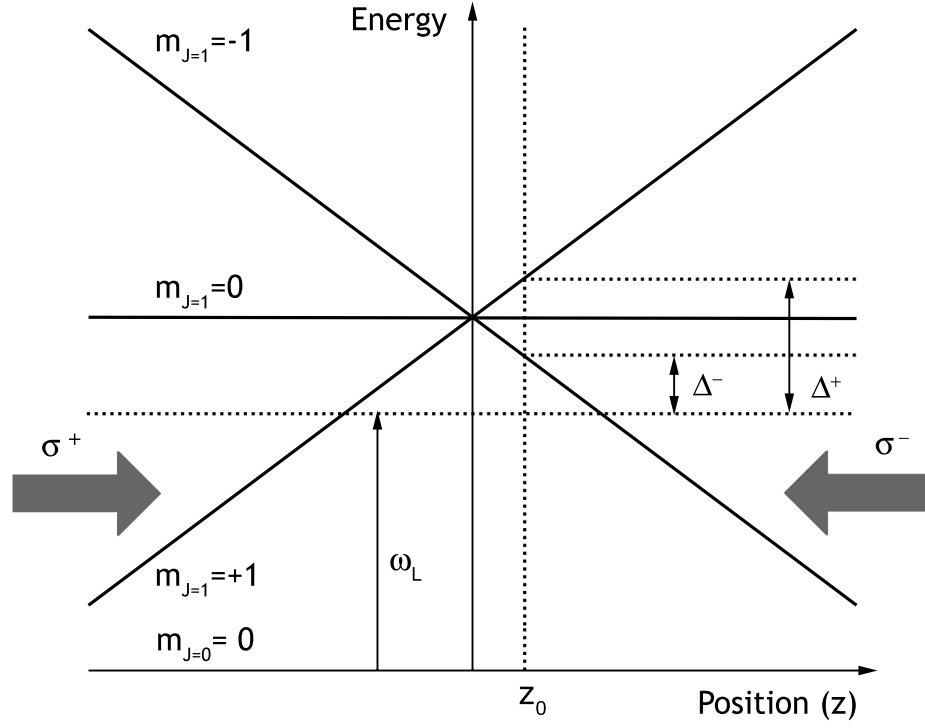


Figure 2.1: Simple MOT trapping scheme. Trapping of atoms in a MOT is shown in one dimension for a  $J = 0 \rightarrow J = 1$  cooling transition. At a position  $z_0$  in the MOT, an atom sees the frequency,  $\omega_L$ , of the counter-propagating  $\sigma^-$  ( $\sigma^+$ ) polarized beams shifted closer (further away) from resonance with the  $m_{J=1} = -1$  ( $m_{J=1} = +1$ ) levels due to the magnetic field gradient  $\mathbf{B} = B_0 z \hat{\mathbf{z}}$ . Since the  $\sigma^-$  beam, travelling in the  $-z$  direction, only drives transitions with  $\Delta m = -1$ , the atom preferentially absorbs photons that force it toward  $z = 0$ . An atom at position  $-z_0$  will preferentially absorb  $\sigma^+$  photons and also be pushed towards  $z = 0$ . In an actual MOT, this trapping occurs in three dimensions and involves atoms which do not have such simple internal structure.

towards  $z = 0$  as well. Moreover, since there is a linear magnetic field gradient, the further the atoms move away from the point of zero field the stronger the scattering imbalance between  $\sigma^+$  and  $\sigma^-$  photons becomes; this system then behaves much like a harmonic trap as long as the force increases linearly with displacement, which is the case if the lasers are not so intense as to cause the scattering rates to saturate. If pairs of laser beams are incident upon the atoms from all three orthogonal directions and there is a magnetic field gradient along each dimension, then a three dimensional MOT is created.

### 2.2.2 Trapping $^{85}\text{Rb}$ and $^{133}\text{Cs}$

In the previous section we assumed a simple energy level structure for an atom. The structure of  $^{85}\text{Rb}$  and  $^{133}\text{Cs}$  (and all other atoms, for that matter) is not so simple and this causes complications in their cooling and trapping in a MOT. The hyperfine interaction in general splits both the ground and excited levels into different manifolds of energy and total angular momentum,  $F$  (nuclear spin plus electron spin and orbital angular momentum), eigenstates. The specific level structure of  $^{85}\text{Rb}$  and  $^{133}\text{Cs}$ , with nuclear spin  $\frac{5}{2}$  and  $\frac{7}{2}$ , respectively, is shown in Figure 2.2. The laser used to cool and trap must be tuned to drive a  $F \rightarrow F' = F + 1$  transition. This is because the atoms need to continuously scatter photons to be cooled substantially and to remain trapped. Since the light is circularly polarized, the atoms quickly get optically pumped into the extreme magnetic sublevels; atoms preferentially scattering  $\sigma^+$  photons are pumped into the  $|F, m_F = F\rangle$  level and can interact only with the  $|F' = F + 1, m_{F'} = F'\rangle$  level while those preferentially scattering  $\sigma^-$  photons are pumped into the  $|F, m_F = -F\rangle$  level and interact only with the  $|F' = F + 1, m_{F'} = -F'\rangle$  level. Therefore, if the cooling and trapping transition is not  $F \rightarrow F' = F + 1$ , the atoms are pumped into states from which they cannot scatter the circularly polarized light and be effectively cooled and trapped; such states are referred to as “dark.”

Typically, the cooling and trapping laser is tuned to the red of the  $5S_{1/2}, F = 3 \rightarrow 5P_{3/2}, F' = 4$  transition in Rb and the  $6S_{1/2}, F = 4 \rightarrow 6P_{3/2}, F' = 5$  transition in Cs. These transitions are chosen because of their relatively large oscillator strengths and because they



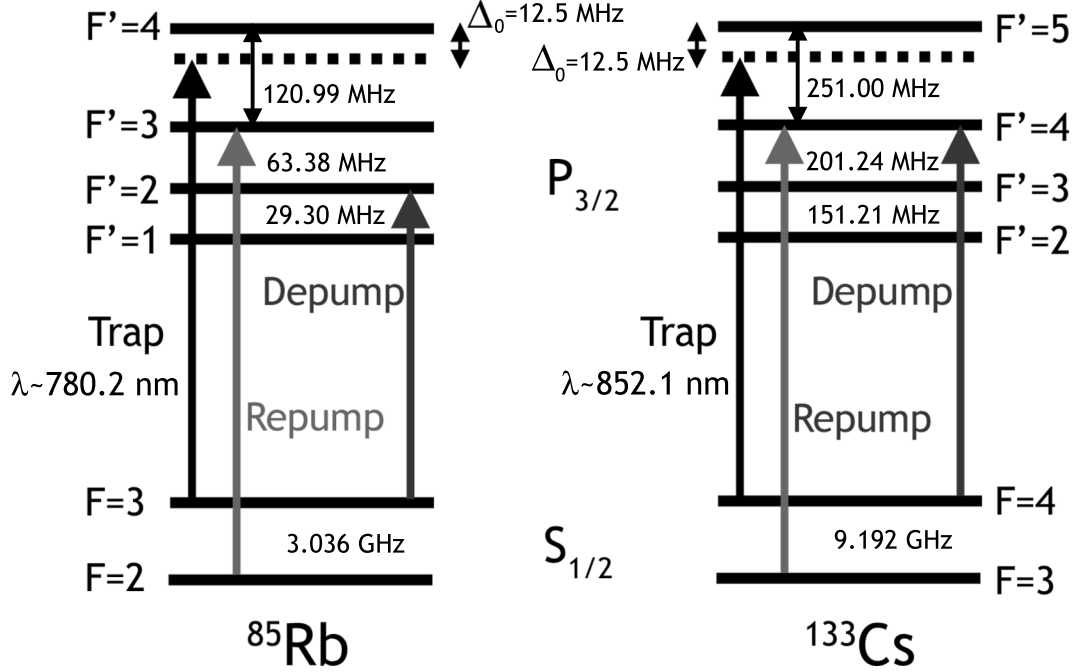


Figure 2.2: Hyperfine structure and MOT transitions in Rb and Cs. The frequency splittings between the hyperfine levels in  $^{85}\text{Rb}$  and  $^{133}\text{Cs}$  that are involved in cooling and trapping are shown. Additionally, the particular transitions driven by the trap, repump, and depump lasers in our experiment are indicated.

are cycling transitions. Since the excited state hyperfine splittings ( $\sim 100$  MHz) are not much larger than the laser detuning from resonance ( $\sim 10$  MHz), a non-negligible fraction of photons are scattered off-resonantly, which drives the atoms into the next lower hyperfine level of the excited state manifold.<sup>4</sup> From this level, the atoms can spontaneously decay into the lower of the two hyperfine ground states. This state is dark since the atoms that populate it do not scatter the laser light used to cool and trap, which is far off resonance due to the large hyperfine ground state splitting ( $\sim 1$ -10 GHz). Since atoms in the upper ground state hyperfine level scatter roughly  $10^7$  photons per second, the entire sample will be quickly pumped into the dark hyperfine state if such a scheme is used. The way to fix this problem is to apply another laser, known as the “repump” laser, tuned to resonance with the  $F = 2 \rightarrow F' = 3$  transition in Rb and  $F = 3 \rightarrow F' = 4$  level in Cs. This acts to

<sup>4</sup>In principle, there is an additional excited state manifold of energy levels, associated with the  $P_{1/2}$  state, which is split from the one associated with the  $P_{3/2}$  state by the fine structure interaction. However, this splitting is much larger than those of the hyperfine interaction and the laser detuning. As a result, laser coupling to these manifolds is completely negligible.

optically pump the “dark” atomic population back into the upper hyperfine ground state where it will continue to scatter photons. This is the reason that most atomic species and all molecules cannot be cooled and trapped using this technique; their relatively complex energy level structure prohibits the creation of closed transitions using an experimentally practical number of repump lasers.

### 2.2.3 Forced Dark SPOT

While the detailed dynamics of atoms trapped in a MOT are beyond the scope of this thesis, a few important points which directly affect the experiments to be discussed should be made. First, it is desired that the density of the trapped atomic sample be maximized (for reasons that will be clear in Chapter 3). The density is limited by atom-atom repulsive forces that result from reabsorption of scattered photons. These repulsive forces clearly increase as the density increases due to the larger reabsorption rate that accompanies more closely spaced atoms. Thus, an equilibrium density is reached when the repulsive forces balance the trapping forces of the MOT. It is also desired that intrinsic atom loss rates from the MOT be minimized. Not only do these losses present another limit to the sample’s density, they limit the ability to detect experimentally induced losses, which is a technique (to be discussed in Chapter 3) used to detect the photoassociation of atoms into molecules. The intrinsic losses in the MOT are dominated (at low background pressures) by light-assisted collisions [44]. They arise from the interaction of atoms in their ground state with atoms excited by the MOT lasers. For identical atoms, the interaction is an attractive resonant dipole-dipole interaction; the potential energy between two such atoms is proportional to  $R^{-3}$ , where,  $R$  is the interatomic separation [45]. In the time before the excited state atom spontaneously decays, the two atoms are accelerated toward each other. The spontaneously emitted photon is lower in energy than that absorbed from the MOT light and the excess energy is shared between the two atoms as kinetic energy. The increase in kinetic energy allows the atoms to escape and be lost from the trap. This process is illustrated schematically in Figure 2.3.

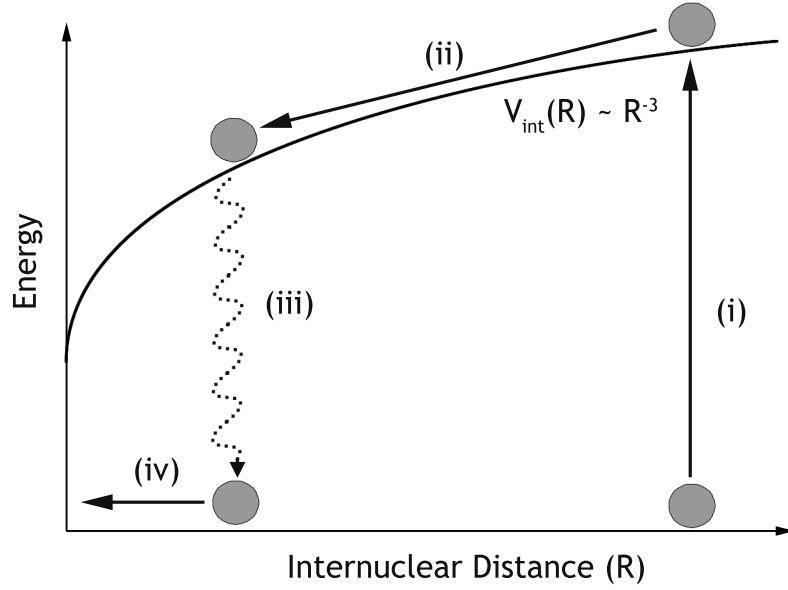


Figure 2.3: Light-assisted collisions. A dominant loss mechanism for atoms in a MOT is shown. (i) A slowly moving atom absorbs a photon from the trap beam and is promoted to an excited state. (ii) The excited atom is accelerated towards a ground state atom of the same species (located at  $R = 0$ ) due to the resonant dipole-dipole interaction. (iii) The excited atom spontaneously decays back to the ground state. (iv) It is now moving at a higher speed due to the acceleration. This process happens repeatedly and atoms can ultimately gain enough kinetic to escape from the trap.

It is clear that the limit to the atomic density can be increased and the light-assisted losses can be decreased by reducing the scattering of MOT laser photons. The way this is often done is to considerably reduce the intensity of repumping light only in the region where the atoms are trapped, while keeping the intensity higher in the much larger (with volume greater by a factor of roughly  $10^4$ ) collection region around the small sample of trapped atoms. This has the effect of continuing to effectively load the trap while allowing the atoms already trapped to be optically pumped into a dark state where they no longer scatter photons. The principal idea is that the light forces necessary for maximizing the MOT loading rate are much higher than those necessary for optimal confinement. The darker region is often created by simply passing the repumping laser through a window with a black spot on it and imaging this spot onto the center of the MOT. This modified MOT is known as the “dark spontaneous-force optical trap” or “dark SPOT” [46].

For  $^{85}\text{Rb}$  and  $^{133}\text{Cs}$  it is also necessary to fill the darker region with “depump” light, a technique referred to as a “forced dark SPOT” [47]. The depump light is resonant with the  $F = 3 \rightarrow F' = 2$  transition in Rb and the  $F = 4 \rightarrow F' = 4$  transition in Cs, as shown in Figure 2.2. This increases the rate of optical pumping into the dark state by actively pumping the atoms rather than waiting for the relatively infrequent off resonant scattering to do so. This becomes more necessary as the excited state hyperfine splittings become larger (as is the case for Rb and Cs compared with, say, Na), since the off resonant scattering decreases as  $\sim \Delta_0^{-2}$ , where  $\Delta_0$  is the laser detuning from resonance. It is important to note that the atoms must not be *completely* shelved into the dark state; they must spend some fraction of the time in the bright state so that they still feel the inward trapping force. Otherwise the trap would be more like a well potential where the atoms move freely until they hit a wall and bounce back. This would not result in a particularly high density given the limitations of how small a dark region can practically be made. One then must choose intensities of repumping and depumping light in the darker region that result in an optimal steady state fraction of atoms in the bright state. These optimal intensities in general depend on the total number of trapped atoms, as discussed in reference [46]. In

practice, the intensities are simply adjusted until experimental conditions are most suitable.

#### 2.2.4 MOT Loading and Loss

The number of atoms in the MOT,  $N$ , is determined by the trap loading and loss rates. It is governed by the rate equation

$$\dot{N}_a = R_a - \gamma_{bkd}N_a - \int_{MOT} \left( K_{a,a}^{MOT} n_a^2 + \frac{1}{2} K_{a,b}^{MOT} n_a n_b \right) dV - \Gamma_{other}, \quad (2.14)$$

where the subscripts  $\{a, b\}$  refer to  $\{\text{Rb}, \text{Cs}\}$ ,  $R_a$  is the MOT loading rate from the background vapor of atomic species  $a$ ,  $\gamma_{bkd}$  is the loss rate per atom due to collisions with background gasses,  $n_{a(b)}$  is the MOT density,  $K_{a,a}^{MOT}$  ( $K_{a,b}^{MOT}$ ) are the intra- (inter-)species two body loss rates (for unit atomic density) in the MOTs, and  $\Gamma_{other}$  are any other loss rates which may be present. The integral in the equation is done over the volume of the MOT. The loading rate,  $R_a$ , depends on many factors including the partial pressure of atomic vapor, the trapping volume created by the intersecting MOT beams, and the light scattering rate [48]. The intra-species two body loss rates include the resonant dipole-dipole light-assisted collisions while the inter-species loss rates include collisions resulting from the van der Waals interaction. The factor of  $\frac{1}{2}$  in front of the inter-species loss term is due to the fact that only one atom of a particular species is lost in a collision. The steady state number of atoms,  $N_{ss}$ , is reached when  $\dot{N}_a = 0$ ; that is, when the total loss rate becomes equal to the loading rate. Thus it can be seen that for MOTs loaded from a vapor, the trap lifetime is equal to the loading time. The steady state number is given by

$$N_{ss} = R_a / \gamma_{total}, \quad (2.15)$$

where  $\gamma_{total}$  is the total loss rate per atom.

## 2.3 Dual Species MOT Experimental Apparatus

In our experiment, we built a dual species forced dark SPOT capable of simultaneously trapping ultracold samples of  $^{85}\text{Rb}$  and  $^{133}\text{Cs}$ . In the following sections, we will discuss the apparatus in detail.

### 2.3.1 Vacuum System

The trapped atoms must be in a region of ultra high vacuum (UHV). Otherwise a high rate of elastic collisions with background gases causes the atoms to be ejected from the trap resulting in an unacceptably small number of atoms and trap lifetime. To this end, we constructed a vacuum system capable of reaching a pressure of  $\sim 10^{-9}$  Torr. A schematic of the vacuum system is shown in Figure 2.4. In order to achieve UHV it is necessary to construct the system with conflat (all-metal) vacuum components. It is also crucial that the entire system be thoroughly “baked.” Baking is a process by which the assembled system is heated while being pumped by a vacuum pump capable of handling relatively high gas loads. The dominant source of background pressure comes from the slow outgassing of hydrogen, nitrogen, and water vapor adsorbed to stainless steel walls of the vacuum components. By baking, the vapor pressure of these unwanted atoms and molecules is increased by orders of magnitude. They boil off the surface and are subsequently pumped away. Thus, upon cooling the system back to room temperature, the background gasses are greatly reduced. We typically bake our system at a temperature of  $150 - 200^\circ\text{C}$  for about one week. To heat, we wrap our system in heater tape, which is a flexible fiberglass insulated high resistive element that heats when current is passed through it. The current is provided by variacs. The background gas partial pressures inside the vacuum system are monitored with a residual gas analyzer (RGA) and baking is terminated when these pressures stop decreasing. During baking, the system is pumped by the  $60\text{ }\ell/\text{s}$  turbomolecular (turbo) pump backed by a small diaphragm roughing pump. After the system is allowed to cool and a pressure below  $10^{-5}$  Torr is reached, the turbo pump is valved off and the  $8\text{ }\ell/\text{s}$  ion

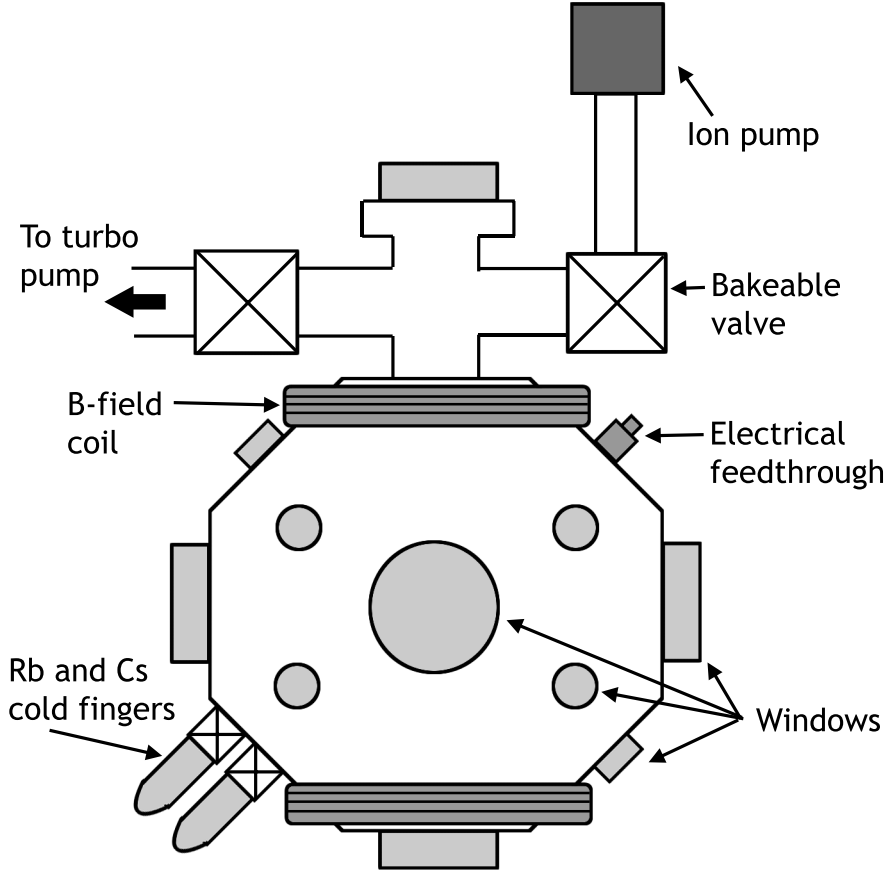


Figure 2.4: Schematic of vacuum system. The essential vacuum components used in our experiments are shown. The turbo and ion pumps allow us to reach a pressure around  $10^{-9}$  Torr. The cold fingers are the sources of Rb and Cs atoms that are loaded into the MOT. The electrical feedthrough allows us to apply voltage to electrodes and generate an electric field inside the vacuum chamber. We apply a magnetic field inside the chamber by running current through coils wound around the outside. Windows allow us to couple laser light into the vacuum system and to monitor fluorescence from the atoms in the MOT.

pump is turned on. The ion pump, which is capable of pumping down to pressures far lower than the turbo pump, will be damaged if it is run at pressures higher than  $\sim 10^{-5}$  Torr. Thus, the turbo pump serves to reach high vacuum enabling the ion pump to subsequently reach UHV. The total pressure of the vacuum system was determined by monitoring the current of the ion pump; the pump controller had an internal calibration that converted pump current into pressure.

Since many lasers are sent into the vacuum system and light coming from the atomic fluorescence inside must be monitored, the chamber must have high quality windows. In the first of two versions of our vacuum chamber, we thought that the optical properties (scratch-dig, anti-reflection (AR) coating) of the glass on standard vacuum viewports would be inadequate for our needs (high transmission and minimal scatter). Furthermore, commercially available viewports are quite expensive and we needed nearly fifteen windows. We thus made an attempt to develop our own glass to metal UHV seals using high quality glass with excellent broadband AR coating. A schematic of the seal is shown in Figure 2.5. Each vacuum chamber opening has a stainless knife edge that makes a seal with a copper gasket when they are forced together. Rings of soft metal solder are then placed both between the gasket and the window and between the window and the top flange. As bolts tighten the entire assembly together, the solder rings are mashed; the lower one makes a seal between the window and the gasket while the other protects the window from being cracked by the hard metal top flange. While window seals had been made using indium solder (with a melting point of  $\sim 200^{\circ}\text{C}$ ) by other groups, home-made seals using higher melting temperature metal, to our knowledge, had not. We initially tried using a solder ring made of an alloy (97.5% Pb, 1.5% Ag, 1% Sn) with a melting point above  $300^{\circ}\text{C}$ . The idea was that this would allow us to bake the system hotter and achieve lower pressures (in a reasonable amount of baking time). Unfortunately, we found that our alloy was not as effective in making reliable seals as was the ordinary indium. Due to reasons not investigated in detail, the seals using the Pb alloy would open upon temperature cycling (heating, then cooling) roughly 20 – 30% of the time. The reason could be that the alloy



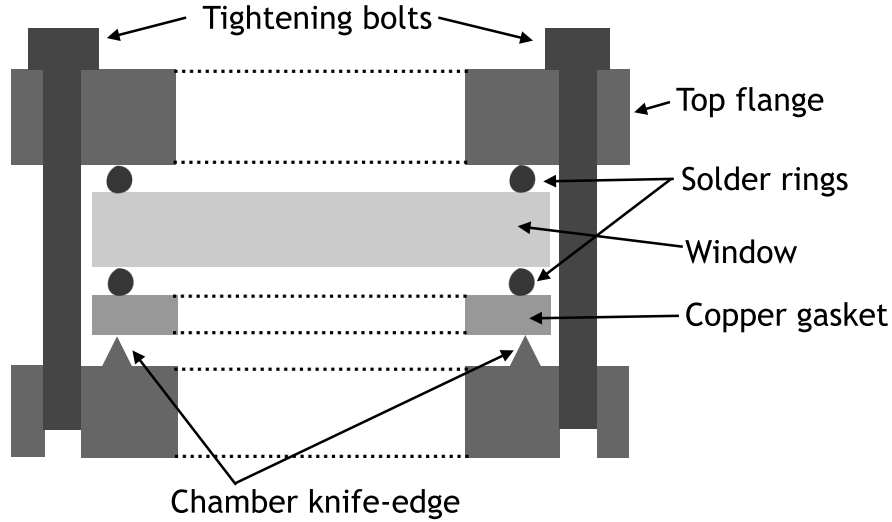


Figure 2.5: Schematic of home-made window seal. Rings of soft solder are placed between a top flange and glass window and between the window and a copper gasket. Tightening bolts which go through the top flange and screw into tapped holes in the chamber squeeze everything together; as a result, the copper gasket is driven into the chamber knife edge creating a vacuum seal, while the mashed lower solder ring creates a seal between the gasket and window. The upper solder ring acts as a cushion to prevent the window from being cracked by the steel top flange.

solder was not as soft and did not bind as effectively to the glass. Indeed, we found it was difficult to remove the indium solder from the window once they had been mashed together but the alloy could be peeled off easily. Whatever the reason, the failure rate, with so many windows, made the high temperature solder ineffective; we eventually used indium seals and baked at a lower temperature. These seals proved completely reliable. In the second version of the vacuum system, we decided that we had been over-cautious with regard to the optical quality of the glass and that commercial viewports would be adequate. Because of their considerable ease of use as compared with the home-made seals, we chose to purchase and use viewports.

The sources of Rb and Cs in the vacuum system were two cold fingers. A cold finger is essentially a glass cell containing a macroscopic ( $\sim 5$  gram) sample of solid Rb or Cs. There is a thermoelectric cooler (TEC) attached to the the cell along with a temperature sensing thermistor, as shown in Figure 2.6a. With feedback electronics, the temperature of the cell can be adjusted and then held steady. The cold finger is kept as the coldest point in the

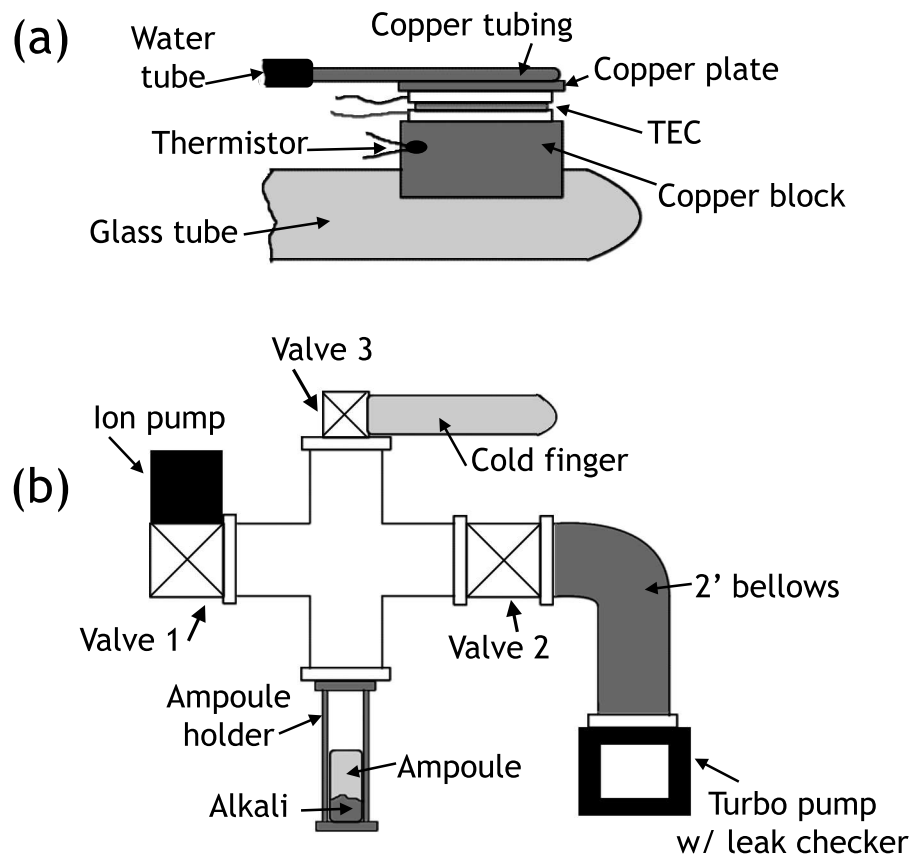


Figure 2.6: Rb and Cs sources (cold fingers). (a) Cold finger schematic. A TEC is used to cool a glass tube containing a sample of Rb or Cs metal. The TEC is attached to a copper block which is attached to the glass tube with thermally conductive glue. The hot side of the TEC is cooled by running water through copper tubing soldered to a copper plate glued to the TEC. A thermistor, placed in a hole in the copper block, measures the temperature; this measurement is used as the input to feedback electronics which stabilize the temperature by regulating the current flowing through the TEC. (b) Cold finger loading scheme. The vacuum components used to load alkali into the cold fingers are shown. The vacuum system is baked with all valves open and the ion pump turned off. After cooling the ion pump is turned on and a pressure near  $10^{-9}$  Torr is reached. Valve 1 is then closed (to protect the ion pump from corrosive alkali at high pressure) and the sealed glass ampoule containing the alkali is cracked by gently crushing the thin-walled ampoule holder. The entire system is then heated except for the cold finger tube and the 2' bellows, driving the alkali into the tube, while not allowing a substantial amount to reach and corrode the turbo pump. Valve 3 is then closed and the loaded cold finger with valve is detached for later use.

vacuum system; since everything condenses on the coldest point, the temperatures of the cold fingers determine the vapor pressures of Rb and Cs in the chamber. The MOT loading rate from a background vapor of atoms is proportional to the background pressure (there are more atoms to load at high pressure) while the trap lifetime is inversely proportional to the pressure (there are more atoms in the background vapor to collide with). There is, then, a tradeoff between having a higher pressure and a faster loading rate (convenient because our experiment required the MOT to be repeatedly loaded) and a lower pressure and longer trap lifetime (essential because our experiment required low MOT loss rates). However, we never investigated the optimal background pressure of Rb and Cs in detail. We found that operating the cold fingers a few degrees below room temperature produced adequate results. It should be noted that in practice, when the cold fingers are first opened to the rest of the system, the Rb and Cs alkali vapor gets “pumped” by the stainless steel vacuum walls which act as excellent getters. It thus takes a while (a few days or more) for any appreciable alkali pressure to build up. After this point, there is a complicated exchange of vapor between the cold finger and the chamber walls such that it is never the temperature of the cold finger alone which determines the value of the alkali pressure. If it did, then with the cold fingers near room temperature, we would expect a Rb and Cs pressures of  $10^{-6} - 10^{-7}$  Torr; however, we never observed the pressure in our chamber to be above  $10^{-8}$  Torr.

The cold fingers were loaded with Rb and Cs separately, as shown in Figure 2.6b. An ampoule of alkali was placed in a thin walled stainless steel tube which was attached to a vacuum system with the empty cold finger cell behind a valve. After UHV was reached, the steel tube was crushed, cracking the ampoule. The entire vacuum system was then heated to  $200^{\circ}\text{C}$  except for the cold finger cell, which was kept at room temperature. After about two days, all the alkali had condensed onto the room temperature cell. The valve was then closed and the cell (with valve) was removed so that it could later be attached to the main vacuum system. The alkali metal is highly reactive and will ignite if exposed to the air. Thus, care must be taken at all times to make sure any macroscopic amount is under

vacuum. We therefore err on the side of waiting more time than necessary to complete the transfer of alkali from the ampoule to the cold finger. Furthermore, we found that the room temperature bellows shown in Figure 2.6b was necessary to prevent the highly corrosive alkali from condensing on the turbo pump and destroying it during the transfer.

### 2.3.2 Magnetic and Electric Fields

In order to create the magnetic field gradient necessary for the MOT, two coils were placed roughly 10 cm above and below the vacuum chamber center (external to the chamber). Each coil had 90 turns of 1 mm thick square copper wire and was 10 cm in diameter. The coils were wired together in series in such a way that the current flowed around the top coil in the opposite sense from the bottom coil. The coils were roughly in an anti-Helmholtz configuration, producing an approximately linear field gradient along all dimensions, with the gradient magnitude along the axis of the coils twice that of the two orthogonal dimensions, and with opposite sign. The zero of the gradient is at the center of the chamber, where the MOT is located. With roughly 7 Amps of current flowing, a gradient of about 13 Gauss/cm (from simulation) along the coils' axis was created. This was the field gradient which yielded optimal MOT densities and atom numbers for the trapping laser beam sizes used. The coils were wound on aluminum mounts that were attached to the vacuum chamber. The coils each dissipate about 30 W of heat and must be cooled. Copper plates with copper tubing soldered to them were screwed onto the coil mounts with heat sink compound placed between plate and mount. Water (non-chilled) was then run through the tubing. With this cooling system, the coils were warm, but not hot, to the touch.

We also desired that a constant electric field be produced inside the chamber. We used this field to measure the dipole moment of the polar RbCs molecules. The field was created by placing two ring electrodes inside the vacuum chamber, as shown in Figure 2.7. The ring geometry, as well as the spacing of the electrodes was chosen so that laser beams were not obstructed from passing through the chamber center. The electrodes were

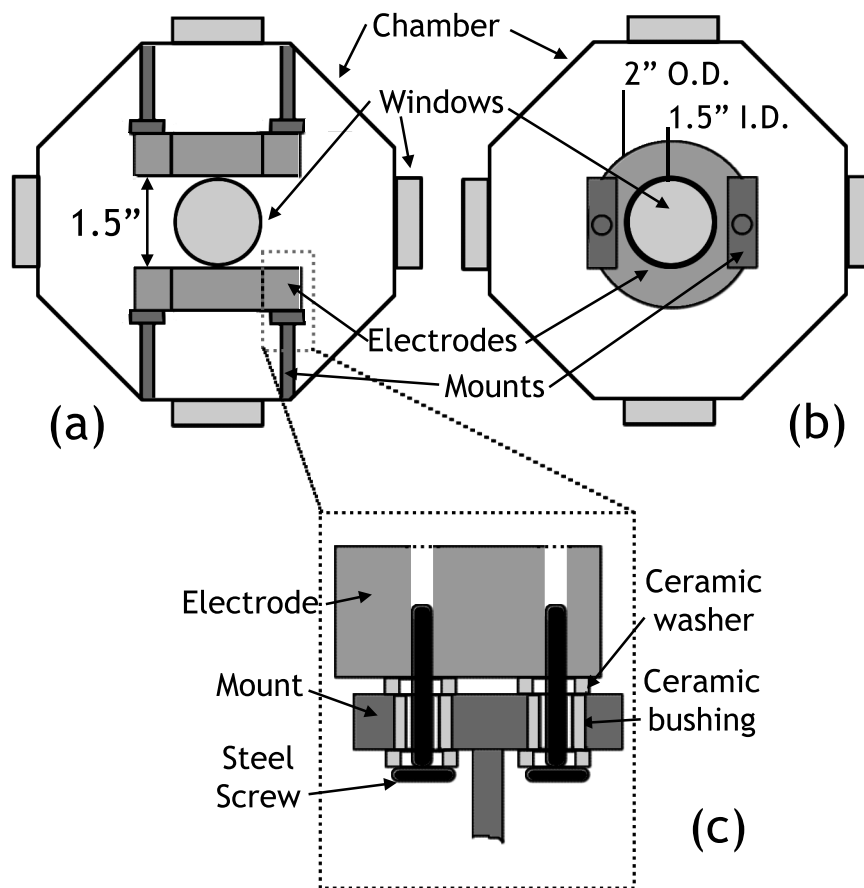


Figure 2.7: Schematic of ring electrodes. (a) Side View. (b) Top View. The electrodes were designed and mounted such that they did not occlude the 1" laser beams passing through the center of the chamber; at the same time, they were capable of producing an electric field of ample magnitude and homogeneity at the location of the MOT. (c) Close-up of electrode mount. The method used to electrically isolate the high voltage electrodes from the vacuum chamber is shown.

held and electrically isolated from the rest of the chamber by mounts shown in Figure 2.7c. The electrodes were electro-polished to prevent sparking and to minimize surface area for unwanted material to adsorb upon. High voltage connection to the electrodes was accomplished using UHV feedthrough attached to the vacuum system and wire with UHV compatible insulation. The electric field produced at the center of the chamber with  $\pm 2000$  V placed on the electrodes was simulated to be  $\sim 1800$  V/cm and was homogeneous to within a few percent over the volume of the MOT ( $\sim$  one millimeter in diameter).

### 2.3.3 Diode Laser System

All light used for the MOT was generated from external cavity diode lasers. We required four frequency-tuneable lasers (TEC200, Sacher Lasertechnik), which we call “Rb trap master,” “Rb repump,” “Cs trap master,” and “Cs repump.” A schematic of one of these lasers is shown in Figure 2.8. The cavity consists of the rear facet of the diode and a grating in the Littrow configuration<sup>5</sup> mounted to a piezoelectric transducer (PZT), which is in turn attached to a tilt mount. The diodes used have an anti-reflection coating on their front facet to improve mode-hop free tuning. Tuning is accomplished (in order of gross to fine) by adjusting the tilt mount horizontal screw, adjusting the temperature of the diode (which is in thermal contact with a TEC), adjusting the current going through the laser diode, and applying a voltage to the PZT which finely adjusts the angle of the grating. A percentage of the light emitted by all four lasers is used to stabilize their frequencies with a technique that will be discussed in §2.3.4. For the “repump” lasers, the remainder of the light is used for the MOT. For the two trap master lasers, the remainder of the light is used to injection lock two additional “slave” lasers. A schematic of a slave laser and the injection locking scheme is shown in Figure 2.9. The slave is essentially a high power diode laser that has no external cavity. Light from the master laser coupled into the slave stimulates the diode to lase at the precise frequency of the master. This technique is useful

---

<sup>5</sup>The Littrow configuration is such that the first order diffracted beam is directed back into the diode while the zeroth order beam is coupled out of the cavity.

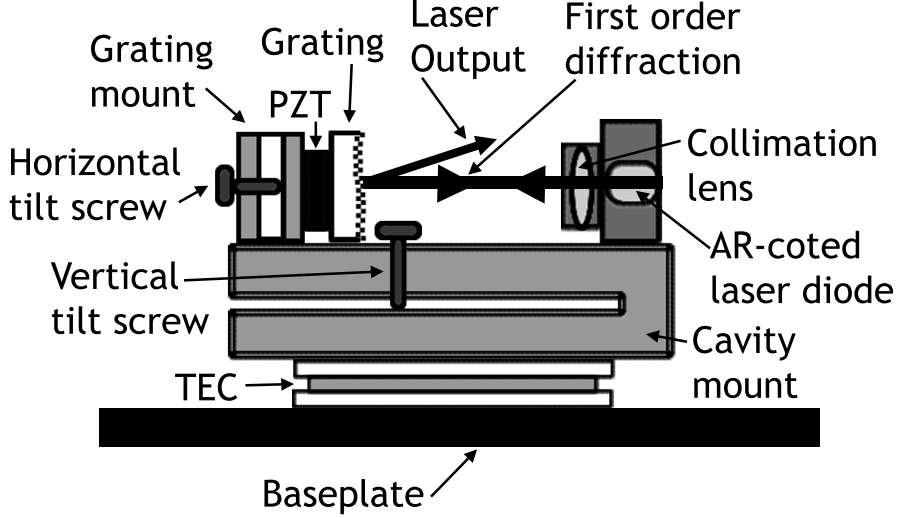


Figure 2.8: Schematic of tuneable diode laser. The design of the tuneable diode lasers used in our experiments is shown. Alignment of the cavity is adjusted with the vertical and horizontal tilt screws. The horizontal screw is also used for gross frequency tuning. Finer tuning is achieved by changing the temperature of the diode by cooling or heating it with the TEC, and by applying a voltage to the PZT which adjusts the angle of the grating. The grating in the cavity is in Littrow configuration so that the first order diffracted beam is used for feedback while the zeroth order beam is coupled out.

since we require more laser intensity in the trap beams than is output by the master lasers. Since the slave requires no frequency tunability or stabilization, the entire diode output can be used for the MOT.

Injecting a slave laser is a non-trivial process and warrants some further discussion. We used two different types of diodes and each type requires a slightly different procedure to be employed. For the Rb slave, we used an ordinary 100 mW,  $\sim 780$  nm diode (Intelite, Inc.); for the Cs slave we used a 150 mW AR-coated diode (SDL; coated by Sacher Lasertechnik). In order to injection lock the ordinary diodes, which have their own internal cavity, they must be “free-running” (lasing without being injection locked) at a frequency very close to that of the master, typically within a GHz. The AR-coated diodes, which lase when free-running even with one facet coated (the weak reflections off the coated facet are enough to build up power and cause stimulated emission), do so at  $\sim 840$  nm, roughly 10 nm to the blue of the master wavelength, but can still be injected. The flip side of this is that it requires only a fraction of 1 mW to inject an ordinary diode while one typically needs

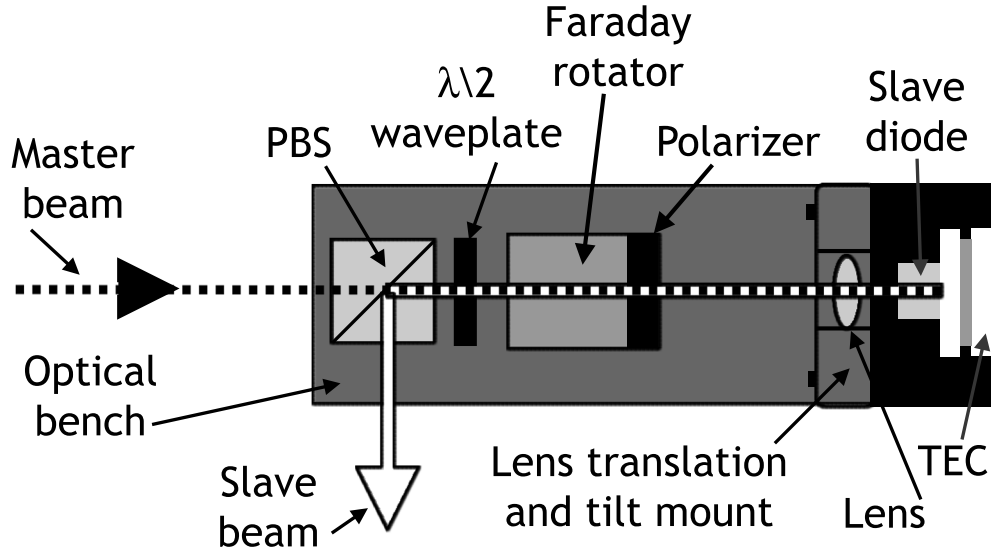


Figure 2.9: Slave laser injection. The method by which we injection lock our slave lasers is shown. The optical isolator is rotated so that the attached polarizer maximally transmits the light coming from the slave diode. The waveplate is then rotated so that the slave beam is vertically polarized and is thus maximally reflected off the PBS cube. The horizontally polarized master beam will then be maximally coupled into the slave diode. The slave laser beam is collimated with a lens placed in a finely controllable translation and tilt mount. To optimize the spatial overlap between the master and slave beams, the waveplate is rotated slightly so that a small amount of the slave light passes through the PBS; the master beam alignment is then adjusted so that the two beams appear overlapped over a few feet of path length in front of the slave laser optical bench. The free running frequency of the slave is changed by heating or cooling the diode with the TEC, as well as by adjusting the current running through it.



greater than 5 mW to inject an AR-coated diode. This is because the internal cavity of the ordinary diode serves to effectively build up the power of the master light. In practice, power was not an issue for us as we had greater than 7 mW of master light to inject each slave. For the Rb slave, the free-running frequency was monitored on a wavemeter with  $\sim 1$  GHz accuracy while adjusting the temperature and current of the diode (in contact with a TEC) to move it close to the known master frequency. The light injecting the Rb slave was mode-matched to the slave output using two lenses; a small amount of the slave light was temporarily allowed to travel along the master input direction so that the two beams could be matched and aligned by eye. The master light injecting the Cs slave did not need to be mode-matched but was aligned as done for the Rb slave. For fine alignment and current adjustment and to verify that the slaves were injected, a small portion of their output was sent into a scanning Fabry-Perot optical spectrum analyzer (630-790 nm, Coherent, Inc.). When free-running, the analyzer transmission peak from the slave light would jump around wildly, but once injection locking was achieved would suddenly stabilize.

All light used for the MOTs was generated from one of the six lasers discussed above. A detailed description of precisely which beams were derived from which lasers will be given in §2.3.5.

### 2.3.4 Diode Laser Frequency Stabilization

It is essential for the operation of the MOTs that the frequency of the trap and repump lasers be stabilized. Left running on their own, the laser frequencies drift a few MHz on short time scales (millisecond-range noise) and much more on longer time scales (second-range and longer). The laser frequencies must be stabilized to within  $\sim 1$  MHz on all time scales so that the excited state hyperfine splittings of the atoms can be resolved and so that the optimal detunings from resonance can be maintained. Stabilization is accomplished by electronic feedback to the laser's PZT (at low frequencies) and current (at high frequencies). In order for the feedback to be effective, a laser frequency-dependent electronic signal must be generated that is narrow (a few MHz wide). A method of doing this employs saturated

absorption spectroscopy of  $^{85}\text{Rb}$  and  $^{133}\text{Cs}$  levels.

Standard absorption spectroscopy involves passing a laser through a gas of atoms in a cell and monitoring the laser power behind the cell. Dips in the power will be seen when the laser frequency is on resonance with an atomic transition due to the atoms' absorption of the light. However, atoms at room temperature are moving fast enough that Doppler shifts play an important role; an absorption signal from such a sample is very broad, typically 300 MHz wide. Saturated absorption spectroscopy is so-called “Doppler-free”; it gets around Doppler broadening by only addressing atoms of a particular velocity and thus produces narrow signals limited only by the natural linewidths of the atomic states being probed, which are typically around 5 MHz.

The technique of saturated absorption spectroscopy is shown schematically in Figure 2.10. A “pump” laser with frequency  $\omega_{\text{pump}}$  passes through a room temperature gas of atoms with a resonance frequency  $\omega_0$ . The beam's intensity is chosen to be large enough to drive a sizeable fraction of the atoms out of the ground state and into the excited state when on resonance; this fraction is maximally 1/2 when the transition is saturated. Under this condition, the atoms with the particular velocity that Doppler shifts them into resonance with the pump beam (i.e.,  $\omega_0 = \omega_{\text{pump}} + \mathbf{k}_{\text{pump}} \cdot \mathbf{v}_0$ ) are equally populated in their excited and ground states. A counter-propagating “probe” beam with frequency  $\omega_{\text{probe}}$  simultaneously passes through the gas of atoms and its intensity is monitored on a photodiode. As a function of  $\omega_{\text{probe}}$ , the photodiode signal will exhibit the usual Doppler broadened absorption shape except when the probe frequency is on resonance with the same atoms that have been addressed by the pump laser (i.e.,  $\omega_0 = \omega_{\text{probe}} + \mathbf{k}_{\text{probe}} \cdot \mathbf{v}_0$ ). At such a frequency, the probe laser is not attenuated due to absorption because the resonant atoms are stimulated to emit the same amount of light as they absorb. As a result, the photodiode signal will have a narrow peak superimposed on the broad doppler dip. Clearly, the pump transition need not be saturated to observe the peak; the sub-Doppler feature will appear (albeit smaller) as long as *some* fraction of the ground state population is

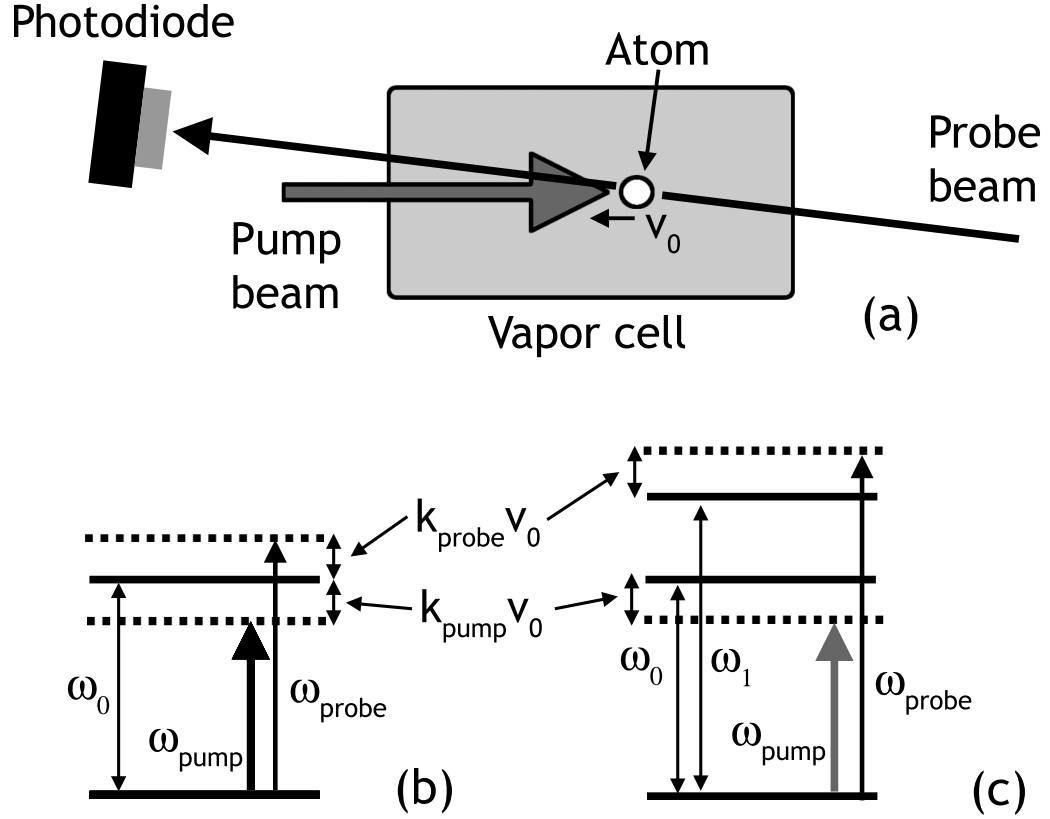


Figure 2.10: Schematic of saturated absorption spectroscopy. (a) The pump and probe beams incident upon an atom moving with velocity  $v_0$  is shown. The intensity of the probe beam after it passes through the vapor cell is monitored by a photodiode. (b) The pump and probe laser frequencies are both resonant with the same excited state of an atom moving at  $v_0$  due to the Doppler shifts  $k_{\text{pump}}v_0$  and  $k_{\text{probe}}v_0$ . As result the photodiode will measure a decreased absorption of the probe beam by atoms with this velocity and a sub-Doppler peak in the signal will be observed. (c) The pump and probe beams are resonant with different excited states for an atom moving at  $v_0$  due to Doppler shifts. As a result, a cross-over sub-Doppler feature will be observed on the photodiode signal.

driven to a level from which the probe light cannot be absorbed.<sup>6</sup>

The location of this peak (and the atomic velocity class addressed) depends on the relative frequency of the pump and probe beams. If, for example, we have  $\omega_{probe} = \omega_{pump} + \Delta$ , then the peak will occur at  $\omega_{probe} = \omega_0 - \frac{\Delta}{2}$ . For Rb and Cs atoms, the hyperfine structure shown in Figure 2.2 can be resolved using this technique and peaks corresponding to transitions to all excited state hyperfine levels are observed. In addition, peaks referred to as “cross-overs” are seen. These arise when the pump beam is resonant with one hyperfine level and the probe beam is resonant with another, for the same velocity class of atoms. If we assume that the atomic resonance frequencies are  $\omega_0$  and  $\omega_1$ , and again assume that  $\omega_{probe} = \omega_{pump} + \Delta$ , then the cross-over peaks will occur at  $\omega_{probe} = \frac{\omega_0 + \omega_1 - \Delta}{2}$ . It should be noted that the cross-over peaks will only be seen between levels that are split by less than the maximum Doppler shift.

The electronic signal of narrow peaks from the photodiode is used to stabilize the frequencies of the master diode lasers in our experiment. The optical setup and electronics necessary to do this are shown schematically in Figure 2.11. A small fraction of the master laser beam, with frequency  $\omega_L$ , is split off and used for the saturated absorption spectroscopy. This beam is further split into a weak probe beam and a stronger pump beam. The probe beam (with frequency  $\omega_{probe} = \omega_L$ ) is directed through a vapor cell of either Rb or Cs and is then monitored on a photodiode as described above. The pump beam is first sent through a 75 mm focal length lens and then into an acousto-optic modulator (AOM), driven with an RF frequency  $\omega_{RF}$  and positioned at the lens’ focal point. The emerging first order diffracted beam, which is shifted in frequency by plus or minus  $\omega_{RF}$  (depending on which diffracted order is used) and spatially deflected by an angle proportional to this shift, is re-collimated by another 75 mm focal length lens positioned a focal length away from the AOM’s center. The diffracted beam is then reflected back into the AOM which

---

<sup>6</sup>Along this line of reasoning, the dip will also appear when the population of the ground state being probed is optically pumped into a dark state; this occurs in atoms, such as Rb and Cs, which possess multiple ground states to which the excited state can decay and that are split by an amount larger than the probe laser linewidth.

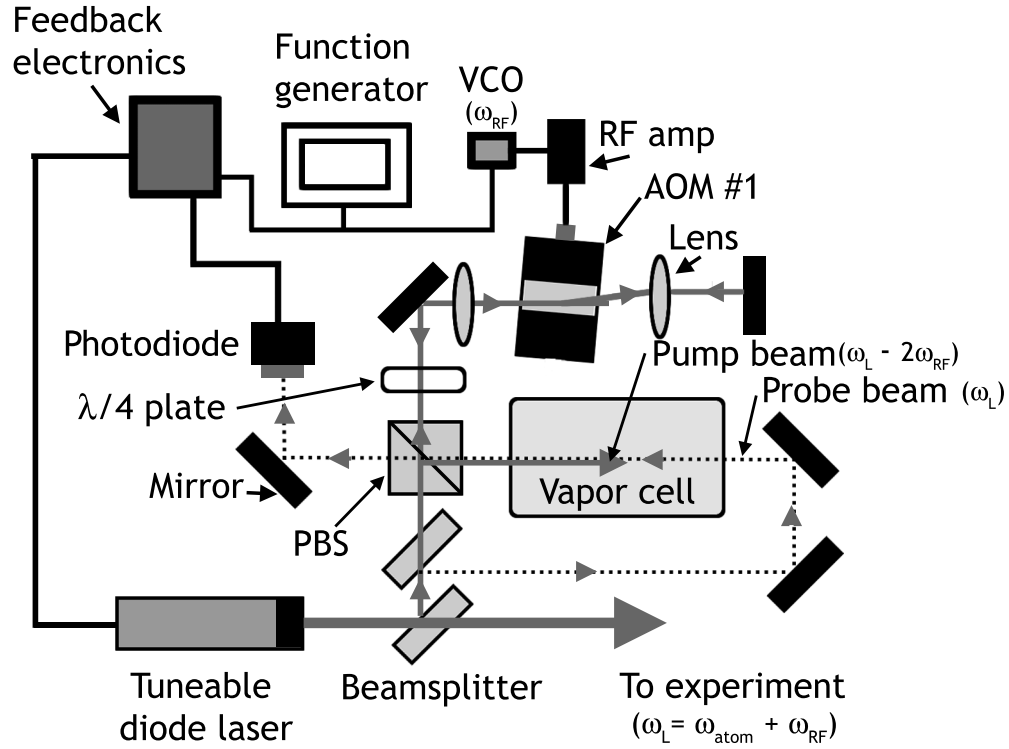


Figure 2.11: Laser frequency stabilization setup. The optics and electronics used to stabilize the frequency of our tuneable diode lasers are shown schematically. A small fraction of the diode laser, with frequency  $\omega_L$ , is split off and is used to generate the pump and probe beams. Before being directed into the vapor cell, the pump beam is double passed through an AOM which is used to shift its frequency by  $-2 \times \omega_{RF}$  and dither its frequency by applying an AC signal to the voltage-controlled oscillator (VCO) from a function generator; the sign of the frequency shift is determined by which AOM diffraction order is used, and we here assume that the -1 order is used for both passes. The feedback electronics generate a derivative of the saturated absorption photodiode signal using lock-in detection (the photodiode signal is mixed with the signal from the function generator and is then sent through a low pass filter). This signal, after being amplified with adjustable proportional and integral gain, is sent to inputs on the laser that control its current and cavity PZT. As a result, the laser is locked at a frequency  $\omega_L = \omega_{atom} + \omega_{RF}$ , where  $\omega_{atom}$  is the lock transition frequency.

yields another first order diffracted beam with frequency  $\omega_{pump} = \omega_L \pm 2\omega_{RF}$ ; the sign is again determined by which AOM order is used. This “double-passed” beam is sent through the vapor cell, spatially overlapping and counter-propagating to the probe beam. The diffraction efficiency of an AOM depends sensitively on the angle with which the beam enters. The configuration of lenses used to double-pass the pump beam is chosen to ensure that on the second pass, the beam enters the AOM at an angle independent of the size of its deflection on the first pass. This allows one to change the frequency shift without having to realign the optics.

In addition to the AOM being used to shift the pump frequency relative to the probe frequency by a constant offset ( $\Delta = \pm 2\omega_{RF}$ ), it is used to modulate the frequency of the pump beam. The RF frequency driving the AOM, which is generated by a voltage controlled oscillator and is tuneable, is dithered at  $\sim 100$  kHz by a function generator. The saturation absorption photodiode signal, which is modulated as a result of the pump frequency dither, is mixed with the function generator signal and the output of the mixer is sent through a low-pass filter. This is essentially lock-in detection. The result is a signal which is proportional to the derivative of the original photodiode signal. This derivative signal is used as the input to the feedback electronics which have their output connected to the laser cavity PZT and diode current supply both of which affect the laser frequency. The feedback electronics serve to control the sign and size of the feedback signal. The lock point is the zero voltage center of the derivative signal corresponding in laser frequency to the center of a particular atomic hyperfine or cross-over transition,  $\omega_{atom}$ . The monotonic slope of the derivative input signal around zero voltage makes electronic locking relatively simple. The tuneability of the VCO driving the AOM in the saturation absorption setup (which we call AOM #1) allows one to change the laser frequency while it is locked; this is convenient for optimizing the MOT laser detunings for MOT number, density and temperature. As the AOM frequency is tuned, the lock signal center shifts and the feedback electronics move the laser frequency to compensate. Typically, the lasers could be tuned as much as 15 MHz without the lock breaking.

The frequency of the laser when locked is  $\omega_L = \omega_{atom} - \frac{\Delta}{2}$ , which is clearly a function of the particular transition we use as the lock point. The lock transition we choose for each laser is not special; however, for reasons discussed in the next section, we must place additional AOMs in the lasers' beams paths and as a result their frequencies are shifted further before being sent to the MOT. We therefore must choose the lock transitions such that we are able to reach the desired MOT laser frequencies using the required number of AOMs.<sup>7</sup>

The locking electronics used in this experiment were home built, while the master laser diode current driver and temperature stabilization electronics were purchased from Sacher Lasertechnik. The slave laser diode current drivers and temperature stabilizers were purchased from Wavelength Electronics.<sup>8</sup>

### 2.3.5 MOT Optics Setup

The simultaneous trapping of two species of atoms and the ability to measure trap parameters such as atom number, density, and temperature, require many laser beams. All beams are generated from either a saturation-absorption locked laser or an injection locked slave laser. This is shown schematically for the trap and repump beams in Figure 2.12. For the two trap master lasers and two repump lasers, the remainder of the beam that is not used for the saturation-absorption spectroscopy lock is first sent through an AOM (AOM #2). For the repump beams the first order diffracted beam from AOM #2 was used for the MOT repumping light; the frequency shifts of AOMs #2 are chosen so that the Rb and Cs repump light is resonant with the  $^{85}\text{Rb } F = 2 \rightarrow F' = 3$  and  $^{133}\text{Cs } F = 3 \rightarrow F' = 4$  transitions, respectively. For the trap lasers, the first order diffracted beam from AOM #2 is used to inject the slave laser. The output of the slave laser is sent through another AOM (AOM #3) and its first order diffracted beam is used for the trapping light. The frequency

---

<sup>7</sup>The available center frequencies of commercial AOMs (around which there is  $\sim 30$  MHz bandwidth) are very limited; as a result we can obtain only certain values of  $\omega_{RF}$ .

<sup>8</sup>Further details of the locking electronics and the circuit schematics can be found in the Ph.D. thesis of Sunil Sainis, the graduate student working on this experiment who designed and built them.

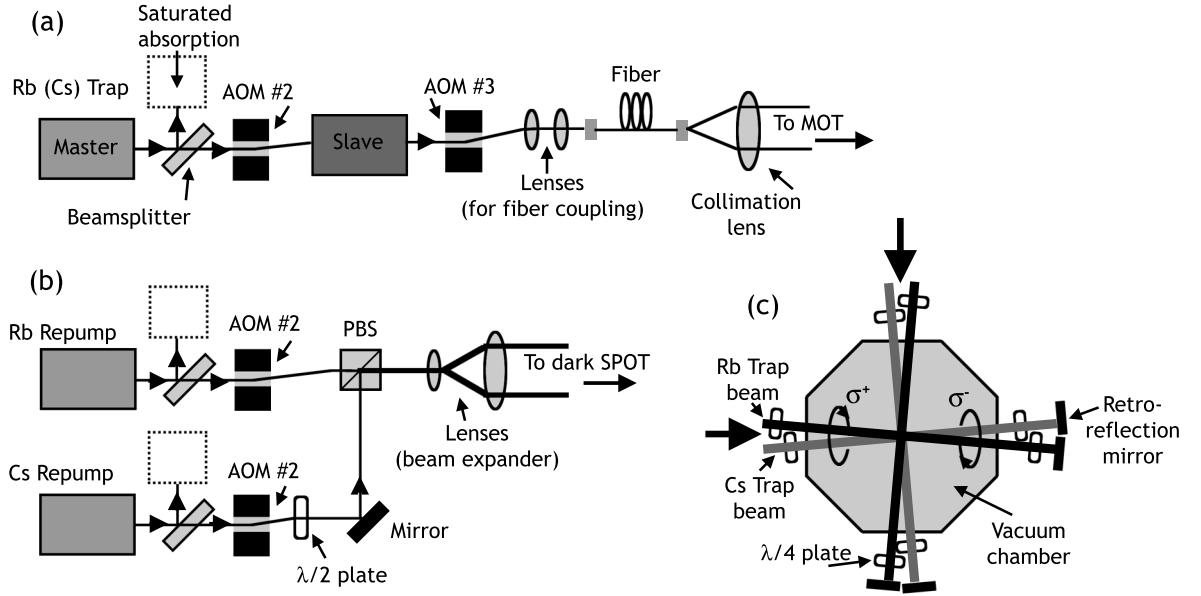


Figure 2.12: Schematic of lasers and optics for trap and repump beams. The lasers and essential optics used to generate the (a) trap beams and (b) repump beams are shown. The Rb and Cs trap optics are the same so only one setup is depicted. The repump beams are combined on a PBS and sent to the dark SPOT setup shown in Figure 2.13 before being sent into the vacuum chamber. (c) The Rb and Cs trap beams are circularly polarized and sent into the vacuum chamber at a slight angle to one another along orthogonal axes; they are then retro-reflected with opposite circular polarization. The repump beams are not shown.



shifts resulting from AOMs #2 and 3 are chosen so that the Rb trap light has a frequency tuned 12.5 MHz below the  $^{85}\text{Rb}$   $F = 3 \rightarrow F' = 4$  cycling transition and the Cs trap light has a frequency tuned 12.5 MHz below the  $^{133}\text{Cs}$   $F = 4 \rightarrow F' = 5$  cycling transition. A summary of the frequency shifting of the trap and repump beams is given in Table 2.1.

Once it has been frequency shifted, the trap light is launched into a polarization-maintaining single mode optical fiber. We use a combination of lenses to mode-match the input beam with the  $\text{TEM}_{00}$  mode of the fiber. This consists of two ordinary lenses for gross shaping and one small lens mounted in a finely adjustable fiber collimation package into which our FC-connectorized fibers are fit. The output of the fiber is allowed to diverge and is then collimated with a 2 inch diameter lens producing a beam approximately 1 inch in diameter. This beam is split into three beams of nearly equal intensity each of which is then properly circularly polarized with  $\lambda/4$  waveplates. The beams are then steered with gold mirrors (as opposed to dielectric mirrors which would ruin the circular polarization) along orthogonal axes into the chamber. Upon exiting the chamber through an opposing viewport, each beam is passed through another  $\lambda/4$  waveplate and is then retro-reflected in order to generate the counterpropagating, oppositely circularly polarized trapping light. The Rb and Cs trapping beams are directed along the same three spatial axes but enter the chamber at a small angle to one another. This allows separate steering optics to be used for each beam. We initially tried spatially overlapping the beams far from the MOT, but it proved essential for our experiments to have them independently adjustable. Without this, we could not simultaneously optimize the spatial overlap and the densities of the two MOTs.

After appropriately shifting the frequencies of the repump beams, they are spatially combined on a polarizing beam splitter cube (PBS) by first rotating the beams' polarizations so that they are orthogonal to one other. The combined, two-color beam is then expanded by a telescope to be approximately 1 inch in diameter and is sent through a piece of glass with a 3 mm diameter piece of black electrical tape stuck on its center. This serves to create the “dark spot” in the repumping beams necessary for the dark SPOT. In order

Laser	Rb Trap	Rb Repump	Cs Trap	Cs Repump
Lock Transition (Frequency, $\omega_{atom}$ )	$3 \rightarrow 3 \times 4$ (384224974.6 MHz)	$2 \rightarrow 1 \times 3$ (384227903.4 MHz)	$4 \rightarrow 4 \times 5$ 351722086.0 MHz)	$3 \rightarrow 4$ (351730902.2 MHz)
AOM #1 Frequency (Locked Laser Frequency, $\omega_L$ )	$2 \times +105$ MHz ( $\omega_{atom} - 105$ MHz)	$2 \times +65$ MHz ( $\omega_{atom} - 65$ MHz)	$2 \times -107.2$ MHz ( $\omega_{atom} + 107$ MHz)	$2 \times +119$ MHz ( $\omega_{atom} - 119$ MHz)
AOM #2 Frequency (Laser Frequency)	$+73$ MHz ( $\omega_{atom} - 32$ MHz)	$+111$ MHz ( $\omega_{atom} + 46$ MHz)	$+83$ MHz ( $\omega_{atom} + 190$ MHz)	$+119$ MHz ( $\omega_{atom}$ )
AOM #3 Frequency (Laser Frequency)	$+80$ MHz ( $\omega_{atom} + 48$ MHz)	NA ( $\omega_{atom} + 46$ MHz)	$-77$ MHz ( $\omega_{atom} + 113$ MHz)	NA ( $\omega_{atom}$ )
Driving Transition (Frequency) (Detuning)	$3 \rightarrow 4$ ( $\omega_{atom} + 65.5$ MHz) ( $-12.5$ MHz)	$2 \rightarrow 3$ ( $\omega_{atom} + 46$ MHz) (on resonance)	$4 \rightarrow 5$ ( $\omega_{atom} + 125.5$ MHz) ( $-12.5$ MHz)	$3 \rightarrow 4$ ( $\omega_{atom}$ ) (on resonance)

Table 2.1: Summary of frequency locking and AOM shifts. The frequencies of the AOMs used to shift the trap and repump lasers are shown. The first row of the table summarizes the transitions to which the lasers are locked; the notation  $F_1 \times F_2$  refers to the crossover saturation absorption peak coming from the  $F_1$  and  $F_2$  hyperfine excited states. The last row summarizes the transitions to which the lasers are ultimately shifted for use in the MOT. The plus or minus sign in front of each AOM frequency specifies whether the plus or minus first order diffracted beam is used.

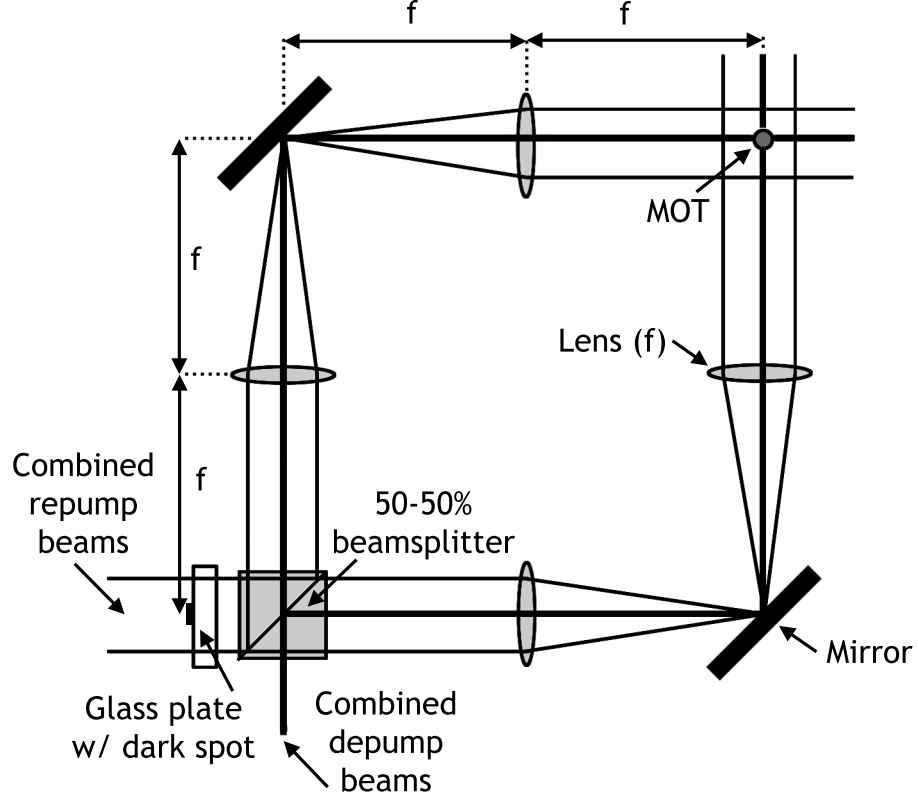


Figure 2.13: Schematic of dark SPOT beams. The optical setup used to implement the dark SPOT is shown. The combined Rb and Cs repump beams are sent through a glass plate with a 3 mm diameter non-transmissive spot in its center. They are split in two and combined with the Rb and Cs depump beams on a 50-50% beamsplitter cube. The spot is imaged at the location of the MOT by passing each beam through two lenses with focal length  $f$ , placed a distance  $2f$  apart, and a distance  $f$  from both the dark spot and the MOT.

to image the dark spot on the center of the MOT, the beam is sent through a 50 – 50% beam splitter cube and each output is sent through a lens system, as shown in Figure 2.13. The two 2 inch diameter lenses (with focal length,  $f$ ) in each path are positioned so that they were a distance  $2f$  apart and a distance  $f$  from both the dark spot and the MOT. In this configuration, the Gaussian and geometric image planes of the dark spot coincide. The two beams are directed along orthogonal axes into the chamber to create a dark volume in the center.

The Rb depump beam is generated by splitting off 50% of the zeroth order beam coming from AOM #3 in the Rb trap line and passing it through an additional AOM. The RF

frequency used to drive the AOM is 92 MHz, chosen so that the  $-1$  diffraction order is resonant with the  $^{85}\text{Rb}$   $F = 3 \rightarrow F' = 2$  transition. The Cs depump beam is generated by double passing the zeroth order beam from AOM #2 in the Cs trap line through another AOM and using the  $-1$  order on each pass; the driving frequency of this AOM is 116 MHz, chosen so that the Cs depump light is resonant with the  $^{133}\text{Cs}$   $F = 4 \rightarrow F' = 4$  transition. The two depump beams are spatially combined on a PBS and then directed through the second port of the beam splitter used to split the repump beam so that they fill the hole created by the dark spot.

In addition to the beams used for cooling and trapping the atoms, we also use beams for absorption imaging of the MOTs, a diagnostic for measuring their density and temperature. In this technique, which will be explained in more detail in §2.4.2, two orthogonally propagating probe beams that are near resonance with the atomic trapping transition are passed through the MOTs and then directed onto two CCD cameras. Lenses are placed before the cameras to image the shadows in the beams cast by the MOT due to absorption (i.e., the plane of the MOT is imaged onto the CCD array). Since we have two MOTs, we must have absorption beams associated with both species. The beams are generated by passing the zeroth orders of AOMs #3 in the Rb and Cs trap beam lines through additional AOMs that are driven by tuneable voltage controlled oscillators. The AOM frequencies are tuneable so that the depth of absorption (which depends on the laser detuning from resonance) can be adjusted to avoid saturation. The  $+1$  order diffracted beam for Rb and  $-1$  order beam for Cs are used so that the absorption imaging light drives the Rb and Cs cycling transitions.

The two diffracted absorption beams are first combined on a PBS and this two-color beam is then split in half with a beam splitter. The two resulting beams are then coupled into single-mode fibers as described earlier. The output is collimated so that the beams are approximately 1 cm in diameter and they are sent along two orthogonal axes through the vacuum chamber. Since we are using dark SPOTs, the trapped atoms are mostly in their lower hyperfine ground state which is dark to our absorption beam. We therefore also

require two “fill-in” beams (one for each atomic species), which have the same frequencies as the repump beams. These beams pass through the MOTs and fill in the dark volume made by the dark spot imaging; this serves to optically pump the atoms into the upper ground hyperfine state so that they are bright to the absorption light. The fill-in beams are generated by passing the zeroth orders of AOMs #2 in the repump lines through additional AOMs that are driven with the same RF frequency oscillators used to drive AOMs #2.

It is important to mention a function of the AOMs that has not yet been explicitly discussed. Not only are the AOMs used to shift the frequencies of the beams, but some are used to *switch* the beams on and off. The switching AOM is always the final one in each beam path before it enters the vacuum chamber. We have the capability to switch every beam discussed above. Fast switching is required for many experimental reasons which will later be made clear. In order to switch the trap and repump light, we clearly require at least one AOM in each of the beam paths; however, the AOMs shift the frequency of the light. This is why we could not simply lock our lasers to the MOT transitions. The switching is accomplished by placing an RF switch between the oscillator driving the AOM and the AOM input. The switches are controlled by sending them TTL signals generated by a Labview software program which runs a multi-digital output card (PCI-DIO-32HS, National Instruments). The beams can be switched on and off in a time less than  $1\ \mu s$ , limited by the beam’s size in the AOM crystal (the time it takes the acoustic wave to propagate through the beam width).

## 2.4 MOT Diagnostics

In the following sections we discuss the diagnostics used to measure the atom number, density, temperature, and spatial overlap of the MOTs. These diagnostics proved to be essential tools for optimizing our MOTs for ultracold molecule formation.

### 2.4.1 Atom Number Measurement

To measure the number of atoms in the MOT, we detect the fluorescence they emit as they scatter the trapping light onto a photodiode. The simplest way to extract the atom number from this measurement is to insure that the fluorescing transition is saturated. The scattering rate is then given by  $\Gamma_{trap}/2$ , where  $\Gamma_{trap}$  is the linewidth of the excited state of the trapping transition.<sup>9</sup> The atom number can then be obtained from the formula

$$N_{atom} = \frac{2P\lambda_{trap}}{\Gamma_{trap}\Omega\hbar c}, \quad (2.16)$$

where  $P$  is the power measured by the photodiode and  $\Omega$  is the detection solid angle. We are able to saturate the transition by jumping the trapping laser frequency to resonance (by sending a voltage to the AOM in the lock). To verify this, we increased the power of the trap laser and observed no increase in fluorescence signal. We use a photodiode with a known active area placed a known distance away from the MOT so that we can calculate  $\Omega$ . We eliminate the background of scattered light not coming from the MOT (i.e., light scattering off chamber walls, by atoms in the background vapor, etc.) by also measuring the photodiode signal with the magnetic field turned off.

### 2.4.2 Density Measurement and MOT Spatial Overlap

The density of the MOT is measured using the absorption imaging technique briefly discussed in §2.3.5. The transmitted intensity of a weak<sup>10</sup> probe beam through the center of an atomic sample, which has an approximately Gaussian density profile (in each spatial dimension), is given by

$$I = I_0 \exp \left[ -\sqrt{\pi \ln 2} \, n_p \, \sigma_{abs} w_0 \left( \frac{1}{1 + \frac{4\Delta^2}{\Gamma_{trap}^2}} \right) \right]. \quad (2.17)$$

---

<sup>9</sup>For the <sup>85</sup>Rb and <sup>133</sup>Cs trapping transitions used,  $\Gamma_{trap}$  is 6.0 MHz and 5.2 MHz, respectively.

<sup>10</sup>Here “weak” here means that the beam is of low enough intensity so as to exert a negligible force on the atoms.

Here  $I_0$  is the unabsorbed beam intensity,  $n_p$  is the peak density along the beam propagation direction,  $\sigma_{abs}$  is the absorption cross section,  $w_0$  is the  $e^{-2}$  Gaussian half-width of the atomic density distribution along the propagation direction, and  $\Delta$  is the detuning of the probe light from resonance. The density of the sample can then be extracted if  $I/I_0$  and  $w_0$  are measured and  $\sigma_{abs}$  is known.

The absorption cross section is given by the formula

$$\sigma_{abs} = \frac{3\lambda^2}{2\pi} L(\alpha, \alpha') \overline{|C(F, m_F, F', m'_F)|^2}, \quad (2.18)$$

where  $C(F, m_F, F', m'_F)$  is a Clebsch-Gordan coefficient and  $L(\alpha, \alpha')$  is the line strength of the transition used for absorption imaging. The line strength is the square of a unitless reduced matrix element that does not depend on  $m_F$  or  $m'_F$ . The label “ $\alpha$ ” stands for a list of the quantum numbers  $\{r, F, J, I, L, S\}$  which specify the levels involved in the transition. In our experiments, we use the MOT trapping transitions for absorption imaging. The line strengths of these transitions are equal to 1 since they are closed.<sup>11</sup>

The overbar in equation 2.18 means we average the squares of the Clebsch-Gordan coefficients over all values of  $m_F$  and sum over all values of  $m'_F$ . This is done because the atoms in the MOT are unpolarized; that is, their spins are oriented randomly with respect to the absorption laser’s linear polarization which defines the quantization axis. This average and sum has an analytic form given by [49]

$$\overline{|C(F, m_F, F', m'_F)|^2} = \frac{2F' + 1}{3(2F + 1)} \quad (2.19)$$

so that

$$\sigma_{abs} = \frac{\lambda^2}{2\pi} \frac{2F' + 1}{2F + 1}. \quad (2.20)$$

---

<sup>11</sup>By “closed”, we mean that after an atom is driven from  $F \rightarrow F'$ , it can only spontaneously decay back to the level  $F$ . Even though the absorption laser is typically detuned by a few linewidths from the closed transition resonance, off-resonant scattering is small enough (given the excited state hyperfine splittings) such that negligible optical pumping occurs into the lower hyperfine ground state in the brief time the absorption laser is on. Thus, a single line strength can be used.

For the absorption transitions used,  $\sigma_{abs}^{85Rb} = 1.25 \times 10^{-9} \text{ cm}^2$  and  $\sigma_{abs}^{133Cs} = 1.41 \times 10^{-9} \text{ cm}^2$ .

The absorption depth,  $I/I_0$ , is obtained by taking two consecutive images: an absorption image and a background image without the presence of the MOT; we then divide the data from the former by that from the latter. The size of the MOT,  $w_0$ , is obtained simply by fitting a Gaussian to the absorption image data. The images are two dimensional and shots are taken along two orthogonal axes, rendering a three dimensional image of the MOT. Determining the volume, along with the density, allows us to make an independent measurement of the atom number.

The procedure for taking an absorption image is as follows. The MOT is allowed to completely load (for approximately 1 s) whereupon the trap, repump, and depump beams are all switched off. The fill-in beam is switched on 50  $\mu\text{s}$  later. After another 50  $\mu\text{s}$ , the absorption beam is switched on for 20  $\mu\text{s}$  and the two cameras (EDC2000N, Electrim Corporation) are triggered via a PCI card to acquire their images. The two-dimensional images are sent from the output of the camera to a computer (through the PCI card) where they can be monitored in real time using a Labview program as an interface. Since the absorption beams are composed of two colors of light, we block the color that will not be absorbed by the atoms being imaged. As a result, we typically take the Rb and Cs MOT density measurements separately, though both MOTs are present at all times.

Absorption imaging also provides a diagnostic for spatially overlapping the two MOTs. This is done simply by monitoring the MOT images taken by the camera (at a rate of about 2 shots per second) on a computer and adjusting the mirrors steering the trapping beams to move the MOTs around until they are coincident. This technique is basically trial-and-error, but it proved vital to have the density information available (by looking at the absorption depth) so that the overlap *and* density were optimized. It is worth noting that when the MOTs are well overlapped, both colors of absorption light can be sent through the atoms and the place in the image where both colors are absorbed represents the size of the overlap region.



### 2.4.3 Temperature Measurement

The MOT temperature is also measured using absorption imaging. The idea is to first acquire an image as described in §2.4.2 and then acquire a second image after allowing the atoms in the MOT to expand freely (under no trapping force) for a fixed amount of time,  $\tau$ . By measuring the size of the atom cloud before ( $w_0$ ) and after ( $w_{exp}$ ) the free expansion, the MOT temperature can be calculated from the formula

$$T_{MOT} = (w_{exp}^2 - w_0^2) \frac{m}{4k_B\tau^2}. \quad (2.21)$$

This equation is obtained by assuming the atoms have Gaussian spatial and velocity distributions and that the width of the latter is related to temperature by equation 2.5. The free expansion was performed by turning off the trap beams. Values of  $\tau$  were typically 5 – 10 ms, chosen so that the cloud diameter expanded to about twice its original size.

## 2.5 Summary

The MOTs described in this chapter are the basis for all the experiments to be discussed in this thesis; our production of UPMs begins with ultracold atoms. In discussing the experimental details used to create the MOTs and the diagnostics used to measure them, no concrete numbers were given regarding laser beam intensities or MOT parameters like atom number, density and temperature. Through the stages (and years) of this experiment, these values have changed; they will therefore be given in the chapters that deal with each experimental stage.

## Chapter 3

# Production of Ultracold RbCs\* Molecules via Photoassociation

In this chapter we discuss the experiments done to produce and detect ultracold, electronically excited RbCs molecules from ultracold atoms. In order to better understand the results of these experiments, we begin by first reviewing the basic relevant theory of molecules and photoassociation. We then go on to discuss the progress that had been made in the experimental photoassociation field prior to our work. Finally we discuss the techniques we used to demonstrate heteronuclear photoassociation and the results we obtained.

### 3.1 Review of Molecular Theory

#### 3.1.1 Born-Oppenheimer Approximation

The general Hamiltonian for a system of electrons and nuclei interacting via the Coulomb interaction is given by

$$H = \sum_{\alpha} \frac{P_{\alpha}^2}{2M_{\alpha}} + \sum_i \frac{p_i^2}{2m} + V(R_{\alpha}, r_i), \quad (3.1)$$

where  $P_\alpha$  is the momentum operator for the  $\alpha^{th}$  nucleus with mass  $M_\alpha$ ,  $p_i$  is the momentum operator for the  $i^{th}$  electron of mass  $m$ , and  $R_\alpha$  and  $r_i$  are sets of nuclear and electronic coordinates, respectively. The potential energy term,  $V(R_\alpha, r_i)$ , is composed of all the Coulomb interactions between the electrons and nuclei. Even for the simplest diatomic molecules it is extremely difficult (if not impossible) to solve the Schroedinger equation,

$$H\Psi(R_\alpha, r_i) = E\Psi(R_\alpha, r_i), \quad (3.2)$$

with this Hamiltonian exactly. The essential idea of the Born-Oppenheimer approximation is to assume that the nuclear motion is much slower than the electronic motion due to the large disparity between the masses of the particles. As a result, the general molecular wavefunction,  $\Psi(R_\alpha, r_i)$ , can be written in the separable form

$$\Psi(R_\alpha, r_i) \approx \psi(R_\alpha, r_i) v(R_\alpha), \quad (3.3)$$

where  $v(R_\alpha)$  is the nuclear vibrational wavefunction which depends only on the nuclear coordinates, and  $\psi(R_\alpha, r_i)$  is the electronic wavefunction which depends on both nuclear and electronic coordinates. One can then separate the Schroedinger equation into two equations: one for the electronic motion and the other for the nuclear motion [50]. In the Born-Oppenheimer approach, one then analyzes the electronic motion by assuming that the nuclei are fixed. This gives the equation for the electronic motion as

$$\left[ \sum_i \frac{p_i^2}{2m} + V(R_\alpha^f, r_i) \right] \psi(R_\alpha^f, r_i) = E'(R_\alpha^f) \psi(R_\alpha^f, r_i), \quad (3.4)$$

where the coordinates  $R_\alpha^f$  are fixed and  $E'(R_\alpha^f)$  is the electronic energy eigenvalue for the particular fixed nuclear coordinates. One can then, in theory, repeatedly solve equation 3.4 for a large enough series of fixed nuclear positions to calculate the dependence of the electronic wavefunctions and energies on  $R_\alpha$  and  $r_i$ .

The equation for the nuclear motion is then approximately given by [50]

$$\left[ \sum_{\alpha} \frac{P_{\alpha}^2}{2M_{\alpha}} + E'(R_{\alpha}) \right] v(R_{\alpha}) = Ev(R_{\alpha}). \quad (3.5)$$

In obtaining equation 3.5, we assume that the electronic wavefunctions are very weakly dependent on the nuclear positions such that we neglect any terms containing derivatives of these wavefunctions with respect to the nuclear coordinates. This is justified in the approximation that the electronic motion can be analyzed assuming the nuclear positions are constant.

Of course, the nuclei are never *completely* fixed; however this approach is valid as long as the nuclear positions change slowly enough, or adiabatically. The condition of adiabaticity is that the electronic wavefunctions change quasi-statically as the nuclear positions change so that the value of the wavefunction satisfies equation 3.4 for each value of  $R_{\alpha}$ . It is for this reason that the Born-Oppenheimer approximation is also known as the “adiabatic approximation.”

Examining equations 3.4 and 3.5 it can be seen that we first find an effective electronic potential,  $V_{B.O.}(R_{\alpha}) = E'(R_{\alpha}^f)$ , as a function of the nuclear coordinates (using 3.4) and then calculate the vibrational nuclear wavefunctions in this potential (using 3.5). As a result, in the Born-Oppenheimer approximation, one then assumes that associated with each electronic eigenstate there is a manifold of vibration levels which represent molecular bound states with different vibrational energies. This picture is somewhat analogous to the quantum mechanical harmonic oscillator, where  $V_{B.O.}(R_{\alpha})$  plays the role of the harmonic potential and the vibrational levels play the role of the quantized phonon modes; of course, the Born-Oppenheimer potentials are, in general, anharmonic and the splittings between vibrational levels are therefore not constant as a function of molecular binding energy. The Born-Oppenheimer approximation is powerful because it allows one to more easily think about and calculate transitions between molecular states, as we will discuss in the next section.

### 3.1.2 Molecular Transitions: The Franck-Condon Principle

As we will see throughout this thesis, it is very important to be able to calculate the strengths of laser driven transitions involving molecular states. In doing so, one will always encounter an overlap integral between initial and final state wavefunctions of the form

$$M = \langle \Psi_f(r, R) | \mathbf{d} \cdot \mathbf{E} | \Psi_i(r, R) \rangle, \quad (3.6)$$

where  $|\Psi_i(r, R)\rangle$  and  $|\Psi_f(r, R)\rangle$  are the initial and final state Born-Oppenheimer wavefunctions, respectively,  $\mathbf{d}$  is the dipole operator, and  $\mathbf{E}$  is the electric field associated with the laser.<sup>1</sup> When calculating such matrix elements, it is extremely useful to make an approximation which rests on what is known as the Franck-Condon principle. The Frank-Condon principle states that during transitions between different electronic molecular states, the positions of the nuclei are fixed. Like the Born-Oppenheimer approximation, the Franck-Condon principle is based on the fact that the electronic motion is much faster than the nuclear motion so that the nuclei cannot move in the time it takes to change the positions of the electrons. As a result, it is often said that transitions take place at a fixed value of internuclear separation, as is shown schematically in Figure 3.1a. Furthermore, since the nuclei are moving most slowly near the turning points of the electronic potential, they are most likely to be located there; as a result, the transition is said to occur at the values of internuclear separation,  $R$ , corresponding to the turning points of the initial vibrational level. Such a point is called the Condon radius,  $R_C$ . Since the Franck-Condon principle states that the nuclear positions cannot change during a molecular transition, it can be seen that the transition will be strong only if  $R_C$  is nearly equal to a turning point of the final state.

Clearly, this is a classical way of thinking about molecular transitions; while it provides valuable intuition into the relative strengths of these transitions, it says little about how

---

<sup>1</sup>In this thesis, we deal with diatomic molecules; from this point on we will drop the subscript “ $\alpha$ ” in the nuclear coordinates and assume there is a single nuclear coordinate,  $R$ , which is defined as the internuclear separation.

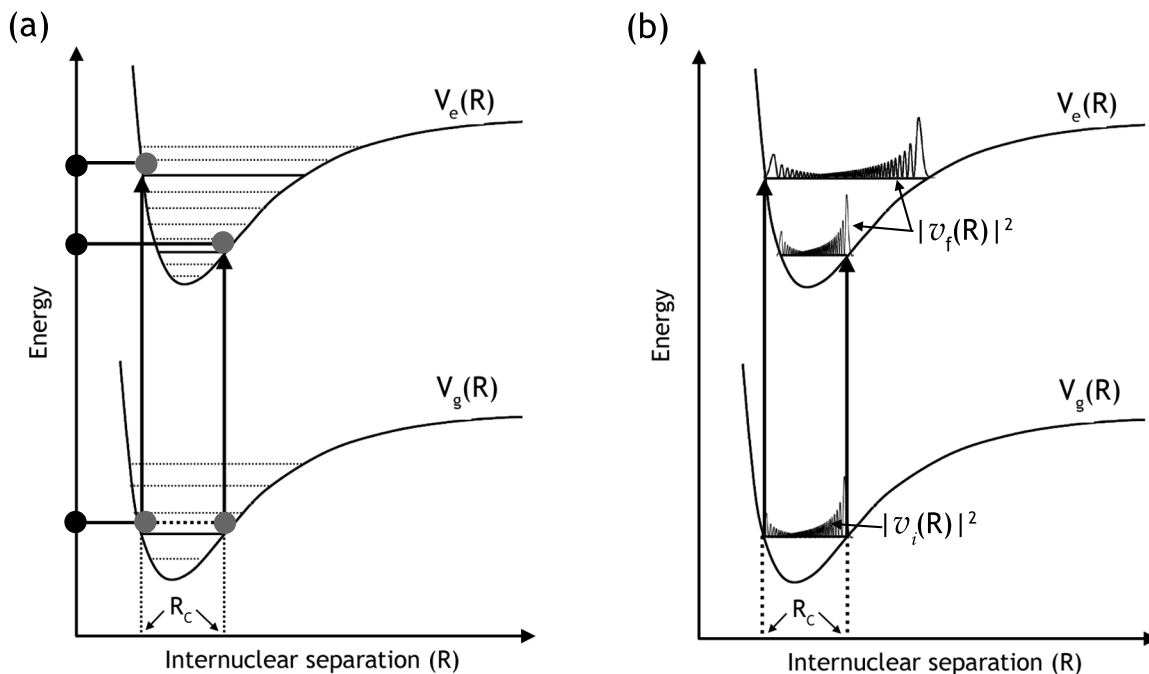


Figure 3.1: The Franck-Condon principle. (a) The classical interpretation of molecular bound-bound transitions is depicted. The nuclei (grey and black circles) are most likely to be separated by a value of  $R$  associated with the inner and outer turning points of the potential in which they move. For the initial state in a transition, these points are known as the Condon radii,  $R_C$ . Transitions are represented by *vertical* arrows since the nuclei do not have time to move, and are most likely to occur at  $R_C$ . (b) The quantum mechanical interpretation is depicted. The vibrational wavefunctions,  $v(R)$ , are peaked at the classical inner and outer turning points of the electronic potential. The transition strength, which is proportional to the square of the integral of  $v_i(R) \times v_f(R)$ , will only be substantial if there is significant overlap between the initial and final vibrational state wavefunctions. Therefore, the transition will only be strong if a final state turning point nearly coincides with a Condon radius.

one goes about quantitatively calculating  $M$  in equation 3.6. Quantum mechanically, the nuclei have wavefunctions that are spread out over space so that it is not quite correct to say a transition occurs at a particular location. The quantum mechanical formulation of the Franck-Condon principle is that the Born-Oppenheimer electronic wavefunction,  $\psi(r, R)$ , varies slowly with internuclear separation, such that the matrix element in equation 3.6 can be written as

$$M = \overline{\langle \psi_f(r, R) | \mathbf{d} \cdot \mathbf{E} | \psi_i(r, R) \rangle} \langle v_f(R) | v_i(R) \rangle . \quad (3.7)$$

We have made the approximation that we can use the average of the electronic wavefunction over  $R$ ,  $\overline{\langle \psi(r, R) \rangle}$ , instead of the true electronic wavefunction, which has allowed us to treat the motion of the electrons and nuclei separately, and to express  $M$  as a product of an electronic and a nuclear matrix element. The value of the electronic part is similar to the electronic matrix elements associated with transitions in free atoms. Atomic transition strengths are often known from measurements or, if not, can be calculated fairly accurately using standard techniques [51]. It is the nuclear overlap integral, then, that usually must be calculated from the vibrational wavefunctions to determine whether or not the transition is strong. The transition strength is proportional to the square of the nuclear matrix element,  $|\langle v_f(R) | v_i(R) \rangle|^2$ , which is called the Franck-Condon factor. Thus, in the language of quantum mechanics, a transition will only be strong if there is significant overlap between the initial and final vibrational state wavefunctions. The classical and quantum mechanical pictures can be unified by noting that the nuclear wavefunctions are peaked at the classical turning points of the electronic potentials (much like the harmonic oscillator wavefunctions);<sup>2</sup> as a result, the integral is dominated by the overlap of the initial and final state wavefunctions at the Condon radii. This is illustrated in Figure 3.1b.

---

<sup>2</sup>The classical velocities at both the inner and outer turning points must be zero; however, the Born-Oppenheimer potentials, in general, have a gentler slope at long range as compared with short range and thus the classical average velocity near the outer turning point is typically smaller than at the inner turning point. Therefore, the wavefunction at the outer turning point is typically much larger than at the inner turning point.

### 3.1.3 Molecular State Labelling and Transition Selection Rules

In order to discuss transitions involving molecular states, it will be useful to review how these states are labelled. Furthermore, it will be useful to discuss here selection rules for transitions between molecular states. For this work, we concern ourselves only with diatomic heteronuclear molecules. Much of this section has been taken and summarized from reference [52].

As for atoms, the electronic states of molecules are labelled by angular momenta quantum numbers; however, the spherical symmetry possessed by atoms is not present in molecules. The usual quantum numbers are then no longer good because they are not associated with operators that represent conserved quantities. For diatomic molecules, however, there is a cylindrical symmetry defined by the axis that joins the two nuclei. The good quantum numbers in these molecules are then, in general, projections of angular momenta along this internuclear axis.<sup>3</sup> The electronic orbital angular momentum,  $\mathbf{L}$ , has a projection along the axis which can have the values

$$M_L = -L, -L + 1, -L + 2, \dots, L. \quad (3.8)$$

One can then define an orbital angular momentum vector,  $\mathbf{\Lambda}$ , which points along the internuclear axis and has a magnitude given by

$$\Lambda = |M_L|. \quad (3.9)$$

An electronic state with a value  $\Lambda = 0, 1, 2, 3, \dots$  is called a  $\Sigma, \Pi, \Delta, \Phi, \dots$  state.

One also defines a projection of the electron spin,  $\mathbf{S}$ , along the internuclear axis. This

---

<sup>3</sup>This breaking of symmetry is essentially equivalent to the problem of an atom in an external electric field. In that problem, eigenstates of  $\mathbf{J}$  are mixed by the field and the associated  $j$  is no longer a good quantum number; however only states with the same  $m_j$  (defined along the field axis) are mixed so that  $m_j$  remains a good quantum number. For the molecule, the electric field is generated between the nuclei along the internuclear axis.



projection can take the values

$$\Sigma = -S, -S + 1, S + 2, \dots, S. \quad (3.10)$$

Then, much in the same way that  $\mathbf{L}$  and  $\mathbf{S}$  are coupled together to form  $\mathbf{J}$  in atoms, we define  $\mathbf{\Omega}$  as the total angular momentum vector along the internuclear axis that has a magnitude given by

$$\Omega = |\Lambda + \Sigma|. \quad (3.11)$$

From equations 3.10 and 3.11 it can be seen that an electronic state with a given value of  $\Lambda$  has a multiplicity of  $2\Sigma + 1$ , corresponding to states with different possible values of  $\Omega$ . These states are, in general, split in energy by the spin-orbit interaction (except for  $\Sigma$  states where  $\Lambda = 0$ ).

In addition to the electronic angular momenta discussed above, there is also an angular momentum,  $\mathbf{N}$ , corresponding to the mechanical rotation of the nuclei around an axis orthogonal to the internuclear axis. All of these angular momenta are then added together to form a resultant total angular momentum vector, which is denoted by  $\mathbf{J}$ . The coupling between  $\mathbf{\Omega}$  and  $\mathbf{N}$  causes both vectors to precess around  $\mathbf{J}$ .<sup>4</sup>

Depending on the relative coupling strengths between the various angular momenta and their coupling to the electric field along the internuclear axis, the way in which  $\mathbf{J}$  is formed varies, as does which of the angular momentum quantum numbers are good. The coupling schemes are known as Hund's cases; the two that will be relevant in this thesis are Hund's cases (a) and (c) which are shown in Figure 3.2.

In case (a), the orbital and spin angular momenta couple much more strongly to the internuclear axis than to each other. This allows us to first define, as above, values of  $\Lambda$  and  $\Sigma$  and then add them to form the vector  $\mathbf{\Omega}$ . This vector is then coupled to  $\mathbf{N}$  to

---

<sup>4</sup>The coupling between the rotational and electronic angular momenta is similar in nature to the spin-orbit effect. The moving charge associated with the rotating nuclei produces a magnetic field that couples to the intrinsic spin of the electrons in the molecule.

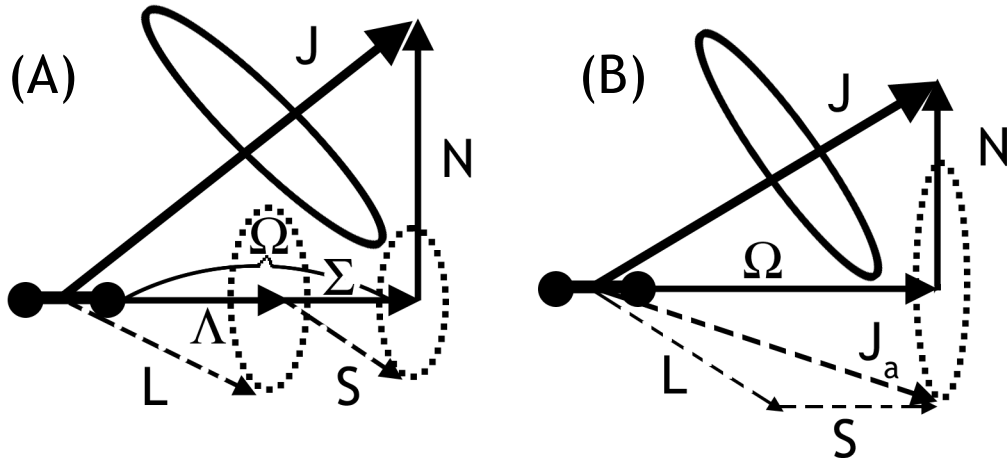


Figure 3.2: Hund's coupling cases. (A) Hund's coupling case (a) is shown. The electronic angular momenta  $\Lambda$  and  $\Sigma$  (projections of  $\mathbf{L}$  and  $\mathbf{S}$  along the internuclear axis) are coupled to produce  $\Omega$ ;  $\Omega$  is then coupled to  $\mathbf{N}$ , the angular momentum associated with the rotation of the nuclei around an axis perpendicular to the line joining them, giving  $\mathbf{J}$ . The angular momentum vectors  $\Omega$  and  $\mathbf{N}$  precess around  $\mathbf{J}$ , which is indicated by the solid ellipse. (B) Hund's coupling case (c) is shown. The electronic angular momenta  $\mathbf{L}$  and  $\mathbf{S}$  are coupled to produce  $\mathbf{J}_a$  which is then projected along the internuclear axis to get  $\Omega$ ;  $\Omega$  is then coupled to  $\mathbf{N}$  as in case (a). Note that in this scheme,  $\Lambda$  and  $\Sigma$  are not defined.

form  $\mathbf{J}$ . The good quantum numbers in this case are  $\Lambda, \Sigma, \Omega, J$ , and  $m_J$ .<sup>5</sup> In case (c), we assume that the coupling between  $\mathbf{L}$  and  $\mathbf{S}$  is stronger than their individual couplings to the electric field along the internuclear axis. In this case, we first couple  $\mathbf{L}$  and  $\mathbf{S}$  to get  $\mathbf{J}_a$ . This resultant vector is then coupled to the internuclear axis to give  $\Omega$ . Finally,  $\Omega$  is coupled to  $\mathbf{N}$  to get  $\mathbf{J}$ . For case (c),  $\Lambda$  and  $\Sigma$  are not defined and only  $\Omega, J$  and  $m_J$  are good quantum numbers. In our situation, where we only ever deal with one species of molecule, these cases describe different ranges of internuclear separation for a particular electronic state. The large internuclear separation associated with many weakly bound vibrational levels results in a diminished internuclear axis electric field; case (c) is then appropriate when dealing with such states. For more deeply bound vibrational levels associated with shorter internuclear distances, case (a) is a better description since the axial electric field is stronger. Electronic states in case (a) are labelled by the nomenclature  $^{2\Sigma+1}\Lambda_\Omega$ , while those in case (c) are simply labelled by  $\Omega$ .<sup>6</sup>

<sup>5</sup>Here,  $m_J$  is the projection of  $J$  along an axis in the laboratory frame.

<sup>6</sup>Actually, Hund's case (b) is also relevant; it is appropriate whenever  $\Lambda = 0$ . In this case,  $\mathbf{S}$  is not coupled

In classifying electronic states, the symmetry properties of their wavefunctions are important as well, since they play a role in determining selection rules for transitions. For heteronuclear diatomic molecules, any plane that contains the internuclear axis is a plane of symmetry, and thus a reflection of the electronic state wavefunction's coordinates in this plane must leave the wavefunction either unchanged or changed only by an overall sign. In the first case, the state is labelled with a superscript “+”, while in the second case it is labelled with a superscript “-”.

We can now write down the selection rules for transitions between molecular states that are coupled by dipole radiation. The proofs of these selection rules will not be discussed here but can mostly be found in reference [52]. Selection rules that hold in both Hund's cases (a) and (c) are

$$\Delta J = 0, \pm 1, \quad (3.12)$$

$$\Delta J = 0 \text{ is forbidden for } J = 0 \rightarrow J = 0 \text{ and } \Omega = 0 \rightarrow \Omega = 0,$$

and

$$\Delta \Omega = 0, \pm 1. \quad (3.13)$$

In Hund's case (a), we have the additional selection rules that

$$\Delta \Lambda = 0, \pm 1 \quad (3.14)$$

$$\Delta \Sigma = 0 \quad (3.15)$$

and that  $\Sigma^+$  states cannot combine with  $\Sigma^-$  states; i.e.,

$$\Sigma^+ \leftrightarrow \Sigma^+, \Sigma^- \leftrightarrow \Sigma^-, \Sigma^+ \nleftrightarrow \Sigma^-. \quad (3.16)$$

---

to the internuclear axis so that the angular momentum projections  $\Sigma$  and  $\Omega$  are not defined. However, one still uses the nomenclature of Hund's case (a), so that states with  $\Lambda = 0$  are termed  $\Sigma$  states.

For Hund’s case (c), there is a selection rule analagous to 3.16, where

$$0^+ \leftrightarrow 0^+, 0^- \leftrightarrow 0^-, 0^+ \leftrightarrow 0^-. \quad (3.17)$$

These selection rules will be essential for subsequent discussions about the path taken towards the production of UPMs.

## 3.2 Photoassociation

Photoassociation is a technique used to form molecules from a gas of atoms using light. In our experiment, it is the first step towards creating a sample of stable, ultracold molecules from our dual species MOT. In a classical picture, photoassociation of a diatomic molecule is a three-body interaction; two free atoms and a photon undergo a collision, after which the atoms are left in a molecular bound state and the absorbed photon serves to conserve energy and momentum. In a quantum mechanical picture, as shown in Figure 3.3, a photon that is red-detuned from an atomic resonance drives two free atoms into a bound level of an electronically excited molecular potential.

This transition from a free atom state to a molecular bound state is somewhat different than the bound-bound molecular transitions discussed in §3.1.2. It turns out that one can still define a Franck-Condon factor which characterizes the strength of the optical coupling between the initial and final states; however, one must also take into account the free atom scattering process in order to calculate a photoassociation rate, i.e., the number of molecules formed from colliding atoms per second. The remainder of this section is devoted to the discussion of the processes which govern this rate.

### 3.2.1 Ultracold Collisions

The photoassociation rate is determined by the inelastic collision rate of the free atoms. The process is clearly inelastic because the outgoing channel (a bound molecule) is different

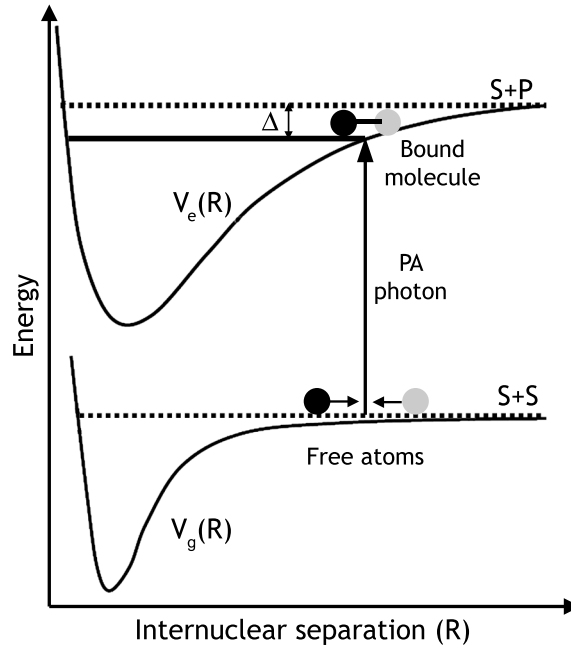


Figure 3.3: The photoassociation process. In photoassociation, two free atoms are promoted to an electronically excited molecular bound state by absorbing a photon. The frequency of the photon is tuned to the red of an atomic transition by an amount  $\Delta$ . The dotted lines represent the dissociation energy of the ground and excited molecular potentials. The dissociation energy in this figure corresponds to two free atoms each in an  $S$  state for the ground potential and to one free atom in an  $S$  state and the other in a  $P$  state for the excited potential.

than the incoming channel (two free atoms). The term “channel” here refers to a distinct state of the atoms involved in scattering. For instance, in a two body process involving atoms  $a$  and  $b$  one could have channels corresponding to the free state  $a + b$ , and the bound state  $(ab)$ . In addition there could be many  $(ab)$  channels corresponding to particular internal states of a molecule as well as many  $a + b$  channels corresponding to free atoms moving in a particular potential.

To analyze a scattering process, one generally constructs an “S matrix,”  $\mathbf{S}$ , which represents the unitary transformation of the incoming scattering state,  $|\Psi_{in}\rangle$ , to the outgoing scattering state,  $|\Psi_{out}\rangle$  as [53]

$$|\Psi_{out}\rangle = \mathbf{S} |\Psi_{in}\rangle. \quad (3.18)$$

Unitarity is demanded, as always, in order to conserve probability. It is important to note that the vectors  $|\Psi\rangle$  represent, in general, a superposition of all scattering channels. The probability of finding the atoms in a particular outgoing state,  $|\Psi_0\rangle$ , is then

$$|\langle\Psi_0|\mathbf{S}|\Psi_{in}\rangle|^2. \quad (3.19)$$

The meaning of the elements of  $\mathbf{S}$  now begins to be clear. The diagonal elements correspond to elastic scattering, while the off-diagonal elements correspond to inelastic scattering.

In the scattering process associated with photoassociation, the interaction potential between two colliding atoms is spherically symmetric, which implies that angular momentum must be conserved. It is therefore convenient to analyze the problem by working in the angular momentum basis,  $|E, \ell, m; \alpha\rangle$ , where  $E$  is the energy,  $\ell$  is the collisional angular momentum,  $m$  is the projection of this angular momentum along some axis, and  $\alpha$  represents the particular scattering channel associated with the basis state. The  $S$  matrix will then be block diagonal,<sup>7</sup> where the blocks will be matrices,  $\mathbf{S}^\ell(E)$ , which have elements  $S_{\alpha\alpha'}^\ell(E)$ ;  $\mathbf{S}^\ell(E)$  will be an  $n \times n$  matrix if there are  $n$  open scattering channels for an

---

<sup>7</sup>The fact that  $\mathbf{S}$  is block diagonal reflects angular momentum conservation.

energy  $E$  and angular momentum  $\ell$ . The block diagonal representation of  $\mathbf{S}$  allows one to analyze the multichannel scattering process in terms of partial waves, much like is done in the treatment of one channel elastic scattering (see reference [54], for example). In fact, in the limit of only one open channel, the single diagonal matrix element,  $S_{11}^\ell(E)$ , is defined as

$$S_{11}^\ell(E) = e^{2i\delta_\ell}, \quad (3.20)$$

where  $\delta_\ell$  is the familiar phase shift associated with elastic scattering.

For multichannel scattering, one defines the partial wave scattering *amplitude* as

$$f_{\alpha\alpha'}^\ell(E) = \frac{S_{\alpha\alpha'}^\ell(E) - \delta_{\alpha\alpha'}}{2i\sqrt{k_\alpha k_{\alpha'}}}, \quad (3.21)$$

where  $k_\alpha$  is the magnitude of the wavevector associated with the scattering channel,  $\alpha$ , and  $\delta_{\alpha\alpha'}$  is the Kronecker delta.<sup>8</sup> Furthermore, as in elastic scattering theory, one can define a total scattering amplitude in the multichannel theory,  $f_{\alpha,\alpha'}$ , as

$$f_{\alpha,\alpha'}(\mathbf{k}_\alpha, \mathbf{k}_{\alpha'}) = \sum_\ell (2\ell + 1) f_{\alpha,\alpha'}^\ell P_\ell(\cos \theta), \quad (3.22)$$

where  $\theta$  is the angle between the wavevectors  $\mathbf{k}_\alpha$  and  $\mathbf{k}_{\alpha'}$  of the incoming and outgoing channels, respectively, and  $P_\ell(\cos \theta)$  is a Legendre polynomial. Finally, we can write the total scattering cross section for atoms beginning in channel  $\alpha$  to scatter into channel  $\alpha'$  as

$$\sigma_T(\alpha, \alpha') = \int |f_{\alpha,\alpha'}(\mathbf{k}_\alpha, \mathbf{k}_{\alpha'})|^2 d\Omega = \frac{\pi}{k^2} \sum_\ell (2\ell + 1) |(S_{\alpha\alpha'}^\ell - \delta_{\alpha\alpha'})|^2, \quad (3.23)$$

where we have taken  $k_\alpha = k_{\alpha'} = k$  as the result of momentum conservation. The scattering cross section is a useful parameter since it can be related to the scattering rate per unit

---

<sup>8</sup>Again, it is instructive to note that  $f_{11}^\ell(E) = \frac{(S_{11}^\ell - 1)}{2ik}$ , which is the partial wave scattering amplitude in the single channel elastic scattering theory. The multichannel scattering formulas always reduce to the elastic scattering formulas when only one scattering channel is present. This correspondence is expected since the incoming and outgoing channel must be identical.

density as

$$K(\alpha, \alpha') = \sigma_T v, \quad (3.24)$$

where  $v$  is the relative speed of the free atoms in the incoming scattering channel.

Analyzing collisions between ultracold atoms in terms of partial waves is extremely useful. This is because there is a repulsive centrifugal term in any spherically symmetric two-body scattering problem given by

$$V_{cent}(R) = \frac{\hbar^2 \ell(\ell + 1)}{2\mu R^2}, \quad (3.25)$$

where  $\mu$  is the reduced mass of the atoms in the collision. This potential has the effect of creating an angular momentum barrier that all partial waves, except  $\ell = 0$  for which  $V_{cent}(R) = 0$ , must overcome in order to contribute to scattering. For an atomic sample with low enough temperature, all partial waves higher than  $\ell = 0$  ( $s$ -wave scattering) are strongly suppressed in the photoassociation process. As we will see in the next section, this is due to the fact that they cannot penetrate to short enough range to reach the Condon radius (typically 10-15 Å) since the barrier height maxima are located at much longer range (typically 50-100 Å). In Rb + Cs scattering, the barrier heights are 80  $\mu K$  and 240  $\mu K$  for  $\ell = 1$  and 2 ( $p$ -wave and  $d$ -wave scattering), respectively. They are calculated assuming the ground state van der Waals potential can be expressed at long range as  $V_{gs}(R) = -C_6/R^6$ , where  $C_6 = 2.6 \times 10^7 \text{ Å}^6 \text{cm}^{-1}$  for RbCs [55]. The barrier heights are comparable to or greater than typical atomic sample temperatures achieved in our MOTs, so that  $s$ -wave scattering is dominant. In the approximation that only  $s$ -wave scattering is present, the  $S$  matrix is greatly simplified; it is reduced to the matrix  $\mathbf{S}^0$ . As a result the *inelastic* scattering cross section ( $\alpha \neq \alpha'$ ) is given by

$$\sigma_T = \sigma_0 = \frac{\pi}{k^2} |S_{\alpha\alpha'}^0(E)|^2. \quad (3.26)$$

For photoassociation experiments, there is never just one incoming free atom channel



associated with single values of  $E$  and  $k$ . Rather, the atomic samples have a temperature,  $T$ , and therefore have a thermal distribution of energy and momentum. To extract an experimentally meaningful scattering rate, we thus do a thermal average of the rate given in equation 3.24 and find for the  $s$ -wave inelastic scattering rate per unit density,

$$K_s(\alpha, \alpha', T) = \langle \frac{\pi v}{k^2} |S_{\alpha\alpha'}^0(E)|^2 \rangle = \frac{\hbar^2}{\mu^{3/2}} \left( \frac{\pi^3}{8k_B T} \right)^{1/2} \langle |S_{\alpha\alpha'}^0(E)|^2 \rangle, \quad (3.27)$$

where  $\langle v \rangle$  is the average relative atomic speed given by

$$\langle v \rangle = \sqrt{\frac{8k_B T}{\pi \mu}}, \quad (3.28)$$

and we have assumed that  $k = \frac{\mu \langle v \rangle}{\hbar}$ . Due to the unitarity of  $\mathbf{S}$  (and  $\mathbf{S}^0$ ), it is easy to see that  $|S_{\alpha\alpha'}^0(E)|^2 \leq 1$ .<sup>9</sup> This inequality is important because it shows that there is a fundamental limit to the total scattering rate for a fixed atomic temperature and density; this is often referred to as the unitarity limit. However, examining equation 3.27 one can see that the total rate (proportional to  $K_s \times n_{atoms}^2$ <sup>10</sup>) increases for increasing density and for decreasing temperature. It is therefore clear that to maximize photoassociation rates in an experiment, one should maximize the density and minimize the temperature of the atomic sample.

So far, we have said little about the role of the optical coupling in determining the photoassociation rate. It is not surprising that it enters by evaluating the matrix elements of  $\mathbf{S}$  since these elements describe in detail the size of the coupling between scattering channels. In the next two sections, we will discuss this coupling and relate it to the Franck-Condon factor picture we used for bound-bound molecular transitions.

---

<sup>9</sup>In the case of single channel elastic scattering  $|S_{11}^0(E)|^2 = 1$ .

<sup>10</sup>This is for single species atomic collisions. For collisions between two atomic species,  $a$  and  $b$ , the total rate is proportional to  $K_s \times n_a \times n_b$

### 3.2.2 Photoassociation as Three Channel Inelastic Scattering

As discussed in the previous section, photoassociation involves an incoming scattering channel corresponding to two free atoms and an outgoing channel corresponding to an electronically excited bound molecule. The free atom channel is coupled to the bound molecular channel by the photoassociation light. The analysis of this scattering process is somewhat involved and will only be roughly sketched here; the details are given in reference [56]. The authors of this paper treat the problem as a three channel process consisting of the incoming free atom channel (channel 0) an intermediate electronically excited bound state channel (channel  $b$ ), and an outgoing, *different* free atom channel that results from molecular dissociation (channel  $a$ ). Channels 0 and  $b$  are coupled by the photoassociation light which results in an off diagonal  $S$  matrix element  $S_{0b}^0$  that is proportional to the free-bound transition rate,  $\Gamma$ . Channels  $b$  and  $a$  are coupled by the spontaneous emission process corresponding to decay of the excited bound state into a ground free atom state; this coupling results in an off-diagonal element  $S_{ba}^0$  which is proportional to the spontaneous emission rate,  $\gamma$ .<sup>11</sup> The matrix element  $S_{0a}^0$  is zero so that there is only coupling between channels 0 and  $a$  via channel  $b$ .

The evaluation of these matrix elements will not be presented here and only the results will be given. It is shown in reference [56] that because one channel is associated with a bound state, the  $S$  matrix can be reduced to a  $2 \times 2$  matrix,  $S^{0,red}$ , where the dimension of the reduced matrix is equal to the number of free atom channels. The square of the single (unique) off-diagonal matrix element is then given by

$$|S_{0a}^{0,red}|^2 = \frac{\gamma\Gamma}{[E - (\Delta_b + E_0)]^2 + \left(\frac{\gamma+\Gamma}{2}\right)^2}, \quad (3.29)$$

---

<sup>11</sup>It might seem troublesome that the analysis is done by assuming the molecule dissociates in the outgoing channel, especially since we are most interested in forming ground, bound state molecules. However, the assignment of a free atom state to the outgoing channel is really just a mathematical trick to make the analysis simpler without affecting the results; it is easier to work with free atom states in the context of scattering theory. The outgoing channel is associated with the free atoms moving in an artificial potential which is chosen so that the strength of the coupling between channels  $b$  and  $a$  accurately reflects the observed spontaneous emission rate from the bound state into *all* ground states (including the bound states we are ultimately interested in).

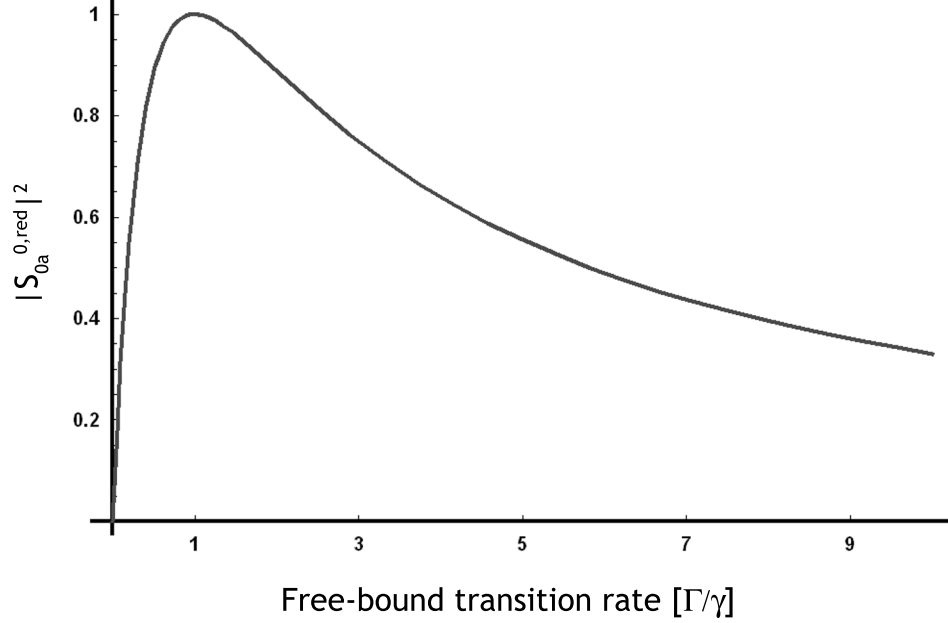


Figure 3.4: Plot of  $|S_{0a}^{0,red}|^2$  versus  $\Gamma$ . A plot of the square of the  $s$ -wave inelastic scattering matrix element is shown versus the free-bound transition rate,  $\Gamma$ . It can be seen that this matrix element (and thus the photoassociation rate) increases sharply as  $\Gamma$  gets larger for  $\Gamma \leq \gamma$ . For  $\Gamma > \gamma$ , the matrix element gradually decreases as  $\Gamma$  increases; the maximum photoassociation rate occurs when  $\Gamma = \gamma$ . In this plot, we have assumed that photoassociation occurs on resonance (i.e.,  $E = \Delta_b + E_0$ )

where  $E_0$  is the energy of the bound state above the free atom ground state energy,  $E$ , and  $\Delta_b$  is the detuning of the photoassociation laser from resonance with the bound state. The expression for  $|S_{0a}^{0,red}|^2$  can then be used in equation 3.27 to obtain the photoassociation rate,  $K_{PA}$ .

It is interesting to examine equation 3.29 and note its dependence on  $\Gamma$ , as is shown in the graph in Figure 3.4. We see that the photoassociation rate will be maximized when the free-bound transition rate is equal to the spontaneous emission rate, i.e., for  $\Gamma = \gamma$ . For  $\Gamma > \gamma$ , the photoassociation rate actually decreases. This is surprising because one would intuitively expect the photoassociation rate to simply saturate at a constant value for  $\Gamma \gg \gamma$ , much like the excited state population does in a two level atom. However, this intuition fails when one of the states belongs to a continuum, as does our incoming free atom scattering state. In terms of the model of photoassociation as a three channel

scattering process, the reason the photoassociation rate decreases for large optical coupling can be explained as follows: we only say that photoassociation has occurred if the outgoing channel is channel  $a$ . When  $\Gamma > \gamma$ , which amounts to the coupling between channels 0 and  $b$  becoming stronger than between channels  $b$  and  $a$ , the outgoing state  $|\Psi_{out}\rangle$  will have a relatively larger amplitude for its 0 channel component than for its  $a$  channel component; in the limit where  $\Gamma \gg \gamma$ , there will be no amplitude in channel  $a$ . A more intuitive way of seeing that the photoassociation rate should decrease for large optical coupling is to note that when  $\Gamma > \gamma$ , the free bound transition is effectively power broadened. If one imagines that the free atom ground state is just a continuum of channels each associated with a different value of the scattering state energy,  $E$ , then the broadening will result in transferral of the population in the excited bound state into many free atom scattering channels (with a spread of  $E$  values) at a rate which is faster than the rate for the molecule to spontaneously decay. Any atoms that are driven from a bound state back to a free scattering state are indistinguishable from atoms that were never photoassociated.<sup>12</sup>

### 3.2.3 Photoassociation Transitions

The free-bound optical coupling rate,  $\Gamma$ , discussed in §3.2.2, can be expressed generally using Fermi's golden rule as

$$\Gamma = \frac{2\pi}{\hbar} |\langle i | e\mathbf{E} \cdot \mathbf{r} | f \rangle|^2 \quad (3.30)$$

where  $|i\rangle$  and  $|f\rangle$  are the initial and final states being coupled. The matrix element is identical to the ones discussed in §3.1.1 and §3.1.2 except that here the initial state is a free scattering state. We can still use the Franck-Condon principle to separate the matrix

---

<sup>12</sup>From this discussion it can be seen that one must rely on spontaneous decay from the excited molecular bound state following photoassociation in order to produce a significant number of ground state molecules. A saturated laser-stimulated downward transition would spread the atomic population equally over all the states connected by the two lasers; since there is a continuum (or infinite number) of initial free atom states, this would result in a negligible fraction of atoms in the final molecular bound state.

element into an electronic and nuclear part so that

$$\Gamma = \frac{2\pi}{\hbar} |\langle \psi_e | e\mathbf{E} \cdot \mathbf{r} | \psi_g \rangle|^2 |\langle v_e(R) | \chi(R) \rangle|^2 = 2\pi\Omega_r^2 |\langle v_e(R) | \chi(R) \rangle|^2, \quad (3.31)$$

where the electronic matrix element has been written in terms of the Rabi frequency,  $\Omega_r$  and  $|\chi(R)\rangle$  is the free scattering state nuclear wavefunction. The factor  $|\langle v_e(R) | \chi(R) \rangle|^2$  is the free-bound Franck-Condon factor, which must be evaluated to determine if the photoassociation rate will be high for a given final molecular bound state.

In calculating the free-bound Franck-Condon factor, one usually uses the WKB approximation for the wavefunction  $|\chi(R)\rangle$  so that it can be written in the form [57]

$$|\chi(R)\rangle = \left( \frac{2\mu}{\pi\hbar^2 k(R)} \right)^{1/2} \sin[k(R)R + \phi], \quad (3.32)$$

where  $k(R)$  is the WKB wavevector given by

$$k(R) = \sqrt{\frac{2\mu(E - V_g(R))}{\hbar^2}}. \quad (3.33)$$

Here  $V_g(R)$  is the ground state van der Waals potential (defined for zero dissociation energy) and  $E - V_g(R)$  is the total kinetic energy. A typical WKB wavefunction associated with the ground state is shown in Figure 3.5. The wavefunction is largest at long range where its kinetic energy is smallest; this can again be explained classically as there being a greater probability to find the atom where it is moving more slowly. Figure 3.5 shows a free-bound photoassociation transition. Applying the Franck-Condon principle, it is clear that the Franck-Condon factor will only be large if the outer turning point of the excited bound vibrational level is at long enough range so that there is substantial overlap between the vibrational wavefunction,  $|v_e(R)\rangle$  and  $|\chi(R)\rangle$ . The Condon radius,  $R_C$ , for free-bound transitions is always defined as the location of the excited level's outer turning point since the ground state,  $|\chi(R)\rangle$ , is not peaked at a turning point, and because the inner turning point of the excited level typically lies at short range where  $|\chi(R)\rangle$  is small.

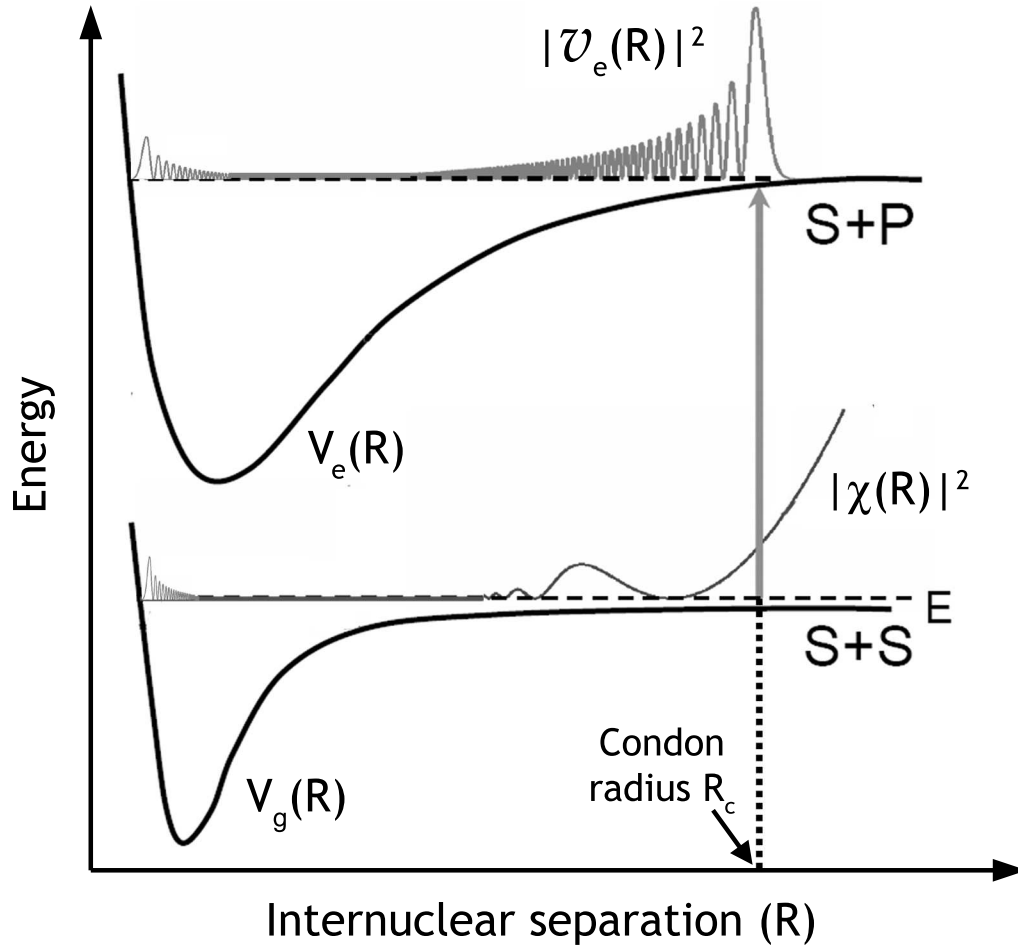


Figure 3.5: The Franck-Condon principle for free-bound transitions. Photoassociation is indicated by a vertical line showing that the internuclear separation does not change during the transition. Photoassociation occurs mainly at the internuclear distance corresponding to the outer turning point of the excited state potential where the wavefunction,  $v_e(R)$  is strongly peaked; this distance is the Condon radius,  $R_c$ . The ground and excited state nuclear wavefunction overlap integral, known as the Franck-Condon factor, is dominated by its value at  $R_c$ . The wavefunction  $v_e(R)$  shown here has a shape typical of a vibrational level near dissociation, and the wavefunction,  $\chi_e(R)$ , is typical of a free atom  $s$ -wave scattering state.

Since the photoassociation rate is largely determined by the value of  $|\chi(R)\rangle$  at  $R_C$ , we can now see why high  $\ell$  partial waves do not contribute to photoassociation if  $R_C$  lies at shorter range than the angular momentum barriers discussed in §3.2.1. As a result of the barriers, the wavefunctions associated with the  $\ell > 0$  partial waves will be greatly reduced at  $R_C$  for low enough atomic temperatures, and their contribution to the Franck-Condon factors (and thus the photoassociation rate) will be negligible.

### 3.2.4 Heteronuclear vs. Homonuclear Photoassociation

Photoassociation using ultracold atoms was first proposed as a way to obtain spectroscopic information on molecular excited states that would not be limited by Doppler broadening [58]. The idea was to scan the frequency of the photoassociation laser incident on a sample of ultracold atoms and look for a signature of molecule production which should occur when the laser is resonant with a molecular bound state. The first experiments that implemented this technique focused on homonuclear molecules; that is, collisions involving only one atomic species [59, 60, 61, 62, 63]. This was surely done for the sake of simplicity; working with a single species MOT is substantially less complicated than working with a dual species MOT. These experiments were extremely successful in obtaining data on the weakly bound molecular states of a number of the homonuclear alkali dimers; this data was used to determine the details of the long range  $R$  dependence of the molecular potentials being probed.

Attempts were then made to obtain similar information for heteronuclear dimers, at first with little success.<sup>13</sup> Heteronuclear molecular ion formation was observed in dual species MOTs (for Na-Cs and Rb-Cs) and was attributed to photoassociation induced by the near resonant MOT trapping light [65, 66]; however, no spectroscopic data was gathered on the molecular states involved because these experiments had no means of scanning the

---

<sup>13</sup>Photoassociation of  $^6\text{Li}$  and  $^7\text{Li}$  into  $^6\text{Li}^7\text{Li}^*$  was seen from a dual species MOT [64] but because of the small isotope shifts involved, the process was essentially homonuclear in character. It should also be noted that because of the identical nuclear charge of the two isotopes, the resulting molecule has a negligible dipole moment.

frequency of the light responsible for photoassociation. It became clear that heteronuclear photoassociation was actually fundamentally more difficult; the Franck-Condon factors involved are far smaller than those for homonuclear photoassociation. The reason for this is illustrated in Figure 3.6 and we discuss it next.

For the homonuclear case, the first excited molecular potentials, which dissociate to atomic S+P states, have an  $R^{-3}$  dependence at long range where the photoassociation occurs. This is due to the resonant dipole interaction discussed in §2.2.3. For the heteronuclear case, however, this dipole interaction is not present and the interaction of an S-state and P-state atom has only the van der Waals  $R^{-6}$  dependence. The heteronuclear excited state potentials are then much shorter range; hence, the Condon radii involved in photoassociation lie at much lower values of  $R$ , where the ground state free atom wavefunction is substantially smaller. Thus, in order to see comparable rates of photoassociation to those observed for homonuclear molecules, heteronuclear experiments must use higher intensity photoassociation lasers (not trivially obtainable), use atomic samples with higher density and lower temperature (also not trivial), or some combination of all three.

### 3.3 Experimental Photoassociation and Detection of RbCs\*

Our experiment with Rb and Cs was the first demonstration of heteronuclear photoassociation where detailed spectroscopic information about the molecular excited states involved in the process was obtained. Furthermore, we were able to experimentally demonstrate the polar nature of the heteronuclear RbCs\* molecule. It should be noted, however, that our main goal was not to do as much spectroscopy as possible. Rather, it was to chart a path towards the production of a stable sample of ground state UPMs; we were essentially interested in obtaining only enough data to do this. In this section, we will discuss the apparatus and techniques used to photoassociate and detect RbCs\* (electronically excited RbCs) molecules.



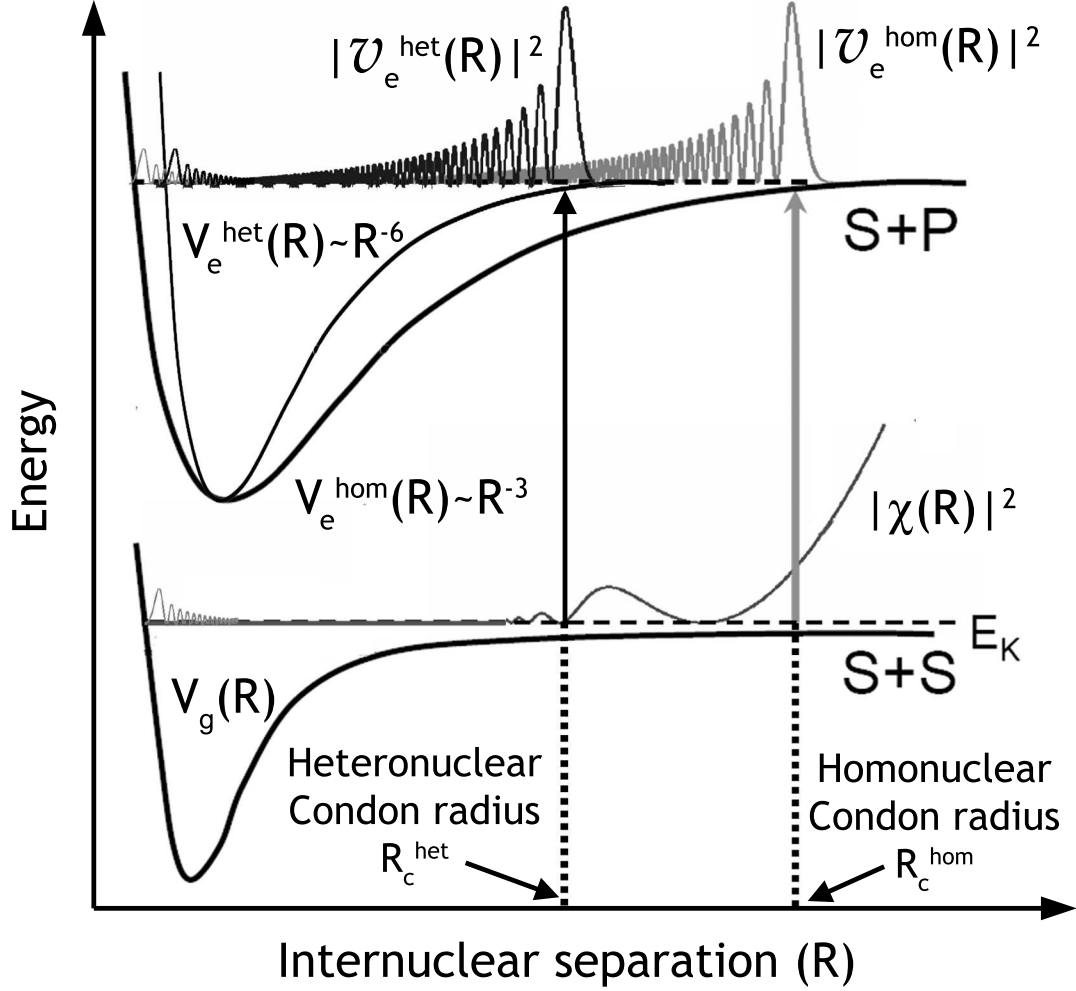


Figure 3.6: Comparison between homonuclear and heteronuclear photoassociation. The Condon radii are shown for homonuclear and heteronuclear photoassociation. Due to the much shorter range heteronuclear excited state potential (which varies at long range as  $R^{-6}$  as opposed to  $R^{-3}$ ), heteronuclear photoassociation occurs at smaller values of  $R$  where the ground state wavefunction,  $\chi(R)$  is considerably smaller. This results in comparatively smaller Franck-Condon factors than in the homonuclear case. Note that this diagram is only schematic and the homonuclear and heteronuclear excited state potentials are not drawn to scale.

### 3.3.1 Photoassociation Experiment Overview

We will now give a brief overview of the processes by which we produce and detect  $\text{RbCs}^*$  in our experiment. The ground and excited molecular states involved in photoassociation are shown in Figure 3.7. We direct an intense laser to be incident on our dual species MOT; the laser is detuned to the red of the atomic  $\text{Rb } 5S_{1/2} + \text{Cs } 6S_{1/2} \rightarrow \text{Rb } 5S_{1/2} + \text{Cs } 6P_{1/2}$  transition. This allows us to drive transitions to vibrational levels associated with a manifold of electronically excited molecular potentials described by the Hund’s case (c) coupling, as shown in Figure 3.7b. We choose to photoassociate to levels dissociating to the lowest energy atomic asymptote to avoid predissociation of the molecules we form [67]. Predissociation can occur when there is a continuum of levels associated with free atoms that have nearly or exactly the same energy as a molecular bound state. The bound state can then effectively couple to the continuum and as a result, the molecule quickly dissociates after it is formed. As an example, molecules in bound levels of potentials dissociating to the  $\text{Rb } 5S_{1/2} + \text{Cs } 6P_{3/2}$  atomic asymptote are subject to predissociation as these levels couple to the continuum states associated with the lower energy  $\text{Rb } 5S_{1/2} + \text{Cs } 6P_{1/2}$  asymptote. Choosing to photoassociate to the lowest energy states, then, allows us to avoid predissociation because there are no continuum states for them to couple to. Predissociation is undesirable because we are mainly interested in forming excited state molecules that remain bound once they spontaneously decay.

Our experiment consists of scanning the frequency of the photoassociation laser and looking for molecule formation associated with the laser being resonant with a molecular bound state. The photoassociation is detected by monitoring the Rb and Cs MOT fluorescence which results from the atoms scattering the trap light. This fluorescence is proportional to the number of atoms in the MOT; forming molecules from these atoms via photoassociation results in a loss of atoms and a reduction of the trap fluorescence. Thus, the signals of photoassociation are resonant dips in the fluorescence as the photoassociation laser frequency is tuned. A key to making this detection technique work well can be

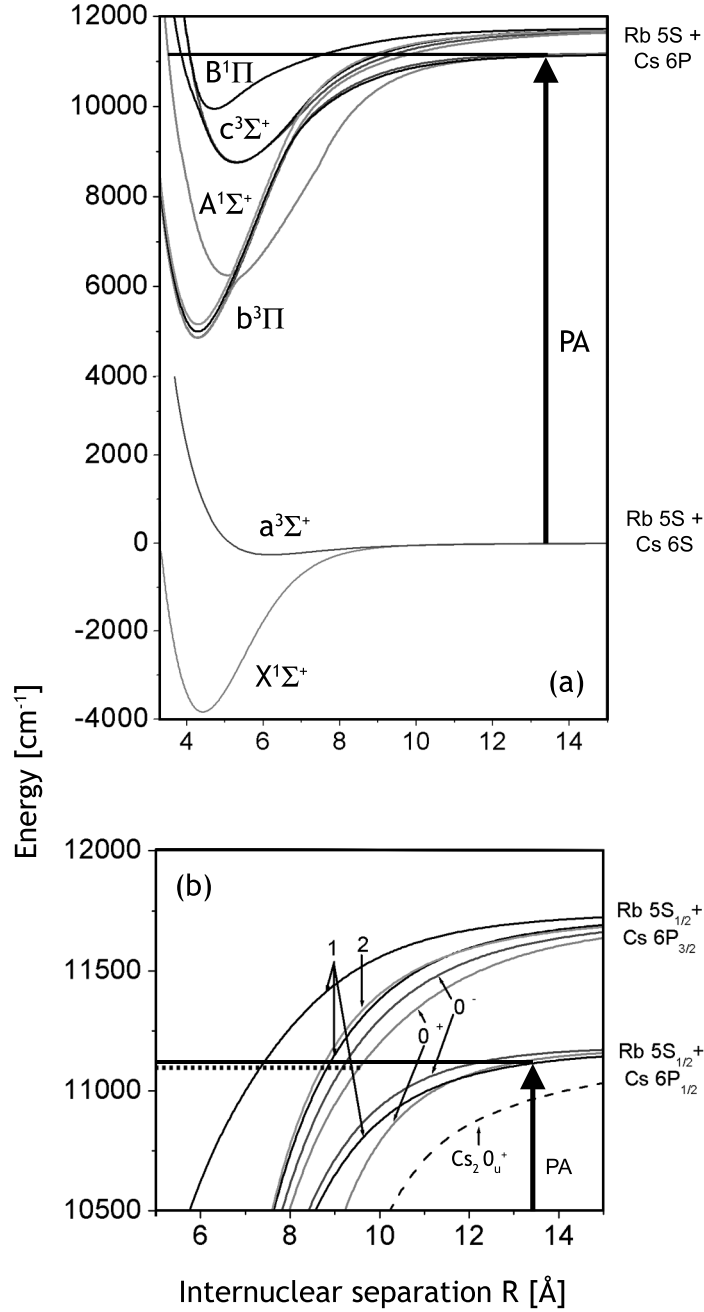


Figure 3.7: RbCs levels involved in photoassociation. (a) The photoassociation (PA) laser is tuned below the  $\text{Rb } 5S_{1/2} + \text{Cs } 6P_{1/2}$  asymptote to avoid predissociation. The ground and excited state molecular potentials are labelled by Hund's case (a) notation. (b) A close-up view of the excited state potentials at long range, labelled by their Hund's case (c) quantum number  $\Omega = 0^+, 0^-, 1, 2$ , is shown. The solid horizontal line indicates a weakly bound vibrational level associated with the  $\text{Cs } 6P_{1/2}$  asymptote; the dotted horizontal line indicates a vibrational level with nearly the same energy but bound more deeply (from the  $\text{Cs } 6P_{3/2}$  asymptote). The dashed curve corresponds to the homonuclear  $\text{Cs}_2 0_u^+$  potential, illustrating its comparatively long range character.

seen by examining equation 2.14. In this equation, we have for the trap loss induced by formation of molecules

$$\Gamma_{other} = \Gamma_{PA} = \frac{1}{2} K_{PA}(I_{PA}) \int_{PA \text{ beam}} n_{Rb} n_{Cs} dV, \quad (3.34)$$

where the photoassociation rate per unit density,  $K_{PA}$ , is a function of the photoassociation laser intensity  $I_{PA}$  and the integral is done over the volume of overlap between the photoassociation beam and the two MOTs. Here,  $\Gamma_{PA}$  is the total loss rate due to photoassociation, which is equal to the formation rate of excited state molecules. Dividing  $\Gamma_{PA}$  by the steady state number of atoms in the MOT gives the steady state photossociation rate per atom,  $\gamma_{PA}$ . It is clear from equations 2.14 and 3.34 that the sensitivity to detecting molecule formation using a trap loss measurement depends on *both* maximizing the loss due to photoassociation *and* minimizing all other losses in the MOTs. Recalling the discussion in §2.2.3, this is best achieved by using the dark-SPOTs. They have both higher densities and lower light-assisted collisional losses than normal MOTs.

### 3.3.2 Experimental Apparatus and Measurement

In this section we will discuss the apparatus used to produce RbCs\* via photoassociation. The MOTs were operated in forced dark SPOT configuration as described earlier. The MOT atom numbers,  $N$ , and densities,  $n$ , were measured using the absorption imaging technique to be  $N_{Rb} = 4 \times 10^8$ ,  $n_{Rb} = 7 \times 10^{11} \text{ cm}^{-3}$  and  $N_{Cs} = 3 \times 10^8$ ,  $n_{Cs} = 3 \times 10^{11} \text{ cm}^{-3}$ .<sup>14</sup>  $N_{Rb}$  and  $N_{Cs}$  were also measured using the fluorescence technique and agreed with the above values to within 30%. The MOTs were approximately spherical and had  $e^{-1}$  radii of 750  $\mu\text{m}$  for both Rb and Cs. The temperatures were measured to be  $T_{Rb} = 55 \text{ } \mu\text{K}$  and  $T_{Cs} = 140 \text{ } \mu\text{K}$ . These MOT conditions were achieved using depump beams with  $e^{-1}$  radii of  $\sim 1.3 \text{ mm}$  and total (before being split) intensities of 0.8 mW/cm<sup>2</sup> and 2.0 mW/cm<sup>2</sup> for Rb and Cs, respectively. The Rb and Cs trapping beams had intensities of

---

<sup>14</sup>In using the dark SPOT, we observed an increase in the densities of the Rb and Cs MOTs by factors of 9 and 4, respectively (as compared with the “bright” MOTs).

3.8 mW/cm<sup>2</sup> and 12 mW/cm<sup>2</sup> per beam, respectively. Both Rb and Cs repump beams had a total intensity of 5.1 mW/cm<sup>2</sup>. The higher Cs trapping beam intensity used resulted in larger loss rates in the Cs MOT, presumably due to increased light assisted collisions; this was done deliberately. When we initially began looking for fluorescence depletion signals with the Cs trapping beam at lower intensity, we encountered many large Cs<sub>2</sub> resonances. As these resonances depleted the Cs MOT, we would observe an *increase* in the Rb MOT fluorescence. This is due to the reduced loss from the Rb MOT resulting from a decrease in collisions with Cs atoms [68, 69, 70].<sup>15</sup> We were worried that these “peaks” might obscure the dips corresponding to RbCs production. We found that using a higher Cs trapping beam intensity did not substantially affect the MOT density but made the Cs MOT much less sensitive to Cs<sub>2</sub> (and ultimately RbCs) photoassociation loss. As a result, we were able to eliminate the unwanted peaks in the Rb fluorescence signal with the effect of reducing our sensitivity to detection of RbCs production from the Cs fluorescence signal. We therefore observed much larger fluorescence depletion in the Rb signal than in the Cs signal.

The light used for photoassociation was generated by a Ti:Sapphire laser (Coherent 899-29). The population inversion in the Ti:Sapphire crystal was created by pumping it with a diode-pumped, frequency doubled Nd:YVO<sub>3</sub> laser (Coherent, Verdi V-10) that had a 10 W output power. The Ti:Sapphire laser output had a power of 600 mW near 895 nm and was internally stabilized to a linewidth of  $\sim 1$  MHz.<sup>16</sup> Due to the relatively small Franck-Condon factors associated with heteronuclear photoassociation, we initially desired more laser power. As a result, we constructed a resonant build-up cavity around our chamber. This 25 cm long half-confocal cavity consisted of a curved (25 cm radius of curvature) input coupler with 97 % reflectivity and a highly reflective rear mirror mounted

---

<sup>15</sup>Indeed, we always observed the fluorescence from one MOT increase significantly (by 20-30%) when the other MOT was extinguished (by blocking one of the trapping beams, say). This increase in steady state atom number can be explained only by a decrease in the loss rate.

<sup>16</sup>The laser frequency was not stabilized at DC; however, the slow drifts were not a problem for the photoassociation experiments because the time spent collecting data at each frequency point was small compared to ratio between the drift rate and the photoassociation resonance linewidth.

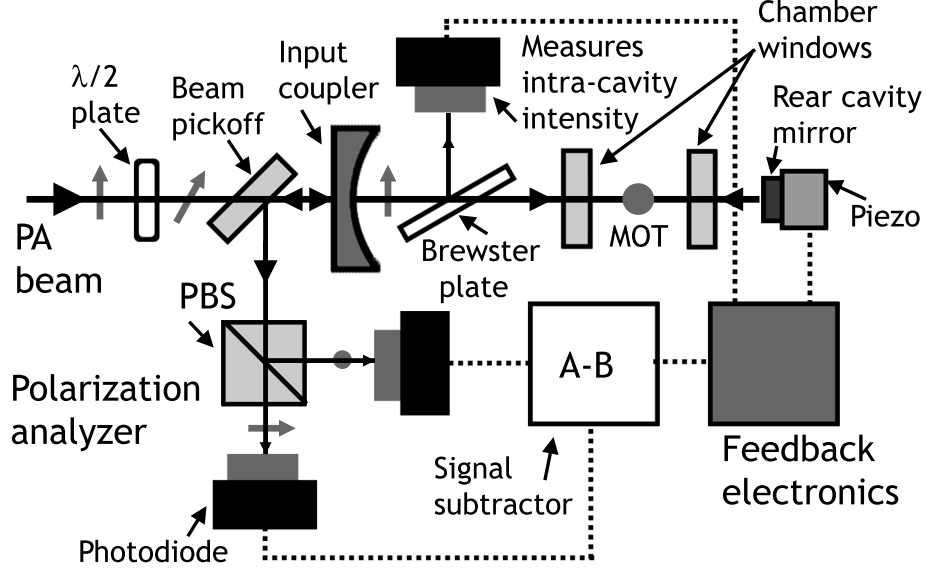


Figure 3.8: Schematic of optics and electronics for build-up cavity lock. The Hänsch-Couillaud method by which we lock our build-up cavity is illustrated. An electronic error signal is generated by analyzing the difference in polarization between the portion of light that enters the cavity and the portion that gets reflected off the input coupler as a function of cavity length. The grey arrows represent the polarization of the light. The error signal is sent to the PZT to stabilize the cavity length via feedback electronics that control the feedback gain. By monitoring the intra-cavity intensity with a photodiode and sending the signal to the feedback electronics, the cavity is made self-locking; if the signal falls below a set value, the electronics attempt to re-lock to a cavity transmission maximum.

on a piezo-electric stack. The input laser beam was modematched into the  $TEM_{00}$  mode of the cavity, which had a  $e^{-2}$  mode waist of  $380 \mu\text{m}$  at the position of the MOTs. The cavity length was stabilized by using electronic feedback to the piezo-electric stack. The cavity length-dependent electronic signal (“error signal”) input for the feedback electronics was generated using the Hänsch-Couillaud method [71]. The optical setup used is shown in Figure 3.8. A Brewster plate, AR coated on one side, is placed inside the cavity and the incident photoassociation laser polarization is rotated with a  $\lambda/2$  plate by a small angle away from the Brewster axis. In addition, a glass pickoff plate is placed in the beam path *before* the cavity so that some light reflecting off both the input coupler and the back mirror would be directed towards a polarization analyzer. This consists of a  $\lambda/4$  plate followed by a PBS cube and two photodiodes positioned to monitor the power exiting each port of the beam splitter. The fast axis of the  $\lambda/4$  plate is oriented at a  $45^\circ$  angle to the axes of the PBS

cube so that any linear polarization entering the analyzer will be split evenly by the PBS. The outputs of the photodiodes are subtracted and the resulting signal has a dispersive lineshape as a function of cavity length. This can be seen to arise in the following way: the incoming laser polarization can be decomposed into a component that lies parallel to the Brewster axis and one that lies perpendicular to it. The perpendicular component always sees a high loss cavity because it is not effectively transmitted through the Brewster plate; as a result it is mostly reflected off the input coupler. The parallel component, however, sees a low loss cavity. When the laser frequency is near a cavity resonance, this component makes multiple passes inside the cavity. The light that is coupled out through the input coupler combines with the reflected perpendicular component; however, it has acquired a relative phase shift. Thus, the light that is directed towards the polarization analyzer will in general be elliptically polarized. Since elliptically polarized light can be decomposed into counter-rotating circularly polarized components with different amplitudes, it is clear that the  $\lambda/4$  plate acts to produce a linearly polarized beam which then gets split by the PBS in a ratio which depends on the magnitude and handedness of the ellipticity. The size and sign of the differential photodiode signal will then depend on the phase shift. In the case where there is no relative phase shift between the perpendicular and parallel components, i.e. when the laser is either so far from a cavity resonance that both components are simply reflected off the input coupler or exactly on resonance where there is no phase shift by definition, the beam sent to the analyzer will be linearly polarized and the differential photodiode signal will be zero.<sup>17</sup> Feedback electronics allow us to lock the cavity so that the laser is resonant and power is built up inside. Since we need to scan the frequency of the photoassociation laser as we take data, we require that the cavity lock be able to follow. This is accomplished by monitoring the intra-cavity intensity with a photodiode via a reflection off the Brewster plate. If the signal fell below a preset value, a circuit

---

<sup>17</sup>It should be noted that the birefringence of the chamber windows have not been taken into account in this explanation. With our home-built viewports, it was not an issue; however, when we switched to the commercial viewports, the birefringence was so large that it distorted the error signal enough to make it unusable.

shorted the integrator in the feedback loop for about 1 ms, allowing the cavity to re-lock itself. The maximum finesse of our cavity was  $\sim 60$ , limited by the chamber windows and the Brewster plate. This corresponded to a build-up factor of roughly 15 and a peak laser intensity at the position of the MOTs of  $\sim 4 \times 10^7$  W/m<sup>2</sup>.

We verified that the photoassociation laser was optimally overlapped with the MOTs by using it to exert a radiation force on the atoms and blow them out of the trap. This was done by tuning the laser to an atomic <sup>133</sup>Cs transition and adjusting the beam position and angle to minimize the fluorescence coming from the MOT. Once this was done, the build-up cavity was aligned around the beam.

The frequency of the photoassociation laser was scanned by applying an external voltage to an input on the laser controller electronics. This voltage would be used to tune the resonance of an internal reference cavity to which the laser was locked. The laser could be scanned up to 30 GHz ( $\sim 1$  cm<sup>-1</sup>) in this way before the main laser cavity had to be adjusted. Conveniently, our laser system has an Autoscan feature which utilizes an internal wavemeter and provides a computer interface so that one can simply enter the desired frequency and a feedback system adjusts the cavity optics to tune it to within an accuracy of a few hundred MHz. Typically, data was collected in  $\sim 0.1$  cm<sup>-1</sup> long scans which were then pieced together. This length was chosen because the time required to complete a scan was a little less than the mean time to failure of a diode laser lock. The scan voltage was applied via an analog output channel of a computer controlled PCI board (PCI-6024E, National Instruments) which was synchronized with data acquisition with a Labview program. The laser frequency was ordinarily monitored using a wavemeter (Burleigh WA-1500) having a 150 MHz absolute accuracy which could write its measurements to our data acquisition computer via GPIB. For some of our data we required a higher accuracy which was obtained as follows: a small fraction of the photoassociation laser, along with some light from the locked Rb trap laser were coupled into a Fabry-Perot optical spectrum analyzer with a free spectral range of 300 MHz. As the photoassociation laser was tuned, the splitting between the two resulting cavity peaks was measured. This gave the relative



spacing between successive frequency points to an accuracy of  $\sim 5$  MHz, limited by the Fabry-Perot resolution. The locked reference laser was used so that the measurement would be insensitive to thermal drifts of the cavity length. The splitting was measured for each frequency point by scanning the cavity and sending the optical spectrum output through an analog input channel on the PCI-6024E board, whereupon a Labview peak finding algorithm was used to analyze the digitized signal in real time.

In order to detect the trap loss due to photoassociation, the MOT fluorescence was imaged onto a photodiode. To reduce electronic noise we used a lock-in detection technique. The frequencies of the Rb and Cs trap lasers were modulated by a few MHz at two different frequencies near 4 kHz by dithering the RF frequencies of the saturation-absorption lock AOMs. The output of the photodiode was fed, in parallel, to two lock-in detectors (Stanford Research Systems, SRS510). The resulting demodulated signals were sent through separate analog input channels of the PCI-6024E board from where they were read in by our Labview program. After each photoassociation laser frequency point, the MOTs were first emptied by briefly switching off the repump light and then allowed to reload. This way, we eliminated coupling between successive data points and were additionally able to monitor the trap loading times for each point. The MOTs were loaded, always in the presence of the photoassociation light, for about 2 s before emptying them and stepping the laser frequency to the next point. This time was chosen to be longer than the typical loading time,  $\tau$ , of the MOTs; typically  $\tau \sim 1.5$  s. The two fluorescence signals (one for each species) obtained for each frequency point were fit, in real time, to a function of the form

$$S(t) = S_0 \left(1 - e^{-t/\tau}\right), \quad (3.35)$$

which is the general solution to equation 2.14; the signal  $S(t)$  is directly proportional to the number of atoms in the MOT and  $1/\tau$  is equal to the total loss rate per atom from the MOT. The steady state fluorescence values,  $S_0^{Rb,Cs}$ , were recorded and plotted versus

measured photoassociation laser frequency.<sup>18</sup>

## 3.4 Results of Photoassociation Experiments

In this section we present the results and analysis of the experiments done to produce RbCs\* via photoassociation.

### 3.4.1 Photoassociation Spectroscopy

We scanned the photoassociation laser frequency over a region from 8 - 93 cm<sup>-1</sup> below the Rb 5S<sub>1/2</sub> + Cs 6P<sub>1/2</sub> asymptote and observed the formation of RbCs\* in numerous rovibrational levels corresponding to the Hund's case (c) electronic potentials  $\Omega = 0^\pm$ , 1, and 2 that dissociate to both the Rb 5S<sub>1/2</sub> + Cs 6P<sub>1/2</sub> and Rb 5S<sub>1/2</sub> + Cs 6P<sub>3/2</sub> asymptotes. Since the  $\Omega = 0^\pm$  levels have no hyperfine structure to leading order (there is no angular momenta to which the nuclear spins can couple), they are identified by their clean rotational progressions. Figure 3.9 shows an example of two such progressions, corresponding to an  $\Omega = 0^-$  and an  $\Omega = 0^+$  level. The relative splittings of the rotational levels follow the form

$$E(v, J) - E(v, 0) = B_v J(J + 1), \quad (3.36)$$

where  $J$  is the rotational quantum number and  $B_v$  is the rotational constant associated with the vibrational state,  $v$ . We typically observe photoassociation into the  $J = 0, 1$ , and 2 rotational levels; we also observe smaller features associated with  $J = 3$ . In general, we found that the  $J = 0$  and 3 features were noticeably larger for photoassociation to  $\Omega = 0^-$  states than for  $0^+$  states, as is evident in Figure 3.9. This, as well as the lack of rotational features corresponding to  $J > 3$ , is consistent with a slight suppression of  $\ell = 1$  scattering and a near total suppression of  $\ell > 1$  scattering due to the centrifugal

---

<sup>18</sup>The uncertainty in the fitted values of  $S_0^{Rb, Cs}$  was much smaller than the experimental noise so that this uncertainty could be neglected.

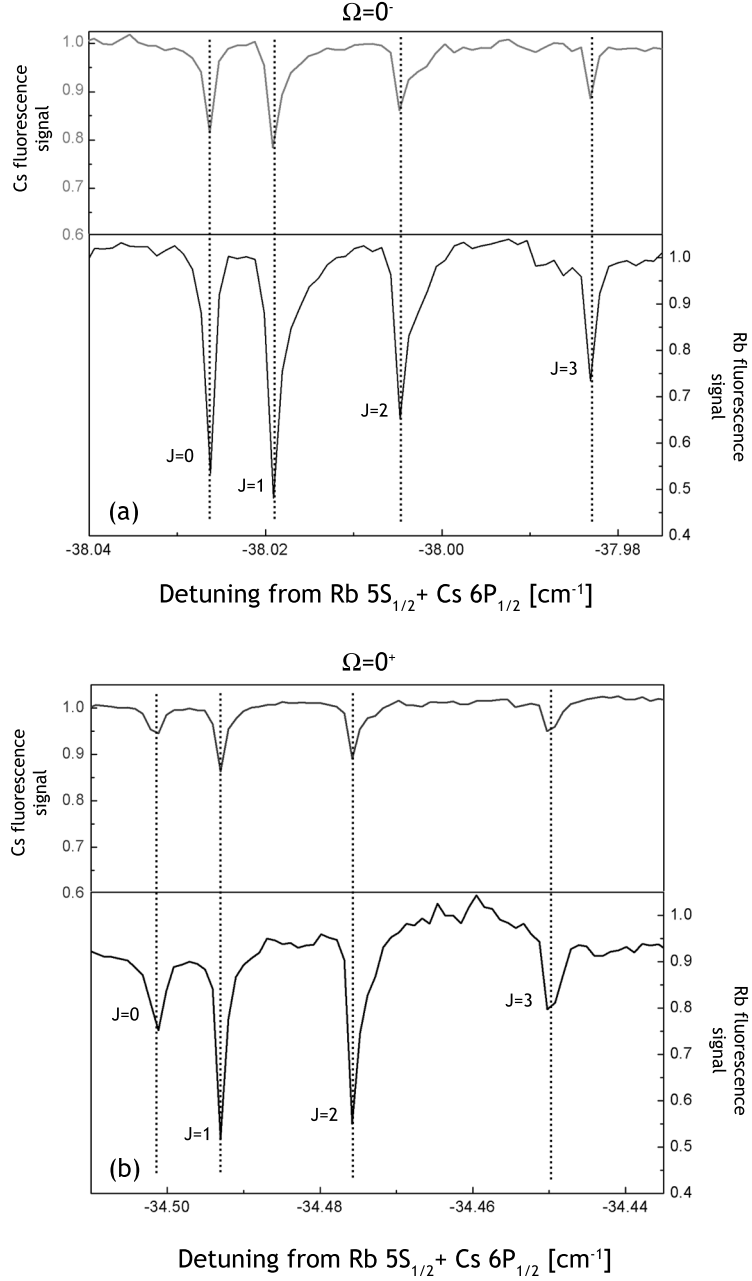


Figure 3.9: Observation of photoassociation to  $\Omega = 0^\pm$  levels. Typical signals indicating photoassociation to a (a)  $0^+$  and (b)  $0^-$  level are shown. These signals are observed by monitoring the MOT fluorescence and detecting trap loss. The vertical axis in the plots represents the fractional depletion of the MOT as a result of photoassociation; the horizontal axis specifies the detuning of the photoassociation laser relative to the Cs  $6S_{1/2}, F = 3 \rightarrow 6P_{1/2}, F' = 3$  atomic transition at  $11178.417 \text{ cm}^{-1}$ . A clean rotational series (from  $J = 0$  to 3) is seen in both cases. The vertical dashed lines show that the Rb and Cs traps are simultaneously depleted indicating the production of RbCs. The smaller depletion of the Cs fluorescence signal is the result of higher non-photoassociation induced loss rates in the Cs MOT.

barrier discussed in §3.2.1;<sup>19</sup> this is what one would expect given the barrier heights and our atomic temperatures.

We observed many rotational progressions, or “bands,” and measured their positions, which are summarized in Table 3.1. The locations of the band heads correspond to vibrational levels of two overlapping series associated with the  $\Omega = 0^+$  and  $0^-$  potentials. Using models of these potentials obtained from a combination of previous experimental data [72] and *ab initio* calculations [73], and adjusting them to fit our data, we were able to determine which vibrational states correspond to which of the potentials.<sup>20</sup> Figure 3.10 shows two plots comparing our data with the best fit values from the models. Each point on the plot corresponds to a rotational band, where its horizontal axis value is the position of the  $J = 0$  level and its vertical axis value is the rotational constant of the progression. For the  $\Omega = 0^-$  levels shown in Figure 3.10a, one can clearly see two distinct vibrational progressions with noticeably different rotational constants. These correspond to the potentials dissociating to the  $5S_{1/2} + \text{Cs } 6P_{1/2}$  and  $\text{Rb } 5S_{1/2} + \text{Cs } 6P_{3/2}$  asymptotes. It can be seen from Figure 3.7b that levels associated with the  $\text{Rb } 5S_{1/2} + \text{Cs } 6P_{3/2}$  asymptote are more deeply bound and have smaller outer turning points; as a result they have larger rotational constants.<sup>21</sup> Figure 3.11 shows an example of a rotational progression corresponding to one of the deeply bound  $\Omega = 0^-$  levels. It is bound by nearly  $600 \text{ cm}^{-1}$  and has an outer turning point of  $\sim 9 \text{ \AA}$ . In the same scan, we observe a rotational band associated with a much more weakly bound  $0^+$  level; this level, bound by  $\sim 28 \text{ cm}^{-1}$  from the

<sup>19</sup>To see why this is so requires familiarity with the concept of parity in molecules, which will be discussed in §5.4.2. We note that a rotational level,  $J^P$ , in a  $0^-$  ( $0^+$ ) state has parity  $P = (-1)^{J+1}$  ( $P = (-1)^J$ ) and that the scattering state has a parity  $P = (-1)^\ell$ . For a dipole allowed transition, the parity of the initial and final states must be opposite. The final state can have a total angular momentum of  $J = 0, \dots, \ell + 2$ , since there is one unit of electron spin and one unit of photon orbital angular momentum. Parity and angular momentum addition then demand that for a  $0^-$  state, the  $J = 0, 2$  features are associated with  $\ell = 0$  scattering while  $J = 1, 3$  are associated with  $\ell = 1$  scattering;  $J = 4$  can come only from even  $\ell \geq 2$ . For a  $0^+$  state, the  $J = 0, 2$  features are associated with  $\ell = 1$  scattering and the  $J = 1$  state is associated with  $\ell = 0$  scattering; the  $J = 3$  feature can come only from even  $\ell \geq 2$  while higher values of  $J$  can arise only from  $\ell > 2$ .

<sup>20</sup>The theoretical analysis used to make these assignments, which was done by our collaborator Thomas Bergeman, will not be given here.

<sup>21</sup>In the approximation that a diatomic molecule can be treated as a symmetric top, the rotational constant is given by  $B_v = \int v^*(R) \frac{\hbar^2}{2\mu R^2} v(R) dR \approx \hbar^2 / 2\mu R_c^2$ , where  $R_c$  is the Condon radius.

$\Omega = 0^+$			$\Omega = 0^-$			$\Omega = 1, 2$		
$\Delta$ [cm $^{-1}$ ]	$B$ [cm $^{-1}$ ]		$\Delta$ [cm $^{-1}$ ]	$B$ [cm $^{-1}$ ]		$\Delta$ [cm $^{-1}$ ]		
-78.455	0.0050		-78.485	0.0047		-75.70		
-55.633	0.0050		-62.531	0.0071		-74.30		
-52.123	0.0051		-61.074	0.0046		-63.45		
-48.390	0.0046		-55.980	0.0041		-48.47		
-37.353	0.0047		-51.099	0.0040		-44.33	z	
-34.506	0.0043		-46.574	0.0039		-42.35	z	
-31.401	0.0037		-44.993	0.0070		-39.64		
-28.300	0.0035		-38.026	0.0036		-36.89		
-20.548	0.0038	x	-34.216	0.0034		-35.80		
-18.486	0.0034	x	-30.698	0.0035		-32.30		
-14.242	0.0027	x	-27.144	0.0040		-29.10		
-12.390	0.0028	x	-28.192	0.0065		-27.04		
			-24.212	0.0030	x	-25.40	z	
			-21.408	0.0028		-22.75	x,z	
			-18.794	0.0027	x	-19.40	x	
			-14.344	0.0039	x	-17.50	x	
			-12.331	0.0027	x	-16.38	x,z	
			-11.304	0.0057	x	-13.33	x	
						-12.43	x	
						-11.84	x	
						-11.04	x	
						-10.74	x	
						-10.34	x,z	
						-9.64	x	
						-9.54	x	
						-9.17		
						-9.15	x	
						-8.79	z	
						-8.10		

Table 3.1: Summary of observed photoassociation resonances. The levels to which we observe photoassociation of RbCs are shown, specified by their detuning,  $\Delta$ , from the Cs  $6S_{1/2}, F = 3 \rightarrow 6P_{1/2}, F' = 3$  atomic transition. The  $\Omega = 0^\pm$  resonance positions are referenced to the location of the  $J = 0$  level, while the  $\Omega = 1, 2$  resonances are referenced to center of mass of the observed structure. The positions of all the resonances were measured with an absolute accuracy of  $0.005 \text{ cm}^{-1}$ , except for those marked with an “x”, which were measured with a lower  $0.05 \text{ cm}^{-1}$  absolute accuracy. For the  $\Omega = 0^\pm$  levels, the measured rotational constant,  $B$ , is given. The  $\Omega = 1, 2$  levels marked with a “z” were observed in places where  $\Omega = 0^\pm$  levels are predicted to lie.

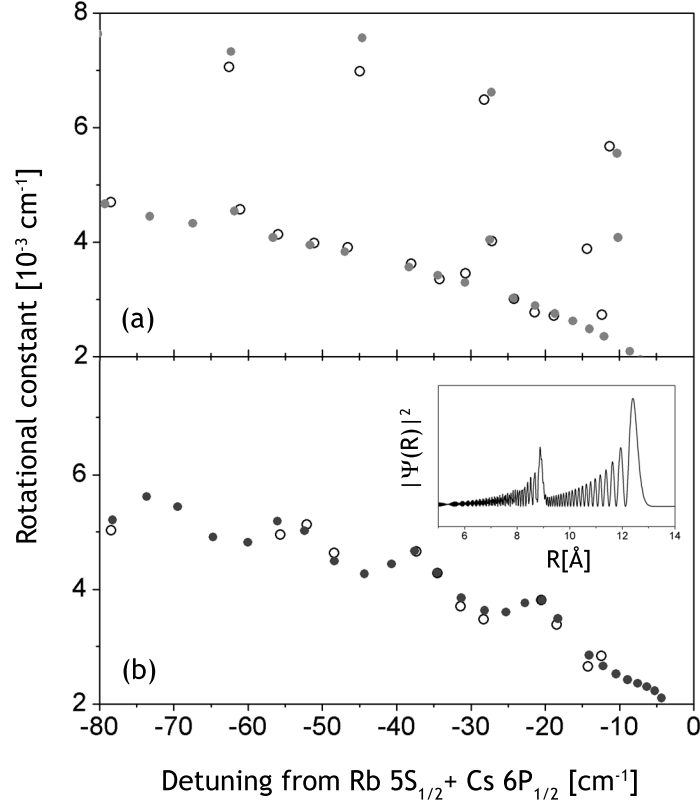


Figure 3.10: Comparison between observed and model  $\Omega = 0^{\pm}$  levels. Fitted RbCs\* potentials are used to calculate the positions and rotational constants of (a)  $\Omega = 0^{-}$  and (b)  $\Omega = 0^{+}$  levels, indicated by the closed circles; these are compared to our observed values (open circles). The inset to (b) shows the vibrational wavefunction for the  $0^{+}$  level at  $\Delta = -55.63 \text{ cm}^{-1}$  demonstrating its mixed short and long range character.

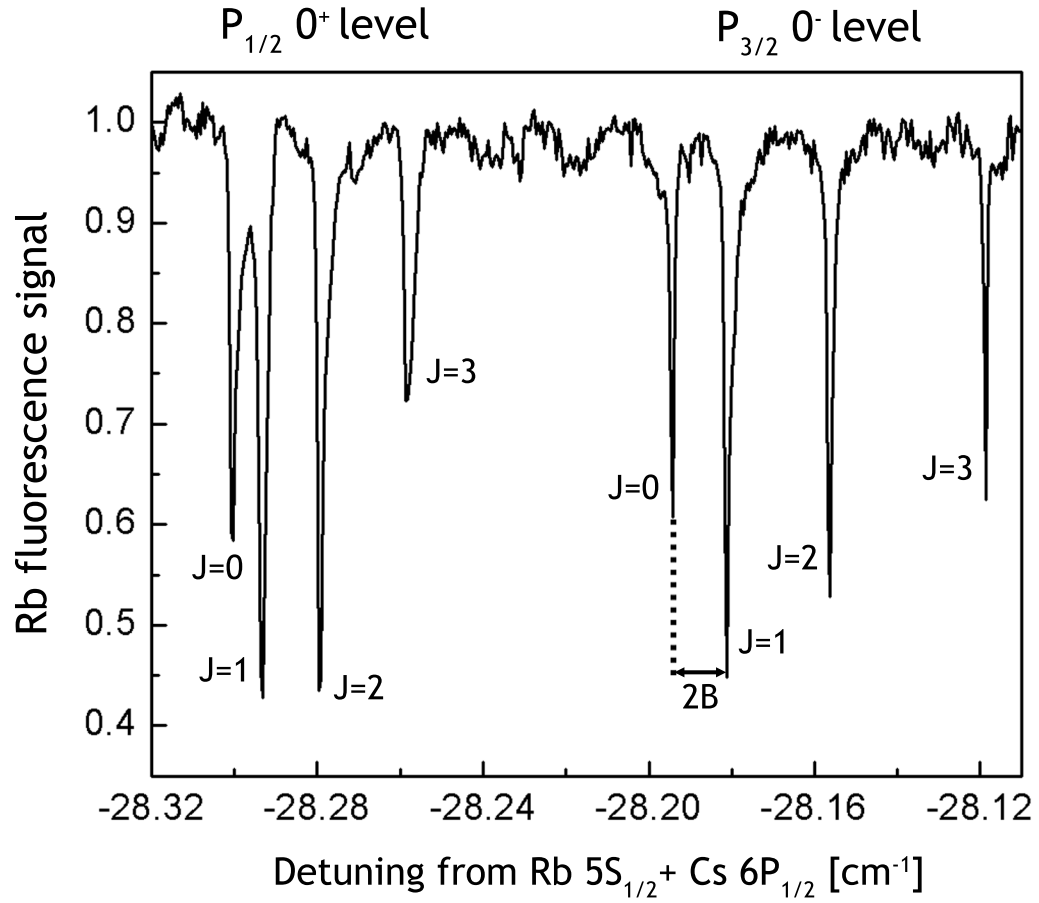


Figure 3.11: Comparison between deeply and weakly bound rotational series. The rotational progression on the left corresponds to a weakly bound  $\Omega = 0^+$  level; the progression on the right corresponds to a  $\Omega = 0^-$  level bound by  $\sim 600 \text{ cm}^{-1}$  from the Cs  $6P_{3/2}$  asymptote. The difference between the rotational constants,  $B$ , can be clearly seen, demonstrating the shorter range character of the deeply bound level.

$5S_{1/2} + \text{Cs } 6P_{1/2}$ , has an outer turning point of  $\sim 15 \text{ \AA}$  and has a noticeably smaller rotational constant. It should be noted that the deeply bound features would be unobservable without our high photoassociation laser intensity because their free-bound Franck-Condon factors are relatively small at such short range; the weakly bound resonances are typically observed with a photoassociation laser intensity of  $\sim 10^6 \text{ W/m}^2$ , while these deeply bound levels require roughly an order of magnitude more intensity to be seen.

Figure 3.10b shows a plot of the  $\Omega = 0^+$  levels, similar to that of Figure 3.10a. Here one can see that the coupling between the two vibrational series is very strong so that they cannot be clearly distinguished; each vibrational level is strongly mixed. The strong mixing in the case of the  $0^+$  states occurs because the avoided crossing of the  $A^1\Sigma_{0+}^+$  and  $b^3\Pi_{0+}$  potentials, which is the result of off-diagonal spin-orbit coupling, occurs near the potential minima (as shown in Figure 3.7) where the nuclei are moving relatively fast. As a result, the Born-Oppenheimer approximation begins to break down and non-adiabatic coupling between the two states exists. Instead of following the adiabatic curves associated with the spin-orbit mixed  $A$  and  $b$  states, the nuclei follow the diabatic  $A$  and  $b$  potential curves. These diabatic potentials are, in general, mixtures of potentials dissociating to the  $5S_{1/2} + \text{Cs } 6P_{1/2}$  and  $\text{Rb } 5S_{1/2} + \text{Cs } 6P_{3/2}$  asymptotes.<sup>22</sup> This means that a vibrational wavefunction associated with one of these strongly mixed states will be peaked at both the long range *and* shorter range outer turning points of the two  $\Omega = 0^+$  potentials, as shown in the inset of Figure 3.10b.

When we initially performed these experiments, we had our sights set on producing molecules in the ground  $X^1\Sigma^+$  state. We were hopeful that if the  $\text{RbCs}^*$  molecules we produced via photoassociation decayed to fairly deeply bound vibrational levels in the  $X^1\Sigma^+$  state, then we would be able to use a single stimulated Raman transition to drive the molecules into the  $v = 0$  ground state. We were therefore encouraged by the observed

---

<sup>22</sup>One can also see in Figure 3.10a that the two  $0^-$  series perturb one another; this is also the result of the non-adiabatic effect in which the nuclei do not follow the spin-orbit mixed  $c^3\Sigma_{0-}^+$  and  $b^3\Pi_{0-}$  potential curves. However, since the spin-orbit coupling occurs at larger  $R$  where the nuclei are moving relatively slower, the non-adiabatic effect, and thus the coupling between the vibrational series, is smaller.



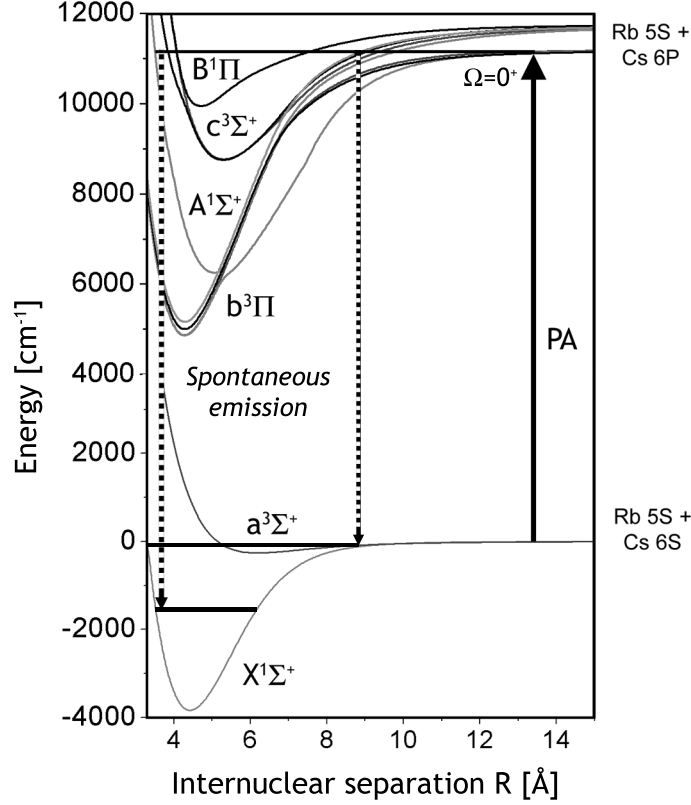


Figure 3.12: Population of the  $X$  state via spontaneous emission. The short range character of the strongly mixed  $0^+$  levels results in considerable wave function amplitude at the short range outer and inner Condon radii of the  $\text{RbCs}^*$  potentials dissociating to the  $\text{Cs } 6P_{3/2}$  asymptote. This suggests that Franck-Condon factors between these and  $X$  state levels will be fairly large and that we can therefore expect a substantial rate of decay to the  $X$  state. Furthermore, the long range character of the excited levels ensures that photoassociation rates are substantial, as well.

strong mixing in the  $0^+$  levels; the wavefunctions being peaked at both long and short range implied that the Franck-Condon factors would be large for both photoassociation and for spontaneous decay of  $\text{RbCs}^*$  to short-range  $X^1\Sigma^+$  levels, as illustrated in Figure 3.12. In addition, because the excited level was associated with the  $0^+$  potential, it possessed the correct symmetry to decay to the  $X^1\Sigma^+$  state. Figure 3.12 also shows the potential of spontaneous decay from an  $0^+$  level to very deeply bound  $X$  levels due to the overlap of the excited and ground state *inner* turning points. We discussed the prospect of exploiting photoassociation to  $0^+$  levels for population of the  $X$  state in detail in reference [74]. However, as we will see in Chapter 4, this is ultimately not the path we took to transfer

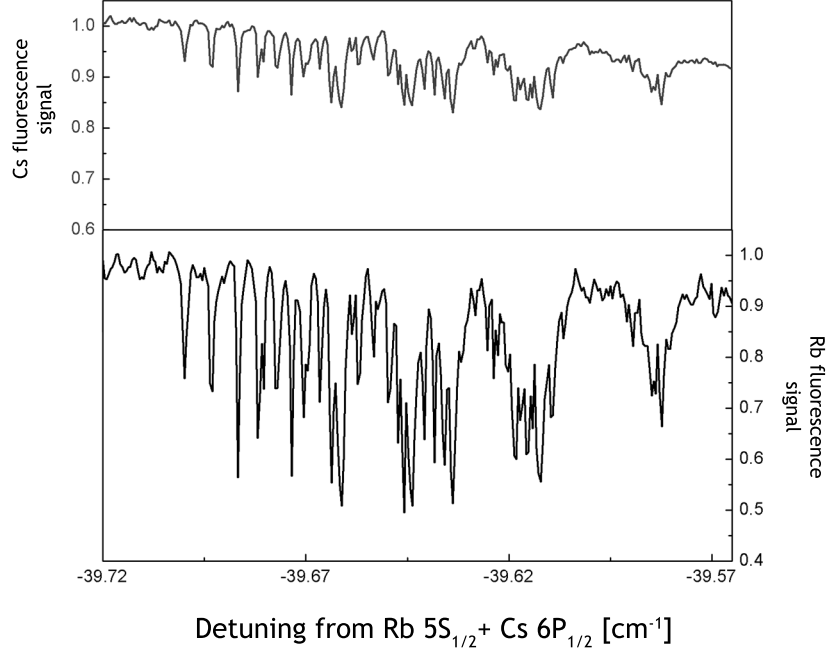


Figure 3.13: Photoassociation to an  $\Omega \neq 0$  level. A typical MOT fluorescence signal of photoassociation to a level with  $\Omega \neq 0$  is shown. There is no simple rotational progression evident due to the resolved hyperfine structure.

RbCs into the  $X^1\Sigma^+(v=0)$  state and we will therefore not go into specifics here.

Levels associated with the  $\Omega = 1$  and 2 potentials will in general have hyperfine structure that can be resolved by our photoassociation laser. Indeed, we observe many photoassociation resonances that have complex structure, an example of which is shown in Figure 3.13; we associate all levels that are not part of a clean rotational series with the  $\Omega = 1$  and 2 potentials. Presently, there has not been an analysis done of this data and we cannot, therefore, say to which of the two potentials the measured levels correspond. However, this data may be of some future use for producing a sample of UPMs in a single hyperfine state, as will be briefly discussed in Chapter 6.<sup>23</sup>

<sup>23</sup>Throughout this section we have only provided a small sample of the total spectroscopic data we collected. The data can be accessed in its entirety at the web address <http://pantheon.yale.edu/~dpd5/RbCsPAdata.htm>.

### 3.4.2 Photoassociation and Molecular Production Rates

The photoassociation rate can be estimated from our measurements. We note that the percent MOT depletion,  $p$ , on a photoassociation resonance is given by

$$p = \frac{N_0 - N_0^{PA}}{N_0}, \quad (3.37)$$

where  $N_0^{PA}$  and  $N_0$  are the steady state atom numbers on and off resonance, which are given by equation 2.15 with the loss term of equation 3.34 set to zero for the latter. Combining equations 3.34 and 2.15 one finds that the photoassociation rate per atom can be expressed as

$$\gamma_{PA} = \frac{p}{1-p} \gamma_0, \quad (3.38)$$

where  $\gamma_0$  is the loss rate per atom with the photoassociation laser off resonance. Thus, by measuring the percent depletion and the loading time of the MOT with the photoassociation laser tuned off resonance (which is equal to  $1/\gamma_0$ ), we can extract the photoassociation rate per atom. The steady state molecular production rate is obtained simply by multiplying this rate by the steady state number of atoms in the MOT with the photoassociation laser on resonance. In our experiments, we deplete the Rb MOT by as much as 70%. We measure an on resonance steady state atom number of  $\sim 1 \times 10^8$  and an off resonance loading time of 1.2 s; from this we calculate a production rate of RbCs\* molecules of  $\sim 2 \times 10^8 \text{ s}^{-1}$ .

One can also estimate the molecule production rate by noting that

$$\gamma_{PA} = 1/\tau_{PA} - 1/\tau_0, \quad (3.39)$$

where  $\tau_{PA}$  and  $\tau_0$  are the MOT loading times measured with the photoassociation laser on and off resonance. Measuring these loading times and calculating the photoassociation rate in this way, we obtain values that can be as much as a factor of three different from those calculated using equation 3.38. We believe that the discrepancy arises from our simplistic

treatment of the MOT loading. The MOT dynamics are given by equation 2.14, which does not include the optical pumping effects of the dark SPOT; the atomic fluorescence signal used to measure the MOT loading time depends on the fraction of atoms in the dark state which complicates the analysis. We have not accounted for these effects and our calculated molecular production rate must therefore be considered only as a rough, order-of-magnitude estimate. This rate is comparable to the unitarity limited rate predicted by equations 3.27 and 3.34. Assuming that the Rb MOT is depleted by 70% and negligible depletion of the Cs MOT, and using our measured MOT densities, photoassociation beam size and the average of the two MOT temperatures, we predict a maximum molecular production rate (for  $\Gamma=\gamma$  in equation 3.29) of  $\sim 1 \times 10^8 \text{ s}^{-1}$ . This suggests that we have, in fact, achieved unitarity limited photoassociation rates.

### 3.4.3 Measurement of RbCs\* Electric Dipole Moment

In order to demonstrate that RbCs is indeed a polar molecule, we measured the effect of an applied external electric field on RbCs\* rotational states. To do this we scanned our photoassociation laser over an  $\Omega = 0^+$  rotational progression with and without  $\pm 1 \text{ kV}$  applied to the two electrodes shown in Figure 2.7. The electric field produced when the high voltage is applied causes Stark shifts in the rotational levels given by [75]

$$\Delta W_{stark} = \frac{\mu_e^2 E^2}{2hB J(J+1)} \frac{J(J+1) - 3m_J^2}{(2J-1)(2J+3)}, \quad (3.40)$$

where  $\mu_e$  is the electric dipole moment of the molecule in the electronic and rovibrational state being probed,  $E$  is the applied electric field,  $B$  is the rotational constant and  $J$  and  $m_J$  are angular momentum quantum numbers. Equation 3.40 holds for all  $J \neq 0$ ; for  $J = 0$ , the Stark shift is given by

$$\Delta W_{stark}^{J=0} = -\frac{\mu_e^2 E^2}{6hB}. \quad (3.41)$$

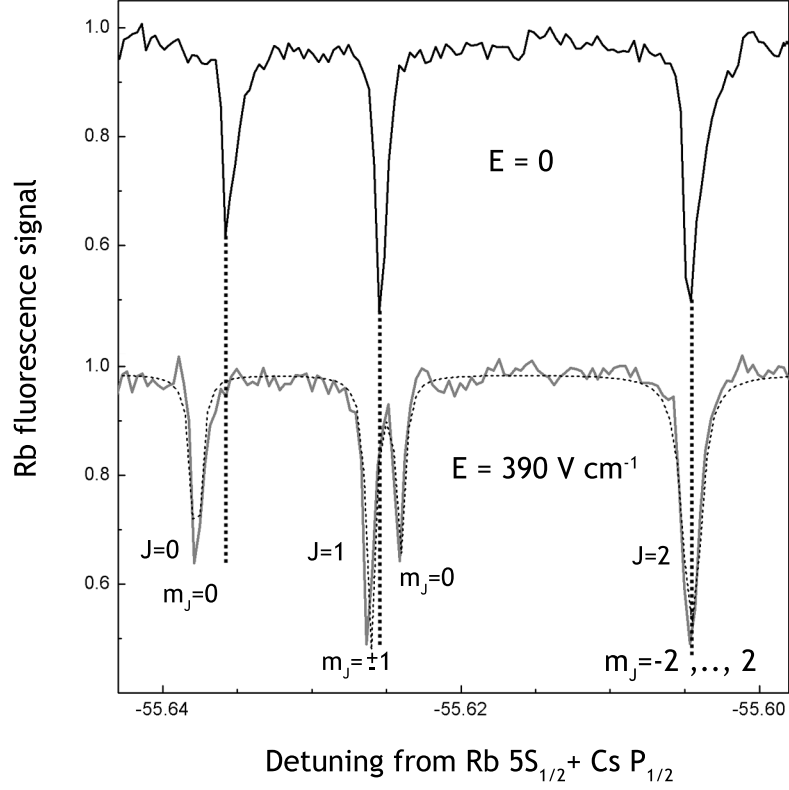


Figure 3.14: Measurement of Stark shift in polar RbCs\*. The upper trace shows an  $\Omega = 0^+$  rotational progression. The lower solid trace shows this same progression with the RbCs molecules in an electric field of 390 V/cm. The dotted trace is a fit of this progression, based on the expected Stark shift induced by such a field. From the fit we extract a dipole moment of  $\mu_e = 1.3$  Debye for RbCs in this state.

We fit our data to equations 3.40 and 3.41 and the results are shown in Figure 3.14. We first fit the data obtained with no applied field and extracted values for  $B$  and for the trap loss depths. We then used these values as fixed parameters for a fit of the data obtained for an applied field of  $\sim 390$  V/cm. We assumed a homogeneous population among the various projections,  $m_J$ . The only free parameter in our fit was the dipole moment for which we extracted the value of  $\mu_e = 1.3 \pm 0.1$  Debye. The uncertainty is limited by our knowledge of the applied electric field strength which we obtain from a computer simulation.<sup>24</sup>

<sup>24</sup>The simulation of the electric field was done with a two-dimensional finite element software package (Field Precision) and we could therefore only model the effect of electrodes with cylindrical symmetry. Since there were metallic objects (at ground) inside our chamber that broke this symmetry, our simulation was only approximate. We estimate that there is a  $\sim 10\%$  uncertainty in the value we obtain for the electric field at the location of the MOTs.

### 3.5 Summary

In this chapter we have discussed the methods used to produce and detect ultracold, polar RbCs\* molecules. At the conclusion of the experiments described above, we did not know to which states these molecules were spontaneously decaying nor did we have any experimental proof that they were not simply dissociating back into free atoms. Using the spectroscopic data we gathered to adjust the RbCs excited state potentials and obtain approximate excited state wavefunctions, we were able to calculate branching ratios for decay to levels in the electronic ground state potentials. Given the quality of the fit of our theoretical model to our data (as shown in Figure 3.10), we were confident that these branching ratios would be at least qualitatively correct and that we would find vibrationally excited electronic ground state molecules should we attempt to detect them. The next chapter details the experiments done towards this end.

## Chapter 4

# State-Selective Detection of Ground State RbCs

In this chapter we discuss the method used to detect the RbCs molecules that have decayed to electronic ground state levels following photoassociation. Our detection technique allowed us to determine which ground state levels were being populated and with what efficiency. Additionally it provided us with crucial spectroscopic information about electronic excited levels that enabled us to chart a path towards populating the lowest electronic and vibrational ground state. We begin by discussing the basics of the detection and the relevant molecular states involved. We then describe the changes made to our apparatus to experimentally implement the detection. Finally we present the results of our experiments and discuss how they point towards a method to produce  $X^1\Sigma^+(v=0)$  state UPMs.

### 4.1 Detection Method

#### 4.1.1 Spontaneous Decay

Electronically excited RbCs molecules formed via photoassociation can either decay back into free atoms or into bound vibrational levels associated with electronic ground state potentials; we are interested in detecting those that decay to metastable bound levels.

The presence of singly unpaired electrons in the Rb and Cs alkali atoms demands that there be one singlet and one triplet potential for the ground electronic state of the RbCs molecule, as shown in Figure 3.7(a). In the Hund’s case (b) nomenclature, which is valid for the ground state due to the lack of any orbital angular momentum ( $\mathbf{L}=\Lambda=0$ ), these potentials are termed the  $X^1\Sigma^+$  and  $a^3\Sigma^+$  states, respectively.<sup>1</sup> As is evident in Figure 4.1, the  $X^1\Sigma^+$  potential has a much lower minimum than the shallow  $a^3\Sigma^+$  potential; the lowest vibrational level ( $v=0$ ) of the  $X$  state thus represents the “true” vibrational ground state we eventually wish to populate.

The  $X^1\Sigma^+$  potential has only an  $\Omega=0^+$  component ( $\Lambda=\Sigma=0$ ) in Hund’s case (c) coupling and therefore selection rules prohibit its population via decay from an  $\Omega=0^-$  state. The  $a^3\Sigma^+$  potential has  $\Omega=0^-$  and  $1^\pm$  Hund’s case (c) components.<sup>2</sup> Since it has components with both “+” and “-” symmetry, selection rules allow decay to  $a^3\Sigma^+$  levels from all excited states populated by photoassociation. As a result, when we intend to populate the  $X^1\Sigma^+$  state, we photoassociate to  $\Omega=0^+$  excited levels (which also leads to unavoidable population of  $a^3\Sigma^+$  levels); when we intend to populate only the  $a^3\Sigma^+$  state, we photoassociate to an  $\Omega=0^-$  level.

#### 4.1.2 Resonance-enhanced Multi-photon Ionization Detection

We detect RbCs molecules formed in  $X^1\Sigma^+$  and  $a^3\Sigma^+$  levels using a technique known as resonance-enhanced multi-photon ionization (1+1 REMPI). In this method, the molecules are resonantly driven to an excited molecular bound state by absorbing a photon from one laser and are then ionized by absorbing a photon (of a different frequency, in general)

---

<sup>1</sup>The “X” and “a” labelling here is a convention used in molecular spectroscopy; it is customary to label the lowest singlet state with an “X” and the lowest triplet state with an “a.” Excited triplet states are labelled with lower case letters beginning with “b”, while singlet states are labelled with upper case letters beginning with “A”.

<sup>2</sup>It is surprising that the  $a^3\Sigma^+$  state has an  $\Omega=0^-$  component in Hund’s case (c). Why this is so is not trivial and can be explained only by examining the details of how the angular momentum is uncoupled in the Hund’s case (b) scheme and recoupled in Hund’s case (c). It should be noted, however, that this is a general property of  $^3\Sigma^+$  states. The  $\Omega=1^+$  and  $1^-$  levels are degenerate in the absence of molecular rotation. However, when the rotation is taken into account, a splitting, referred to as  $\Omega$ -doubling, occurs. It arises from an interaction between the electronic and rotational angular momentum but is unresolvable in our experiments given the small rotational energy of the RbCs molecule in the low  $J$  levels we populate, and the linewidths of our lasers.



from another, as shown in Figure 4.1. The positive ions are subsequently attracted to a negatively biased detector. The resonant laser is tuneable so that bound-bound spectra may be obtained by monitoring the number of ions detected as a function of resonant laser frequency. The advantage of using two lasers is that the resonant and ionization laser intensities can be controlled independently so that one need not worry about power broadening the resonant transition when attempting to saturate the ionization step. Also, there is typically more than one ionization threshold (see Figure 4.1) and one often wishes to control which is used in the ionization step; having two lasers allows one to choose the frequency of light driving each step so that a particular threshold can be used independent of which resonant transition is driven.

We use pulsed lasers to carry out both resonant and ionization steps. Pulsed lasers are ideal since they can readily deliver a very large instantaneous power to overcome small Franck-Condon factors and ionization cross-sections, to drive weak molecular transitions. To give an example of this, let us look at a laser pulse with 1 mJ of energy, 10 ns pulse width and a 5 GHz linewidth in a 2 mm diameter beam (this is very close to the specifics of the pulsed lasers we use). Such a pulse corresponds to a peak intensity of  $10^9$  mW/cm<sup>2</sup>. If we use this pulse to drive a transition involving an excited state with a typical natural linewidth of 5 MHz, the actual resonant part of the pulse has an intensity smaller by a factor of  $10^3$  (the natural linewidth divided by the laser pulse linewidth). We can compare this intensity of  $10^6$  mW/cm<sup>2</sup> with a typical atomic saturation intensity of  $\sim 1$  mW/cm<sup>2</sup>. Assuming the electronic matrix element is similar in molecules as for atoms (which should be a good approximation), this means that this pulse can be used to saturate a molecular transition having a Franck-Condon factor as small as  $10^{-6}$ . The fact that the laser is not continuous is not a problem for our detection method. In a typical detection experiment, molecules are photoassociated and subsequently populate the ground states continuously. They are then excited and ionized by the pulsed lasers and detected at the pulsed laser repetition rate. The number of ions detected per pulse then depends on the ratio between the rate the molecules are being formed in the particular ground state being probed and

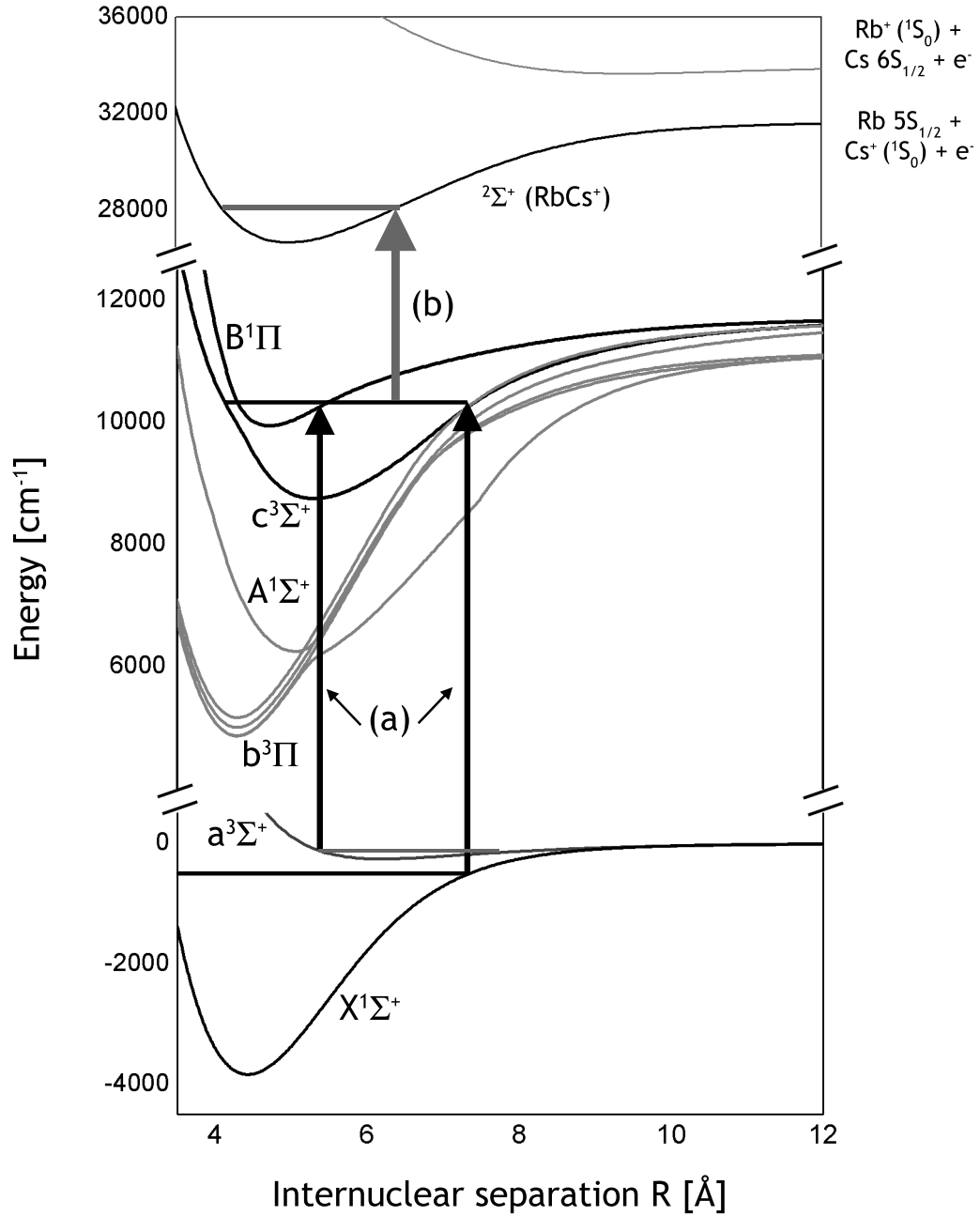
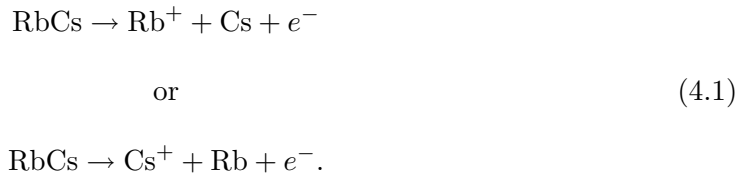


Figure 4.1: Detection of ground state RbCs. (a) A resonant laser pulse drives RbCs molecules from a level in either the  $X^1\Sigma^+$  or  $a^3\Sigma^+$  ground states to an intermediate excited state. (b) An intense pulse then ionizes the population of this excited state. The  $18797 \text{ cm}^{-1}$  (532 nm) ionization pulse frequency is smaller than the splitting between the excited states and the  $\text{Rb}^+$  and  $\text{Cs}^+$  dissociation limits, so that a  $\text{RbCs}^+$  molecular ion is selectively formed.

the rate at which the untrapped molecules are leaving the volume of the ionization beams. For our experimental conditions the ion detection rate is large enough for us to see ample signals from ground state molecules.

The ionization laser pulses are intense enough that they off-resonantly ionize Rb and Cs atoms in the MOT, as well as Cs<sub>2</sub> molecules being produced via photoassociation by the Cs trap light. Atomic Cs<sup>+</sup> and Rb<sup>+</sup> ions can also be formed by ionizing a ground state RbCs molecule with enough energy to dissociate it into either



For this reason, we use an ionization laser pulse with a frequency low enough so that we selectively form a RbCs<sup>+</sup> ion, as shown in Figure 4.1.<sup>3</sup> It is necessary to differentiate the RbCs<sup>+</sup> molecular ion from the others so that there is neither a large off-resonant background on the ion signal nor spurious features in the bound-bound spectrum we obtain due to atomic or Cs<sub>2</sub> resonances that may arise. To differentiate the ions produced by the pulsed lasers, we employ time-of-flight mass resolved detection. A schematic of our detector setup is shown in Figure 4.2. We place, equidistant from the MOTs, the negatively biased detector (to be discussed in more detail in §4.2.1) and an opposing positively biased electrode that aids in guiding the ions towards the detector. If potentials  $\pm V$  are placed on the detector and opposing electrode, then the time it takes for an ion of mass,  $M$ , to reach the detector is given by

$$t_{TOF} = \sqrt{\frac{Md^2}{2eV}}, \tag{4.2}$$

where  $e$  is the fundamental electric charge and  $d$  is the distance between the detector and the MOT. The detector, which responds fast enough to resolve the different arrival

---

<sup>3</sup>Atomic ions may still be formed due to multiphoton processes; however these are higher order than the single photon resonant step and are relatively suppressed.

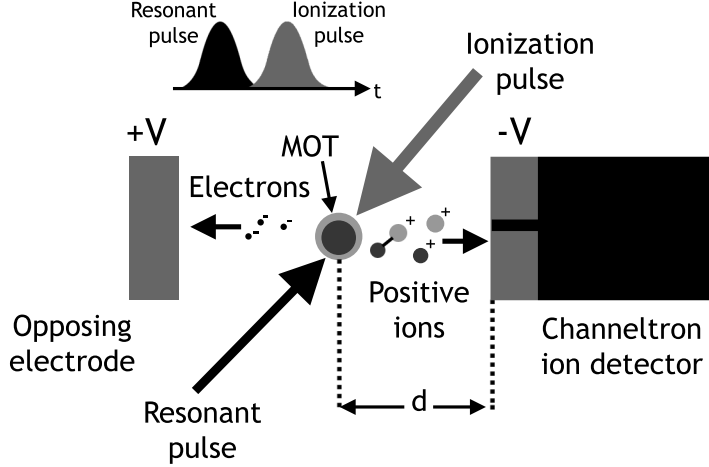


Figure 4.2: Ion detection. The way in which we detect the ions formed via 1+1 REMPI is shown schematically. The resonant and ionization pulses arrive in succession at the MOT and ionize Rb, Cs, RbCs and  $\text{Cs}_2$ . The atomic and molecular ions are repelled from the positively biased ( $+V$ ) opposing electrode and are attracted to the negatively biased ( $-V$ ) channeltron, where they are detected. The channeltron and opposing electrode are each positioned a distance,  $d$ , from the MOT; in our experiments,  $d \sim 3$  cm. The arrival time of an ion at the channeltron is a function of its mass so that time of flight detection can resolve the different species of ions.

times of ions with different mass, produces an output electronic current proportional to the number of ions that arrive. By monitoring this current as a function of time, one observes, in general, four peaks corresponding to  $\text{Rb}^+$ ,  $\text{Cs}^+$ ,  $\text{RbCs}^+$ , and  $\text{Cs}_2^+$  that are spaced according to equation 4.2.

The states to which we resonantly excite the ground state RbCs molecules before ionization are shown in Figure 4.1. In the absence of any coupling between these excited states, the selection rule 3.15 allows transitions only between ground  $X^1\Sigma^+$  and excited  $A^1\Sigma^+$  and  $B^1\Pi$  levels or between ground  $a^3\Sigma^+$  and excited  $b^3\Pi$  and  $c^3\Sigma^+$  levels. However, theoretical calculations [76] predict that there is a fairly strong off-diagonal spin-orbit coupling that mixes different states with the same value of  $\Omega$  (but different values of  $\Lambda$  and  $\Sigma$ ). This implies that transitions can be driven between those excited states with mixed singlet/triplet character and the singlet and triplet ground states, provided all the other selection rules are followed. A direct result of this is that molecules decaying to vibrational levels in the  $a^3\Sigma^+$  state following photoassociation may be transferred to levels in the

$X^1\Sigma^+$  by going through an excited level with mixed singlet/triplet character and with the correct symmetry for the transfer to be allowed. We began the experiments to be discussed in the remainder of this chapter with the intent of detecting ground state molecules that could be transferred to the  $X^1\Sigma^+(v=0)$  state. This requires finding an excited level (or levels) that efficiently couple to both a ground state populated via photoassociation and to the  $X(v=0)$  state.

## 4.2 Experimental Apparatus

In this section we will discuss the additions and changes made to our apparatus from what was described in §2.3 and §3.3.2. We continued to operate our MOT as a dark SPOT. At this stage of our experiments, the atomic number and atom density were measured to be  $N_{Rb} = 2 \times 10^8$ ,  $n_{Rb} = 7 \times 10^{11} \text{ cm}^{-3}$  and  $N_{Cs} = 8 \times 10^8$ ,  $n_{Cs} = 1 \times 10^{12} \text{ cm}^{-3}$ . The intensities of the various beams used for the MOT were initially adjusted to maximize the MOT density. We were not concerned with minimizing the MOT losses as the ionization detection technique is not sensitive to them. Once we were reliably detecting ground state molecules, we adjusted the beam intensities simply by maximizing the  $\text{RbCs}^+$  ion signal. The intensities had to be adjusted on a day to day basis to restore the ion signal to its optimal value; as a result, we found that the optimal intensities varied from day to day. They were approximately equal to those quoted in §3.3.2 except that the Rb trap intensity was not kept low; its power in these experiments was  $\sim 7 \text{ mW/cm}^2$ , roughly double the value used for the photoassociation detection. The two MOT temperatures were both measured to be  $\sim 75 \text{ } \mu\text{K}$ .

### 4.2.1 Ion Detector and Vacuum System

For the 1+1 REMPI detection we use a channeltron 5901 MAGNUM (Burle Industries) detector. The detector and opposing electrode are positioned roughly 3 cm from the center of the MOTs. The channeltron works in a way similar to a photomultiplier tube. An ion

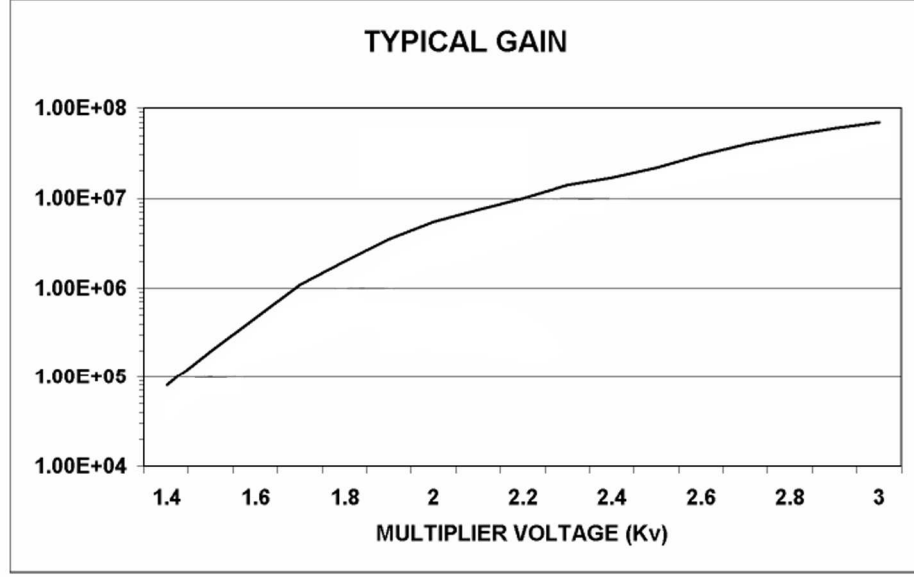


Figure 4.3: Channeltron gain vs. bias voltage. The manufacturer specified gain curve is shown for the 5901 Magnum channeltron we use for ion detection. Courtesy of Burle Industries.

striking the detector, which has its input biased at a high negative voltage, causes electrons to be released from a  $\text{SiO}_2$  layer; the electrons are then accelerated down the channeltron by the high voltage where they continually strike the  $\text{SiO}_2$  layer and release more electrons creating a cascade. Depending on the bias high voltage applied, roughly  $10^6 - 10^8$  electrons are produced at the signal output pin per incident ion, resulting in a large current that can be easily measured. The gain of the detector versus applied bias voltage is shown in Figure 4.3. High voltage of up to  $\pm 3000$  V is generated by two supplies (Stanford Research Systems, PS350.) and is applied to the channeltron and opposing electrode via high voltage vacuum feedthroughs. Since the bias voltage on the channeltron controls the detector's gain, we often had to change it based on the size of our ion input; this resulted in the shifting of the offset of our ion signals' arrival time which we compensated for by adjusting the voltage on the opposing electrode to maintain a constant electric field. This proved convenient for data collection where we sampled the output current using fixed time windows, as will be described in §4.2.4.

Putting the channeltron and opposing electrode in our vacuum system obviously re-

quired venting the chamber to air and we therefore made two minor changes while the chamber was open. We replaced all of our home-made viewports with commercial viewports (Insulator Seal) since we happened to have them around (for a future application) and because of their relative ease of use. This had one drawback. The glass in the commercial viewports apparently possess a much higher degree of birefringence than do our home-made seals, perhaps due to the stress placed on them as they are sealed. This prevented our resonant build-up cavity locking scheme, which depends critically on polarization, from functioning properly as we were unable to generate the required error signal. However, this did not prove detrimental to our experiment since we used photoassociation transitions that we could saturate without the power build-up. We also removed the ring electrodes described in §2.3.2 to make room for the channeltron.

When first using the channeltron in our vacuum system, we found that every so often the high voltage supply used to bias it would trip and turn itself off, most likely due to a sparking to ground somewhere inside the vacuum chamber. This posed a serious problem when the trip was not immediately noticed (i.e., if it happened overnight). When the supply was turned back on after it had been off for some time, we would observe a large (2-3 order of magnitude) spike in the vacuum pressure. Initially, we would wait about one day when this happened and the pressure would return to its original value; however, after this happened a few times (in only a month or two of use), the channeltron completely stopped working and we had to replace it (and break vacuum again). We hypothesized that it was the interaction of the very chemically active alkali vapor with the channeltron material that caused the failure. With the voltage off and no resulting base current flowing through the  $\sim 10\text{ M}\Omega$  channeltron, the detector's temperature was lower due the lack of resistive heating. This resulted, we suspect, in a higher rate of alkali condensation on the detector so that whatever damage was being done was amplified. This hypothesis is consistent with the pressure spike observed when applying the high voltage since the heating would result in the boiling off of condensed alkali atoms. To fix this problem we decided to do two things. The first was to continually heat the channeltron to about 5 degrees above room

temperature by wrapping the air side of the channeltron mount with a heating tape. The second involved insuring the supply would never trip by putting a  $R_{lim} = 3 \text{ M}\Omega$  current limiting resistor in series with the channeltron. By simultaneously setting the supply's maximum output current (over which the supply trips) to be  $I_{max} = V_{max}/R_{lim} \sim 1 \text{ mA}$ , we insured that even a spark from the channeltron to ground would not result in the voltage being switched off. Of course, the introduction of  $R_{lim}$ , results in a voltage divider being created with the channeltron resistance  $R_C$ ; we therefore are not applying the supply's entire voltage,  $V_{supply}$ , to the detector but instead apply

$$V_C = V_{supply} \left( \frac{R_C}{R_C + R_{lim}} \right). \quad (4.3)$$

We need to know the value of  $V_C$  because it determines the detector gain. We thus measure the current being drawn out of the supply with the supply's internal meter to determine the channeltron resistance, which changes as the detector ages, and then use equation 4.3 to calculate  $V_C$ . These steps taken towards insuring the channeltron stays warm worked well; the detector was put into our system nearly two years ago and is currently still functioning.

#### 4.2.2 Photoassociation Laser Frequency Stabilization

Our detection method requires that the photoassociation laser be locked to a particular resonance so that the number of ions we detect changes only due to the scanning of the resonant pulse frequency and not due to a varying photoassociation rate. A typical scan lasted roughly 5-10 minutes. However the frequency stability of the Ti:Sapphire laser is not sufficient, as mentioned in §3.3.2. We therefore had to work to prevent low frequency drifts by externally stabilizing the laser. This was done by using the same digitized Fabry-Perot trace that was discussed in §3.3.2. The basic idea is shown in Figure 4.4. Once the PA laser is tuned to resonance (which is verified by monitoring the  $\text{RbCs}^+$  ion signal) a Labview peak finding algorithm is started which determines the spacing between the locked Rb trap laser peak and the Ti:Sapphire laser peak at that moment. The peak finding algorithm



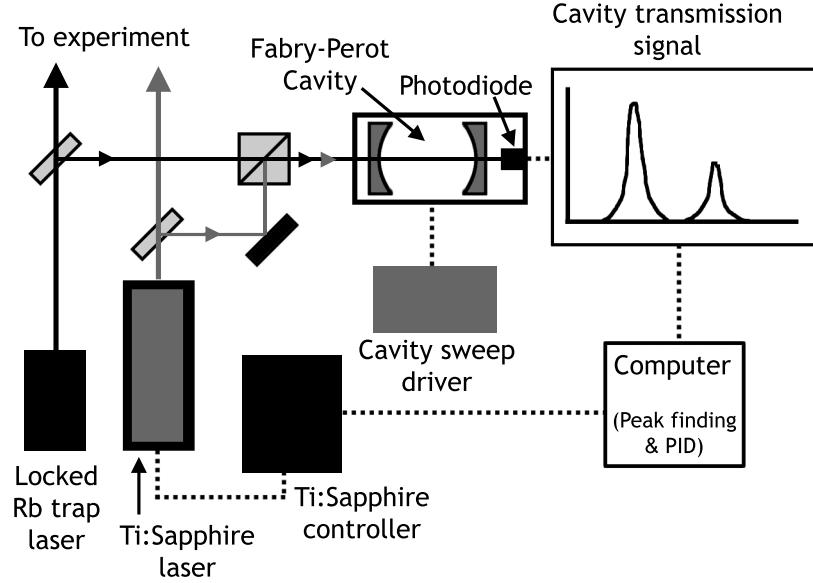


Figure 4.4: Schematic of photoassociation laser lock. The optics and electronics used to stabilize our photoassociation laser frequency are shown schematically. The Ti:Sapphire photoassociation laser and Rb trap laser (locked using saturation absorption spectroscopy) are combined on a polarizing beam splitter and are sent into a Fabry-Perot cavity. The cavity length is scanned via a PZT attached to one of the cavity mirrors and driven by a high voltage ramp. The light transmitted through the cavity, as a function of cavity length, is detected on a photodiode. This electronic signal is then digitized and processed by a computer; the computer outputs an error signal that is sent to the Ti:Sapphire laser controller which adjusts the laser frequency. In order for the computer's peak finding algorithm to discern which transmission peak belongs to which laser, we deliberately misalign the Rb trap into the cavity so that its peak is smaller than that of the Ti:Sapphire laser.

then continuously makes measurements of the peak separation and outputs numbers proportional to the deviations of this separation from its initially measured value. This array of numbers is then sent to a Labview PID (proportional/integral/differential gain) program that turns each number into a voltage value. This voltage is then sent out through the computer's PCI card to the input used to externally control the Ti:Sapphire laser frequency, completing the feedback loop. The sign and magnitude of the proportional, integral, and differential gain are all adjustable within the Labview PID program. Since we only need to stabilize the frequency drifts over long time scales, the significant time delays ( $\sim 100$  ms) which accompany our software feedback scheme are not a problem. With this locking technique, we are able to stabilize the PA laser to within a few MHz over long times, which is much smaller than the typically 30 MHz wide photoassociation resonances to which we lock. The PA laser had a peak intensity of  $\sim 1 \times 10^6$  W/m<sup>2</sup> in these experiments.

#### 4.2.3 Pulsed Laser System

The pulsed light used for the resonant step of detection was generated by a tuneable dye laser (Cobra, Sirah Laser- und Plasmatechnik GmbH). The dye is pumped by the 532 nm second harmonic of a Nd:YAG pulsed laser (Spectra Physics, Quanta Ray PRO-Series), which has a 10 Hz repetition rate and a 220 mJ output pulse energy. A small fraction of this pump light (a few mJ at most) was split off and used for the ionization step. A schematic of the dye laser cavity and the pump laser optics is shown in Figure 4.5. Dye is circulated through a cell in the cavity by a pumping station. There are two gratings with a line density of 1800 lines/mm in the cavity that perform the frequency selection. The first is oriented so that the spontaneous emission from the dye strikes it at grazing incidence. The second is attached to a voltage controlled motor capable of rotating it so that the laser output frequency can be tuned by applying an external signal. The cavity output coupler consists of two 90° turning prisms that direct the beam through the dye cell for a second time so that it can be amplified before leaving. The pump beam is split by a beam splitter as it enters the dye laser. One portion is sent immediately to the dye

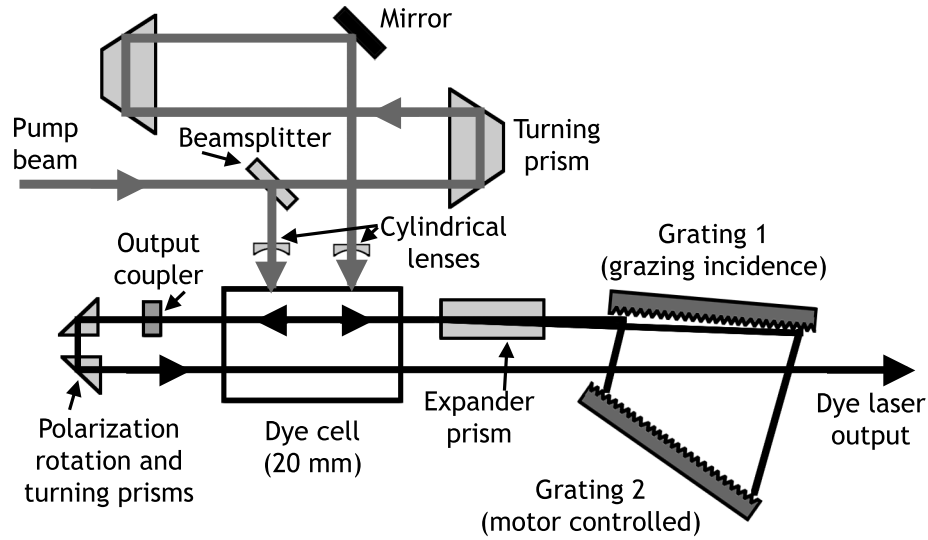


Figure 4.5: Schematic of Sirah dye laser. The pump and Sirah dye laser optics are shown schematically. The Nd:YAG pump beam is split into two beams. The first pumps one half of the 20 mm dye cell for the oscillator stage. The frequency of emission of the dye is tuneable, and is selected by a motor controlled grating which provides feedback by directing a particular frequency of light back into the dye cell. The dye beam exits the oscillator cavity via the output coupler and is then directed back through the dye cell where it is amplified in the preamplifier stage. The preamplifier stage is pumped by the second part of the Nd:YAG beam which is sent through an optical delay path after the split and is then directed into the second half of the dye cell.

cell to pump the initial oscillator stage, while the other portion is first sent through a delay path before being directed into the cell to pump the amplifier stage. Dye efficiencies vary and they generally get worse with decreasing output frequency. We obtained an output pulse energy from our dye laser as high as 23 mJ giving a maximum efficiency of roughly 10%. By using multiple dyes, we operated our dye laser from 547 nm to 745 nm. However, we observed a sharp decrease in the efficiency in the range from 563 nm to 568 nm; the output pulse energy here was too low to be useful. This decrease in efficiency is due to an effect called Wood's Anomaly. In normal operation of a grating laser, all of the light diffracted from the grating is in the first order, which is directed through the gain medium; its energy is thus what determines the amount of output energy. However, for a certain range of wavelengths, determined by the angle of incidence of the light on the grating and the grating's line density, second order diffraction is possible which removes energy from

the first order diffracted beam and results in a reduced output power. We were able to avoid using this “forbidden” range, as will be discussed later in this section. A summary of the dyes used in this experiment is given in Table 4.1. The dye laser had a spectral width of  $\sim 0.05 \text{ cm}^{-1}$  limited by the degree of frequency selection achieved by the two gratings. Both the dye laser and pump pulses were of  $\sim 7 \text{ ns}$  duration.

The dye laser output could usually not be used directly because we required laser frequencies in the infra-red to drive the resonant transitions we typically employed for detection. This range is not accessible with the dye laser due to poor dye efficiency at such long wavelengths. To generate the necessary frequencies, we sent the dye laser output through a  $\text{H}_2$  Raman cell (Light Age, LAI 101 PAL-RC). This cell, shown schematically in Figure 4.6(a), is essentially a 0.5 m long stainless steel tube which holds and circulates hydrogen gas at a pressure of  $\sim 400 \text{ psi}$ . The two glass windows that allow light to be coupled in and out are curved so that collimated incoming light is focused in the center by the input and is then re-collimated at the output. The Raman cell coherently produces additional frequency sidebands offset from the input frequency by  $\omega_v = 4155.25 \text{ cm}^{-1}$ , the  $\text{H}_2$  ground state vibrational splitting. The process by which this happens is stimulated Raman scattering, which is shown schematically in Figure 4.6(b). The input laser pulse with frequency  $\omega_L$ , which is always far-detuned to the red from any electronic transition in  $\text{H}_2$ , drives the  $\text{H}_2$  molecular population in the  $v = 0$  vibrational ground state through a virtual excited level which can then decay either back to the ground state or to the  $v = 1$  first excited state at energy  $\hbar\omega_v$ . Note that the ground state is initially highly populated since  $\hbar\omega_v > k_B T$ . Population of the first excited state is accompanied by the emission of a red-shifted (Stokes) photon with frequency  $\omega_s = \omega_L - \omega_v$ . If the initial driving pulse is intense enough, the resulting Stokes radiation will stimulate the virtual level to emit more light at the frequency  $\omega_s$ , thus building up a coherent beam. The amplified Stokes radiation will also be able to drive population from the ground state which can end up populating the first excited state. In this case, one will see the appearance of “second Stokes” radiation with a frequency  $\omega_{s2} = \omega_L - 2\omega_v$ . This radiation will also be coherently

Frequency Range	Dye Name	Dye Center Wavelength	Dye Concentration (in Ethanol)	Dye Laser Peak Output	Stokes Order Used	Raman Peak Output
8355 $\rightarrow$ 9140 $\text{cm}^{-1}$	Pyrromethene 597	597 nm	.16 $g/\ell$	19 mJ	Second	850 $\mu\text{J}$
9140 $\rightarrow$ 9295 $\text{cm}^{-1}$	Rhodamine 6G	570 nm	.09 $g/\ell$	18 mJ	Second	1.0 mJ
9270 $\rightarrow$ 9500 $\text{cm}^{-1}$	Pyridine 2 (LDS722)	722 nm	.25 $g/\ell$	12 mJ	First	800 $\mu\text{J}$
9451 $\rightarrow$ 9970 $\text{cm}^{-1}$	Pyrromethene 580	555 nm	.20 $g/\ell$	23 mJ	Second	1.2 mJ
9950 $\rightarrow$ 10680 $\text{cm}^{-1}$	Pyridine 1 (LDS698)	698 nm	.25 $g/\ell$	14 mJ	First	650 $\mu\text{J}$

Table 4.1: Summary of dyes and Stokes orders used to generate the resonant detection pulse. The first column represents the range of resonant detection pulse frequencies that we obtained with a particular dye and a particular Stokes order (first or second) from the Raman cell. The dye center wavelength corresponds to the wavelength for which we observed the peak output energy from the dye laser. The Raman output corresponds to the observed pulse energy in the specified Raman order at the center wavelength of the dye. The dye concentration in ethanol solvent that we used to obtain these pulse energies is also given.

stimulated if the initial pulse energy is high enough.

As the first excited state begins to be populated, light from the input pulse can drive the population back to the ground state resulting in the emission of blue-shifted (anti-Stokes) light with frequency  $\omega_a = \omega_L + \omega_v$ , which will also be coherently produced via stimulated emission for an input pulse energy above some threshold value. The threshold values for second Stokes and first anti-Stokes radiation are higher than for first Stokes since the former processes are inherently second order. All threshold values scale with frequency as  $\omega^{-4}$ , the well-known scattering cross-section scaling that explains the color of the sky. Using the Raman cell in conjunction with the tuneable dye laser, we are able to generate pulsed laser light continuously from roughly 400 to 1200 nm. We work around the hole in our dye laser output (due to the Wood's anomaly) simply by operating the laser at a different wavelength and using the Raman shift to access wavelengths in the hole. For example, if we wanted to generate light at 565 nm, we would use the first anti-Stokes beam with the dye laser operating at 738 nm. To generate light at 939 nm we would not use the second Stokes light generated by the dye laser operating at 565 nm; instead we would use the first Stokes light with the dye laser output at 675 nm.

The light exiting the Raman cell looks white to the eye because it is composed of the various colors of the input and Raman shifted beams. We separate the components with a dispersing prism placed at the output of the cell. We use either the first or second Stokes beams to drive the resonant step of the 1+1 REMPI process and we typically measure the fundamental or first anti-Stokes beams with a wavemeter with a  $0.05 \text{ cm}^{-1}$  accuracy to determine the frequency of light we are sending to the molecules, which we calculate by subtracting the appropriate number of Raman frequency shifts,  $\omega_v$ . A summary of which Stokes orders are used to access which frequencies is given in Table 4.1. For a given final frequency that we wish to use for detection, we found that we were able to generate roughly the same power using first and second Stokes radiation (typically  $\sim 1 \text{ mJ}$ ) since the dye laser had to be operated at longer wavelengths when using the first Stokes; even though the first Stokes light is more efficiently generated in the Raman cell, the dye laser is less

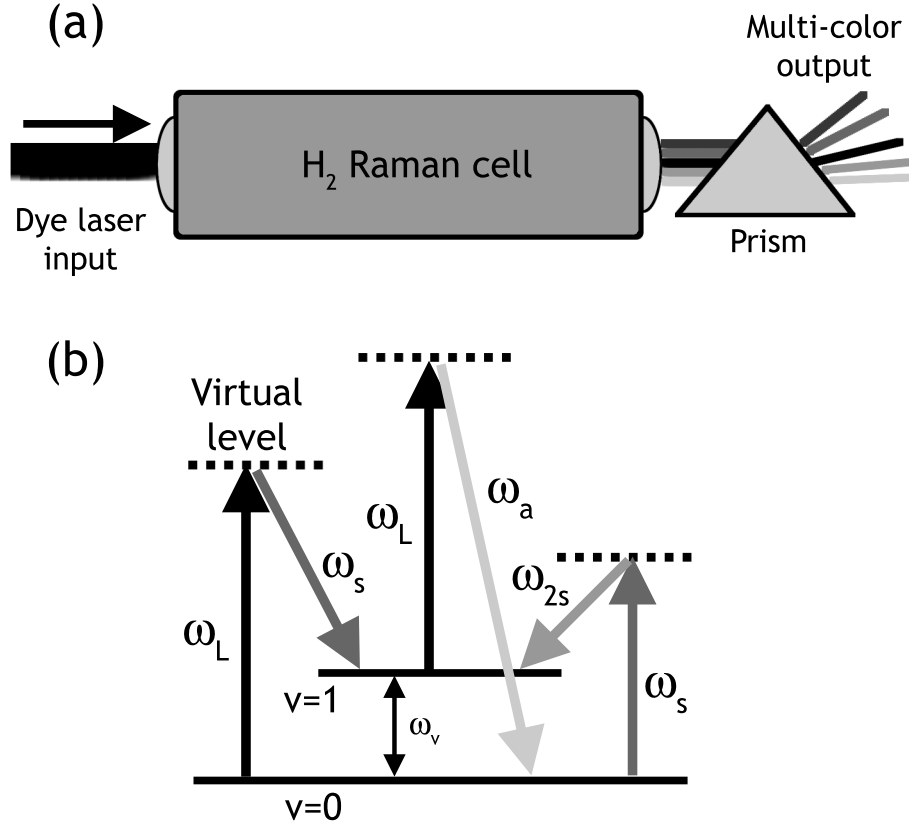


Figure 4.6: Stimulated Raman scattering. (a) A schematic of the Raman cell is shown with the single frequency pulse dye laser beam entering. The output is a multi-frequency beam consisting of the input and the various Stokes and anti-Stokes Raman orders. A prism is used to spatially separate these orders. (b) The process of stimulated Raman scattering is shown. The dye laser input with frequency  $\omega_L$  drives H<sub>2</sub> molecules from the  $v = 0$  ( $v = 1$ ) level to a virtual level (dotted line) where they can decay to the  $v = 1$  ( $v = 0$ ) level and emit first Stokes (anti-Stokes) radiation at frequency  $\omega_s$  ( $\omega_a$ ). This frequency is offset from  $\omega_L$  by  $\mp\omega_v$ , the splitting between the ground and first excited vibrational levels. If the input beam intensity is above some threshold value, the Stokes and anti-Stokes radiation will be stimulated coherently. Coherent second Stokes light, at a frequency  $\omega_{2s} = \omega_L - 2\omega_v$ , is also observed as a result of the amplified Stokes radiation driving population from  $v = 0$  to  $v = 1$  in the same way done by the dye laser input.

efficient at longer wavelengths and thus the input to the cell is lower.

The resonant and ionization detection beams were directed into the vacuum chamber along the same axis, but counter-propagating. In order to make sure that the resonant step is driven before the ionization pulse arrives, the pulses were separated in time by 10 ns by adding a 3 m long delay path in the ionization beam line. Both beams were shaped with lenses to have a  $\sim 2$  mm diameter at the center of the chamber. The energies of the resonant and ionization pulses were typically adjusted while monitoring the ion signal. We generally increased the individual energy of a pulse until the signal began to saturate. Increasing it any further would usually just increase the amount of multi-photon off resonant ionization, which added an undesirable background to our signal. Typical values of pulse energies were in the range of 1-100  $\mu\text{J}$ . Specific values, which depend on the particular transitions we were driving, will be given when we discuss our detection results. The pulse energies could be adjusted continuously by attenuating the beams with rotatable  $\lambda/2$  waveplates placed before high damage threshold Glan-Thompson polarizers. Pulse energies in the  $\mu\text{J}$  range were measured with a pyroelectric detector (Gentec, ED-200L UV); high energy pulses (like those coming directly out of the Nd:YAG and dye lasers) were measured with a thermal detector (Coherent, Inc.). In general, we had to steer the pulsed laser beams with high damage threshold mirrors, as the pulses, with their large instantaneous power, would burn holes in our standard optics.

#### 4.2.4 Data Acquisition and Processing

The task of taking data to detect ground state molecules and measure positions of excited state bound levels required stepping the dye laser frequency, acquiring the time of flight ion signal for a set number of pulses, or “shots”, that were averaged, and then stepping the laser to the next frequency point once the set number of shots was taken. A typical time of flight signal, averaged over 20 shots, is shown in Figure 4.7. The  $\text{Rb}^+$  and  $\text{Cs}_2^+$  peaks that appear are due to the ionization of Rb atoms and  $\text{Cs}_2$  molecules, as discussed in §4.1.2. The larger  $\text{Cs}^+$  peak is due primarily to off resonant multiphoton ionization of



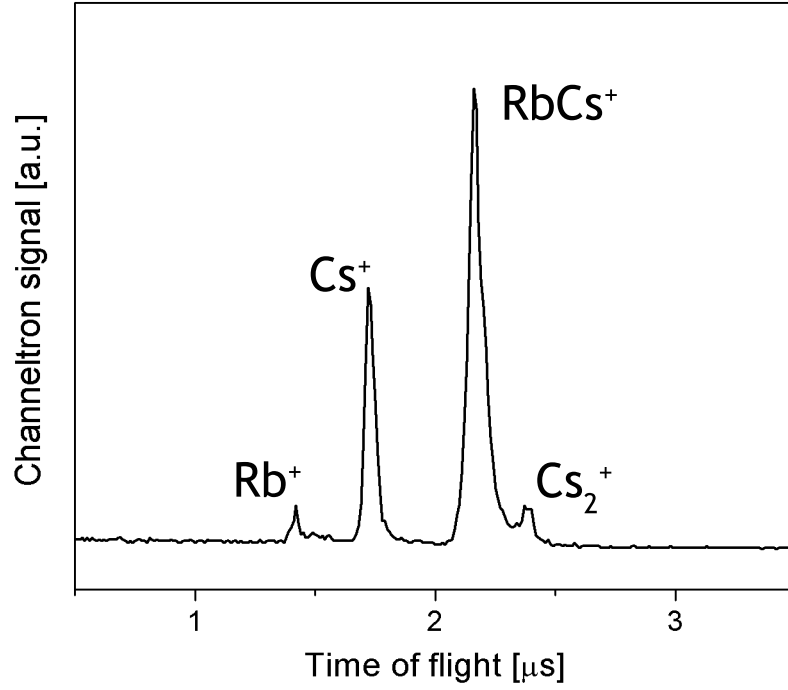


Figure 4.7: Time of flight ion signal. The channeltron current, averaged over 20 shots, is shown versus delay time after the ionization laser pulse. The four mass peaks corresponding to the detected atomic and molecular ions are resolved. The photoassociation laser is tuned to the  $\text{RbCs}^* \Omega = 0^-, J = 1$  level at  $\Delta = -38.02 \text{ cm}^{-1}$ .

RbCs in which the molecule is dissociated (verified by observing the signal go away when the photoassociation laser is tuned off resonance). A much bigger  $\text{Cs}^+$  peak was initially observed due to ionization of Cs atoms which we were worried would saturate the ion detector and affect the  $\text{RbCs}^+$  ion signal arriving later. To reduce the  $\text{Cs}^+$  ion peak size to that shown in Figure 4.7, we switched the MOT trapping, repumping, and depumping light off for a  $\sim 100 \mu\text{s}$  interval around the time of the ionization pulses. This way, we guaranteed that all the atoms were in their ground state, thus making it more difficult to off-resonantly ionize them due to the higher number of photons (and higher-order process) required to do so.

When initially scanning the frequency of the dye laser, we often observed resonant features that did not depend on the presence of the ionization pulse; we attributed them to the driving of resonant multi-photon transitions to high lying electronic potentials. These features only served to complicate the spectra we were interested in, namely, levels associated with the potentials dissociating to the Cs 6P asymptotes. We eliminated them by placing a shutter in the ionization beam path and chopping the beam off every other shot. By subtracting the ion signals with and without the presence of the ionization light, the features that did not depend on it were removed from the spectra. This technique had the additional advantage of eliminating any non-resonant background coming only from the first pulse. To make sure that any ion signals we measured were coming from ground state levels, we also placed a shutter in the photoassociation beam path. We chopped off the beam for  $100 \mu\text{s}$  before the pulsed light arrived, giving any molecules present in the excited state ample time to decay.

The detected ion signal data was acquired as follows. The current signal coming from the channeltron was converted to a voltage signal with a transimpedance amplifier (Ortec, Ser. 4160) that had a  $50 \Omega$  transimpedance resistor and an additional gain of 5. This voltage signal was then sent to a  $1 \text{ M}\Omega$  input of a computer data acquisition card (National Instruments, NI 5112 for PCI) which is fast enough to handle the  $\sim 100 \text{ ns}$  ion signals and could be controlled by a Labview program. Ion signal data was taken at the 10

Hz repetition rate of our pulsed lasers and the data acquisition card was triggered using a trigger output signal from the power supply of the Nd:YAG laser, which produced electronic pulses synched to the laser's Q-switch. The MOT beams were switched on and off by sending TTL pulses from a pulse generator (Quantum Composers, 9300 Series) to the RF switches controlling the AOMs in the beam paths. The photoassociation beam chopping was controlled by another output of the pulse generator that was sent to the driver of the shutter. The pulse generator was triggered by the Nd:YAG trigger output so that the switching and chopping was synchronous with the pulsed lasers. The chopping of the ionization beam for background subtraction was done by sending the Nd:YAG trigger to a digital counter and using the output of the second bit to control the shutter in the beam path; this way, the shutter would close and open for alternating pulses.

Obtaining bound-bound spectra, which involves tuning the dye laser while acquiring and processing the resulting ion signals, clearly requires a synching of the dye laser stepping and the data acquisition. A Labview program provided by the dye laser manufacturer allows one to do a "triggered scan" of the laser frequency. This program requires the entry of four parameters: the scan's starting frequency, ending frequency, step size, and the number of trigger pulses to wait before stepping the dye laser to the next frequency point. This last parameter is equivalent to the number of averages we wish to do of the data at each frequency point. The program generates a calibrated voltage value that is sent, through an analog output on one of our PCI boards, to the motor that adjusts the laser cavity grating and moves the dye laser to the appropriate frequency. We wrote another Labview program to acquire and process the ion signal data, which requires the entry of the same parameters as for the dye laser's triggered scan program and is designed to associate each incoming data shot with the correct value of laser frequency. The dye laser program and our data acquisition program are coordinated as follows: there is an input on the dye laser that is connected to an internal counter to which we send the trigger output of the Nd:YAG laser. Once this counter counts the number of pulses specified in the Labview program, the frequency is stepped. When the dye laser has reached its destination after being stepped

(i.e., when the grating has stopped moving), it conveniently outputs a high TTL signal (it is low when the grating is moving). We send this TTL signal to one input of an AND gate and the Nd:YAG trigger signal to the other; the output of the AND gate is sent to another input channel on the NI 5112 PCI card. This channel serves as both a trigger for the data acquisition in our program and as a counter that counts the number of Nd:YAG pulses sent to its input. Our program compares the number of counted trigger signals to the specified number of averages so that the program knows when to begin assigning incoming data to the next frequency point. Due to the AND gate, our program only begins counting trigger pulses and acquiring data when the dye laser counter begins counting so that we acquire the correct number of data shots at each frequency point before the dye laser is stepped.

Each data shot results in a time of flight signal that we process in real time so that we can generate plots of the size of each of the four mass peaks as a function of frequency while the experiment is running, in addition to writing the data to a file that can be reviewed at a later time. The processing, which is done by our Labview program, involves first averaging the shots for each data point. The background subtraction is done by adding and subtracting every other shot. We then integrate the averaged signal over narrow time “windows” of 140 ns around the center of each mass peak and plot the integrated values against laser frequency; we thus generate four plots corresponding to the ion signal coming from  $\text{Rb}^+$ ,  $\text{Cs}^+$ ,  $\text{RbCs}^+$ , and  $\text{Cs}_2^+$ .

### 4.3 Results of Ground State RbCs Detection

In this section we present and discuss the bound-bound spectra of RbCs obtained using 1+1 REMPI detection. From these spectra we are able to extract information about the levels to which RbCs molecules decay following photoassociation, as well as the excited state levels to which we subsequently excite them.

### 4.3.1 Searching for $X^1\Sigma^+$ State Molecules

In our effort to detect ground state RbCs molecules, we first searched for  $X^1\Sigma^+$  molecules, since finding a large population in a particular level would not necessitate exploiting the (yet to be confirmed) singlet/triplet mixing of the excited states to transfer this population to the  $v = 0$  ground state. As discussed in §4.1.1, in order to produce molecules in the  $X^1\Sigma^+$  state, we must photoassociate to an  $\Omega = 0^+$  level which has the undesirable effect of simultaneously populating the  $a^3\Sigma^+$  state. This makes it challenging to unravel which signals resulting from 1+1 REMPI detection are associated with which state.

To get around this we initially tried to drive transitions to the  $(4)^1\Sigma^+$  state which dissociates to the Cs  $6D_{3/2}$  asymptote; since there has been extensive spectroscopy done on both this state [77] and the X state [55], we had a good idea which laser frequencies to tune to in order to resonantly drive the first step of ionization. Driving these transitions requires light from roughly 550 nm to 710 nm, which we generated directly from our dye laser. Figure 4.8 shows a typical scan, taken around  $\sim 704$  nm ( $\sim 14200$   $\text{cm}^{-1}$ ) while photoassociating to the  $0^+$  level at  $\Delta = -55.6$   $\text{cm}^{-1}$ .

This frequency range was chosen to access the weakly bound  $X$  state levels; we began here because the predicted Franck-Condon factors for decay to these levels were large. As can be seen from the scan, there are many features present in the RbCs<sup>+</sup> ion signal; however we were never able to discern a pattern and identify which levels were involved in the  $X^1\Sigma^+(4) \rightarrow (4)^1\Sigma^+$  transitions with any degree of certainty due to such a dense and irregular spectrum. We then tried tuning the frequency of the resonant pulse to larger values to search for more deeply bound  $X$  levels which we predicted would be populated. We hoped that the resulting spectrum would be much less dense due to the relatively larger vibrational splittings between these levels. However, when we did this we saw no signals. We then searched for weakly bound  $X$  state molecules by attempting to drive them to the states dissociating to the Cs  $6P$  asymptotes. Our idea was to photoassociate to nearby  $0^+$  and  $0^-$  levels and scan the dye laser (now passing through the Raman cell) over the

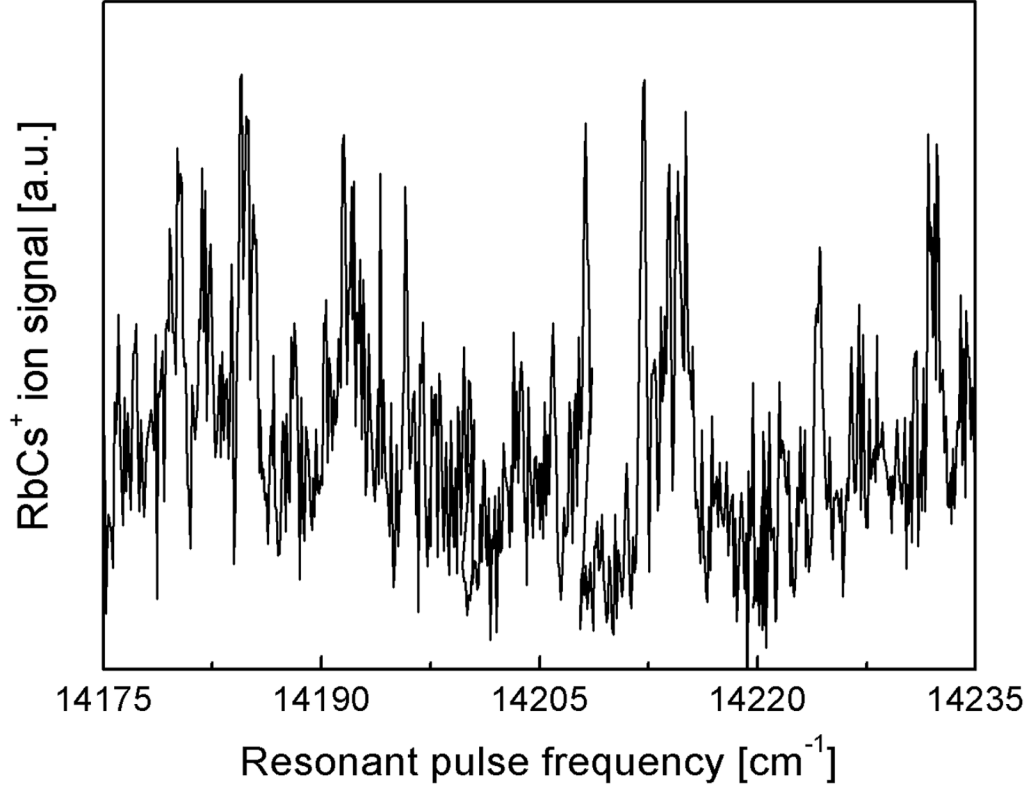


Figure 4.8: Search for weakly bound  $X^1\Sigma^+$  state molecules. The scan shows an ion spectrum observed while attempting to drive  $X^1\Sigma^+ \rightarrow (4)^1\Sigma^+$  transitions. The frequency splitting between the atomic Cs  $6S_{1/2}$  and  $4D_{3/2}$  levels (the latter of which corresponds to the  $(4)^1\Sigma^+$  state dissociation limit) is  $\sim 14499 \text{ cm}^{-1}$ . The scan was taken with photoassociation to the  $\text{RbCs}^* 0^+, J = 1$  level at  $\Delta = -55.6 \text{ cm}^{-1}$ . Due to the small signals (compared to the noise) and dense spectrum we could not identify the transitions associated with the ion signal peaks, and were thus unable to confirm the production of  $X$  state molecules.

same range in each case. Since photoassociation to a  $0^-$  level can only result in  $a^3\Sigma^+$  state population, any ion signal peaks in the  $0^+$  scan not present in the  $0^-$  scan would suggest X state population.<sup>4</sup> A typical comparison between scans is shown in Figure 4.9, in which we used the  $0^+$  and  $0^-$  levels bound below the Rb 5S + Cs 6P<sub>1/2</sub> asymptote by 34.5 and 38.0 cm<sup>-1</sup>, respectively. By examining this comparison, especially in the range from 8530  $\rightarrow$  8540 cm<sup>-1</sup>, one might try to make a case for the appearance of peaks in the  $0^+$  scan that are not found in the  $0^-$  scan; however these “peaks” are small, perhaps in the noise, and this case would be tenuous at best without any other supporting data. What is most interesting about the comparison, though, is the nearly complete disappearance of the larger peaks in the  $0^-$  scan from the  $0^+$  scan. This suggests two things: that molecules decaying from the  $0^+$  level are mostly populating the X state and that the transitions from the weakly bound  $X^1\Sigma^+$  levels to the excited state levels being probed are much less strong than from the weakly bound  $a^3\Sigma^+$  levels. The latter observation prompted us to re-examine the classical turning points of the various levels to get a qualitative sense of the relative Franck-Condon factors involved. We noticed that the *inner* turning point of the  $a^3\Sigma^+$  potential overlapped quite well with the outer turning points of some of the excited states being used for the 1+1 REMPI detection. We speculated that this was the reason for seeing more prominent ion peaks associated with  $a^3\Sigma^+$  state molecules. The relative ease of detecting these molecules prompted us to change directions and try to use them to gain spectroscopic information on the excited level positions and their singlet/triplet mixing, while simultaneously determining exactly which  $a^3\Sigma^+$  levels were being populated.

### 4.3.2 Detection of $a^3\Sigma^+$ State Molecules

To detect molecules in the  $a$  state, we locked our photoassociation laser to the J=1 rotational level of the  $0^-$  resonance bound by 38.019 cm<sup>-1</sup>. We scanned the dye laser and sent its output through the Raman cell, generating light continuously from 8350  $\rightarrow$  10650 cm<sup>-1</sup>

---

<sup>4</sup>Since it is possible that even closely spaced photoassociation levels will produce different  $a^3\Sigma^+$  state populations, this is not a completely rigorous test.

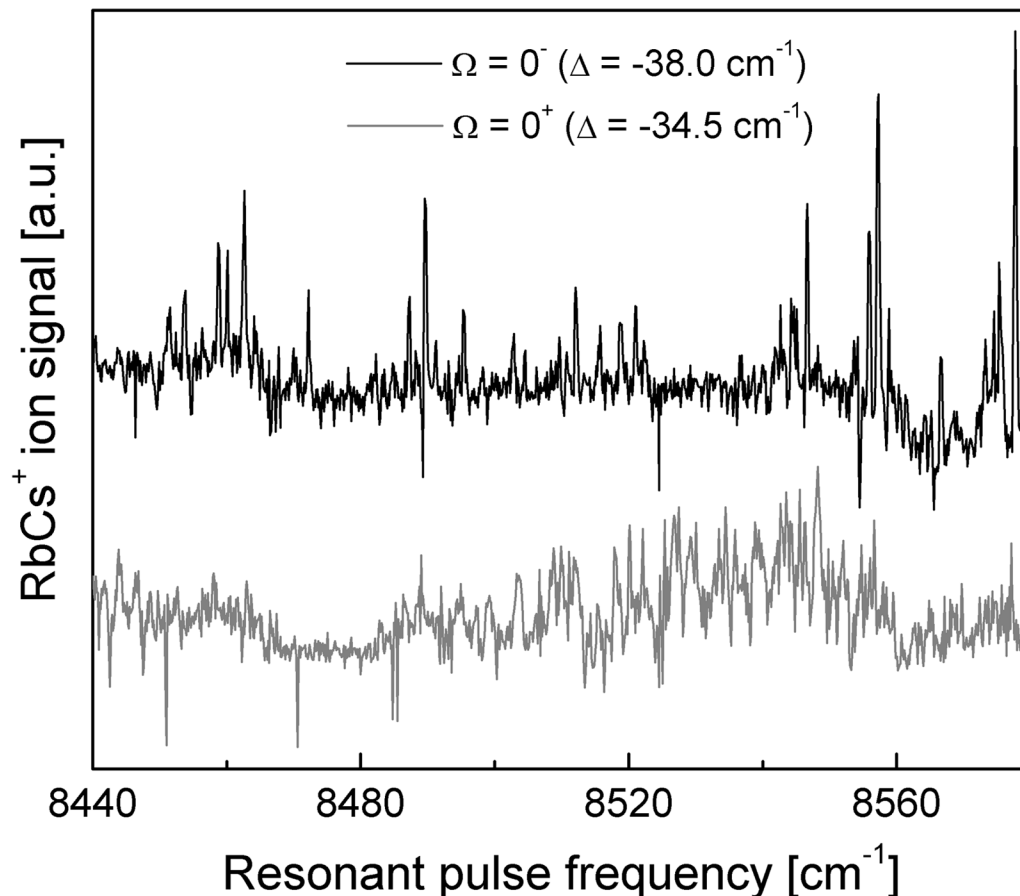


Figure 4.9: Search for  $X^1\Sigma^+$  state molecules by comparison of ion data for  $0^+$  and  $0^-$  photoassociation. Two 1+1 REMPI scans are shown over the same frequency range for photoassociation to a  $0^+$ ,  $J = 1$  level (lower) and a  $0^-$ ,  $J = 1$  level (upper). The resonant detection pulse frequency is tuned to drive transitions to states dissociating to the Cs  $6P$  asymptote. Observation of any ion peak in the lower scan not present in the upper suggests the signal arises from  $X$  state molecules. Peaks in common to the two scans must come from  $a$  state molecules since photoassociation to a  $0^-$  level cannot populate the  $X$  state. In the range from  $8530 \rightarrow 8540 \text{ cm}^{-1}$ , there are possibly peaks in the lower trace not evident in the upper; however these peaks are barely above the noise making the case for  $X$  state molecule detection tenuous.



that had a typical pulse energy of 40  $\mu\text{J}$ . The ionization pulse, at 532 nm, had a typical pulse energy of 200  $\mu\text{J}$ . The data from this scan, shown in Figure 4.10, was taken with each point averaged over 20 shots and with a step size of  $\sim .07 \text{ cm}^{-1}$ . To generate this large scan, we took data in smaller, ( $\sim 30 \text{ cm}^{-1}$ ) scans. We measured the frequency of the dye laser at the beginning and end points of each small scan with a wavemeter with 0.05  $\text{cm}^{-1}$  absolute accuracy and used these values to piece together the individual scans. As a result, all of our ionization data has the absolute accuracy of the wavemeter.

In Figure 4.10(a)-(b) a vibrational progression is evident beginning at  $\sim 8776.4 \text{ cm}^{-1}$ , consisting of a series of doublets, which we associate with the  $c^3\Sigma^+$  excited state. The observed vibrational splitting of  $31.6 \text{ cm}^{-1}$  (for the lower vibrational levels) agrees well with the splitting predicted by *ab initio* potentials ( $32.2 \text{ cm}^{-1}$ ) and the observed location of the onset of the series is close to the predicted location of the  $v = 0$  level (at  $8776.7 \text{ cm}^{-1}$ ) [76]. The doublet structure is associated with the second-order spin-orbit splitting between the  $\Omega = 0^-$  and 1 components of the  $c^3\Sigma^+$  state, which occurs due to mixing with the  $B^1\Pi_1$  and  $b^3\Pi_{0,1}$  states; this splitting is observed here to be  $\sim 9 \text{ cm}^{-1}$ . The doublets are the two interlaced vibrational progressions associated with the  $c^3\Sigma_0^+$  and  $c^3\Sigma_1^+$  potentials.

All of the doublets in Figure 4.10 have a characteristic substructure, as shown in Figure 4.11. This substructure is associated with the weakly bound vibrational levels of the  $a^3\Sigma^+$  state. The observed splittings between the peaks in the data agree well with the predicted locations of the  $a$  state levels based on *ab initio* potentials [76]. In addition, since we use enough laser intensity to saturate the resonant step of ionization (verified by observing the signals to plateau as the intensity is increased), the relative sizes of the features reflect the population distribution among the  $a$  state levels. This distribution resembles that predicted from Franck-Condon factors, which were calculated using the *ab initio*  $a$  state potential and our knowledge of the photoassociation state wavefunction determined from the spectroscopy discussed in Chapter 3. The most highly populated  $a^3\Sigma^+(v = 37)$  level, resulting from spontaneous decay following photoassociation, is observed to lie  $4.96 \pm 0.6 \text{ cm}^{-1}$  below the  $\text{Rb } 5S + \text{Cs } 6P$  asymptote, where the uncertainty is in the dissociation limit

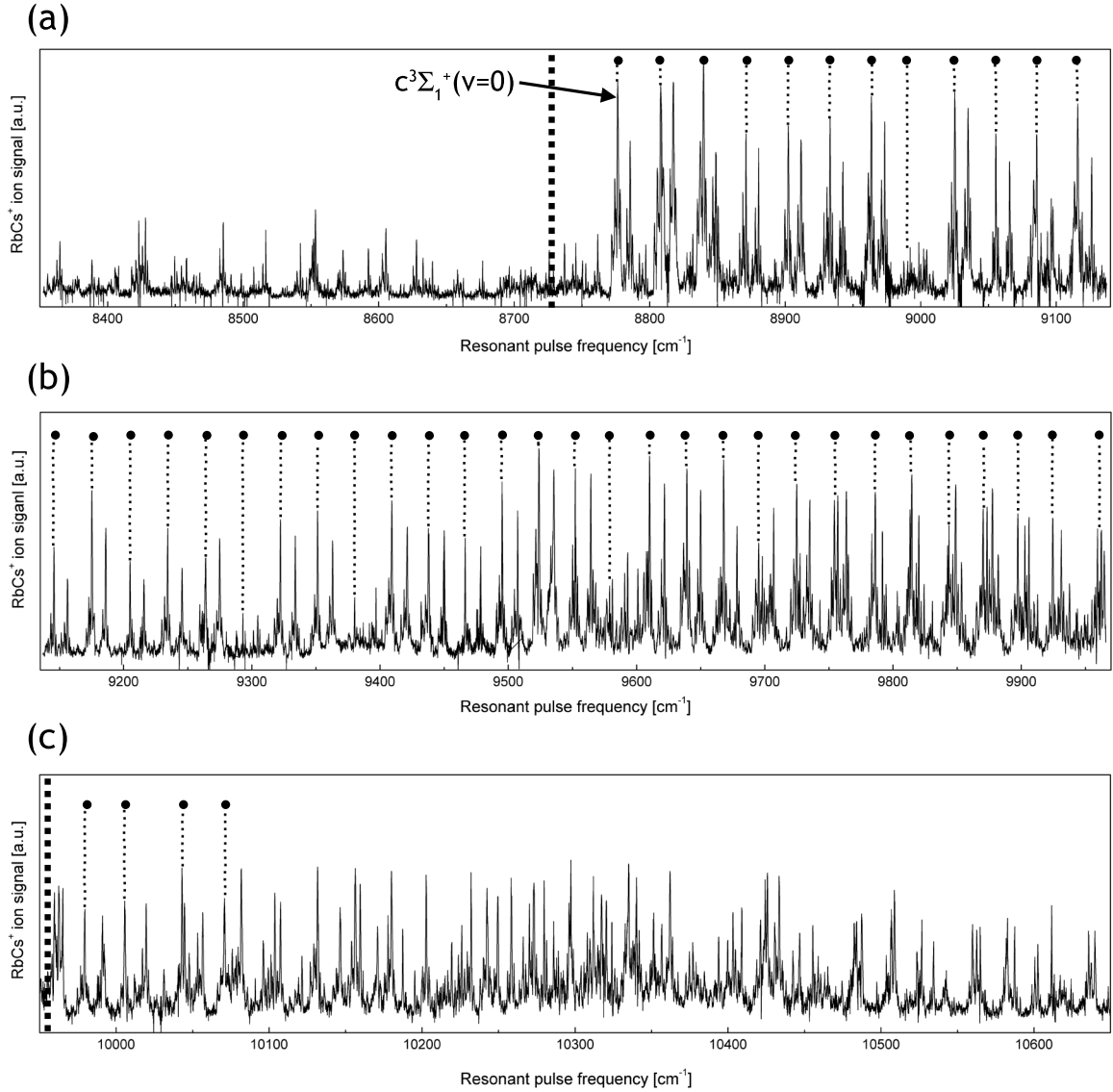


Figure 4.10: Detection of ground state  $a^3\Sigma^+$  molecules and excited state spectroscopy. (a)-(c) The continuous bound-bound ion spectrum obtained by ionizing  $a$  state molecules through the excited states of Figure 4.1 is shown. The photoassociation laser is tuned to the  $0^-$ ,  $J = 1$  level at  $\Delta = -38.02$  cm<sup>-1</sup>. The strong progression indicated by the black circles is associated with the  $c^3\Sigma^+$  state whose  $v = 0$  level corresponds to the onset of the series. The circles are only used to guide the eye to this progression and do not represent any fit to a theoretical model. The dotted line in (a) represents the predicted minimum of the  $c$  state potential. The observed peak doublets below each circle come from the spin-orbit splitting of the  $c$  state's  $\Omega = 0^-$  and 1 components due to mixing with the  $B^1\Pi$  and  $b^3\Pi$  states. The dotted line in (c) represents the predicted minimum of the  $B^1\Pi$  state, above which the clear vibrational progression evident in (a) and (b) becomes more complicated due to the presence of  $B^1\Pi$  levels. The smaller features at the lowest energies in (a) correspond to transitions to the coupled  $A^1\Sigma^+$  and  $b^3\Pi$  states.

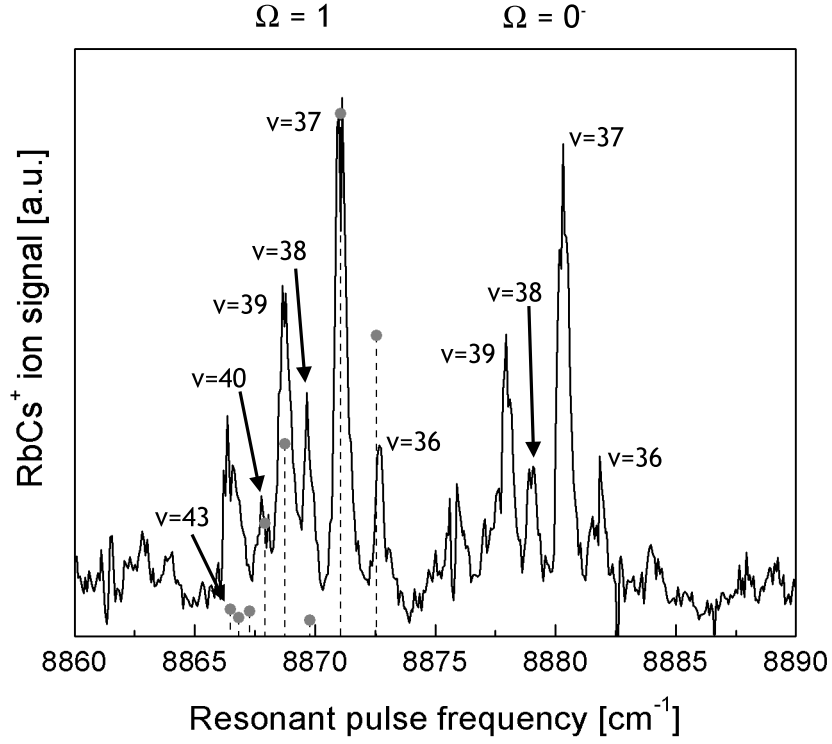


Figure 4.11: Spectroscopy and population distribution of the  $a^3\Sigma^+$  state. The substructure of the  $a^3\Sigma^+ \rightarrow c^3\Sigma^+$  spectrum is shown. The doublet peak structure corresponds to the  $\Omega = 0^-$  and 1 components of the excited state. The finer structure within each peak corresponds to vibrational structure of the  $a$  state. The dashed lines show the predicted locations of the  $a$  state vibrational levels; the absolute position of this pattern was adjusted to match the observed features, which fixes the excited state level positions. The grey circles represent the predicted  $a$  level populations.

and arises from the non-perfect agreement between the predicted and observed population distributions [78].

The smaller features seen in the beginning of the scan in Figure 4.10(a), which appear at energies below the minimum of the  $c$  state, have the same  $a$  state vibrational structure as observed in the prominent  $c$  state doublets and arise due to transitions from these  $a$  state levels to the coupled  $A^1\Sigma^+$  and  $b^3\Pi$  states. These features are smaller presumably because the outer turning points of the  $A$  and  $b$  potentials do not line up nearly as well with the  $a$  state inner turning point as compared to the  $c$  state, hence leading to smaller Franck-Condon factors.

A detailed theoretical discussion of the excited state mixing based on our data is given in reference [78], and only the salient points will be discussed here.<sup>5</sup> For the lower vibrational levels of the  $c$  state, which lie below the predicted minimum of the  $B$  state, the  $\Omega = 1$  component is shifted down in energy since it is repelled by the  $B$  state levels above it; the  $\Omega = 0$  component of the  $c$  state is unaffected by the  $B$  state, which only has an  $\Omega = 1$  component, since the spin-orbit interaction does not mix levels with different values of  $\Omega$ . As mentioned above, the levels in the  $c$  state are also mixed with the  $b$  levels which have both  $\Omega = 0$  and 1 components. As discussed in reference [78], the  $b$  and  $c$  state coupling is due predominantly to  $c$  levels mixing with the  $b$  levels lying below them in energy (due to Franck-Condon overlap factors) so that both the  $c$  state  $\Omega = 0$  and 1 components are repelled and shifted up. However, the off-diagonal spin-orbit interaction is a factor of  $\sqrt{2}$  bigger for the  $\Omega = 0$  component; hence the  $b$  state mixing also has the net effect of shifting the  $\Omega = 1$  component down in energy relative to the 0 component. Thus, the lower in energy of the two components of the doublet is unambiguously associated with the  $\Omega = 1$  component of the  $c^3\Sigma^+$  state, which contains a mixture of the  $B^1\Pi_1$  and  $b^3\Pi_1$  states.

The degree of  $B^1\Pi_1$  character possessed by a given excited level determines the strength of coupling from this level to the  $X$  state, since only the singlet part of the wavefunction will contribute to the transition matrix element. By contrast, the  $\Omega = 0$  component cannot

---

<sup>5</sup>This work was done primarily by our collaborator Thomas Bergeman.

be connected to the  $X$  state because it has no  $B^1\Pi_1$  character. Thus, we must drive the molecules through the  $\Omega = 1$  component if we hope to populate the  $X^1\Sigma^+(v = 0)$  ground state via a predominantly  $c^3\Sigma^+$  state level.

Figure 4.10(c) shows the ion data above  $9950\text{ cm}^{-1}$ , near where the minimum of the  $B$  state is predicted to lie [76]. Comparing this data to that shown in Figure 4.10(a)-(b), it is clear that the spectrum in (c) is much more complicated, i.e., the clean vibrational progression is no longer evident, especially above  $10150\text{ cm}^{-1}$ . This arises from the stronger mixing between the overlapping  $B$  and  $c$  levels. This complexity makes it difficult to tell by eye which levels belong predominantly to which electronic potential (assuming they are not *completely* mixed). Nevertheless, by adjusting the *ab initio* potentials and spin-orbit functions, the observed positions of these levels, as well as those lying below the  $B$  state minimum, can be reproduced to some degree. The fitted potentials are then used to calculate the electronic and vibrational wavefunctions of the mixed excited levels. The electronic part contains the quantitative information about the degree of excited state mixing, while the vibrational part is useful in calculating the Franck-Condon overlap with the  $X^1\Sigma^+(v = 0)$  ground state we wish to populate. As mentioned above, only the  $B^1\Pi$  component of the excited state wavefunctions will contribute to this overlap. A summary of this analysis is given in Table 4.2, in which levels calculated to have a non-negligible singlet character are listed. The table shows the observed positions of these levels and their difference from the positions calculated using the theoretical model. The calculated fraction of  $c$ ,  $B$ , and  $b$  character is also given. The last column of the table shows the product of the vibrational overlap integral with the fraction of singlet character possessed by the excited state; this represents the strength of the coupling to the  $X^1\Sigma^+(v = 0)$  state. For most of these excited levels, this coupling strength is large enough to saturate the transition to the  $X^1\Sigma^+(v = 0)$  state. For instance, we observe a large ion signal for a resonant pulse frequency of  $9754.26\text{ cm}^{-1}$ , indicating a high transfer efficiency to this level from the  $a$  state. The coupling strength for a transition to the  $X^1\Sigma^+(v = 0)$  state is  $\sim 3 \times 10^{-5}$ . According to the discussion in §4.1.2, this transition can be saturated with

a pulse energy of roughly 30  $\mu\text{J}$  which is trivially attainable at the required frequency of  $13560.04\text{ cm}^{-1}$  ( $\sim 737\text{ nm}$ ).

It should be noted that we expect this analysis to be only qualitatively correct given the number of overlapping potentials and the limited information available on the strength of the spin-orbit coupling. In fact, as we shall see in Chapter 5, some levels that had been assigned as having no singlet character were observed to couple effectively to the  $X^1\Sigma^+$  state. In addition, since our pulsed lasers did not resolve any rotational structure we were unable to extract rotational constants and use them to constrain the positions of the outer turning points of the excited state potentials. There is thus uncertainty in the absolute horizontal positions (along the  $R$  axis) of these potentials and therefore uncertainty in the calculated Franck-Condon factors for coupling to the ground state. We use this analysis now, as we did at the time of our experiments, to give us a rough idea of the degree of singlet/triplet mixing in the excited levels and to obtain an order of magnitude estimate of the Franck-Condon factors for coupling to the  $X^1\Sigma^+(v=0)$  state. Given the values shown in Table 4.2, we were confident that by attempting to use a number of these levels, we would find some that have a large enough singlet character and Franck-Condon factor to permit population of the absolute ground state.

Photoassociation to levels other than the one used for the data above results in slightly different population distributions of the  $a$  state, as shown in Figure 4.12. For instance, photoassociation to the  $0^-$  level at  $\Delta = -56.0$  results in the absence of molecules in the  $v = 37$  level but populates the more deeply bound  $v = 34$  state, which lies lower by  $\sim 4\text{ cm}^{-1}$  than any level populated via photoassociation to the state at  $\Delta = -38.0$ . Furthermore, photoassociation to a level at  $\Delta = -35.8$  which we assign as either  $\Omega = 1$  or 2, does not seem to populate the  $a^3\Sigma^+$  ground state as efficiently as does photoassociation to the  $0^-$  levels, as can be inferred by the markedly smaller ion signals. The reason for this was not investigated in detail. However, we also observed that photoassociation to  $\Omega = 0^+$  levels did not efficiently populate the  $a$  state, resulting in ion signals similar to the one shown in Figure 4.12 for the  $\Omega = 1$  or 2 level. Note that the reason for the

Observed Position [cm <sup>-1</sup> ]	Difference Obs.-Calc. [cm <sup>-1</sup> ]	Calculated Fractions			FCF to $X^1\Sigma^+(v=0)$ × Singlet Fraction
		$c^3\Sigma_1^+$	$b^3\Pi_1$	$B^1\Pi_1$	
9552.11	0.61	0.954	0.045	0.001	$2.59 \times 10^{-6}$
9581.09	0.37	0.949	0.050	0.001	$6.32 \times 10^{-6}$
9609.99	0.20	0.943	0.056	0.001	$2.11 \times 10^{-6}$
9639.14	-0.20	0.936	0.062	0.001	$1.10 \times 10^{-5}$
9667.90	-0.20	0.929	0.069	0.002	$1.36 \times 10^{-6}$
9695.17	1.30	0.922	0.076	0.002	$1.68 \times 10^{-5}$
9697.86	-0.31	0.176	0.818	0.006	$9.17 \times 10^{-5}$
9724.83	0.44	0.914	0.084	0.002	$2.13 \times 10^{-6}$
9754.26	-0.18	0.906	0.091	0.003	$2.95 \times 10^{-5}$
9783.36	-0.47	0.898	0.099	0.003	$3.10 \times 10^{-6}$
9873.26	0.90	0.230	0.762	0.008	$1.14 \times 10^{-4}$
9902.76	-0.05	0.237	0.755	0.008	$1.25 \times 10^{-4}$
9964.95	-0.04	0.128	0.023	0.849	$6.84 \times 10^{-4}$
10043.04	-0.54	0.268	0.723	0.010	$1.42 \times 10^{-4}$
10096.21	0.05	0.125	0.029	0.846	$2.26 \times 10^{-3}$
10103.77	-1.29	0.672	0.164	0.164	$2.39 \times 10^{-5}$
10146.45	4.79	0.284	0.704	0.011	$1.85 \times 10^{-4}$
10156.61	0.10	0.678	0.180	0.142	$1.03 \times 10^{-4}$
10170.90	-4.90	0.124	0.032	0.844	$1.92 \times 10^{-3}$
10177.77	0.28	0.287	0.701	0.012	$1.86 \times 10^{-4}$
10187.36	-2.31	0.663	0.181	0.156	$1.82 \times 10^{-3}$
10232.10	-0.88	0.293	0.694	0.013	$2.31 \times 10^{-4}$
10242.53	1.59	0.706	0.210	0.084	$5.31 \times 10^{-4}$
10258.40	-0.08	0.043	0.014	0.943	$6.93 \times 10^{-3}$
10270.12	1.78	0.724	0.226	0.050	$3.54 \times 10^{-4}$
10279.75	4.05	0.298	0.688	0.014	$2.46 \times 10^{-4}$
10309.60	0.27	0.300	0.685	0.015	$2.87 \times 10^{-4}$
10320.40	0.12	0.090	0.032	0.878	$6.72 \times 10^{-3}$
10334.88	0.90	0.302	0.683	0.016	$3.11 \times 10^{-4}$
10351.34	-2.40	0.21	0.075	0.715	$2.23 \times 10^{-3}$
10356.80	0.01	0.548	0.187	0.265	$6.23 \times 10^{-4}$
10361.54	0.01	0.303	0.680	0.017	$3.47 \times 10^{-4}$
10377.05	0.29	0.220	0.078	0.702	$5.57 \times 10^{-3}$

Table 4.2: Summary of theoretical model of  $c/B/b$  mixing. Observed excited state levels with a calculated non-negligible singlet character are shown. The fraction of  $c/B/b$  state character for each level is given. The observed level positions are referenced from the  $a^3\Sigma^+(v=37)$  level, which lies  $\sim 3831.18$  cm<sup>-1</sup> above the  $X$  state minimum. The second column represents the deviations of the calculated level positions, based on the theoretical model, from the observed positions. The calculated fractions are the squares of the mixed state amplitudes. The final column is the product of the singlet fractional character of a particular excited level and the calculated Franck-Condon factor between this level and the  $X^1\Sigma^+(v=0)$  ground state. This quantity takes into account both the nuclear and electronic wavefunction overlap.

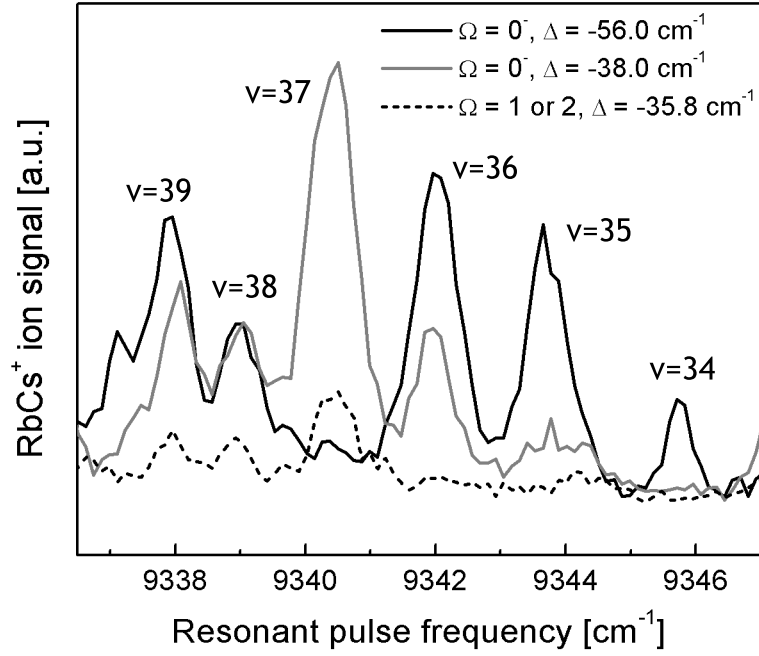


Figure 4.12: Dependence of  $a$  state population on photoassociation to different  $\text{RbCs}^*$  levels. The population of the  $a^3\Sigma^+$  state via decay from three different levels is shown. Photoassociation to a  $0^-$  level at  $\Delta = -56.0 \text{ cm}^{-1}$  results in the disappearance of population in  $v = 37$  and an appearance of population in  $v = 34$ . Photoassociation to the  $\Omega = 1$  or  $2$  level does not appear to effectively populate the  $a$  state.



smaller ion signals cannot be simply that the photoassociation rate to  $\Omega = 0^+, 1, 2$  states is smaller since we observe comparable trap loss when photoassociating to  $\Omega = 0^-$  levels. These smaller signals are most likely a result of there being an additional channel for the  $\Omega = 0^+, 1, 2$  states to decay to, namely the  $X^1\Sigma^+$  state. Another possibility is that the Franck-Condon factors for decay from the  $\Omega = 0^+, 1, 2$  states to the  $a$  state are smaller due to less favorable locations of the outer turning points of the  $\Omega = 0^+, 1, 2$  potentials.

### 4.3.3 Temperature Measurement of $a^3\Sigma^+$ State Molecules

To estimate the temperature of the ground state  $a^3\Sigma^+$  molecules being produced, we monitor the  $\text{RbCs}^+$  ion signal as we vary the time delay between when we shutter off the photoassociation laser and the arrival of the ionization pulses. During the period when the photoassociation beam is off, the number of molecules in the region defined by the pulsed beams decreases exponentially with time as the untrapped molecules fly away. The number of molecules detected then varies with time delay as

$$N_{det}(t) = N_{det}^0 e^{-t/\tau_m}, \quad (4.4)$$

where  $N_{det}^0$  is the number of molecules detected with zero time delay, and  $\tau_m$  is the characteristic time for a molecule to leave the detection region. This time can be used to approximate the temperature by assuming that a molecule leaves the detection region with an average speed<sup>6</sup>

$$v_{avg}^{2D} = \sqrt{\frac{\pi k_B T}{2m}} \quad (4.5)$$

in a time

$$\tau_m = \frac{\omega_b}{v_{avg}}, \quad (4.6)$$

---

<sup>6</sup>To calculate this speed we use the two dimensional speed distribution given by  $f_{speed}^{2D} = \frac{v}{\Delta v^2} \exp[-\frac{v^2}{2\Delta v^2}]$ , where  $\Delta v$  is related to temperature as in equation 2.5. The two dimensional distribution is used since only movement in a direction transverse to the axis defined by the detection beams results in molecules leaving the detection volume. The average speed is calculated in the usual way as  $v_{avg}^{2D} = \int v f_{speed}^{2D}(v) dv$ .

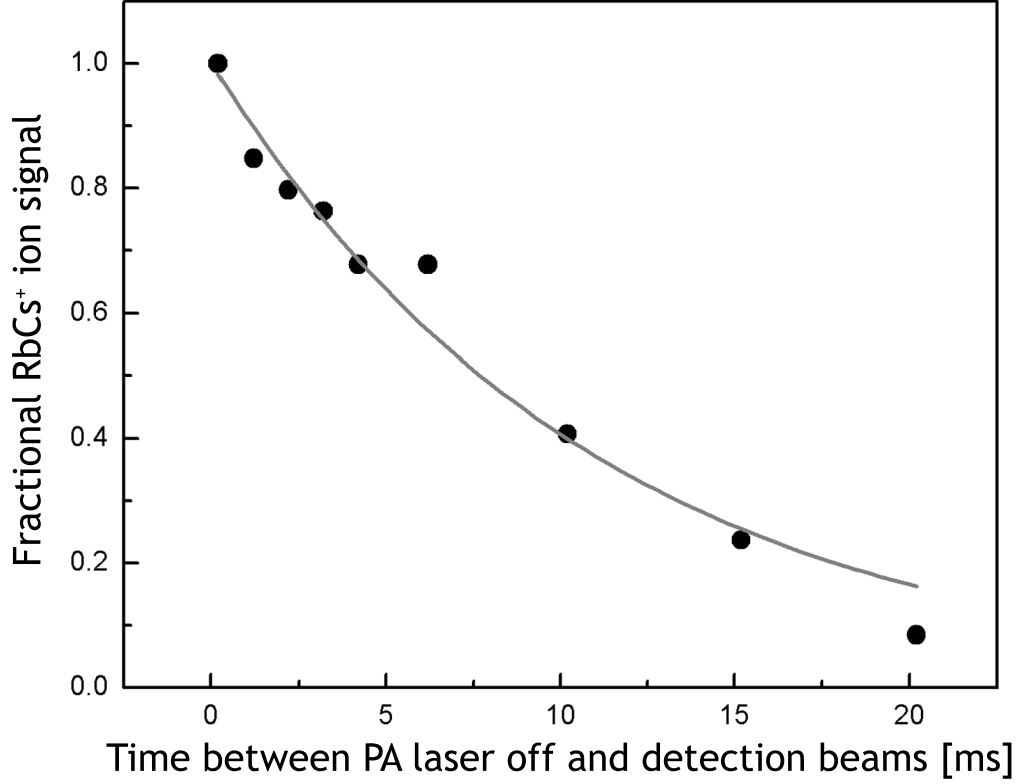


Figure 4.13: Temperature measurement of  $a^3\Sigma^+(v = 37)$  state molecules. The number of  $a^3\Sigma^+(v = 37)$  state molecules detected is plotted versus time between chopping off the photoassociation laser and the arrival of the detection pulse beams. The absolute number is normalized to the value for zero time delay. A fit of this data to a decaying exponential yields a time constant of 11 ms for the untrapped molecules to leave the detection region. From this value we extract a temperature of  $\sim 140 \mu\text{K}$  for the  $a^3\Sigma^+(v = 37)$  state molecular sample.

where  $\omega_b$  is the pulse beam radius. The temperature measurement data is shown in Figure 4.13, from which we extract the value  $\tau_m \sim 11$  ms. Given our  $\sim 1$  mm radius pulsed beams, we obtain an approximate temperature of  $T \sim 140 \mu\text{K}$  for our  $a$  state molecular sample. There is a  $\sim 75\%$  uncertainty in this value dominated by the uncertainty in our detection beam size which we know to an accuracy of only  $\sim 50\%$ . Our estimate of the temperature of the molecular sample is comparable with the measured temperature of our atoms and is consistent (given our uncertainty) with there being negligible heating due to the photoassociation and spontaneous decay processes. This is what one would expect, considering that the recoil velocity associated with the scattering of two photons

is less than 10% of the velocity spread of our 75  $\mu\text{K}$  Rb and Cs atoms. In addition, other experiments have measured the temperature of a sample of ground state molecules produced via photoassociation more accurately than done here, and have also found the temperature to be consistent with that of their atomic sample [79].

#### 4.3.4 Ground $a^3\Sigma^+$ State Molecule Production Rate

Based on the  $\text{RbCs}^+$  signal generated by driving a saturated  $a^3\Sigma^+(v = 37) \rightarrow c^3\Sigma^+(v')$  transition and then ionizing the  $c$  state population, we attempt to infer the rate of  $a^3\Sigma^+(v = 37)$  state molecule production via photoassociation. The gain of the channeltron (biased at -2 kV) is  $\sim 4 \times 10^6$ ; from our measurement of the current at the output of the detector, we estimate that we detect  $\sim 250$  ions per pulse. Our knowledge of the channeltron gain comes from the manufacturer's specifications and has not been independently calibrated. Due to our incomplete understanding of how the gain quantitatively scales with ion mass and detector age, we must treat the above estimate as a rough, order-of-magnitude one.<sup>7</sup> As discussed in §4.3.3, the untrapped molecules leave the detection region in a characteristic time of 11 ms; the detected steady state molecule number must therefore be maintained with an equivalent loading time.<sup>8</sup> In our estimate of the molecule production rate, we must also account for the unresolved  $a$  state structure. The features shown in Figure 4.11 are  $\sim 1 \text{ cm}^{-1}$  wide, which is 20 times our laser linewidth. We assume that the observed width of these features is dominated by the  $a$  state hyperfine/rotational structure and that the contribution from the  $c$  state is negligible. This assumption should be valid given that the  $\Omega = 0$  component of the  $c$  state should have negligible hyperfine structure (due to its lack of angular momentum to which the nuclear spins can couple) and that the features corresponding to the  $\Omega = 1$  component have a comparable width. Also, the spread of accessible

---

<sup>7</sup>Also, we believe that we were operating our detector in a saturated regime, as will be discussed in §5.3; since we did not investigate the saturation in detail at the time, this clearly adds to the uncertainty in the detected ion number.

<sup>8</sup>It is clear from this point that even though the photoassociation laser is kept on continuously (for the 100 ms between the detection pulses), only 11 ms are actually required to achieve a steady state population in the detection volume.

rotational levels in the excited state in the absence of hyperfine/rotational coupling is small (see §5.4.2). As a result, we only transfer 1/20 of the total population in the  $a^3\Sigma^+(v = 37)$  level to the excited state. Including all of the above factors, we estimate a production rate of  $a^3\Sigma^+(v = 37)$  molecules of  $\sim 5 \times 10^5 \text{ s}^{-1}/E$ , where  $E$  is the ionization efficiency into the  $\text{RbCs}^+$  channel. While we observe the resonant detection step to be saturated, the ionization step displays a more complex behavior; as the ionization pulse intensity is increased, broadened features appear in both the  $\text{Rb}^+$  and  $\text{Cs}^+$  channels, indicating that multiphoton and possibly predissociation processes are involved. As a result, we do not have complete knowledge of the ionization efficiency and thus the absolute ground state molecule production rate. By using our estimation of the total photoassociation rate ( $\sim 2 \times 10^8 \text{ s}^{-1}$ ) and a predicted branching ratio of  $\sim 5\%$  for decay of the  $\text{RbCs}^*$  molecules into the  $a^3\Sigma^+(v = 37)$  level (based on calculated Franck-Condon factors), we expect this level to be populated at a rate of  $\sim 10^7 \text{ s}^{-1}$ . For this expected value to be consistent with that of our estimation, we require an ionization efficiency of  $\sim 5\%$ , which is comparable with ionization efficiencies reported by groups operating under similar conditions [80]. We therefore crudely estimate a  $10^7 \text{ s}^{-1}$  production rate of  $a^3\Sigma^+(v = 37)$  molecules.

## 4.4 Summary

It is clear from the above data and discussion that a promising route towards the production of UPMs in the  $X^1\Sigma^+(v = 0)$  vibronic ground state exists. We have shown that we can efficiently populate the  $a^3\Sigma^+(v = 37)$  level via photoassociation and that we can drive this population to various excited  $c^3\Sigma^+$  levels, which contain a non-negligible mixture of the  $B^1\Pi$  state. Analysis of our data suggests that the fraction of singlet character coming from the  $B^1\Pi$  state component, as well as the Franck-Condon factors associated with transitions from the excited levels to the  $X^1\Sigma^+(v = 0)$  ground state are large enough to be able drive such transitions with an additional pulsed laser.

## Chapter 5

# Production of Ultracold RbCs in the $X^1\Sigma^+(v=0)$ State

In this chapter we discuss how we transfer the RbCs molecules formed in the  $a^3\Sigma^+$  state via photoassociation to the  $X^1\Sigma^+(v=0)$  state. We begin by discussing the transfer technique and the ways in which we detect that the ground state is being populated. We then discuss the additional apparatus required to experimentally implement the transfer. Finally, we discuss the results of our experiments and show that we are able to produce a sample of UPMs with a translational temperature of  $\sim 100 \mu\text{K}$  in the  $X^1\Sigma^+(v=0)$  state, with a narrow spread of rotational levels such that all external and internal degrees of freedom are cold.

### 5.1 Stimulated Emission Pumping and Detection

The method we use to drive the  $a^3\Sigma^+$  molecules into the ground state is known as stimulated emission pumping (SEP) [81] and is shown schematically in Figure 5.1. A “pump” pulse drives the  $a^3\Sigma^+(v=37)$  molecules to a mixed  $c/B/b$  excited state,  $i$ . A “dump” pulse, with a frequency equal to the splitting between levels  $i$  and  $X^1\Sigma^+(v=0)$  (or  $X^1\Sigma^+(v=1)$ , for diagnostic purposes) is then applied which drives the population down to the ground

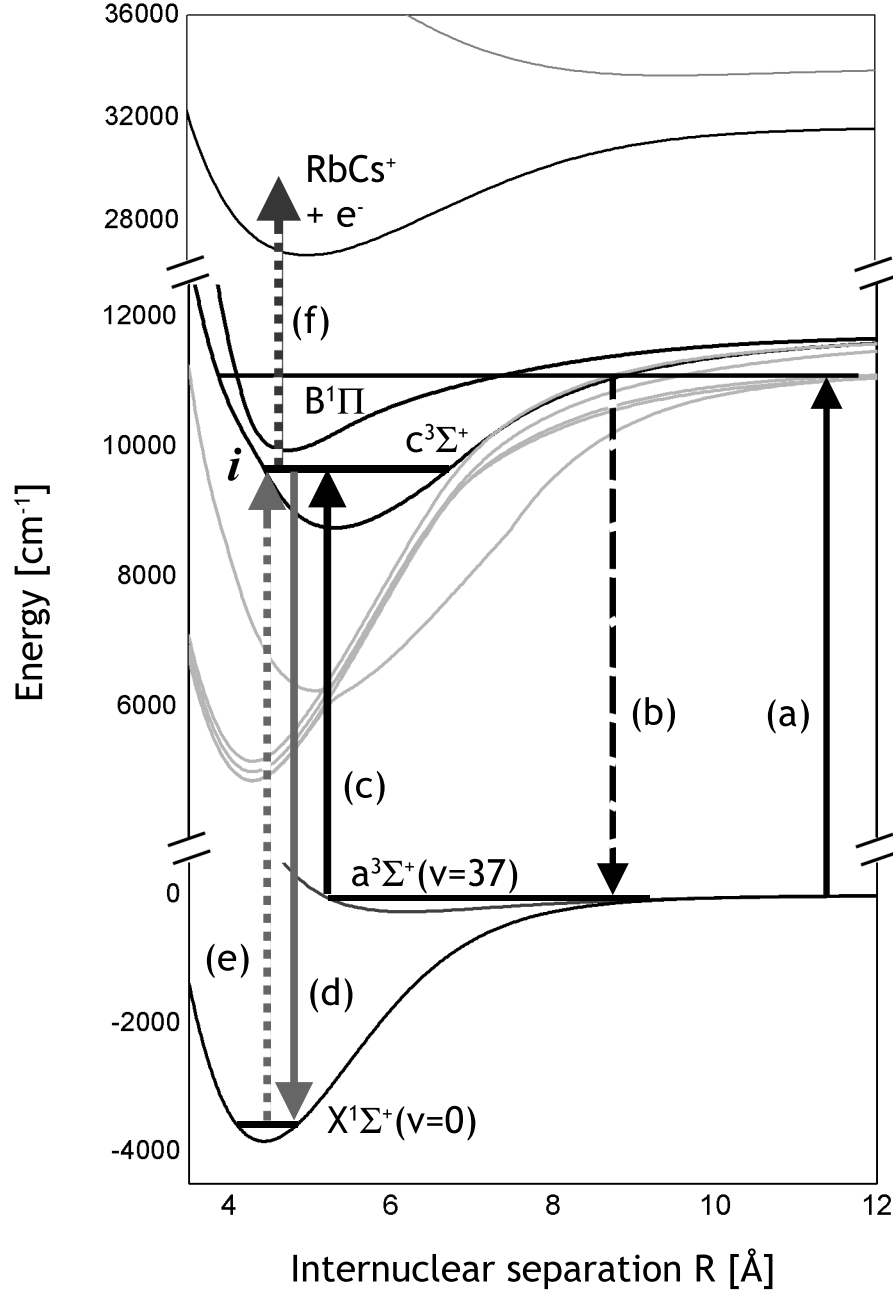


Figure 5.1: Formation and detection of  $X^1\Sigma^+(v=0)$  state RbCs. The method by which we produce and detect RbCs molecules in the absolute ground state is shown. (a) Colliding atom pairs are excited into bound  $\text{RbCs}^*$  molecules which (b) decay prominently to the  $a^3\Sigma^+(v=37)$  level. These molecules are transferred to the  $X(v=0)$  ground state via SEP; they are (c) driven to an excited state  $i$  with a pump pulse, and then (d) stimulated into the  $X(v=0)$  state with a dump pulse. The ground state molecules are detected directly by (e) driving them back to level  $i$  with a re-excitation pulse and (f) ionizing them. They are detected indirectly by observing depletion of the  $i$  level population due to the dump pulse transfer; this indirect method does not require step (e).

state. In order to detect that ground state molecules are being formed, we employ two techniques. In the first, called ion dip spectroscopy [82], we apply an “ionization” pulse, which arrives after the dump pulse, in order to ionize and monitor the population of state  $i$ . The frequency of the ionization pulse is chosen so that a single photon can form  $\text{RbCs}^+$  ions from state  $i$  but not from the ground state. We scan the frequency of the dump laser and look for a resonant depletion in the ion signal which should occur when population has been transferred to the ground state.

This method works well but is complicated by the fact that the dump pulse can resonantly drive the  $i$  state population upward to higher lying, spectrally uncharacterized excited levels. Since the ionization pulse may form  $\text{Cs}^+$  and/or  $\text{Rb}^+$  ions from such highly excited states, one can observe resonant depletion of the  $\text{RbCs}^+$  ion signal that does not correspond to ground state molecule production. Integration of the entire ion signal (i.e., monitoring the sum of all the ion mass peaks) does not help since our ion detector has different (and unknown) relative efficiencies for detecting ions of different mass. It is known that the efficiency increases with increasing mass<sup>1</sup> so that one will still see a depletion in the integrated ion signal whenever the lower mass  $\text{Cs}^+$  and  $\text{Rb}^+$  ions are formed. Additionally, the ionization efficiency from these higher lying levels may be lower than from level  $i$ , resulting in a false depletion signal.

We therefore also use a “direct” detection technique that has the advantage of eliminating any spurious resonant ion signals. In this technique, after the dump pulse arrives, the remaining population<sup>2</sup> in the  $i$  state is allowed to spontaneously decay for a duration many times the excited state lifetime. This effectively empties the excited state. Another pulse, the “re-excitation” pulse, which has the same frequency as the dump pulse, then drives the stable  $X^1\Sigma^+(v = 0, 1)$  molecules back to state  $i$  where they are ionized by the ionization pulse. We monitor the  $\text{RbCs}^+$  ion signal as we scan the identical dump and re-

---

<sup>1</sup>This information is provided by Burle Industries in the documentation for our ion detector; the general dependence of detection efficiency on ion mass should hold over the range of ion masses used in these experiments.

<sup>2</sup>This fraction will be roughly one half in the case where the dump transition is saturated.

excitation pulse frequency; a resonant peak in this signal must correspond to the detection of stable ground state molecules. The definitive signatures of UPM production (in both detection techniques) are then resonances at the exact frequencies predicted by our earlier spectroscopy of the  $a^3\Sigma^+$  and  $i$  states in combination with spectroscopy done elsewhere on the  $X^1\Sigma^+$  state [55].

## 5.2 Experimental Apparatus

In this section we discuss the various additions and changes made to our experimental apparatus in order to implement the SEP transfer and ground state molecule detection. The vacuum system and MOT optics are the same as described in Chapters 3 and 4. At this stage of our experiments, we measured the atomic density  $n$  and atom number  $N$  to be  $n_{Rb} = 1.4 \times 10^{11} \text{ cm}^{-3}$ ,  $N_{Rb} = 2 \times 10^8$  and  $n_{Cs} = 3.5 \times 10^{11} \text{ cm}^{-3}$ ,  $N_{Cs} = 3 \times 10^8$ .<sup>3</sup> The temperature of both atomic species was  $\sim 75 \text{ } \mu\text{K}$ .

### 5.2.1 Photoassociation and Pulsed Lasers

In order to populate the  $a^3\Sigma^+(v = 37)$  level, our photoassociation laser was tuned to the  $\Omega = 0^-$ ,  $J = 1$  level located  $38.02 \text{ cm}^{-1}$  below the  $\text{Rb } 5S_{1/2} + \text{Cs } 6P_{1/2}$  asymptote. The laser, which was frequency stabilized as discussed in §4.2.2, had an intensity of  $3 \text{ kW/m}^2$ .

The pump laser pulse was generated with a combination of the Sirah dye laser and Raman cell as discussed in Chapter 4; it had a pulse energy of  $\sim 150 \text{ } \mu\text{J}$ . The ionization pulse was also generated as discussed in Chapter 4 and here had a pulse energy of  $750 \text{ } \mu\text{J}$ . In order to generate the pulses for the dump and re-excitation steps, we used an additional tuneable pulsed dye laser (TDL60, Quantel International). This dye laser (the “red” laser) was operated from  $\sim 13500 - 14000 \text{ cm}^{-1}$  ( $\sim 714 - 740 \text{ nm}$ ) and had a spectral linewidth of  $\sim 0.2 \text{ cm}^{-1}$ . The red laser optics and pumping scheme is shown schematically in Figure

---

<sup>3</sup>One may notice that these densities are lower than they were for the photoassociation and ionization experiments. In this experiment, we did not take special care to optimize the MOTs; we will give a justification for this later.



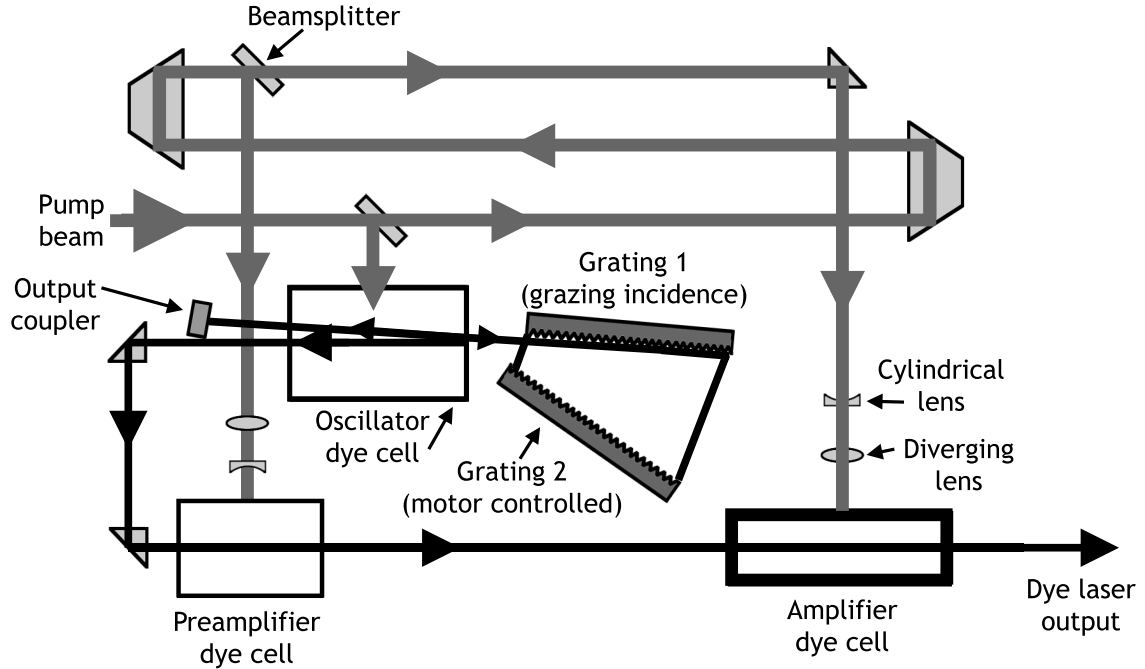


Figure 5.2: Schematic of the TDL60 (“red”) dye laser. The red dye laser optics are shown. The three dye cells (oscillator, preamplifier, and amplifier) are pumped transversely with light from the Nd:YAG laser. The folded paths of the pump beams provide the necessary time delay to optimize the preamplifier and amplifier stages. The oscillator cavity consists of two gratings, one of which is motor controlled and whose orientation determines which frequency of light is directed through the dye gain medium, and a highly reflective output coupler that allows light to exit the cavity via diffraction around one of its edges. Upon exiting the oscillator cavity, the dye laser pulse is directed through the two remaining dye cells where it is amplified.

5.2. The laser has an oscillator and pre-amplifier as well as an additional amplifier stage, each requiring its own dye cell. To pump the three cells, we split off  $\sim 100$  mJ of the Nd:YAG laser, leaving  $\sim 100$  mJ to pump the Sirah dye laser. An uncoated glass plate in the Nd:YAG beam path inside the laser diverts 5% of the light into the oscillator and an achromatic beam splitter diverts 10% into the preamplifier. The rest is used to pump the final amplifier stage. The oscillator cavity of the red laser consists of two gratings with 1800 lines/mm and an output coupler. One grating is oriented at grazing incidence while the other could be rotated by an externally controllable motor for frequency tuning purposes. The output coupler is actually a totally reflecting mirror positioned so that light is coupled out by diffraction around one of its edges. It was necessary to have a lower dye

concentration in the amplifier stage to optimize the output; we found that with roughly a factor of 5 reduction in concentration compared with that used for the oscillator and pre-amplifier stages, we generated an output pulse energy as high as 5 mJ at  $\sim 720$  nm. We only used a small fraction of this, typically 20  $\mu J$ , for each of the dump and re-excitation pulses. The pulse energy sent to the experiment was controlled using a variable beam splitter consisting of a Glan-Thompson polarizer and  $\lambda/2$  waveplate. All the pulsed beams had a diameter of  $\sim 3$  mm.

### 5.2.2 Pulsed Laser Timing

In order to properly time the arrival of the various laser pulses, it was necessary to insert multiple delay paths in the beam lines. A schematic of these delay paths is shown in Figure 5.3. The Nd:YAG (532 nm green) light used to pump the red laser was split from that used to pump the Sirah laser by a variable beam splitter (like the one described in §5.2.1), placed directly in front of the Sirah laser’s input. This beam was then sent along a  $\sim 3$  m delay path by passing it three times over a 1 m distance using two horizontally offset  $180^\circ$  turning prisms. We then sent the beam through another variable beam splitter; most of this light was split off and sent directly to pump the red laser. The rest was sent through a  $\sim 4$  m delay path generated like the one above except with the turning prisms placed slightly farther apart. This beam was then combined with the output of the red laser on a dichroic mirror. The combined red and green beam was then sent through a 50-50% beam splitter. The first half was sent into the vacuum chamber; the red component was used for the dump pulse while the green was used for the ionization pulse in ion dip detection. The second half of the split two color beam was coupled into a 22 m long 550  $\mu m$  core multimode fiber (3M, FG-550-LER TECS).<sup>4</sup> The output of this fiber, which was delayed with respect to the first half of the split beam by 110 ns, was then collimated with a lens and sent into the vacuum chamber; the red component was used for the re-excitation pulse

---

<sup>4</sup>The large core was necessary due to the high instantaneous power of our pulsed lasers; it allows the beam to be relatively large inside the fiber and thus less intense, allowing one to couple in more power without damage.

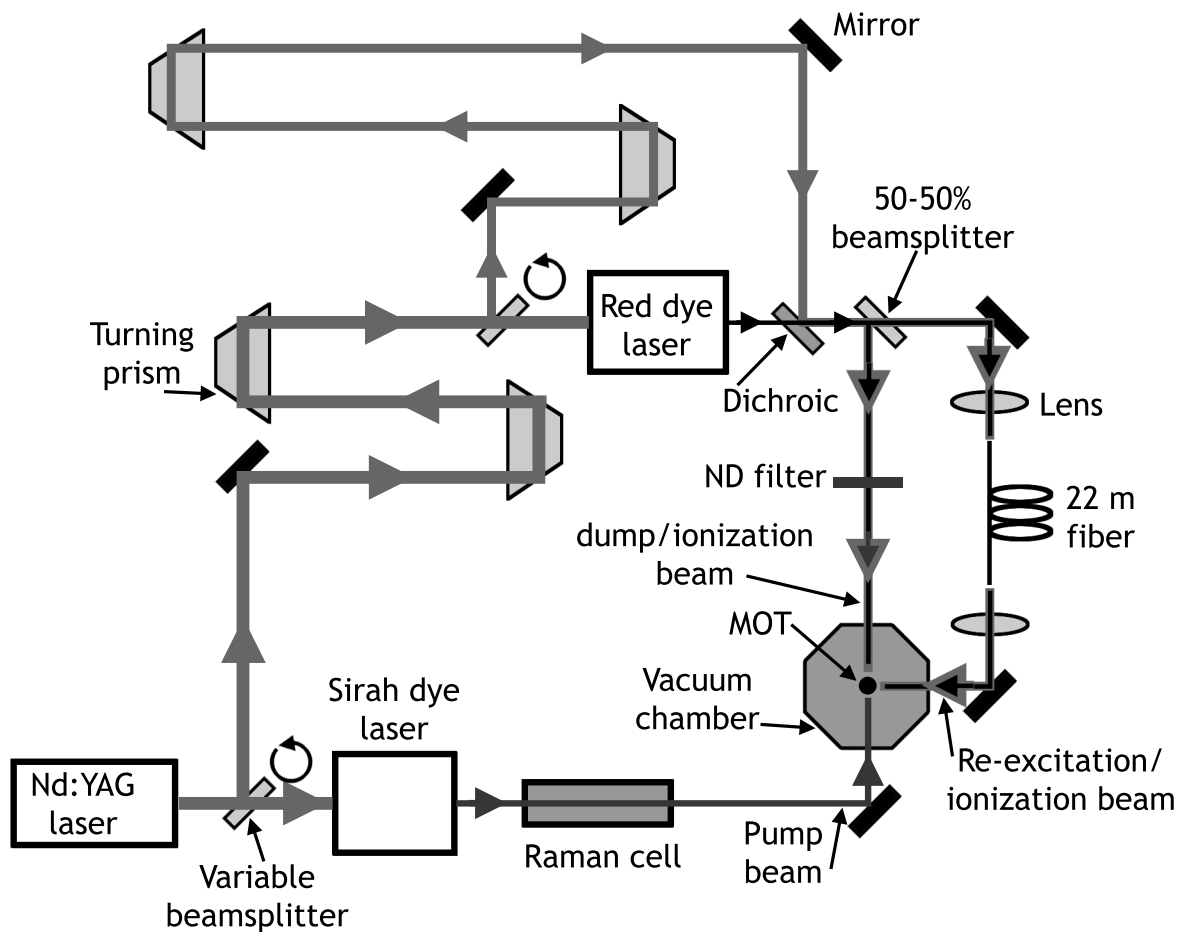


Figure 5.3: Schematic of optical setup for SEP and detection beams. The optics used to generate the various beams required for SEP and ground state molecule detection are shown. The turning prisms are used to delay the arrival at the center of the vacuum chamber of the dump pulse with respect to the pump pulse and to delay the arrival time of the ionization pulse with respect to the dump and re-excitation pulses. The 22 m long fiber serves to delay the arrival of the re-excitation pulse with respect to the dump pulse. See text for full description.

and the green was used for the ionization pulse in the direct detection method. Typical efficiencies through the fiber were 60% and 30% for the green and red beams, respectively; the difference was the result of the superior mode quality of the Nd:YAG light. We found we could send roughly 4 mJ of light into the fiber before damaging its input end, which merely required re-cleaving it. The pump pulse was sent into the vacuum chamber along the same direction but counter propagating to the dump pulse. We measured the arrival times of the various pulses with a fast photodiode (Thorlabs, DET210) and a fast oscilloscope triggered by the Nd:YAG electronic output trigger signal. The photodiode was placed where the pump pulse entered the chamber (and where the dump and first ionization pulse exited). By measuring the distance from that point to the center of the chamber, we inferred the pulse arrival times at the location of the molecules. The dump pulse arrived 10 ns after the pump pulse, and the first ionization pulse arrived 13 ns after the dump. The re-excitation pulse and the second ionization pulse (also separated in time by 13 ns) arrived over 100 ns later.

To switch between the two detection methods, a dichroic mirror which passes red light and reflects green light was placed in the path of the combined dump/first ionization beam right before the beam entered the chamber. This mirror was mounted on a “flip-up” mount so that it could be easily rotated in and out of the beam line. Ion dip detection was done with the mirror rotated out and with the multimode fiber output blocked. Direct ion detection was done with the fiber output unblocked and the dichroic mirror rotated in so that the first ionization pulse would not enter the chamber. Also for direct detection, we placed a neutral density filter in the beam path of the first half of the split red and green beam; we used filters of various optical density to adjust the ratio between the dump and re-excitation pulses.

For direct detection, we initially observed a background on our ion signal due to off-resonant excitation of *a* state molecules by the red laser and subsequent ionization by the ionization pulse. To remove this background (which added undesirable noise), we subtracted the signal with and without the pump pulse by placing a shutter in the pump

beam path and chopping the beam off every other shot; the data processing required to do the subtraction is identical to that discussed in §4.2.4. No background subtraction was done for ion dip detection.

### 5.2.3 Data Acquisition

In order to acquire and process the ion signal as a function of the red laser frequency, we used a very similar method to that discussed in §4.2.4. The main differences stemmed from the fact that we were tuning the red laser, not the Sirah dye laser. The red laser lacked the convenient input and output triggers possessed by the Sirah, as well as a triggered scan program to step its frequency. Additionally, this laser (which was an older piece of equipment that was graciously lent to us by another group<sup>5</sup>) was designed to be controlled by software running on a computer with a 286 MHz processor and a DOS operating system. In order to use the same basic data acquisition system we had used previously, our task was to generate something to mimic both the Sirah's triggered scan program and the Sirah's output trigger signal.

The 286 computer program is designed to receive a string containing a command to move the laser frequency to a specified value. This can be done through the serial port of the 286 computer which allowed us to use our Labview program to scan the laser frequency by sending out the appropriate command strings on the serial port of the data acquisition computer. When the 286 computer receives a command, it writes a return string out on its serial port which we send to the read input of the data computer's port where it can be read into our Labview program. We use the return string as a signal that the laser has begun moving. Our program detects that a string has been sent and then, after a fixed time delay (which is chosen to be long enough to be certain that the laser has stopped moving), creates an internal logical HIGH signal that is used to gate on the counting of the Nd:YAG trigger pulses. Once the counter reaches the value specified by the number of desired shots (or averages) taken at each frequency point, the internal logic signal is set to LOW where

---

<sup>5</sup>R. Hilborn at Amherst College.

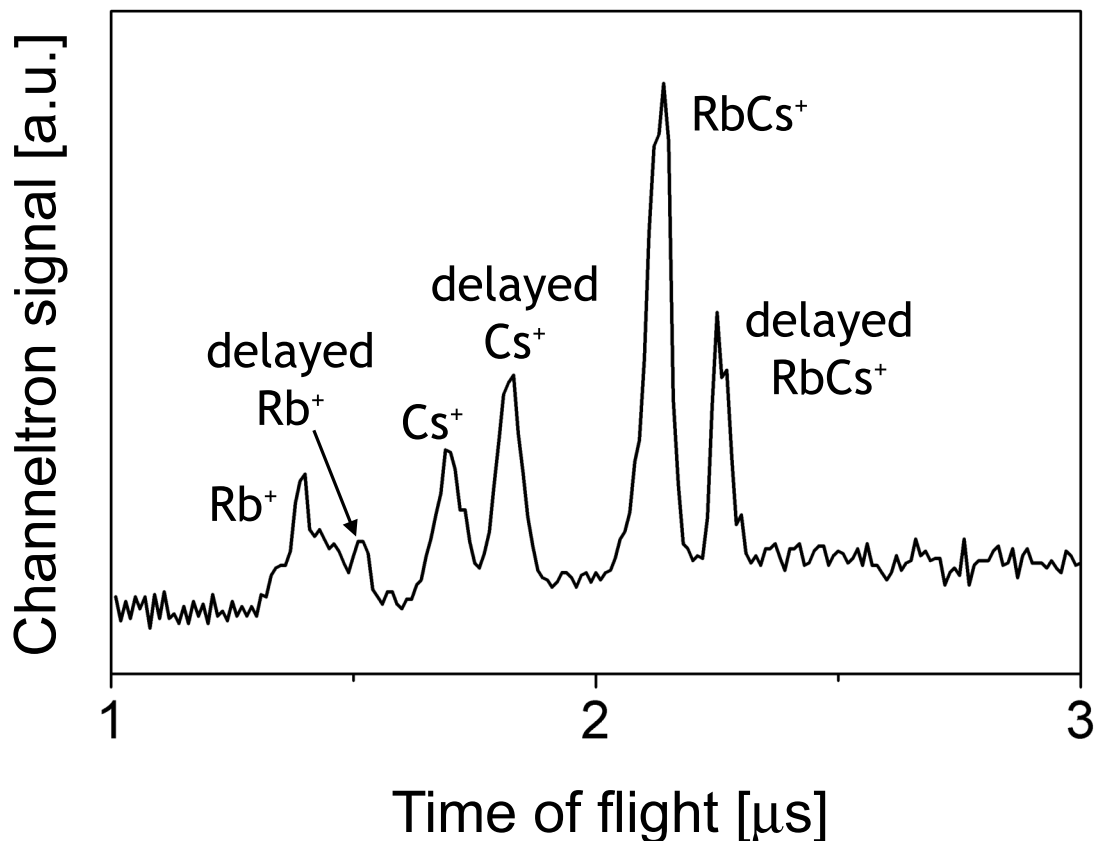


Figure 5.4: Time of flight signal for direct ion detection. A typical time of flight mass spectrum is shown illustrating direct detection of  $X^1\Sigma^+(v=0)$  molecules. The ion signal is averaged over 200 shots. The delayed  $\text{RbCs}^+$  peak signifies ground state molecule production.

it remains until the 286 computer sends out the next return signal, signifying that the laser has moved to the next frequency point. The data processing in these experiments is identical to that discussed in §4.2.4 except that there are additional integration windows that are used to process the signal coming from the delayed re-excitation ion mass peaks. A typical time of flight signal obtained using the direct detection method is shown in Figure 5.4. For clarity, we allowed some light from the first ionization pulse into the chamber so that one can see both the delayed and undelayed ion peaks.

The 286 computer needed to be calibrated so that the frequency entered into the computer corresponded to the frequency to which the laser was moved. There is supposedly a means to do this by entering a single independently measured frequency point (measured

using a wavemeter) into the 286 that it would use to calibrate itself. However, we found this calibration to be off by many nanometers. We therefore calibrated the red laser ourselves by entering a series of frequency values into the 286 and measuring the red laser output with a wavemeter. Plotting the entered 286 computer frequency versus the measured frequency and fitting a line to the data (which fit well, implying the relation was linear), we obtained two calibration constants (slope, y-intercept). These constants were entered into our Labview program and were used to determine the appropriate frequency command to send to the 286 computer.

We typically took individual scans of the red laser frequency over a  $\sim 4 \text{ cm}^{-1}$  range. We measured each scan's endpoint frequencies on a wavemeter with  $0.05 \text{ cm}^{-1}$  accuracy and used interpolation to determine the other frequency points with similar accuracy. We typically used a frequency step size of  $0.2 \text{ cm}^{-1}$  (comparable to the red laser linewidth) and we did 50 or 100 averages for each point, depending on the signal to noise in the experiment on a particular day.

### 5.3 Ion Dip Detection Diagnostic

When we first began trying to produce and detect  $v = 0$  molecules, we used the ion dip detection method because of its relative experimental simplicity and, perhaps more importantly, because the idea of direct detection had not yet occurred to us. We tuned the pump laser frequency to resonance with several excited states,  $i$ , and looked for an ion signal depletion as we scanned the dump frequency around the values predicted to be resonant with the  $v = 0$  and 1 ground states. We saw no such depletion despite the fact that our dump pulse energy, together with the predicted Franck-Condon factors for stimulation, should have been large enough. At a loss for what else to try, we attempted to observe an ion signal depletion using the Rb atoms, which have well-known level positions and transition strengths, in order to test the detection method itself.

The  $^{85}\text{Rb}$  level scheme is shown in Figure 5.5. We used the pump pulse to drive a

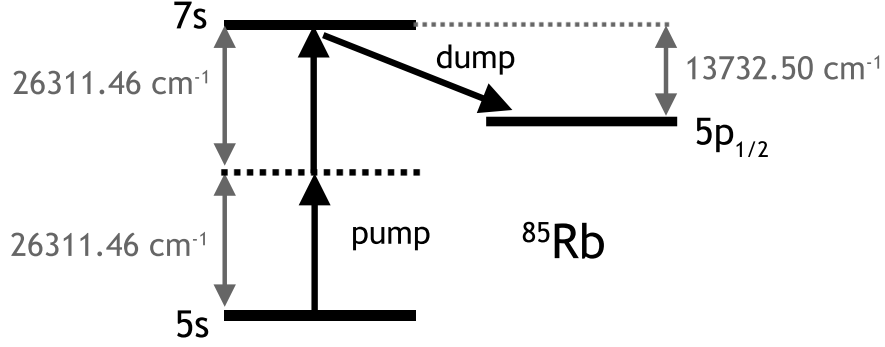


Figure 5.5: Rb level scheme for ion dip detection diagnostic. The  $^{85}\text{Rb}$  levels used to simulate the ion dip detection technique of RbCs molecules are shown. The pump transition is simulated by driving the two photon  $5s \rightarrow 7s$  transition and ionizing the Rb atoms from the  $7s$  state. The dump transition is simulated by driving the single photon  $7s \rightarrow 5p_{1/2}$  transition.

two-photon transition from the  $5s$  ground state to the  $7s$  excited state. Driving a transition between these two levels, split by  $26311.46 \text{ cm}^{-1}$ , required each photon to have a frequency of  $13155.73 \text{ cm}^{-1}$  (or a wavelength of  $760.125 \text{ nm}$ ); this frequency was generated by operating the Sirah laser at  $577.525 \text{ nm}$  and using the first Stokes beam from the Raman cell. The population in the  $7s$  state was monitored by ionizing it with a single photon from the ionization pulse. We searched for depletion in the ion signal by scanning the dump pulse frequency around the value resonant with the transition from the  $7s$  state to the  $5p_{1/2}$  state; this frequency, which is  $13732.50 \text{ cm}^{-1}$  (or  $728.2 \text{ nm}$ ), was generated directly from the red laser. Two  $532 \text{ nm}$  ionization pulse photons are required to ionize the Rb atoms from the  $5p_{1/2}$  state. We therefore turned the ionization pulse energy down until the ion signal from the  $7s$  state began to decrease; in this way, we insured that the weaker two-photon transition from the  $5p_{1/2}$  state would not be driven effectively. We calculated the strength of the  $7s \rightarrow 5p_{1/2}$  transition using the Bates and Damgaard method [51] which gave an estimated saturation energy per unit area for the dump pulse of  $I_{\text{sat}} = 5 \times 10^{-10} \text{ J/mm}^2$ .

When we scanned the red laser with an intensity equal to the saturation intensity through the predicted resonance, we observed no ion signal depletion. This was encouraging with regard to ground state molecule production since it implied that something was wrong



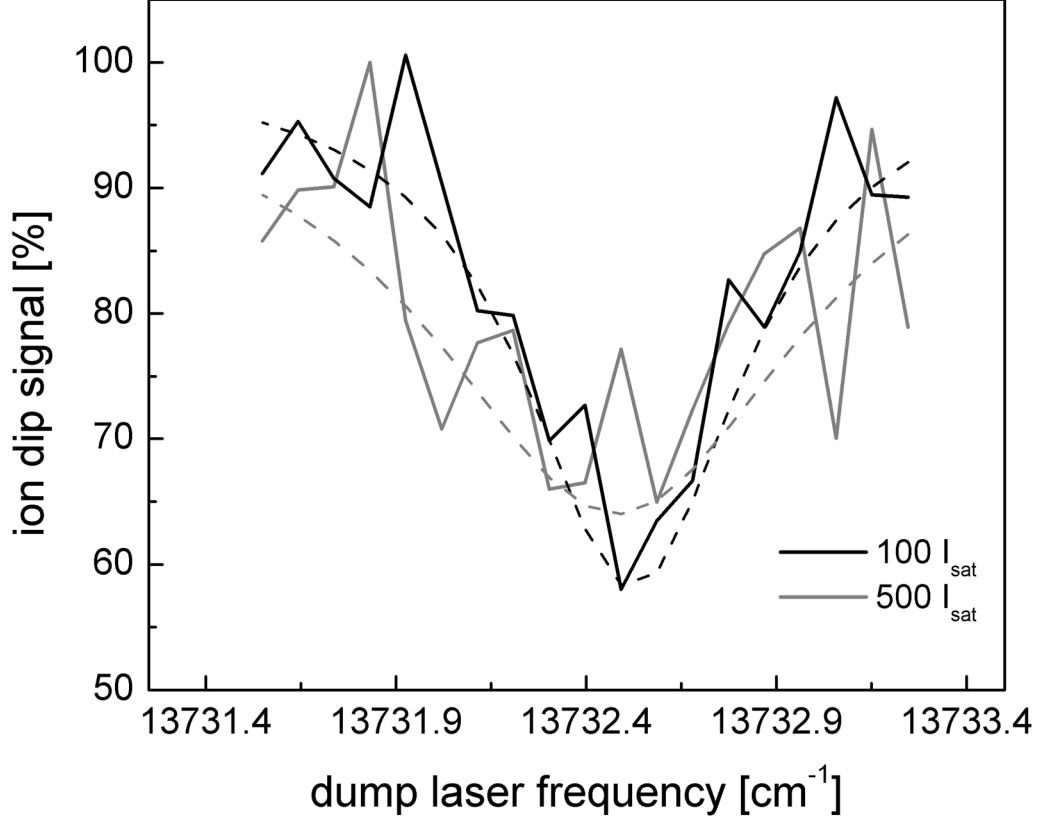


Figure 5.6: Ion dip detection in Rb atoms. Depletion of the Rb ion signal by driving population from the  $7s$  to  $5p_{1/2}$  state is shown for two different dump pulse intensities. The intensities are referenced with respect to the calculated saturation intensity of this dump transition. We observe a maximum depletion of  $\sim 40\%$  at an intensity of  $100I_{sat}$ . At higher intensity, the depletion signal broadens but does not get deeper, as is shown in the trace corresponding to a dump intensity of  $500I_{sat}$ . The dotted curves are fits of the dips to Lorentzian functions; the ratio of the two widths extracted from these fits is  $\sim 2$ .

with our detection and not necessarily with the SEP transfer technique. We decided to check that our ion detector output was responding linearly to changes in the ion input. If it was being heavily saturated, then any depletion in the ion input might not be seen on the output signal. We checked for saturation by measuring the ion signal from the  $7s$  state as a function of ionization pulse energy and found that the signal was flattening out at pulse energies per unit area of only  $\sim 100 \mu\text{J}/\text{mm}^2$ . It is known that the cross section for ionization of Rb atoms is  $\sim 1 \times 10^{-17} \text{ cm}^2$  [83]; from this we calculate that saturation of the ionization step should begin at energies per unit area of  $\sim 500 \mu\text{J}/\text{mm}^2$ .<sup>6</sup> This

<sup>6</sup>The relation between ionization cross section,  $\sigma_{ion}$  and the saturation energy per unit area,  $I_{sat}$ , is

suggested that our detector was being saturated. We turned the detector gain down until the ionization signal became linear as a function of ionization pulse energy; the voltage on the detector was set to  $V_C = -1300$  V, corresponding to an output ion current of  $\sim 20$   $\mu\text{A}$  and a gain of  $\sim 1 \times 10^5$ . To compensate for the resulting decreased signal size, we placed a low noise amplifier (Minicircuits, ZFL500-LN) with a gain of  $\sim 30$  after the transimpedance amplifier connected to the ion detector output. We then scanned the red laser again and observed a small ion dip at the predicted frequency. Increasing the dump pulse intensity to  $100 \times I_{sat}$ , we observed a depletion of up to  $\sim 40\%$ . As we increased the dump pulse energy further, the depletion stayed the same size but the dip broadened, indicating we were saturating the transition. Depletion signals are shown for two different dump intensities in Figure 5.6. The ratio of the widths of the features roughly agrees with a  $\sqrt{I/I_{sat}}$  dependence consistent with power broadening. One would naively expect to see a 50% depletion at the point of saturation since this corresponds to the condition where the population is equally distributed between the two levels of the transition. However, as discussed in reference [84], one should actually expect smaller depletion due to the sparse comb-like spectral structure typical of pulsed lasers with multiple longitudinal modes, like the ones we use. The reason for this is illustrated in Figure 5.7. The longitudinal modes are typically spaced apart in frequency by an amount a few times the size of their spectral width (and the natural linewidth of the transition). Thus, on a given shot of the dump pulse, the probability that the transition is driven even when the peak intensity should be enough to saturate it is roughly equal to the ratio between the mode width and the spacing between modes. When averaging over many shots, as we do in our experiment, this ratio then determines the maximum depletion percentage one should see without deeply saturating and broadening the transition.

This diagnostic of our ion dip detection method was thus extremely valuable; not only did it allow us to diagnose and fix our problem with detector saturation, but it provided insight into what dump pulse intensity was likely to be optimal for detecting depletion in

---

given by  $I_{sat} = h\nu/\sigma_{ion}$ , where  $\nu$  is the energy of the ionization photons.

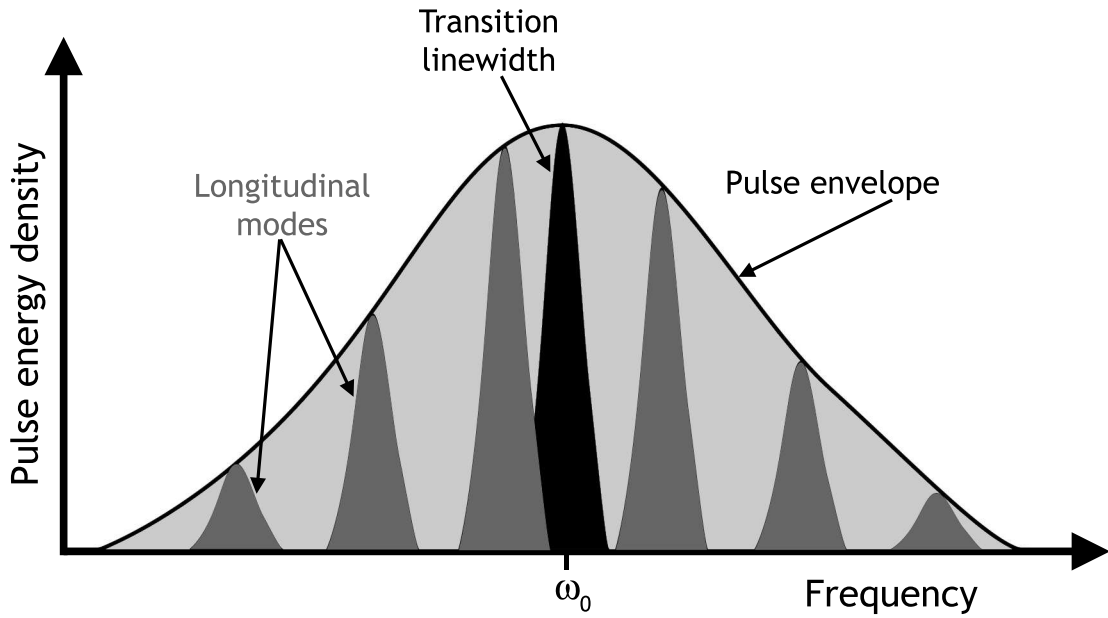


Figure 5.7: Spectral distribution of a pulsed laser with multiple longitudinal modes. The frequency spectrum of a typical laser pulse is shown. If the longitudinal modes are spaced by more than the width of the transition (shown in black), then even if the center of the spectral envelope is tuned to the resonance frequency,  $\omega_0$ , a longitudinal mode will not necessarily be on resonance. Since the absolute position and relative sizes of the longitudinal mode pattern within the pulse envelope jumps around randomly from shot to shot, any signal averaged over many shots will reflect the average overlap of the longitudinal modes with the transition width. If the pulse is so intense that there is always enough power in the wings of the longitudinal modes to saturate the transition, any observed signal will be independent of the shot to shot variations of the longitudinal mode positions. This corresponds to power broadening.

our  $\text{RbCs}^+$  ion signal.

## 5.4 Results of SEP Transfer

### 5.4.1 Observation of Ground State Transfer

With confidence that our ion dip detection method was working, we again tuned the pump laser to resonance with several RbCs excited states,  $i$ , and scanned the red laser around the predicted frequency splittings between those states and the  $X^1\Sigma^+(v=0,1)$  levels. We observed ion signal depletion at the predicted frequencies for many of these levels, indicating transfer to the ground state. The results are shown for three such levels, consecutive in energy, in Figure 5.8. It should be noted that there is an uncertainty in the predicted absolute position of these levels due to the uncertainty in the position of the  $a^3\Sigma^+(v=37)$  level below dissociation; however, the  $49.791\text{ cm}^{-1}$  splitting between the ground state  $v=0$  and  $v=1$  levels is known to a higher accuracy than our experiment can resolve [55]. We are therefore able to compare this well-known value with our measured splitting of the  $v=0$  and 1 features arising from SEP transfer via the same level  $i$ , as a cross-check that our results make sense.<sup>7</sup> As a further cross-check, we can use our measured splittings between features arising from transfer via *different*  $i$  levels since these splittings should be exactly equal to the differences in the pump laser frequencies used to drive the first step of the transfer. We observed transfer to the  $X^1\Sigma^+(v=0)$  ground state via a total of seven  $i$  levels with the ion dip detection technique; this data is summarized in Table 5.1. Some of these levels lie well above the  $B^1\Pi$  state minimum while others lie well below, suggesting that there need not be some particularly fortunate positioning of  $c^3\Sigma^+$  and  $B^1\Pi$  levels to create a large enough mixing to make transfer possible. Rather, the data supports the idea that this transfer technique is quite insensitive to the precise positions of the mixed c/B levels.

As another cross-check of our ion dip detection results, we scanned the red laser over

---

<sup>7</sup>This is the main reason we chose to transfer molecules to the  $v=1$  level.

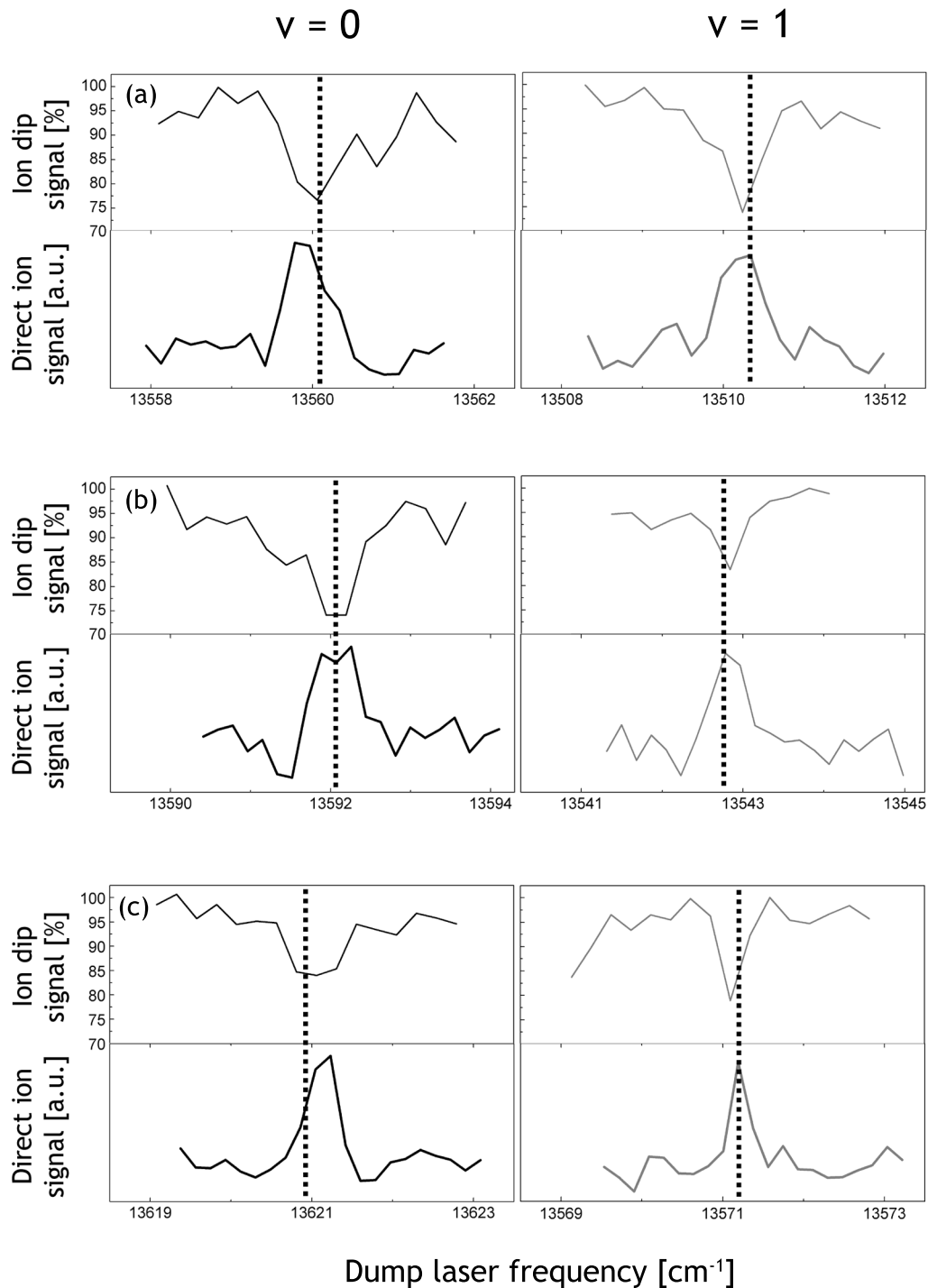


Figure 5.8: Detection of  $X^1\Sigma^+(v = 0, 1)$  molecules. Results are shown for ion dip detection (upper) and direct detection (lower) for three consecutive levels  $i$ , located at energies (a)  $9754.26 \text{ cm}^{-1}$ , (b)  $9786.10 \text{ cm}^{-1}$ , and (c)  $9814.60 \text{ cm}^{-1}$  above the  $a^3\Sigma^+(v = 37)$  state. The dotted lines indicate the predicted locations of the resonant features. All data is averaged over 100 pulses.

Pump frequency [cm <sup>-1</sup> ]	Dump frequency (to $v = 0$ ) [cm <sup>-1</sup> ]	Measured $v = 0 - 1$ splitting [cm <sup>-1</sup> ]	$v = 0$ peak deviation [cm <sup>-1</sup> ]
9754.26	13596.93	49.8	-0.03
9786.10	13592.16	49.8	0.24
9814.60	13620.56	50.0	0.14
9843.46	13649.46	*	0.17
10042.96	13848.79	49.9	0
10232.06	14037.85	49.9	-0.04
10258.34	14064.33	49.8	0.14

Table 5.1: Summary of observed ion dip resonances. The seven levels  $i$  from which we observed depletion due to transfer to the  $X(v = 0)$  state are shown. The first column gives the location of the  $i$  levels above the  $a^3\Sigma^+(v = 37)$  state. The second column gives the dump frequency for which we observed the depletion. For all  $i$  levels except for the one marked with “\*”, we also observed depletion due to transfer to the  $v = 1$  state. For these levels, the measured  $v=0-1$  splitting is given and should be compared with the known value of 49.8 cm<sup>-1</sup>. The final column lists the deviation of the  $v=0$  peak location from the value expected from our measured splittings of the  $i$  levels; here we have arbitrarily used the  $v = 0$  feature corresponding to the  $i$  level at 10042.96 cm<sup>-1</sup> to define the absolute positions. Using a different reference does not qualitatively affect the agreement. The uncertainty in all values listed in the final two columns is estimated to be  $\sim 0.3$  cm<sup>-1</sup>, dominated by the widths of the observed features.

the regions between the observed  $v = 0$  and 1 features hoping to find no other instance of depletion. This would clearly suggest that our data was not an artifact of some other effect. However, as mentioned in §5.1, we observed many depletion features in these regions; a typical example of this is shown in Figure 5.9. This density of depletion features made us worry that the features we associated with ground state UPM production might be due to the multi-photon excitation processes discussed in §5.1; these results were certainly cause for skepticism.

At this point, we developed and implemented the direct detection method. We chose to do the SEP transfer via three  $i$  levels that we had used to observe ground state production with the ion dip detection technique. We scanned the red laser through the predicted frequency required for transfer. The results of the direct detection are shown in Figure 5.8, where one can see that peaks in the ion signal appear at the predicted locations. In addition, these peaks are located precisely where we observed the ion dips; the data from the two detection methods is therefore consistent, which suggests that the ion dip

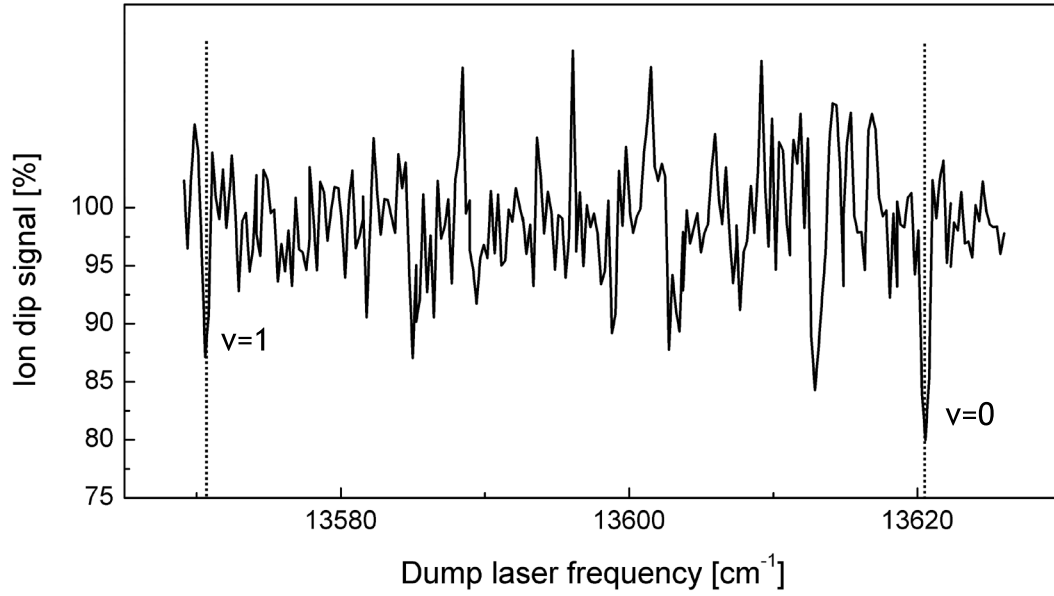


Figure 5.9: Scan between  $v = 0$  and 1 resonances using ion dip detection. A scan of the dump frequency over the entire region between the  $v = 0$  and  $v = 1$  features using ion dip detection is shown; the pump pulse is resonant with the  $i$  level at  $9814.60 \text{ cm}^{-1}$  above the  $a^3\Sigma^+(v = 37)$  state. In addition to the observation of dips corresponding to dump driven transitions to  $X(v = 0, 1)$  at the predicted locations (dotted lines), we observe several other dips. We also observe peaks in the signal which result from ionization of  $a$  state molecules being resonantly driven to some intermediate state by the dump laser. The data is averaged over 100 shots.

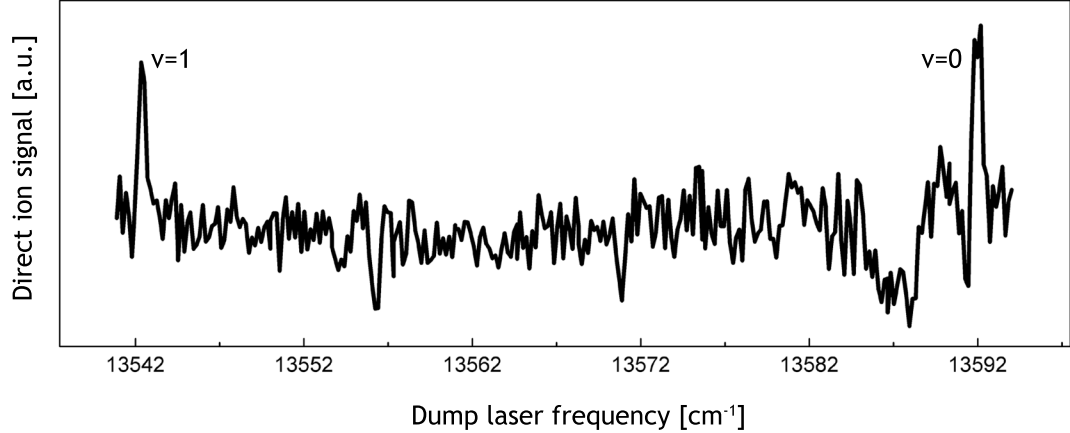


Figure 5.10: Scan between  $v = 0$  and  $1$  resonances using direct detection. A scan of the dump frequency over the entire region between the  $v = 0$  and  $v = 1$  features using direct detection is shown; the pump pulse is resonant with the  $i$  level at  $9786.10 \text{ cm}^{-1}$  above the  $a^3\Sigma^+(v = 37)$  state. We observe no additional features like those seen in Figure 5.9. The data is averaged over 100 shots.

features are indeed due to ground state UPM production. Furthermore, we scanned the red laser over the region between the  $v = 0$  and  $1$  features and, employing the direct detection method, we observed no other peaks in the ion signal. These data, which are shown in Figure 5.10, unambiguously show that we are producing RbCs molecules in the  $X^1\Sigma^+(v = 0)$  state. As a final cross-check, we attempted to do the SEP transfer via an excited  $\Omega = 0$  component of a mixed  $c^3\Sigma^+/b^3\Pi$  level, which should not couple to the singlet ground state. As expected, we observed no evidence for ground state molecule production.

#### 5.4.2 Properties of the Ground State Molecular Sample

Our sample of  $X^1\Sigma^+$  molecules is of high purity with respect to the vibrational degree of freedom. The states  $i$  used in the SEP transfer have predominantly  $c^3\Sigma^+$  character; as a result the probability of spontaneous emission into any  $X^1\Sigma^+$  levels during the transfer is very small. Using our analysis of the excited state level mixing, we calculated branching ratios for such spontaneous decay. While these calculations are only qualitative due to our incomplete knowledge of the relevant state wavefunctions, they show that the total population in all other  $X$  state vibrational levels is only  $\sim 1\%$  of the population we stimulate



into the  $v = 0$  level. There is a substantial background of molecules remaining in  $a^3\Sigma^+$  levels following the transfer; however, we have developed (though, not yet experimentally demonstrated) a scheme to remove this background by exploiting the difference in dipole moments between the deeply bound polar  $X^1\Sigma^+(v = 0)$  molecules and the weakly bound  $a$  state molecules which have vanishingly small polarity [20]. This scheme will be discussed briefly in Chapter 6.

The rotational and hyperfine state distribution of the  $X^1\Sigma^+(v = 0)$  molecules is determined by selection rules and the spectral resolution of our lasers. The hyperfine structure is unresolved in all stages of the ground state UPM production process and the nuclear spin degrees of freedom are therefore unconstrained. Even though the rotational structure is also unresolved due to the spectral width of our pulsed lasers, we can nonetheless determine which rotational states our  $v = 0$  molecules may populate. We photoassociate to a  $J = 1$  level of an  $\Omega = 0^-$  state; this level has even parity.<sup>8</sup> The three subsequent photons involved in the transfer to the  $X$  state (one in spontaneous emission and two in the SEP process) must leave the molecule in an *odd* state of parity and can add up to a maximum of three units of angular momentum. The parity,  $P$ , of rotational levels in the  $X^1\Sigma^+$  state is given by the rule  $P = (-1)^J$ ,<sup>9</sup> which suggests that only  $J = 1$  and 3 could be populated. However, the molecule could potentially acquire rotational angular momentum from the nuclear spins if the rotational and nuclear angular momenta are coupled. The 7/2 and 5/2 nuclear spin of Cs and Rb atoms, respectively, and the three units of angular momentum coming from the emission and SEP photons can add up to a maximum angular momentum

---

<sup>8</sup>The parity refers to whether or not the total (electronic, vibrational, and rotational) molecular wavefunction changes sign under reflection of all its coordinates through the origin. Such a reflection can be seen to consist of two transformations; the first is a reflection of all particles through a plane perpendicular to the internuclear axis and passing through its center, and the second is a reflection of the electrons through a plane containing the internuclear axis. Clearly, the vibrational wavefunction cannot change under either of these transformations since it must only depend on the relative separation of the nuclei. The electronic wavefunction cannot change in the first transformation because the electron positions are not being altered with respect to the nuclei; however, in the second transformation, the electronic wavefunction must change sign because it is a  $0^-$  state. The sign of the rotational wavefunction under a parity transformation is given by the usual  $(-1)^J$  rule which comes from the properties of the spherical harmonics. Thus, the parity,  $P$ , of an  $\Omega = 0^-$  state is given by  $P = (-1)^{J+1} = +1$  for  $J=1$ .

<sup>9</sup>See previous footnote and note that instead of a  $0^-$  state we have a  $\Sigma^+$  state which has the opposite symmetry with respect to reflections through a plane containing the internuclear axis. Thus, the total parity is given by  $P = (-1)^J$ .

of 9, resulting in the potential population of the  $J = 1, 3, 5, 7, 9$  rotational states.

We derive a bound on the range of populated rotational levels from the absence of large shifts of the observed resonances from the predicted absolute locations of the  $J = 1$  lines. Our observations deviate by at most  $0.3 \text{ cm}^{-1}$  from these predictions, which have an uncertainty of  $\pm 0.6 \text{ cm}^{-1}$  arising from the uncertainty in the position of the  $a^3\Sigma^+(v = 37)$  level below dissociation; the maximum possible deviation is therefore  $0.9 \text{ cm}^{-1}$ . We calculate the dump frequencies needed to transfer molecules from all potentially populated rotational levels of a particular  $c$  state to all accessible rotational levels in the ground state; to do this we use the known  $X^1\Sigma^+(v = 0)$  rotational constant of  $B_{v=0} = 0.017 \text{ cm}^{-1}$  [55] and our estimation of the particular  $c$  state rotational constant (obtained from the level's classical outer turning point). From this calculation we find that, although the spread of frequencies can be narrow because the excited and ground state rotational constants are not very different, the maximum  $0.9 \text{ cm}^{-1}$  deviation of our observations from prediction precludes population of any ground state rotational level greater than  $J = 7$ ; thus we conclude that at most,  $J=1,3,5$ , and  $7$  can be populated. However, the spectral width of the dump pulse and re-excitation resonances suggest an even narrower distribution. A typical dump transition linewidth of  $0.18 \text{ cm}^{-1}$ , calculated by subtracting our laser linewidth from the  $0.27 \text{ cm}^{-1}$  measured resonance width in quadrature, agrees well with the predicted  $0.17 \text{ cm}^{-1}$  splitting between the  $J = 1$  and  $3$  levels. This suggests that the coupling between the rotation and nuclear spin is weak and that only the two  $J = 1$  and  $3$  rotational levels are populated.

As discussed in §4.3.3, the temperature of the  $a^3\Sigma^+$  molecules was measured to be  $\sim 100 \text{ } \mu\text{K}$  and the scattering of two photons necessary to transfer the molecules to the  $X$  state should cause negligible heating. We were initially concerned that the pulsed lasers could heat the molecules due to spatially varying AC-Stark shifts arising from the inhomogeneity in intensity of the laser beam profile; that is, deep potentials capable of substantially accelerating the molecules might be created. However, the most conservative calculations of these AC-Stark shifts (assuming a laser detuning less than the laser linewidth

and unity Franck-Condon factors) show these potentials to be shallow enough to not cause significant heating. We thus conclude that our sample of  $X^1\Sigma^+(v=0)$  state molecules has a translational temperature of  $\sim 100 \mu\text{K}$ .

### 5.4.3 UPM Production Rate

The efficiency of the SEP process is  $\sim 13\%$ . This is obtained from the measured  $\sim 25\%$  dump efficiency (determined from the size of the ion signal depletion) and inference of a 50% pump efficiency, due to our observed saturation of the pump transition.<sup>10</sup> We detect, on average,  $\sim 1$  ion per pulse with the re-excitation detection technique; since our pulsed lasers operate at 10 Hz, we detect a total of  $\sim 10$  ions/s from the  $X^1\Sigma^+(v=0)$  state.

We measure a  $\sim 25\%$  efficiency for the re-excitation step by comparing the number of ions observed via direct detection with the number of ions detected from the  $i$  state before the SEP process. This re-excitation efficiency is consistent with the measured dump efficiency, as it should be, considering we are driving an identical transition with an identical laser. Using the above re-excitation efficiency and assuming a 5% efficiency for the ionization step (see §4.3.4), we estimate a production rate of  $\sim 8 \times 10^2$  UPMs/s. Again, we must emphasize that there is considerable uncertainty in both the channeltron gain and the ionization efficiency, so that this rate is only really known up to an order of magnitude.

We can compare this production rate with that predicted from our estimate of the number of  $a^3\Sigma^+(v=37)$  molecules we form via photoassociation, and our assumed SEP transfer efficiency and rate. After scaling for the lower MOT densities in this experiment compared with the  $a$  state molecule detection experiment (there is a factor of  $\sim 12$  difference in density product,  $n_{Rb} \times n_{Cs}$ , resulting in a 12 times lower photoassociation and  $a$  state molecule production rate), we find a predicted UPM production rate of  $\sim 5 \times 10^2 \text{ s}^{-1}$ , which roughly agrees with the value calculated above.

---

<sup>10</sup>Note that this efficiency does not include the fact that we drive only 1/20 of the total population in the  $a^3\Sigma^+(v=37)$  level in the pump step.

## 5.5 Summary

We have demonstrated the production of ultracold polar RbCs molecules in the  $X^1\Sigma^+(v=0)$  absolute ground state at rates on the order of 500 molecules/s. The resulting sample has a temperature of  $\sim 100\ \mu\text{K}$  and is spread over a narrow distribution of rotational levels. The main focus of this work was to demonstrate the technique of UPM production and thus emphasis was not placed on maximizing the production rate; hence we did not concern ourselves with restoring the MOT densities to their optimal values in the last stage of the experiment. In the next chapter, we will discuss improvements to the technique demonstrated here that we predict can result in higher production rates of even colder samples of molecules in a single rotational level.

## Chapter 6

# Conclusion

To summarize, we have produced a sample of RbCs UPMs in their absolute vibrational ground state. The population of this state ensures that these molecules are stable with respect to inelastic collisions. Although we did not explicitly measure the  $X^1\Sigma^+(v = 0)$  state dipole moment, it has been calculated to be  $\sim 1.3$  Debye using techniques of demonstrated reliability for other bi-alkali species [85, 20]. We began with laser cooled Rb and Cs atoms in a dual species dark SPOT. We then used photoassociation to an  $\Omega = 0^-$ ,  $J = 1$  level and subsequent spontaneous decay in order to populate the  $a^3\Sigma^+$  triplet ground electronic state. We transferred a fraction of the molecules in the most populated ( $v = 37$ ) vibrational level of the  $a$  state to the  $X^1\Sigma^+(v = 0)$  ground state, via a pulsed stimulated emission pumping technique. This optical method of UPM production resulted in a sample with a translational temperature of  $\sim 100$   $\mu$ K. This method should be quite general. Mixing of the  $c^3\Sigma^+$  and  $B^1\Pi$  levels, as well as the favorable location of the classical turning points of the potential curves, is present in all heteronuclear alkali dimers [86]. Although the spin-orbit interaction necessary for the mixing increases with the mass of the molecules [87], it may be sufficiently large for even the lightest heteronuclear bi-alkalis. Also, the SEP transfer is fairly insensitive to the particular vibrational levels used in the process (considering that we observe transfer for a number of excited levels) and completely insensitive to the molecular temperature. Thus, higher phase-space densities of

UPMs could be produced by photoassociating colder atoms or by starting with molecules formed by Feshbach resonance in a single  $a^3\Sigma^+$  level [88, 89, 90].

We imagine several improvements to the experiments described in this thesis. By using transform-limited laser pulses, we could replace the SEP transfer with a stimulated Raman adiabatic transfer (STIRAP) technique; as a result the  $a(v = 37)$  to  $X(v = 0)$  transfer efficiency could approach 100%. The transform-limited laser pulses, with their narrow spectral width, would be able to resolve the rotational structure in the transfer steps, allowing us to populate a single rotational level in the ground state.

The spread of the molecular population over hyperfine levels, which are completely unresolved in these experiments, could potentially be controlled by using samples of spin polarized atoms and photoassociating to a hyperfine resolved  $\Omega = 1$  level. Using the narrow band pulsed lasers discussed above, one could then resolve the hyperfine structure of the  $a$  and  $c$  states and thus transfer the molecules to a single hyperfine/rotational component of the  $X^1\Sigma^+(v = 0)$  state.

Colder samples of molecules can be produced by implementing a stage of polarization gradient cooling of the MOTs, which requires the ability to quickly turn off the magnetic field used to trap the atoms. This is because the Zeeman shifts induced in the atoms from the field tend to ruin the coherence between the magnetic sublevels, resulting in a decreased cooling efficiency. In our current setup, we (unwisely) wound our magnetic field coils around aluminum mounts which sustain substantial eddy currents when we attempt to turn off the field. By using stainless steel mounts with higher resistance, these currents can be made negligible. Not only would colder atoms result in a colder molecular sample, but they would increase the unitarity-limited photoassociation cross section, and result in a higher UPM production rate.

Currently, the molecules we produce are unconfined and fly away once they are formed. We believe that we can produce substantial samples of UPMs by trapping them in a far-detuned optical trap, such as the quasi-electrostatic trap (QUEST) [91]. The QUEST is generated by focusing a red-detuned,  $10.6\ \mu\text{m}$   $\text{CO}_2$  laser such that atoms and molecules

are attracted to and are trapped in the region of highest intensity. Tight confinement along the beam propagation direction can be achieved by retro-reflecting the beam so that a standing wave is created, resulting in a one-dimensional optical lattice. We envision loading the QUEST with atoms from the MOTs and then performing the photoassociation and the ground state transfer steps in the trap. Loading of  $\sim 10^6$  atoms into a QUEST has been observed [92]. In addition, high atomic densities and low temperatures are achievable in the QUEST (densities as high as  $3 \times 10^{13} \text{ cm}^{-3}$  and temperatures as low as  $15 \text{ } \mu\text{K}$  have been obtained [92]), which will result in larger photoassociation rates than those observed in the experiments discussed in this thesis. However, it should be pointed out that the loss rates from the QUEST due to molecule-atom and molecule-molecule collisions also increase for higher density and lower temperature. As a result, the number of molecules collected in the trap, which depends on the ratio between the rates of molecule production and trap loss, will not necessarily increase with a larger photoassociation rate. Recent experiments have observed near-unity limited molecule-atom collisional trap losses between Cs atoms and  $\text{Cs}_2$  molecules trapped in a QUEST [93, 94]. Assuming that the loss rates for RbCs are comparable and that photoassociation in the QUEST proceeds at the unitarity limited rate, we expect  $\sim 50\%$  of the RbCs molecules formed in the  $a^3\Sigma^+(v=37)$  state to remain trapped and to be available for transfer to the ground state by the STIRAP pulses. Given the number of atoms that can be loaded into the QUEST before photoassociation, and the ground state transfer efficiency, we expect to produce a sample of  $\sim 3 \times 10^4$  trapped molecules in the  $X^1\Sigma^+(v=0)$  state in a single rotational level.

As mentioned in §5.4.2, we have developed a scheme to remove the substantial background of  $a^3\Sigma^+$  molecules (as well as any weakly bound  $X^1\Sigma^+$  state molecules) that will unavoidably accumulate in the QUEST as a result of  $X^1\Sigma^+(v=0)$  molecule production. This scheme is illustrated in Figure 6.1. The molecules are produced in the QUEST which is oriented so that the one-dimensional optical lattice is along the direction of gravity. Two cylindrical electrodes are placed on either side of the QUEST trap just above the trap focus.

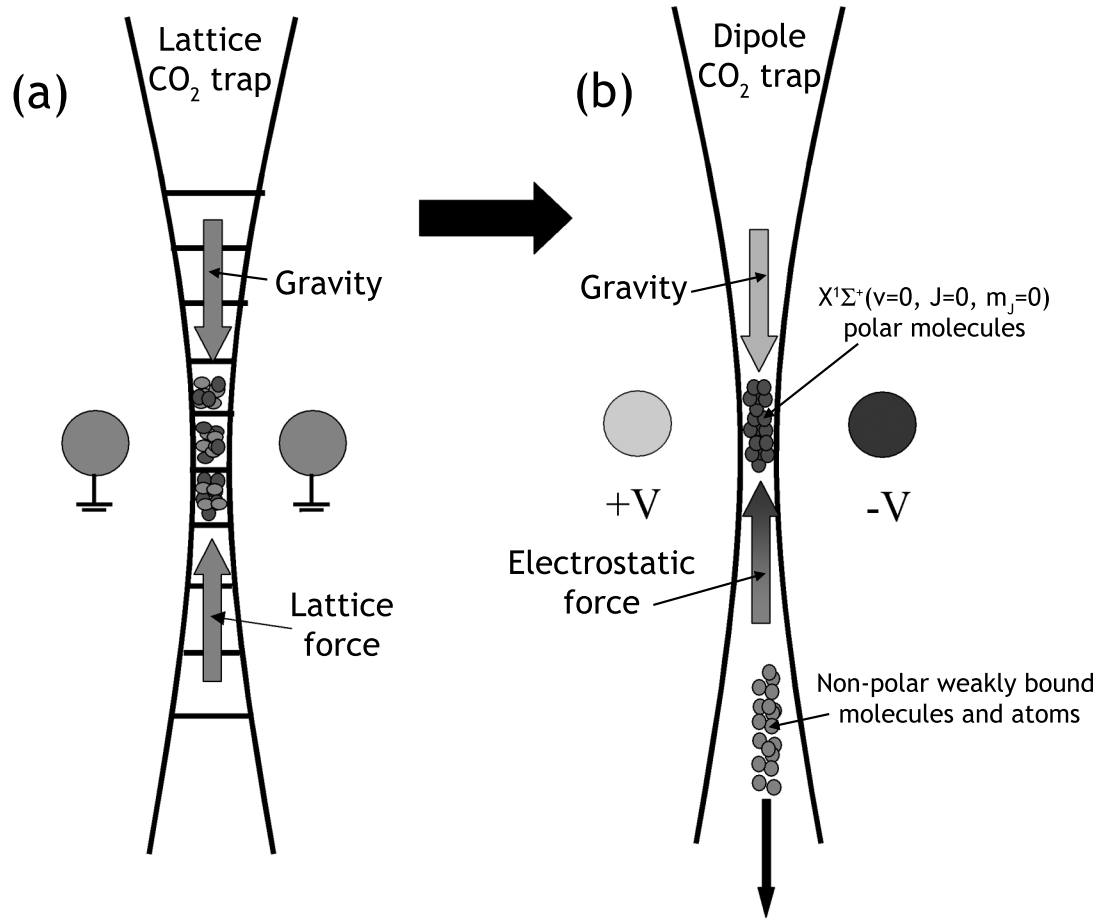


Figure 6.1: Scheme for purifying the  $X^1\Sigma^+(v = 0)$  molecular sample in a QUEST. (a) Deeply bound, polar  $X^1\Sigma^+(v = 0)$  molecules, as well as non-polar atoms and weakly bound molecules are trapped in a one dimensional lattice QUEST. (b) An electric field gradient is turned on and the QUEST is converted from a lattice to a dipole trap. Only the polar, strong field seeking  $X^1\Sigma^+(v = 0, J = 0, m_J = 0)$  molecules are held against gravity due to the electrostatic force; all non-polar species and low-field seeking state molecules leave the trap leaving a pure sample of ground state UPMs.



By applying voltages of  $\pm V$  on the electrodes, an electric field gradient is created which exerts a force on the polar molecules in the strong field seeking  $J = 0$ ,  $m_J = 0$  state in the direction opposing gravity. In the presence of the lattice potential, this force is negligible. However, we imagine adiabatically (with respect to the QUEST trap vibrational frequency) changing the QUEST from an optical lattice to an ordinary dipole trap configuration. This can be done by adjusting a waveplate in the path of the retro-reflected CO<sub>2</sub> laser beam to rotate its polarization and eliminate the standing wave. In the ordinary dipole trap configuration, the molecules cannot be held against gravity by the dipole force alone (due to the small beam intensity gradient along the axis of propagation). If the applied electric field gradient is large enough, however, the high field seeking, polar  $X^1\Sigma^+(v = 0, J = 0, m_J = 0)$  molecules can be held against gravity in the vertical dimension by the electrostatic force, and confined in the other dimensions by the QUEST. Any weakly bound molecules, with their vanishingly small polarity [20], will not be held and will thus leave the trap. The optical lattice can then be turned back on and the electric field gradient turned off, resulting in a pure, trapped sample of deeply bound, polar  $X^1\Sigma^+(v = 0, J = 0, m_J = 0)$  molecules. Calculations show that only  $\pm 7$  kV is required for the electrode potentials in order to implement this scheme, assuming a standard QUEST trap geometry and the 1.3 Debye dipole moment of  $X^1\Sigma^+(v = 0)$  RbCs molecules; this voltage can be easily applied.

The above improvements are challenging, but all are technically feasible. Efforts are already underway to implement them.

# Bibliography

- [1] T.W. Hänsch and A.L. Shawlow. Cooling of gasses by laser radiation. *Optics Communications*, 13(1):68, 1975.
- [2] D. Wineland and H. Dehmelt. Proposed  $10^{14} \Delta\nu < \nu$  laser fluorescence spectroscopy on  $Tl^+$  mono-ion oscillator III. *Bulletin of the American Physical Society*, 20:637, 1975.
- [3] S. Chu, L. Hollberg, J.E. Bjorkholm, A. Cable, and A. Ashkin. Three-dimensional viscous confinement and cooling of atoms by resonance radiation pressure. *Physical Review Letters*, 55(1):48, 1985.
- [4] E.L. Raab, M. Prentiss, A. Cable, S. Chu, and D.E. Pritchard. Trapping of neutral sodium atoms with radiation pressure. *Physical Review Letters*, 59(23):2631, 1987.
- [5] M. Takamoto, F. Hong, R. Higashi, and H. Katori. An optical lattice clock. *Nature*, 435:321, 2005.
- [6] T. Ido, T.H. Loftus, M.M. Boyd, A.D. Ludlow, K.W. Holman, and J. Ye. Precision spectroscopy and density-dependent frequency shifts in ultracold Sr. *Physical Review Letters*, 94:153001, 2005.
- [7] K. Gibble and S. Chu. Laser-cooled Cs frequency standard and a measurement of the frequency-shift due to ultracold collisions. *Physical Review Letters*, 70:1171, 2003.

- [8] M. Kasevich and S. Chu. Atomic interferometry using stimulated Raman transitions. *Physical Review Letters*, 67:181, 2001.
- [9] K. Davis, M-O. Mewes, M. Andrews, M. van Druten, D. Durfee, D. Kurn, and W. Ketterle. Bose-Einstein condensation in a gas of sodium atoms. *Physical Review Letters*, 75:3969, 2005.
- [10] M.H. Anderson, J.R. Ensher, M.R. Matthews, C.E. Weiman, and E.A. Cornell. Observation of Bose-Einstein condensation in a dilute atomic vapor. *Science*, 269:198–201, 2005.
- [11] D. DeMille. Private communication.
- [12] D. DeMille. Quantum computation with trapped polar molecules. *Physical Review Letters*, 88(6):067901, 2002.
- [13] E. Bodo, F.A. Gianturco, and A. Dalgarno. F+D<sub>2</sub> reaction at ultracold temperatures. *Journal of Chemical Physics*, 116(21):9222, 2002.
- [14] M.A. Baranov, M.S. Mar’enko, Val. S. Rychkov, and G.V. Shlyapnikov. Superfluid pairing in a polarized dipolar fermi gas. *Physical Review A*, 66:013606, 2002.
- [15] A.V. Avdeenkov and J.L. Bohn. Linking ultracold polar molecules. *Physical Review Letters*, 90(4):043006, 2003.
- [16] K. Góral, L. Santos, and M. Lewenstein. Quantum phases of dipolar bosons in optical lattices. *Physical Review Letters*, 88(17):170406, 2002.
- [17] M.G. Kozlov and L.N. Labzowsky. Parity violation effects in diatomics. *Journal of Physics B: Atomic, Molecular and Optical Physics*, 28:1933–1961, 1995.
- [18] J.L. Bohn. Inelastic collisions of ultracold polar molecules. *Physical Review A*, 63:052714, 2001.

- [19] S. Kotochigova, P.S. Julienne, and E. Tiesinga. *Ab initio* calculation of the KRb dipole moments. *Physical Review A*, 68:022501, 2003.
- [20] S. Kotochigova and E. Tiesinga. *Ab initio* relativistic calculation of the RbCs molecule. *Journal of Chemical Physics*, 123:174304, 2005.
- [21] P.W. Shor. Algorithms for quantum computation: discrete logarithms and factoring. In *Proceedings, 35<sup>th</sup> Annual Symposium on Foundations of Computer Science*, Los Alamitos, CA, 1994. IEEE Press.
- [22] P. Orth. Private communication.
- [23] A. Barenco, D. Deutsch, A. Ekert, and R. Josza. Conditional quantum dynamics and logic gates. *Physical Review Letters*, 74:4083, 1995.
- [24] Ph. Courteille, R.S. Freeland, D.J. Heinzen, F.A. van Abeelen, and B.J. Verhaar. Observation of a Feshbach resonance in cold atom scattering. *Physical Review Letters*, 81:69, 1998.
- [25] J.L. Roberts, N.R. Claussen, J.P. Burke, C.H. Greene, E.A. Cornell, and C.E. Wieman. Resonant magnetic field control of elastic scattering in cold  $^{85}\text{Rb}$ . *Physical Review Letters*, 81:5109, 1998.
- [26] S. Inouye, M.R. Andrews, J. Stenger, H.J. Miesner, D.M. Stamper-Kurn, and W. Ketterle. Observation of Feshbach resonances in a Bose-Einstein condensate. *Nature*, 392:151, 1998.
- [27] D. Jaksch, C. Bruder, J.I. Cirac, C.W. Gardiner, and P. Zoller. Cold bosonic atoms in optical lattices. *Physical Review Letters*, 81:3108, 1998.
- [28] M. Greiner, O. Mandel, T. Esslinger, T.W. Hänsch, and I. Bloch. Quantum phase transition from a superfluid to a Mott insulator in a gas of ultracold atoms. *Nature*, 415:39, 2002.

- [29] B.C. Regan, E.D. Commins, C.J. Schmidt, and D. DeMille. New limit on the electron electric dipole moment. *Physical Review Letters*, 88(7):071805, 2002.
- [30] P.G.H. Sandars. The electric dipole moment of an atom. *Physics Letters*, 14(3):194–194, 1965.
- [31] O.P. Sushkov and V.V. Flambaum. Parity breaking effects in diatomic molecules. *Soviet Physics-JETP*, 48(4):608–611, 1978.
- [32] J.J. Hudson, B.E. Sauer, M.R. Tarbutt, and E.A. Hinds. Measurement of the electron electric dipole moment using YbF molecules. *Physical Review Letters*, 89(2):023003, 2002.
- [33] M.G. Kozlov and D. DeMille. Enhancement of the electric dipole moment of the electron in PbO. *Physical Review Letters*, 89(13):133001, 2002.
- [34] J.D. Weinstein, R. deCarvalho, T. Guillet, B. Friedrich, and J.M. Doyle. Magnetic trapping of calcium monohydride molecules at millikelvin temperatures. *Nature*, 395:148–150, 1998.
- [35] J.L. Bohn, A.V. Avdeenkov, and M.P. Deskevich. Rotational Feshbach resonances in ultracold molecular collisions. *Physical Review Letters*, 89:203202, 2001.
- [36] D. DeMille, D.R. Glenn, and J. Petricka. Microwave traps for cold polar molecules. *European Physical Journal D*, 31:375–384, 2004.
- [37] W. Paul. Electromagnetic traps for charged and neutral particles. *Reviews of Modern Physics*, 62(3):531–540, 1990.
- [38] J. van Veldhoven, H.L. Bethlem, and G. Meijer. ac Electric trap for ground state molecules. *Physical Review Letters*, 94:083001, 2005.
- [39] H.L. Bethlem, G. Berden, F.M.H. Crompvoets, R.T. Jongma, A.J.A van Roijji, and G. Meijer. Electrostatic trapping of ammonia molecules. *Nature*, 406:491–494, 2000.

- [40] M.S. Elioﬀ, J.J. Valentini, and D.W. Chandler. Subkelvin cooling NO molecules via “billiard-like” collisions with argon. *Science*, 302:1940–1943, 2003.
- [41] H.J. Metcalf and P. van der Straten. *Laser Cooling and Trapping*. Springer-Verlag New York, Inc., 1999.
- [42] P.D. Lett, R.N. Watts, C.I. Westbrook, W.D. Phillips, P.L. Gould, and H.J. Metcalf. Observation of atoms laser cooled below the doppler limit. *Physical Review Letters*, 61:169, 1988.
- [43] J. Dalibard and C.C. Tannoudji. Laser cooling below the doppler limit by polarization gradients: simple theoretical models. *Journal of the Optical Society of America B*, 6(11):2023–2045, 1989.
- [44] D. Sesko, T. Walker, C. Monroe, A. Gallagher, and C. Wieman. Collisional losses from a light-force atom trap. *Physical Review Letters*, 63(9):961–964, 1989.
- [45] G. W. King and J. H. Van Vleck. Dipole-dipole resonant forces. *Physical Review*, 55(11):1165–1172, 1939.
- [46] W. Ketterle, K. B. Davis, M. A. Joffe, A. Martin, and D. E. Pritchard. High densities of cold atoms in a dark spontaneous-force optical trap. *Physical Review Letters*, 70(15):2253–2256, 1993.
- [47] M. H. Anderson, W. Petrich, J. R. Ensher, and E. A. Cornell. Reduction of light-assisted collisional loss rate from a low-pressure vapor-cell trap. *Physical Review A*, 50(5):R3597–R3600, 1994.
- [48] K.E. Gibble, S. Kasapi, and S. Chu. Improved magneto-optic trapping in a vapor cell. *Optics Letters*, 17:526, 1992.
- [49] D. Budker, D.F. Kimball, and D.P. DeMille. *Atomic Physics: An Exploration through Problems and Solutions*. Oxford University Press, 2004.

- [50] Mitchel Weissbluth. *Atoms and Molecules*. Academic Press, 1978. Pages 551-555.
- [51] D.R. Bates and A. Damgaard. The calculation of the absolute strengths of spectral lines. *Philosophical Transactions of the Royal Society of London*, 242:101–122, 1949.
- [52] Gerhard Herzberg. *Molecular Spectra and Molecular Structure, Volume I- Spectra of Diatomic Molecules*. Krieger Publishing Company, second edition, 1950.
- [53] J.R. Taylor. *Scattering Theory*. John Wiley & Sons, Inc., 1972.
- [54] J. J. Sakurai. *Modern Quantum Mechanics*. Addison-Wesley Publishing Company, revised edition, 1994.
- [55] C.E. Fellows, R.F. Gutterres, A.P.C. Campos, J. Verges, and C. Amiot. The RbCs  $X^1\Sigma^+$  ground electronic state: New spectroscopic study. *Journal of Molecular Spectroscopy*, 197:19–27, 1999.
- [56] J.L. Bohn and P.S. Julienne. Semianalytic theory of laser-assisted resonant cold collisions. *Physical Review A*, 60:414, 1999.
- [57] P.S. Julienne. Cold binary atomic collisions in a light field. *Journal of Research of the National Institute of Standards and Technology*, 101:487, 1996.
- [58] H.R. Thorsheim, J. Weiner, and P.S. Julienne. Laser-induced photoassociation of ultracold Na atoms. *Physical Review Letters*, 58:2420, 1987.
- [59] C.M. Dion, C. Drag, O. Dulieu, L. Tolra, F. Masnou-Seeuws, and P. Pillet. Resonant coupling in the formation of ultracold ground state molecules via photoassociation. *Physical Review Letters*, 86:2253, 2001.
- [60] Gabbanini C, A. Fioretti, A. Lucchesini, S. Gozzini, and M. Mazzoni. Cold Rb molecules formed in a magneto-optical trap. *Physical Review Letters*, 84:2814, 2000.

- [61] A.N. Nikolov, J.R. Ensher, E.E. Eyler, H. Wang, W.C. Stwalley, and P.L. Gould. Efficient production of ground-state potassium molecules at sub-mK temperatures by two-step photoassociation. *Physical Review Letters*, 84:246, 2000.
- [62] R. Wynar, R.S. Freeland, D.J. Han, C. Ryn, and D.J. Heinzen. Molecules in a Bose-Einstein condensate. *Science*, 287:1016, 2000.
- [63] F.K. Fatemi, K.M. Jones, P.D. Lett, and E. Tiesinga. Ultracold ground-state molecule production in sodium. *Physical Review A*, 66:053401, 2002.
- [64] U. Schloder, C. Silber, T. Deuschle, and C. Zimmerman. Saturation in heteronuclear photoassociation of  $^6\text{Li}^7\text{Li}$ . *Physical Review A*, 66:061403R, 2002.
- [65] J.P. Shaffer, W. Chalupczak, and N.P. Bigelow. Photoassociative ionization of heteronuclear molecules in a novel two-species magneto-optical trap. *Physical Review Letters*, 82:1124, 1999.
- [66] H. Wang. Progress toward making ultracold heteronuclear RbCs molecules via photoassociation. *Bulletin of the American Physical Society*, 48:J1.025, 2003.
- [67] T. Bergeman, P.S. Julienne, C.J. Williams, E. Tiesinga, M.R. Manna, H. Wang, P.L. Gould, and W.C. Stwalley. Photoassociation in  $0_u^+$  and  $1_g$  states of  $\text{K}_2$ . *Journal of Chemical Physics*, 117:7491, 2002.
- [68] G.D. Telles, L.G. Marcassa, S.R. Muniz, S.G. Miranda, A. Antunes, C. Westbrook, and V.S. Bagnato. Trap loss in a two-species Rb-Cs magneto-optical trap. *Physical Review A*, 59:R23, 1998.
- [69] G.D. Telles, W. Garcia, L.G. Marcassa, V.S. Bagnato, D. Ciampini, M. Fazzi, J.H. Mller, D. Wilkowski, and E. Arimondo. Inelastic cold collisions of a Na/Rb mixture in a magneto-optical trap. *Physical Review A*, 63:033406, 2001.
- [70] L.G. Marcassa, G.D. Telles, S.R. Muniz, and V.S. Bagnato. Collisional losses in a K-Rb cold mixture. *Physical Review A*, 63:013413, 2001.



- [71] T.W. Hänsch and B. Couillaud. Laser frequency stabilization by polarization spectroscopy of a reflecting reference cavity. *Optics Communications*, 35:441, 1980.
- [72] T. Bergeman, C.E. Fellows, R.F. Gutterres, and C. Amiot. Analysis of strongly coupled electronic states in diatomic molecules: Low-lying excited states of RbCs. *Physical Review A*, 67:050501, 2003.
- [73] A.R. Allouche, M. Korek, K. Fakherddin, A. Chaalan, M. Dagher, F. Taher, and M. Aubert-Frecon. Theoretical electronic structure of RbCs revisited. *Journal of Physics B*, 33:2307, 2000.
- [74] A.J. Kerman, J.M. Sage, S. Sainis, T. Bergeman, and D. DeMille. Production of ultracold, polar RbCs\* molecules via photoassociation. *Physical Review Letters*, 92:033004, 2004.
- [75] C.H. Townes and A.L. Shawlow. *Microwave Spectroscopy*. McGraw-Hill Book Company, Inc., 1955.
- [76] H. Fahs, A.R. Allouche, M. Korek, and M. Aubert-Frecon. The theoretical spin-orbit structure of the RbCs molecule. *Journal of Physics B*, 35:1501, 2002.
- [77] B. Kim and K. Yoshihara. Resonance enhanced two photon ionization spectroscopy of RbCs in a very cold molecular beam. *Journal of Chemical Physics*, 100:1849–1857, 1994.
- [78] T. Bergeman, A.J. Kerman, J. Sage, S. Sainis, and D. DeMille. Prospects for production of ultracold  $X^1\Sigma^+$  RbCs molecules. *The European Physical Journal D*, 31:179, 2004.
- [79] D. Comparat, C. Drag, B. Laburth Tolra, A. Fioretti, P. Pillet, A. Crubellier, O. Dulieu, and F. Masnou Seeuws. Formation of cold Cs<sub>2</sub> ground state molecules through photoassociation in the  $1_u$  pure long-range state. *The European Physical Journal D*, 11:59, 2000.

- [80] C. Drag, B.L Tolra, O. Dulieu, D. Comparat, M. Vatasescu, S. Boussen, S. Guibal, A. Crubellier, and P. Pillet. Experimental versus theoretical rates for photoassociation and for formation of ultracold molecules. *IEEE Journal of Quantum Electronics*, 36:1378, 2000.
- [81] C.E. Hamilton, J.L. Kinsey, and R.W. Field. Stimulated emission pumping: New methods in spectroscopy and molecular dynamics. *Annual Review of Physical Chemistry*, 37:493, 1986.
- [82] D.E. Cooper, C.M. Klimcak, and J.E. Wessel. Ion dip spectroscopy: A new technique of multiphoton ionization spectroscopy applied to  $I_2$ . *Physical Review Letters*, 46:324, 1981.
- [83] T.P. Dinneen, C.D. Wallace, K.N. Tan, and P.L. Gould. Use of trapped atoms to measure absolute photoionization cross sections. *Optics Letters*, 17:1706, 1992.
- [84] Th. Weber, E. Riedle, and H.J. Neusser. Rotationally resolved fluorescence-dip and ion-dip spectra of single rovibronic states of benzene. *Journal of the Optical Society of America B*, 7:1875, 1990.
- [85] G. Igel-Mann, U. Wedig, P. Fuentelaba, and H. Stoll. Ground-state properties of alkali dimers XY (X, Y=Li to Cs). *Journal of Chemical Physics*, 84:5007–5012, 1986.
- [86] W.C. Stwalley. Efficient conversion of ultracold Feshbach-resonance-related polar molecules into ultracold ground state  $X^1\Sigma^+(v = 0)$ , ( $J = 0$ ) molecules. *European Physical Journal D*, 31:221–225, 2004.
- [87] H. Lefebvre-Brion and R.W. Field. *The Spectra and Dynamics of Diatomic Molecules*. Elsevier, 2004.
- [88] S. Inouye, J. Goldwin, M.L. Olsen, C. Ticknor, J.L. Bohn, and D.S. Jin. Observation of heteronuclear Feshbach resonances in a mixture of bosons and fermions. *Physical Review Letters*, 93:183201, 2004.

- [89] C. A. Stan, M.W. Zwierlein, C.H. Schunck, S.M.F. Raupach, and W. Ketterle. Observation of Feshbach resonances between two different atomic species. *Physical Review Letters*, 93:143001, 2004.
- [90] E.A. Donley, N.R. Claussen, S.T. Thompson, and C.E. Wieman. Atom-molecule coherence in a Bose-Einstein condensate. *Nature*, 417:529, 2002.
- [91] T. Takekoshi, J.R. Yeh, and R.J. Knize. Quasi-electrostatic trap for neutral atoms. *Optics Communications*, 114:421–424, 1995.
- [92] S. Friebe, R. Scheunemann, J. Walz, T.W. Hänsch, and M. Weitz. Laser cooling in a CO<sub>2</sub>-laser optical lattice. *Applied Physics B*, 67:699–704, 1998.
- [93] P. Staunum, S.D. Kraft, J. Lange, R. Wester, and M. Weidemüller. Experimental investigation of ultracold atom-molecule collisions. *Physical Review Letters*, 96:023201, 2006.
- [94] N. Zahzam, T. Vogt, M. Mudrich, D. Comparat, and P. Pillet. Atom-molecule collisions in an optically trapped gas. *Physical Review Letters*, 96:023202, 2006.